TECHNISCHE UNIVERSITÄT MÜNCHEN

Max-Planck-Institut für Astrophysik

Synthetic spectra and light curves of Type Ia supernovae

Markus Kromer

Vollständiger Abdruck der von der Fakultät für Physik der Technischen Universität München zur Erlangung des akademischen Grades eines

Doktors der Naturwissenschaften (Dr. rer. nat.)

genehmigten Dissertation.

Vorsitzender:		Univ.-Prof. Dr. L. Oberauer
Prüfer der Dissertation:		
	1.	Hon.-Prof. Dr. W. Hillebrandt
	2.	Univ.-Prof. Dr. W. Weise

Die Dissertation wurde am 23.09.2009 bei der Technischen Universität München eingereicht und durch die Fakultät für Physik am 27.11.2009 angenommen.

Contents

List of Figures

List of Tables

1 Introduction

Ever since the dawn of mankind people have been fascinated by the myriads of stars twinkling on a clear night sky, asking questions such as “What are those objects and how do they work?”. Although these questions were mainly of spiritual nature in ancient times, even then people followed closely the movements of the Sun and the Moon to calculate the calendar. This was of great importance not only for religious celebrations but also to determine the sowing dates [see e.g. the recently discovered sky disc of Nebra (Meller 2003, Schlosser 2003), which dates back to 1600 B.C.].

In making these observations our ancestors realized quite early that the night sky is not immutable. They observed the planets on their periodical orbits on the sky and learned to predict their movements. Besides these regular moving objects they also discovered “guest stars” which appeared suddenly and faded away after some time: these objects – some of them so bright that they have been visible at daytime – were named novae as a shorthand note for the Latin stellae novae (i.e. new stars).

It took until the 20th century to realize, that these novae are not a unique class of objects. Based on the observation of (super)nova S Andromedae in the Andromeda galaxy in 1885 (see de Vaucouleurs & Corwin 1985 for a historical review on this event), which appeared much brighter than earlier novae which had been observed in the Andromeda galaxy, Lundmark (1925) proposed two different classes of novae: an “upper” and a “lower” class different by about four orders of magnitude in brightness. Baade & Zwicky (1934) eventually introduced the name supernova to distinguish these bright events from the classical novae.

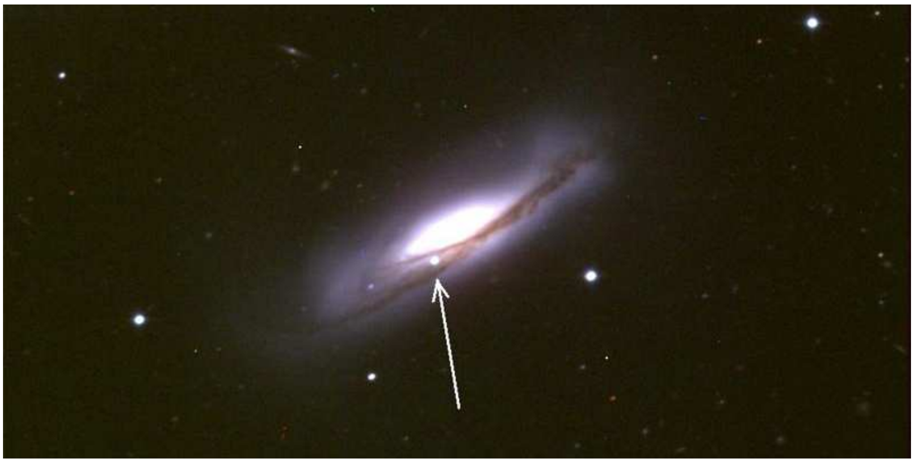

Figure 1.1: SN 2002bo in NGC 3190 (European Supernova Collaboration & Benetti et al. 2004).

Supernovae are characterized by a rapid rise (typically $\sim 20\,$days) in brightness and tremendous peak luminosities of $10^{42} \ldots 10^{43}$erg s^{-1}, comparable to the luminosity of an entire galaxy (see Figure 1.1). After maximum light they fade away over several years leaving behind a gaseous object, the supernova remnant. The total energy release in a supernova amounts to $10^{51} \ldots 10^{53}$ erg. This enormous energy represents a significant fraction of the energy bound in a star, which led to the idea that supernovae are associated with the death of stars (Baade & Zwicky 1934, Hoyle & Fowler 1960). The final fate of a star depends crucially on its initial mass M_i. For $M_\mathrm{i} \lesssim 8\,\mathrm{M}_\odot$ ($\mathrm{M}_\odot = 1.989 \cdot 10^{33}$ g denotes a solar mass, Unsöld & Baschek 2002) fusion processes in the stellar interior end with the burning of helium to carbon and instabilities during the final burning phases lead to a large mass loss. Thus the total mass of those stars falls below the Chandrasekhar limit and the degenerate-electron pressure can stabilize their cores against gravity such that they end as White Dwarfs (Chandrasekhar 1931). For $M_\mathrm{i} \gtrsim 8\,\mathrm{M}_\odot$ fusion goes all the way up to silicon burning which produces iron. Since iron has the largest binding energy of all elements, fusion cannot provide any further energy. Thus, those stars collapse under the influence of their gravitational forces, resulting in either a neutron star or a black hole. Due to the strong temperature dependence of the nuclear fusion reactions, more massive stars consume their fuel faster and thus live shorter lives (for a detailed discussion of stellar evolution see e.g. Kippenhahn & Weigert 1990).

In contrast, the less luminous classical novae are associated with phenomena due to mass transfer in close binary systems, the so-called cataclysmic variable stars (see Warner 1995 for a detailed discussion).

1.1 Supernova classification

Originating from the work of Minkowski (1941), the supernova classification scheme is still purely empirical and based on the optical spectra at maximum light [an up-to-date version according to Turatto (2003) is shown in Figure 1.2]. Minkowski (1941) separated the supernovae into two distinct classes – Type II and Type I – depending on whether they show or do not show hydrogen lines in their maximum light spectra, respectively.

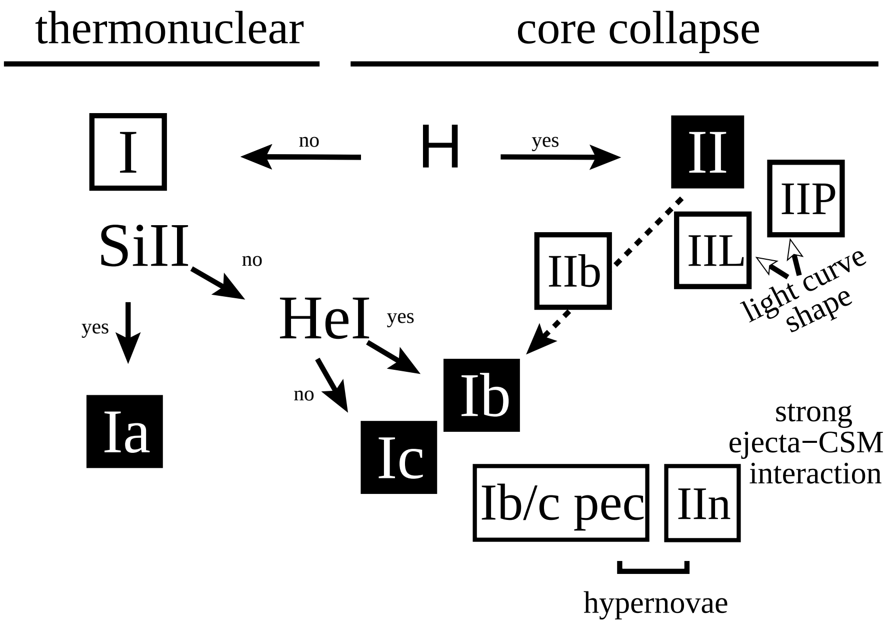

Figure 1.2: Supernova classification scheme according to Turatto (2003).

With the growing amount of observational data in the 1980s, it became obvious that the initially remarkably homogenous hydrogen-deficient Type I supernovae had to be distinguished further (e.g. Harkness & Wheeler 1990). By then Type I objects had been found, which did not show the strong absorption feature of Si II[1] characteristic for the majority of Type Is, now referred to as Type Ia. The objects without the Si II feature were separated into Type Ib or Type Ic depending on whether they show helium lines or not, respectively.

Type II events are less homogeneous. Thus the light curve shape is used as a further criterion to sub-categorize those events. Recently some objects have been discovered which show prominent hydrogen lines in early-time spectra but not in late-time spectra (Filippenko 1988, Matheson et al. 2000). These hybrid events, between Type II and Type Ib/c, are now referred to as Type IIb.

Figure 1.3 shows characteristic spectra of the different supernova types and their evolution with time (for a detailed discussion see e.g. Filippenko 1997). At early epochs supernova spectra are dominated by P-Cygni absorption profiles. Named after the luminous blue variable star P Cygni, in whose spectra they were first observed, these profiles are the characteristic feature of resonant line scattering in an expanding atmosphere above a photosphere. They consist of an absorption trough blue-shifted relative to the resonance wavelength of the line and an accompanying emission wing to the red. A qualitative explanation for this line profile is given in Figure 1.4.

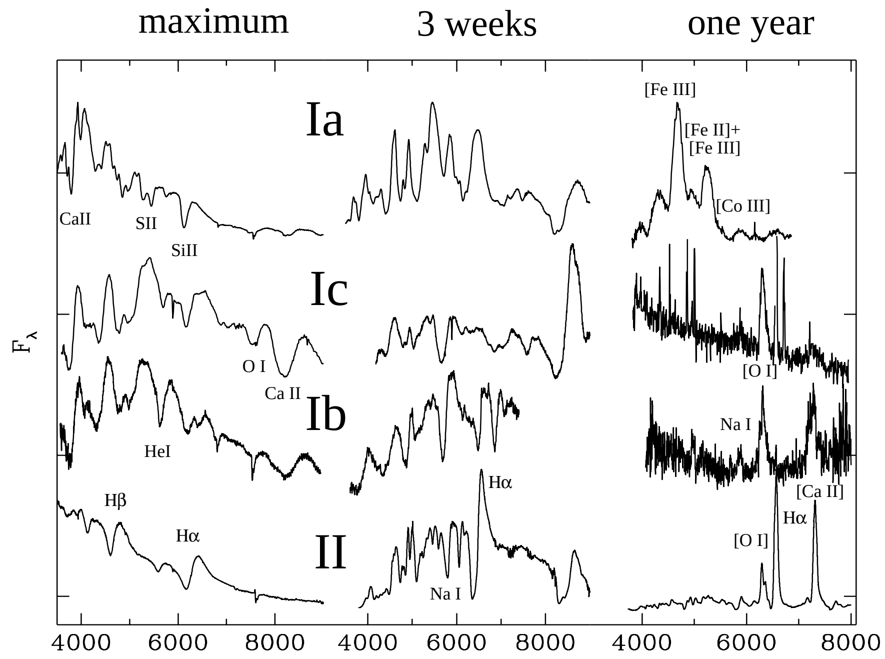

Figure 1.3: Characteristic spectra for the different supernova types at various epochs (Turatto 2003).

Type Ia supernovae around maximum light show prominent lines of singly ionized intermediate mass elements like calcium, silicon and sulphur. Characteristic is a strong absorption feature around 6150 Å which is due to a blue-shifted doublet of Si II at 6347 and 6371 Å ($4s\,^2S_{1/2} - 4p\,^2P_{1/2}$, $4s\,^2S_{1/2} - 4p\,^2P_{3/2}$), respectively. At later times iron-group elements become more important until

---

[1] In astrophysics it is common to denote the neutral state of an element X with X I. The following ionization states are then X II, X III and so on.

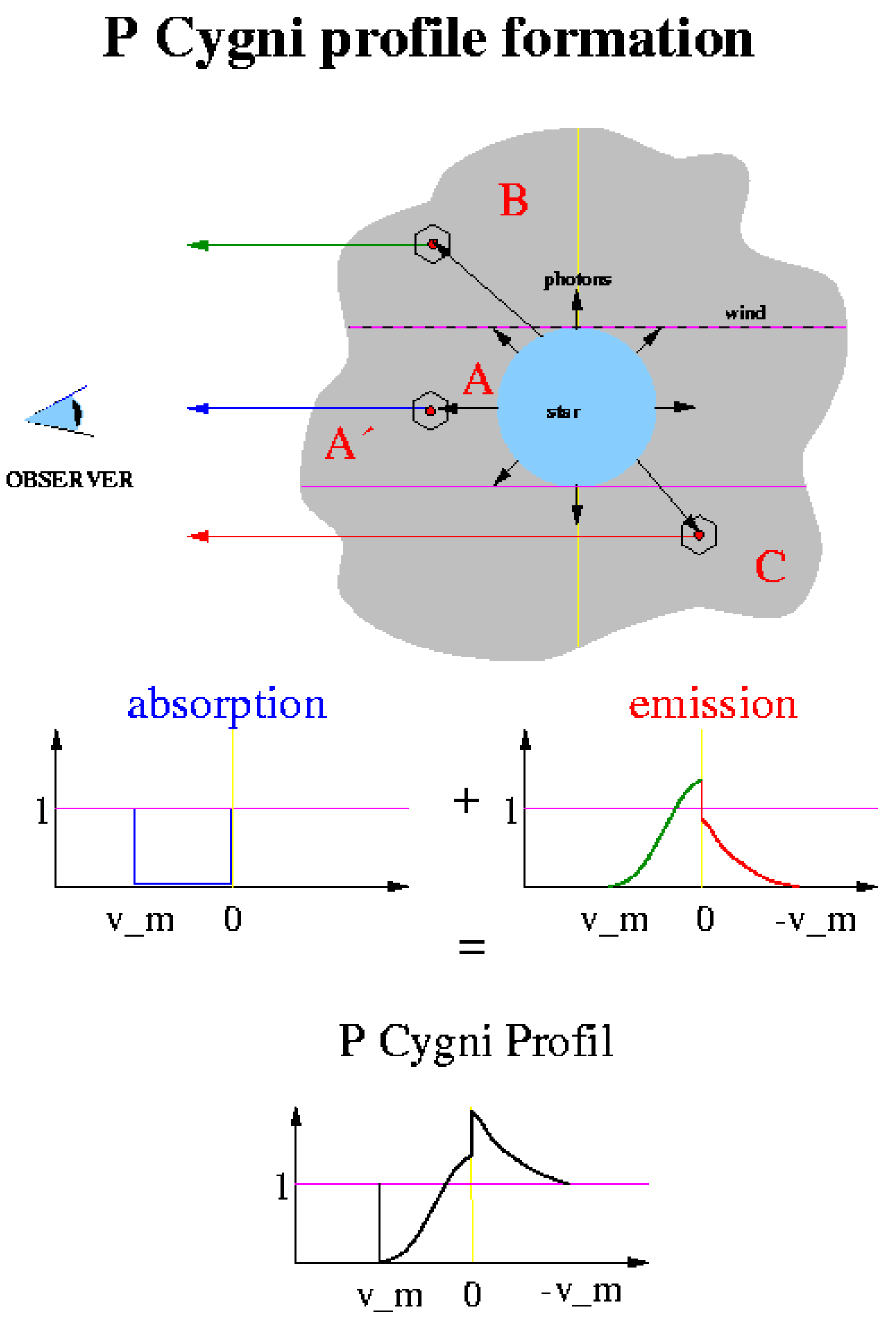

Figure 1.4: Qualitative explanation of the formation of a P-Cygni line profile. A photosphere emits a continuum to an expanding atmosphere (maximum velocity v_{m}). Photons initially emitted towards the observer (A) may be scattered out of his line-of-sight by resonance scattering in an atomic line transition. Since the atmosphere in that region is moving towards the observer, this leads to a blue-shifted absorption trough extended up to the maximum velocity v_{m}. At the same time photons initially not directed towards the observer can be scattered into the observer's line-of-sight. Depending on the projected velocity of the atmosphere this leads to a blue- (B) or red-shifted (C) emission wing. Since the material behind the star is occulted, the region from which emission at positive projected velocities occurs is slightly larger. Thus the blue-shifted emission is more pronounced than its red-shifted counterpart and the symmetry of the emission profile is distorted. Absorption and emission contributions together yield the characteristic P-Cygni profile of an outflow. (Image courtesy: J. Puls)

they completely dominate the spectra of the nebular phase through prominent blends of forbidden line transitions (i.e. transitions of higher order than an electrical dipole transition) of singly and doubly ionized iron. In the following forbidden line transitions of the i-th ionization stage of element X are denoted as $[\mathrm{X}\, i+1]$.

Type Ib/c spectra differ from this in not showing the characteristic Si II feature at maximum light. Type Ib instead show moderately strong helium lines (e.g. He I $\lambda 5876$[2], $1\mathrm{s}2\mathrm{p}\,^3\mathrm{P}-1\mathrm{s}3\mathrm{d}\,^3\mathrm{D}$). In the nebular phase, characterized by relatively unblended emissions of [O I] and [Ca II], the differences to Type Ia spectra are stronger. Type II spectra at maximum light are dominated by the hydrogen Balmer lines. In the nebular phase they are similar to Type Ib/c but also show prominent Hα emission.

Type Ia supernovae are observed in all types of galaxies including ellipticals (e.g. Turatto et al. 1994, Barbon et al. 1999). Since ellipticals have typically very old stellar populations, this shows that Type Ia supernovae cannot be related to the core collapse of massive stars (initial mass $M_\mathrm{i} \gtrsim 8\,\mathrm{M}_\odot$), which are short-lived objects. This is also in agreement with the absence of hydrogen and helium in Type Ia spectra. Being the only elements of which relevant amounts have been synthesized during the Big Bang, hydrogen and helium are the most abundant elements in the Universe. Most of the heavier elements originate from fusion processes in the stellar interiors. Thus their lack in Type Ia spectra and the features of highly processed material, which are observed instead, point to rather old progenitors that have lost their hydrogen and helium envelopes during their evolution. According to Hoyle & Fowler (1960) we are thus left with thermonuclear explosions of degenerate material as the most plausible origin of Type Ia supernova events. This also explains the lack of compact objects in remnants of Type Ia supernovae. The currently favoured progenitor systems are White Dwarfs in binary systems, which accrete matter from their companion stars (for a more detailed discussion of the progenitors scenarios of Type Ia supernovae see Section 2.3).

Supernovae of Type II and Ib/c occur predominantly in S0 and later galaxies in the Hubble classification scheme (Hubble 1936) and show a correlation with their spiral arms (e.g. Maza & van den Bergh 1976), indicating a dependence on recent star formation. This has led to their identification with the collapse of the iron cores of massive stars ($M_\mathrm{i} \gtrsim 8\,\mathrm{M}_\odot$), which become gravitationally unstable if nuclear burning ceases (Hoyle & Fowler 1960). Recently it has been speculated that some of the more peculiar events are pair-instability supernovae (see Heger et al. 2003 for a discussion).

The different Types of core-collapse supernovae, from II over Ib to Ic, are believed to form a sequence of increasing mass loss of the progenitor stars which leads to a stripping of the hydrogen (Type Ib) and hydrogen plus helium (Type Ic) envelopes. This mass loss may be caused by strong stellar winds or mass-transfer episodes to a possible binary companion. Since more massive stars develop stronger stellar winds, they undergo more violent mass-loss periods, indicating that the sequence of increasing mass loss from Type II over Ib to Ic correlates with a sequence of increasing initial mass of the progenitor star. Further heterogeneity of the different types is attributed to the actual mass-loss history the progenitor system underwent.

We note that ultimately all types of supernovae are triggered by gravitational forces.

---

[2] In the following λ accompanied by a number denotes a wavelength in Ångströms. $\lambda\lambda$ accompanied by multiple comma separated numbers denotes multiple wavelengths.

1.2 Astrophysical impact

Being among the brightest objects in the Universe and connecting stellar evolution, explosive nucleosynthesis and radiative transfer, supernovae are well worth studying on their own merit. However, they also have a strong influence on their environments by releasing metal-rich[3] material, which was created by nuclear reactions in the progenitor star or in the explosion itself, into the interstellar medium, thus contributing to the chemical enrichment of the Galaxy (Chiappini et al. 2001). Type Ia supernovae are believed to be the main producers of iron in the Universe, making them a convenient tool to measure the metal enrichment of matter. Core-collapse supernovae produce mainly α-elements. Thus, owing to the different life-times of the different progenitor stars – the more massive progenitors of core-collapse supernovae are significantly short-lived compared to those of Type Ia – the relative abundances of α-elements and iron-group elements follow a characteristic relationship (Renzini 1999).

By their dynamical interaction with the interstellar medium, due to the explosion shock waves, supernovae also play an important role in the star formation history of galaxies (Efstathiou 2000), leading to mass loss and both triggering and quenching bursts of star formation. The interaction regions of supernova shock waves and the interstellar medium are also believed to be the accelerators of the galactic component of the cosmic rays (Koyama et al. 1995), which are among the highest energy particles in the Universe. The intrinsic brightness of supernovae makes them furthermore ideal tools to study the star formation history of the Universe out to large distances (Madau et al. 1998).

The enormous luminosities and the, at that time, rather homogeneous sample of supernovae led already Wilson (1939) and Zwicky (1939) to suggest to use these objects to measure cosmic distances via their luminosity distance

$$d_{\mathrm{L}} = \sqrt{\frac{L}{4\pi F}}. \tag{1.1}$$

This "standard candle" method makes use of the fact that the distance to an object of known absolute luminosity L can be derived from the observed flux F. Astronomical distance measurements rely strongly on such standard candles. This is mainly due to the fact that direct distance measurements, applying the parallax method, are only possible up to distances of $\sim 1\,\mathrm{kpc}$. For larger distances different types of standard candles of increasing intrinsic luminosity are used (among them luminous variable stars like RR Lyrae or δ Cephei, for which an empirical relation between their absolute luminosity and pulsation period was found and Type Ia supernovae are most prominent). Calibrating standard candles in our near neighbourhood, where parallax measurements are available, makes it then possible to determine distances to objects farther away (RR Lyrae $\sim 100\,\mathrm{kpc}$, Cepheids $\sim 1\,\mathrm{Mpc}$). These are in turn used to calibrate brighter standard candles as e.g. Type Ia supernovae, for which no direct distance measurements are available, but which can be measured further out since they are intrinsically more luminous. This step-by-step method is referred to as the cosmological distance ladder (Rowan-Robinson 1985).

With the availability of more and better observational data, however, the assumption of a global homogeneity of all supernovae had to be dropped rather early, but up to the 1980s there was still the hope that the remarkably homogeneous sample of Type Ia supernovae could be used as standard

---

[3] In astrophysics all elements heavier than helium are referred to as metals.

candles. This became dubious with the increased efforts for finding nearby Type Ia supernovae which led to the discovery that they show quite a large scatter in peak luminosity. Nevertheless Phillips (1993), based on earlier assumptions (Barbon et al. 1973, Pskovskii 1977), succeeded in deriving empirical relations to calibrate the peak luminosity of Type Ia supernovae by distance independent light curve properties, thus making them "standardizeable candles". He considered only spectroscopically normal Type Ia supernovae (see Section 2.1.1) and found that their absolute peak magnitude in the B band is correlated with their light-curve decline rate – expressed by the parameter $\Delta m_{15}(B)$, which gives the change in B-band magnitude between maximum light and 15 days thereafter (Figure 1.5). This method has been refined (Phillips et al. 1999) and additional criteria connecting light curve shape and peak luminosity have been incorporated (Riess et al. 1996, Perlmutter et al. 1997, Guy et al. 2005), making Type Ia supernovae currently the best distance indicators beyond the Virgo cluster (Leibundgut 2000). Hicken et al. (2009) have shown that the different methods agree quite well in light curve shape and reddening/colour parameters.

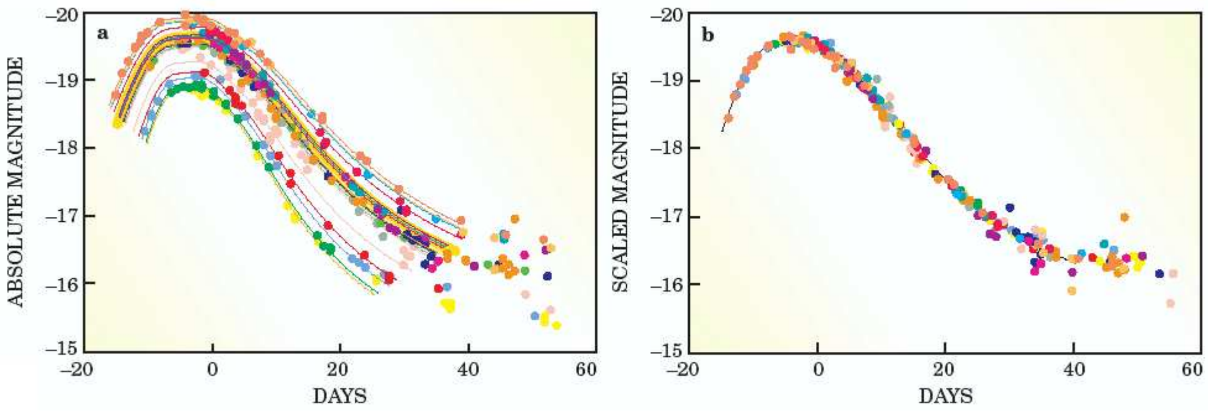

Figure 1.5: Light curve width-luminosity relation of Type Ia supernovae (Perlmutter 2003). The left panel shows light curves of Type Ia supernovae as observed. Although many of them populate the yellow band, there is non negligible scatter around it. After correcting for the width-luminosity relation the light curves agree remarkably well and reach about the same peak magnitudes (right panel).

Leibundgut (2001) identified two different regimes for cosmological applications of Type Ia supernovae. The first is the determination of the current expansion rate of the Universe in the local Hubble flow (Hubble 1929), given by the Hubble constant H_0. For redshifts $z < 0.1$ the relation between the luminosity distance and the redshift can be expressed, in the zeroth-order approximation, as

$$d_\mathrm{L} = \frac{cz}{H_0}. \tag{1.2}$$

In the ideal case of exactly known redshift and absolute luminosity (and thus d_L) of a distant object, this allows the derivation of H_0 from a single observation. In reality, however, neither z nor d_L are exactly known, but H_0 can be inferred statistically from a sample of distant objects. The calibration of the absolute luminosities of the supernovae is achieved by applying the cosmological distance ladder. An alternative would be the use of models which predict the absolute luminosity of the supernovae. But so far the models are not exact enough to do so and only lower limits for H_0 can be derived by this approach (Stritzinger & Leibundgut 2005).

In the second regime Type Ia supernovae at larger redshifts ($z \gtrsim 0.1$) can be used to probe the expansion history of the Universe. There the zeroth-order approximation for the luminosity distance breaks down and d_L must be obtained from an integration over the line-of-sight of the photon propagation. Assuming that the Cosmological Principle holds, which states that the Universe is homogeneous and isotropic on large scales ($\gtrsim 100\,\mathrm{Mpc}$), this is given by a radial null geodesic of the Robertson-Walker metric (see e.g. Misner et al. 1973). For an expanding universe with a cosmological constant Carroll et al. (1992) derive

$$d_\mathrm{L} = \frac{(1+z)\,c}{H_0\,|\Omega_\mathrm{k}|^{1/2}}\mathcal{S}\left\{|\Omega_\mathrm{k}|^{1/2}\int_0^z \left(\Omega_\mathrm{k}\left(1+z'\right)^2 + \Omega_\mathrm{m}\left(1+z'\right)^3 + \Omega_\Lambda\right)^{-1/2}\mathrm{d}z'\right\}, \tag{1.3}$$

where $\Omega_\mathrm{k} = \rho_\mathrm{k}/\rho_\mathrm{c}$, $\Omega_\mathrm{m} = \rho_\mathrm{m}/\rho_\mathrm{c}$ and $\Omega_\Lambda = \rho_\Lambda/\rho_\mathrm{c}$ are the contributions of the curvature, matter and cosmological constant to the energy density in the Universe relative to the critical density ρ_c for a flat universe. Note that the curvature term Ω_k relates to the others by $\Omega_\mathrm{k} = 1 - \Omega_\mathrm{m} - \Omega_\Lambda$. $\mathcal{S}(x)$ is given by

$$\mathcal{S}(x) = \begin{cases} \sin(x) & \Omega_\mathrm{k} < 0 \\ x & \Omega_\mathrm{k} = 0 \\ \sinh(x) & \Omega_\mathrm{k} > 0. \end{cases} \tag{1.4}$$

Thus d_L depends directly on the energy content of the Universe, which can be determined, if the redshifts z and luminosity distances d_L for a sample of distant objects have been determined independently. Note that here the absolute luminosity is not needed, in contrast to the case for the determination of H_0. However, H_0 itself enters the calculation as a parameter.

Using the above mentioned light curve width-luminosity relation to calibrate the luminosities of Type Ia supernovae, this approach has been applied by different groups (Riess et al. 1998, Perlmutter et al. 1999). Based on a very small sample, they found independently that Type Ia supernovae at $z \sim 0.5$ appear ~ 0.2 mag fainter than expected in an empty universe ($\Omega = 0$), indicating an accelerated expansion driven by some sort of "dark energy", which has a negative pressure like Einstein's cosmological constant (Einstein 1917, Weinberg 1989, Carroll et al. 1992, Turner & Tyson 1999)[4]. At about the same time, measurements of the anisotropies of the cosmic microwave background (de Bernardis et al. 2000) revealed, that our Universe is flat (i.e. $\Omega_\mathrm{k} = 0$). Together these results led to the currently favoured concordance cosmology with $\Omega_\Lambda = 0.7$ and $\Omega_\mathrm{m} = 0.3$. Follow-up studies using supernovae (e.g. Astier et al. 2006, Riess et al. 2007, Wood-Vasey et al. 2007, Kowalski et al. 2008; see Figure 1.6), the cosmic microwave background (e.g. Dunkley et al. 2009) and baryon acoustic oscillations (e.g. Eisenstein et al. 2005) confirmed these results.

After the discovery of the acceleration by Riess et al. (1998) and Perlmutter et al. (1999), it was hotly debated whether it was real. The main points of criticism concerned the small sample sizes, difficulties in the photometric calibration of the data, the treatment of the extinction correction due to dust in the supernova host galaxies, the empirical calibration of the peak luminosities and possible evolutionary effects in the supernova Ia sample over the look-back time. Thanks to the significantly increased sample sizes and the improved observational techniques, many of these points have been resolved. Moreover, the Hubble Space Telescope recently detected Type Ia supernovae

---

[4] Actually it was already noted in the early 1990s (e.g. Efstathiou et al. 1990; Ostriker & Steinhardt 1995), that different cosmological measurements, including large scale structure surveys, indicated that a non-zero cosmological constant could solve many of the problems of the standard cold dark matter model, favoured at that time.

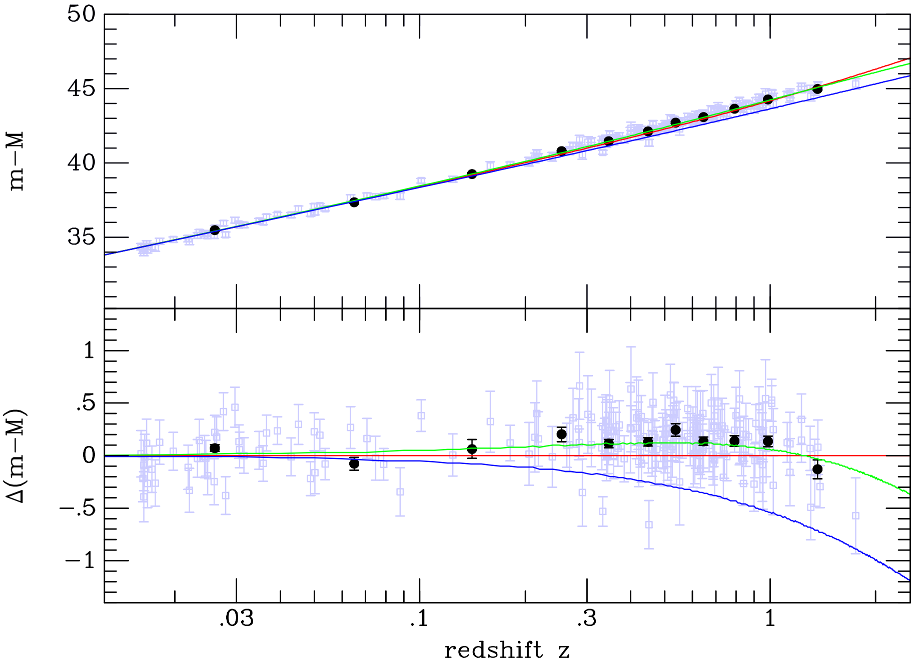

Figure 1.6: The Hubble diagram of Type Ia supernovae, showing distance modulus $[m - M = 5\log(d_{\rm L}/10\,{\rm pc})]$ vs. redshift (Leibundgut 2008). The black points are binned median values to guide the eye. The green line indicates the currently favoured concordance cosmology ($\Omega_\Lambda = 0.7$, $\Omega_{\rm m} = 0.3$). For comparison an empty universe ($\Omega_\Lambda = \Omega_{\rm m} = 0$, red) and an Einstein-de-Sitter universe ($\Omega_\Lambda = 0$, $\Omega_{\rm m} = 1$) are shown. The bottom panel shows the residuals relative to an empty universe.

at $z \sim 1.5$ (Riess et al. 2004, Riess et al. 2007), which clearly indicate that at very early times the expansion of the Universe was not accelerating but decelerating. This provides further confidence in the applied methods, since this argues against a simple bias introduced by evolutionary effects of Type Ia progenitors with time.

The discovery of the accelerated expansion of the Universe tells us that there is some sort of dark energy contributing to the energy budget, but does not explain the physical reason behind it. Currently it is hotly debated if the dark energy is caused by the vacuum energy density, which could be related to Einstein's cosmological constant or if more exotic “quintessence” models (Caldwell et al. 1998) are required. The different models can be discriminated by different values for their equation-of-state parameter w which relates pressure p and density ρ ($p = w\rho c^2$). While a cosmological constant is characterized by $w = -1$, quintessence models have a time-dependent w (for comparison w is 0 for non-relativistic matter and 1/3 for radiation). By extending the sample sizes, it is possible to constrain different kinds of dark energy models. Thus ongoing supernova surveys such as ESSENCE (Wood-Vasey et al. 2007) and SNLS (Astier et al. 2006), were able to show, that the present day value of w is close to -1 (within $\sim$ 10% errors). In the current surveys, statistical and systematical errors contribute at comparable levels. It is conceivable, however, that with the growing sample sizes of the upcoming surveys systematical errors are going to dominate over pure statistical errors and thus limit the accuracy of the method.

To constrain the time evolution of w and further distinguish between the different dark energy models the absolute magnitudes must be determined to an accuracy of $\sim 0.02\,$mag (Kowalski et al. 2008). This requires an improved control on systematical errors. For a detailed discussion of this, see e.g. the review by Leibundgut (2001). We give here only a very brief summary. From an observational point of view the main effects contributing to the systematical error are the uncertainty of photometric zero points and K-corrections. The latter are required to convert the observed photometry to the supernova rest frame to make different supernovae comparable (see e.g. Leibundgut 1990, Jha et al. 2007). From an astrophysical point of view the extinction of supernovae due to dust in their host galaxies and the Milky Way, a secular evolution of the Type Ia progenitors, selection biases in the surveys, gravitational lensing or an uncertainty in the local Hubble flow are possible error sources.

1.3 Objective of this thesis

The rising interest in Type Ia supernovae, due to their cosmological applications, has led to a plethora of new observational data in the last decade. While up to the 1980s only a few extragalactic supernovae had been discovered per year, in the 1990s the appearance of CCD detectors and automated search programs such as the Calan/Tololo Supernova Search (Hamuy et al. 1993) has led to the discovery of ~ 50 events per year. Today, thanks to the large search programs as e.g. the SDSS (Sloan Digital Sky Survey) Supernova Survey[5], the Lick Observatory Supernova Search[6] or the Nearby Supernova Factory[7], about 500 supernovae are detected per year.

Despite this substantial increase in the available data and the significant progress, which has been made in the theoretical modelling of Type Ia supernovae in the last years (see Hillebrandt & Niemeyer 2000 and references therein), there are still many open questions concerning the physical mechanisms behind these explosions, which we discuss in Chapter 2. These relate to the nature of their progenitor systems (see e.g. Livio 2000), which are still uncertain, the ignition conditions (Woosley et al. 2004) and the actual explosion mechanism (Hillebrandt & Niemeyer 2000). These questions cast a shadow on the purely empirical relations which are used to calibrate the peak luminosity of Type Ia supernovae for the cosmological distance measurements. In particular the questions of whether all Type Ia events arise from the same type of progenitor system or if different populations contribute to the progenitors as indicated by studies of supernova rates (Mannucci et al. 2005, Scannapieco & Bildsten 2005) are of vital interest. Also precision measurements of the cosmic expansion history, as intended by future supernova surveys, require a handle of the systematic errors arising from the diversity in Type Ia supernovae.

To solve these problems a thorough theoretical understanding of Type Ia supernovae is needed. This requires both further observational efforts and refined models. Today, fully three-dimensional (3D) explosion models (e.g. Reinecke et al. 2002, Gamezo et al. 2003, Röpke & Hillebrandt 2005, Röpke & Niemeyer 2007) are the state-of-the-art and have shown that 3D effects are essential to properly simulate the instabilities and turbulence effects which drive the thermonuclear combustion (see Section 2.4). Furthermore they show that ejecta asymmetries can arise, either by hydrodynamical instabilities during the burning phase or an asymmetric ignition (Höflich & Stein 2002, Kuhlen et al. 2006).

---

[5] http://sdssdp47.fnal.gov/sdsssn/sdsssn.html

[6] http://astro.berkeley.edu/∼bait/kait.html

[7] http://snfactory.lbl.gov/

However these simulations – which give velocities, densities and composition of the explosion ejecta – are not directly comparable to observations of real Type Ia supernovae. For that purpose synthetic spectra and light curves must be obtained by radiative transfer calculations. This requires a solution of the multi-line transfer problem in expanding media where the opacity is dominated by the wealth of lines associated with the iron-group elements which were synthesized in the thermonuclear explosion (an introduction to the theory of radiative transfer is given in Chapter 3). Many 1D studies have addressed this problem in the past either assuming pure resonance scattering (e.g. Branch et al. 1982, Branch et al. 1983, Mazzali & Lucy 1993) or pure absorption (e.g. Jeffery et al. 1992) in the lines. Lucy (1999b) introduced an approximate treatment of line fluorescence. But that work is still in 1D as are the studies done with the general-purpose radiation transport code PHOENIX (e.g. Lentz et al. 2001). Recently following Lucy (2005), Kasen et al. (2006) described a 3D time-dependent radiative transfer code which is capable of treating line fluorescence in an approximate way (similar to Lucy 1999b, Pinto & Eastman 2000b).

Such studies have shown that to address the complexity of the hydrodynamic explosion models a 3D treatment of radiative transfer which simulates the γ-deposition and spectrum formation in detail is needed. In particular, a careful treatment of the ionization balance and a proper simulation of the redistribution of flux by line fluorescence (crucial for the near-infrared light curves, see Kasen 2006) is essential. During this thesis we developed a new Monte Carlo code (ARTIS, Applied Radiative Transfer In Supernovae) which, based on the approach of Lucy (2002, 2003, 2005), solves the time-dependent 3D radiative transfer problem in chemically inhomogeneous models of supernova ejecta from first principles using a generalized treatment of line formation and prioritizing a detailed treatment of ionization. The radiative transfer calculation is parameter-free, depending only on the input model and atomic data, giving a maximum of predictive power for a given hydrodynamical model. Details of this code are given in Chapter 4.

In Chapter 5 we test this code using two simply-parameterized explosion models and compare our results to observations and earlier synthetic studies. Moreover, we discuss the basic effects of different approximations concerning the treatment of the plasma state incorporated to our code and investigate the influence of completeness of atomic data. Finally, line-of-sight dependent spectra and light curves are calculated to demonstrate the multi-dimensional capabilities of our code and to study the effect of large scale asymmetries of explosion ejecta.

In Chapter 6 we apply our code to hydrodynamical simulations of different explosion models which have been carried out within the supernova group at the Max-Planck-Institut für Astrophysik (MPA) and derive synthetic observables. Using these, we discuss the outcome of the different models and compare them to the observational data. In Chapter 7 we finally summarize our work and draw conclusions before giving an outlook on future work.

2 Thermonuclear supernovae

Since this thesis deals only with thermonuclear supernovae, i.e. those of Type Ia (in the following abbreviated as SNe Ia), this chapter provides an overview of our current understanding of these objects. Following a summary of their observational characteristics, the potential progenitor scenarios and explosion mechanisms are presented.

2.1 Observational characteristics

2.1.1 Spectra

As already discussed in Section 1.1, the spectra of SNe Ia are characterized by the absence of hydrogen and helium lines and a strong absorption feature around 6150 Å due to the Si II doublet $\lambda\lambda6347, 6371$ at maximum light. A large fraction ($\sim 70\%$, Li et al. 2001) of the observed events shows both remarkably similar spectra at maximum light and almost identical spectral evolution as the example shown in Figure 2.1. These are the so-called spectroscopically normal or Branch-normal SNe Ia (Branch et al. 1993). Prominent well-observed examples of this sub-class are SNe 1994D, 2001el and 2005cf.

Besides the characteristic silicon feature, another doublet of Si II ($\lambda\lambda5958, 5979$; $4\mathrm{p}\,^2\mathrm{P}_{1/2} - 5\mathrm{s}\,^2\mathrm{S}_{1/2}$, $4\mathrm{p}\,^2\mathrm{P}_{3/2} - 5\mathrm{s}\,^2\mathrm{S}_{1/2}$) and several other lines of intermediate-mass elements show up in the maximum light spectra, e.g. the H and K lines and the near-infrared (NIR) triplet of Ca II at $\lambda\lambda3934, 3968$ ($4\mathrm{s}\,^2\mathrm{S}_{1/2} - 4\mathrm{p}\,^2\mathrm{P}_{3/2}$, $4\mathrm{s}\,^2\mathrm{S}_{1/2} - 4\mathrm{p}\,^2\mathrm{P}_{1/2}$) and $\lambda\lambda8498, 8542, 8662$ ($3\mathrm{d}\,^2\mathrm{D}_{3/2} - 4\mathrm{p}\,^2\mathrm{P}_{3/2}$, $3\mathrm{d}\,^2\mathrm{D}_{5/2} - 4\mathrm{p}\,^2\mathrm{P}_{3/2}$, $3\mathrm{d}\,^2\mathrm{D}_{3/2} - 4\mathrm{p}\,^2\mathrm{P}_{1/2}$), respectively. There are also prominent features of Mg II ($\lambda4481$; $3\mathrm{d}\,^2\mathrm{D} - 4\mathrm{f}\,^2\mathrm{F}$), O I ($\lambda\lambda7772, 7774, 7775$; $2\mathrm{p}^3\left(^4\mathrm{S}\right)3\mathrm{s}\,^5\mathrm{S}_2 - 2\mathrm{p}^3\left(^4\mathrm{S}\right)3\mathrm{s}\,^5\mathrm{P}_3$, $2\mathrm{p}^3\left(^4\mathrm{S}\right)3\mathrm{s}\,^5\mathrm{S}_2 - 2\mathrm{p}^3\left(^4\mathrm{S}\right)3\mathrm{s}\,^5\mathrm{P}_2$, $2\mathrm{p}^3\left(^4\mathrm{S}\right)3\mathrm{s}\,^5\mathrm{S}_2 - 2\mathrm{p}^3\left(^4\mathrm{S}\right)3\mathrm{s}\,^5\mathrm{P}_1$) and S II ($\lambda\lambda5468, 5612, 5654$), the latter being blends of several lines. From their blue-shifted P-Cygni absorption troughs (see Figure 1.4) we see that the supernova is expanding and expansion velocities of up to $20\,000\,\mathrm{km\,s^{-1}}$ can be inferred for the ejecta (e.g. Branch et al. 2005). Thus, the density of the ejecta decreases with time and the regions in which the line interactions take place recede deeper into the ejecta. Observationally reflected in a decreasing blue-shift of the absorption features with time, this shows that the velocity in the ejecta decreases from outside-in. Thus, different velocities in absorption features of different elements indicate that they form at different depths of the ejecta. This is used to infer the abundance stratification in the ejecta of individual supernovae by detailed studies of their spectral evolution (abundance tomography, Stehle et al. 2005).

The recession of the line forming regions with time also causes the weakening (and finally disappearance of some) of the features associated with the intermediate-mass elements. Instead, a multitude of strongly blended singly-ionized iron-group elements (mostly Fe II, Co II) start to dominate the

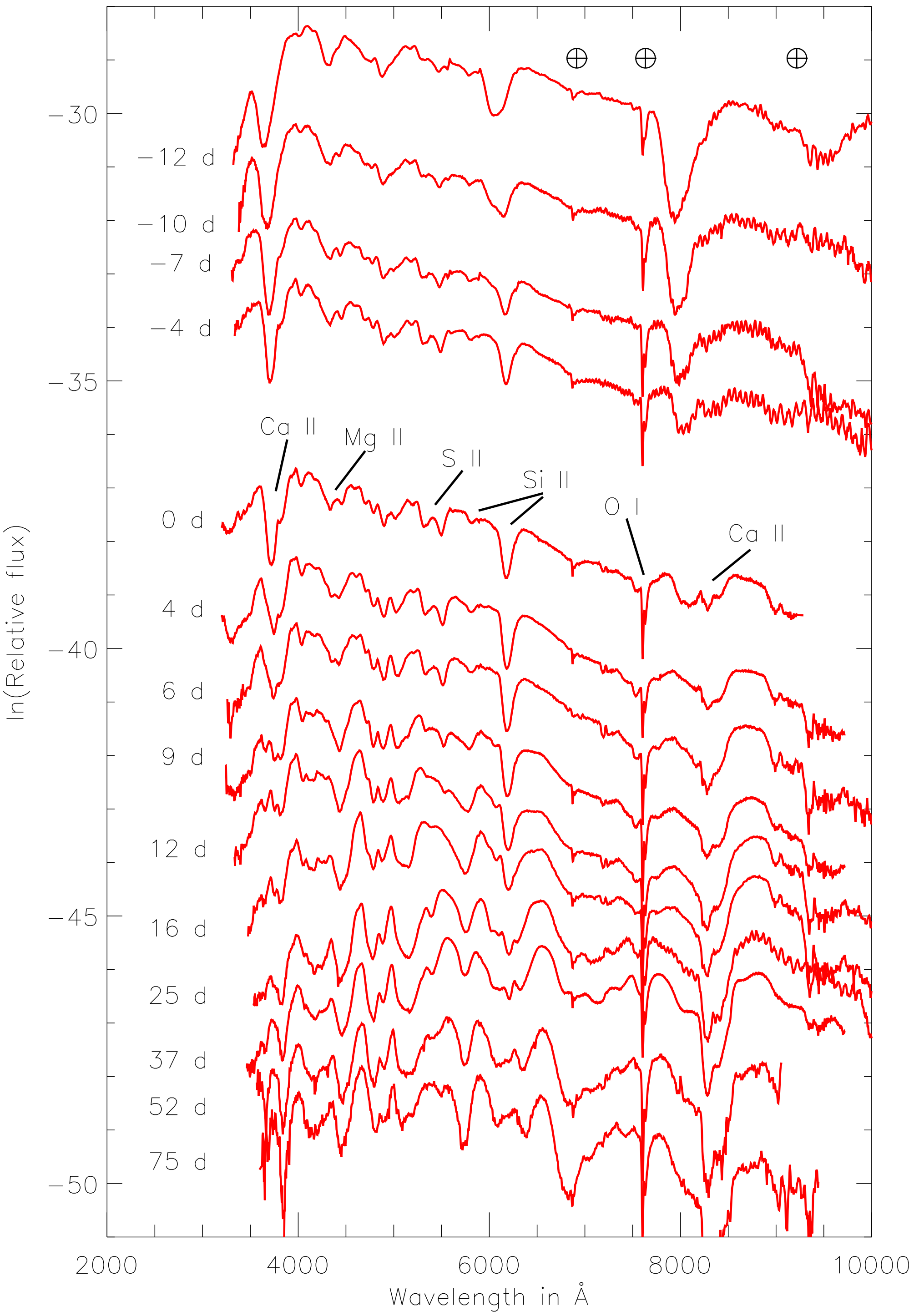

Figure 2.1: Spectral evolution of SN 2005cf as an example of a normal SN Ia (spectra from Garavini et al. 2007; times are relative to *B* band maximum). The absorption features discussed in the text are identified for the maximum light spectrum. Main telluric absorption features are indicated by ⊕.

spectra, indicating an iron-group dominated composition of the ejecta core. The combination of the high ejecta velocities and the wealth of UV and blue lines associated with the iron-group elements, leads also to the suppression of flux in the UV part of the spectrum. This is known as line-blocking.

Even later (~ 100 d) after maximum light, the spectra start to become dominated by emission in forbidden line transitions of [Fe III] and [Co III]. By then the ejecta have expanded sufficiently that they are optically thin and, due to the low densities in the dilute plasma, collisional deexcitations are too weak to balance collisional excitations and non-thermal excitations by γ-rays from the decay of radioactive nuclides. Then spontaneous radiative deexcitations become important, leading to radiative cooling in forbidden lines. Kuchner et al. (1994) showed, that the ratio of [Co III] to [Fe III] emission evolves according to the abundance ratio of cobalt and iron characteristic for the radioactive decay of $^{56}\mathrm{Co} \rightarrow {}^{56}\mathrm{Fe}$. Together with the time-scale of the exponential decay of the late-time light curves of SNe Ia (Section 2.1.2), this strongly supports the hypothesis that the energetic display of SNe Ia is powered by the radioactive decay of $^{56}\mathrm{Ni} \rightarrow {}^{56}\mathrm{Co} \rightarrow {}^{56}\mathrm{Fe}$ (Truran et al. 1967, Colgate & McKee 1969).

The large search programs for nearby supernovae in the last years led to the discovery of a variety of spectroscopically peculiar SNe Ia in addition to the Branch normals. Although sharing the main characteristics of SNe Ia, some of them seem to form distinct sub-classes on their own. Among the most-luminous SNe Ia a group of events similar to SN 1991T emanates (Filippenko et al. 1992, Jeffery et al. 1992, Phillips et al. 1992, Mazzali et al. 1995, Lira et al. 1998, Altavilla et al. 2004). These are referred to as 1991T-like objects. Compared to the bulk of the normal SNe Ia, these are brighter by 0.3 mag and show spectra dominated by doubly-ionized states around maximum light. Later their spectra become very similar to normal SNe Ia.

In contrast, the 1991bg-like objects (with SN 1991bg as the archetypical event; Filippenko et al. 1992, Leibundgut et al. 1993, Turatto et al. 1996, Mazzali et al. 1997) are dimmer by about ~ 2 mag compared to Branch normals. Their spectra are generally redder and show a strong absorption-trough redward of 4000 Å due to a blend of lines of Ti II, which is not observed in normal SNe Ia. Moreover, the $\lambda\lambda 7772, 7774, 7775$ feature of O I is much more prominent in these objects and $\mathcal{R}\,(\mathrm{Si})$, denoting the relative strength of the Si II features at $\lambda\lambda 5958, 5979$ to $\lambda\lambda 6347, 6371$, is larger – indicating a lower excitation-temperature (Nugent et al. 1995, Hachinger et al. 2008). Figure 2.2 shows maximum-light spectra of the peculiar 1991bg-like and 1991T-like objects compared to the range of spectroscopically normal SNe Ia.

Besides the 1991bg-like and 1991T-like objects there are other peculiar SNe Ia which mostly have luminosities and spectral properties between these two groups and the spectroscopically normal SNe Ia, thus showing a transitional character. However, spectroscopic properties seem to change rapidly at the faint end of the observed SNe Ia distribution. Recently some extremely luminous ($M_{\mathrm{max}}\,(V) \sim -20$ mag) and slowly declining [$\Delta m_{15}\,(B) \sim 0.7$] objects have been detected (SN 2003fg, Howell et al. 2006; SN 2006gz, Hicken et al. 2007; SN 2009dc, Yamanaka et al. 2009) which seem to form another sub-class.

2.1.2 Light curves

Light curves are the easiest data to obtain for supernova explosions and are typically taken in the various optical (U,B,V,R,I) and NIR (J,H,K) broad-band filters of the Bessell system (Bessell &

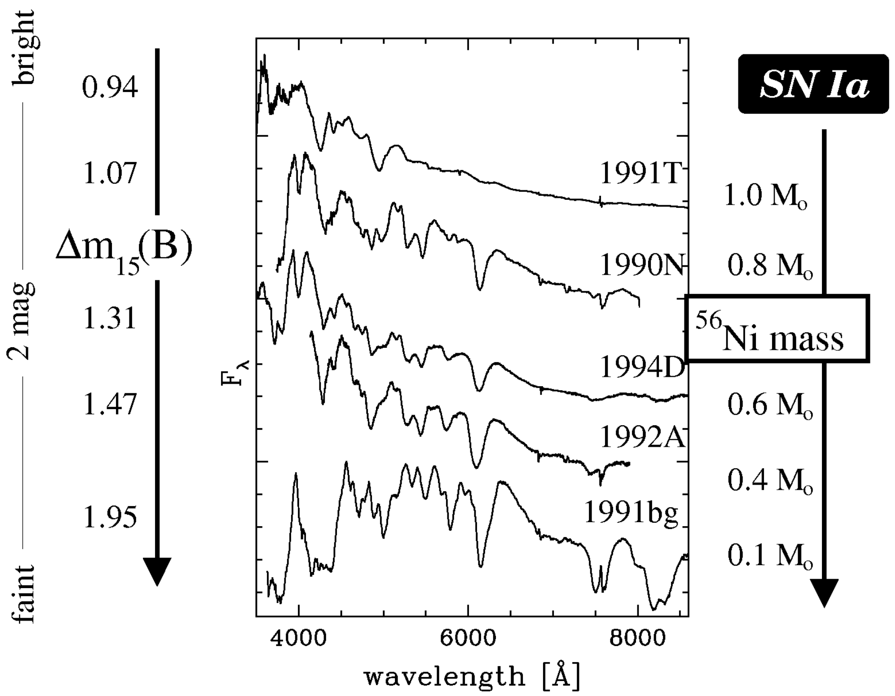

Figure 2.2: Spectroscopic diversity of SNe Ia (Cappellaro & Turatto 2001). Compared to the normal events, SN 1991T and 1991bg are spectroscopically peculiar (see text for a discussion). The luminosity of the supernovae shown decreases from top to bottom.

Brett 1988, Bessell 1990). They provide an important tool to constrain the explosion energetics. SNe Ia light curves are characterized by a rapid rise to maximum light (typically within about 18 to 20 days; see e.g. Riess et al. 1999, Conley et al. 2006) followed by a somewhat slower decline. After about 50 days post maximum light, the light curves of all SNe Ia become very similar and follow an exponential decline (Leibundgut 2000).

Earlier on there is a distinction between the different sub-classes of SNe Ia both in luminosity and light curve shape. Spectroscopically normal SNe Ia reach absolute peak magnitudes of $M_{\mathrm{max}}\,(B) \sim -19.2$ and show B-band decline rates of $\Delta m_{15}\,(B) \sim 0.9 \ldots 1.6$ obeying the Phillips relation (Phillips 1993, Phillips et al. 1999). Their NIR light curves (J,H,K-bands) peak before $t_{\mathrm{max}}\,(B)$ and show distinct secondary peaks about 20 to 30 days after maximum light. A similar behaviour is seen in the I band. The R band shows only a weak shoulder. The colours change from blue before maximum light to red thereafter with a particularly strong evolution in the $B-V$ colour (from ~ 0.1 at about 10 days before maximum light to ~ 1.1 about 30 days after). Overall the light curves of spectroscopically normal SNe Ia are rather homogeneous (see Figure 2.3).

Although the light curves of 1991bg-like objects differ significantly from normal SNe Ia, they form a remarkably homogeneous sample on their own. Their most obvious differences, compared to normal SNe Ia, are the small peak magnitudes of $M_{\mathrm{max}}\,(B) \sim -17$ and the lack of secondary maxima in the NIR bands. Moreover their NIR light curves do not peak earlier than the B-band light curve. Finally their light curve shape in the optical bands is also different, showing a significantly faster decline than the normal SNe Ia [$\Delta m_{15}\,(B) \sim 1.8 \ldots 1.95$] which does not follow the Phillips relation (Figure 2.4; Garnavich et al. 2004, Taubenberger et al. 2008). With $M_{\mathrm{max}}\,(B) \sim -19.5$ the 1991T-like objects are slightly brighter than the bulk of normal SNe Ia and decline somewhat more slowly

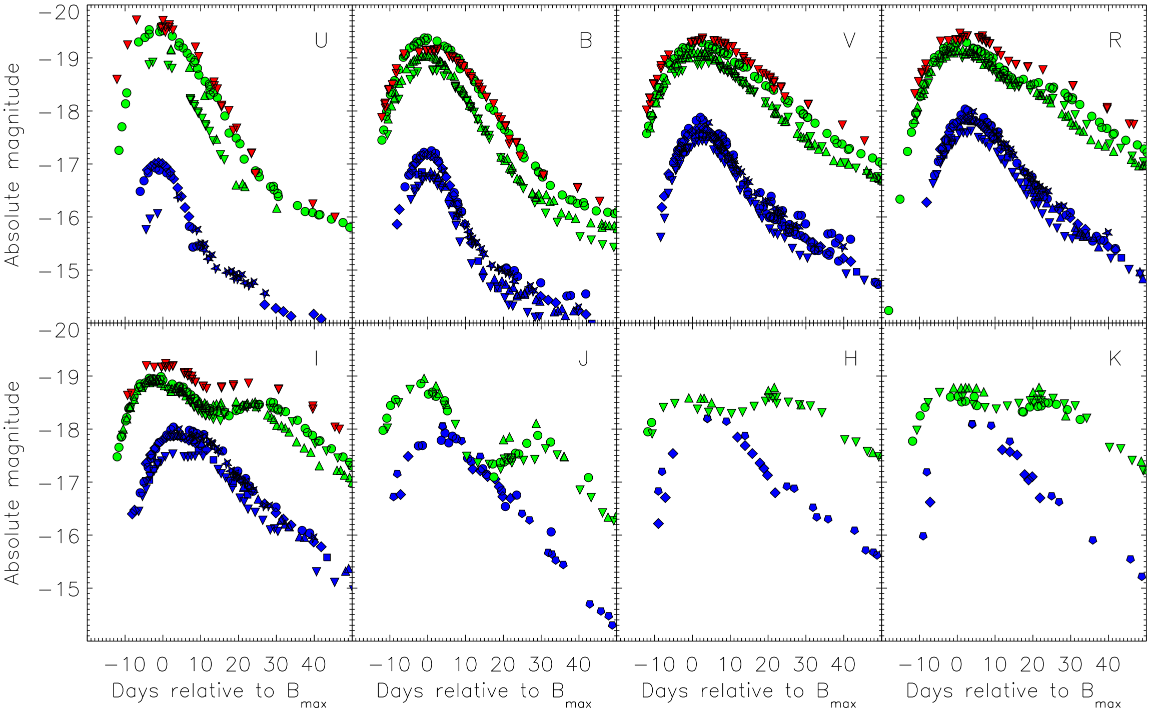

Figure 2.3: Broad-band light curves of Type Ia supernovae. While the subluminous 1991bg-like objects (blue symbols) are significantly different from the spectroscopically normal SNe Ia (green symbols), the light curves of 1991T-like objects (red symbols) are comparable to the brightest events among the normal SNe Ia. The different symbols correspond to different supernovae.

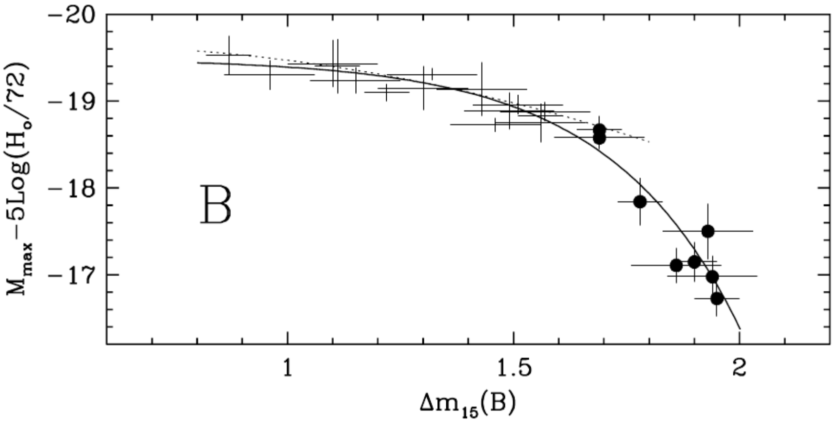

Figure 2.4: Peak B-band magnitude vs. light curve decline parameter $\Delta m_{15}(B)$ for a sample of SNe Ia (Garnavich et al. 2004). While the normal and bright SNe Ia [$\Delta m_{15}(B) \lesssim 1.7$] follow the Phillips relation (dotted line, Phillips et al. 1999) quite well, the fainter and in particular the 1991bg-like objects [$\Delta m_{15}(B) \gtrsim 1.8$] differ from this. Whether there is a general relation between $M_{\max}(B)$ and $\Delta m_{15}(B)$ valid for all SNe Ia as indicated by the exponential fit of Garnavich et al. (2004) in this figure is not clear. Due to the obvious difference of the 1991bg-like objects from normal SNe Ia in this plot and other indications (see Section 2.1.5 and Section 6.2) it is debated whether 1991bg-like objects result from a different explosion mechanism and/or progenitor systems than normal SNe Ia.

[$\Delta m_{15}(B) \sim 0.75 \ldots 1.0$], but still follow the Phillips relation and show secondary maxima in the NIR light curves.

Given the complex physics which determines the radiative transfer in supernova ejecta, the broadband light curves are highly sensitive to the detailed structure of a particular explosion model (compare Chapter 5 and 6). Thus, to constrain the overall explosion energetics, bolometric light curves, which account for the total flux (from γ-rays to the radio), would be the tool of choice. However, they are observationally difficult to obtain since only radiation at optical, NIR and radio wavelengths can penetrate the Earth's atmosphere. Instead, so-called UVOIR light curves which sum over the observed flux in the near-UV, optical and NIR are commonly used as a proxy for bolometric light. This is assumed to be a good approximation up to about a few weeks after maximum light (Leibundgut 2000) since SNe Ia are strongly suppressed in the UV range due to line blocking and the IR contribution to the total flux is negligible (actually there was no radio detection of SNe Ia so far, Weiler et al. 2009). From these UVOIR light curves, bolometric peak luminosities from $\sim 2 \cdot 10^{42}\,\mathrm{erg\,s^{-1}}$ for the 1991bg-like objects to $\sim 2 \cdot 10^{43}\,\mathrm{erg\,s^{-1}}$ for 1991T-like objects have been inferred.

2.1.3 Spectropolarimetry

Spectropolarimetric data for SNe Ia is still rare (for a recent review see Wang & Wheeler 2008) and for the few objects where it is available, in contrast to core-collapse supernovae, only marginal continuum polarization was detected. However, there is line polarization for some of the observed events, especially those with associated high-velocity spectral features (Wang et al. 2003). The polarization data could be used as a complementary information to study the spatial structure of the ejecta – particularly potential asymmetries. This will help to constrain the explosion mechanism. Interestingly the one sub-luminous 1991bg-like object SN 1999by, for which polarization data are available (Howell et al. 2001), shows the strongest continuum polarization among the SNe Ia. Howell et al. (2001) speculate that this might indicate a different explosion mechanism or progenitor scenario (see also Section 6.2).

2.1.4 Light echoes

Another interesting observational tool is provided by scatterings of the light from the actual event by the interstellar medium in the supernova's neighbourhood into our line-of-sight, the so called light echoes (Patat 2005, Patat et al. 2006). Those have been detected for a few recent supernovae (SN 1991T, SN 1995E, SN 1998bu, SN 2006X; Crotts & Yourdon 2008), but also for some of the historical supernovae (e.g. Tycho's SN and Cas A, Rest et al. 2008). For Tycho's SN it was even possible to use light echoes to identify this object retrospectively as a Type Ia, since maximum-light spectra could be obtained in this way (Krause et al. 2008). In general, light echoes should provide the possibility to examine individual supernovae not only at different times but also from different directions, thus allowing the direct study of asymmetries. However, this turns out to be rather difficult since typically a superposition of different epochs and viewing angles is observed. Furthermore the interactions of the supernova light with the near neighbourhood of the object provide direct constraints on progenitor models.

2.1.5 Rates

Supernova rates and their dependence on the environment provide valuable constraints on the progenitor systems and the explosion mechanism of SNe Ia. However, the measurement of these rates (for a review see van den Bergh & Tammann 1991) is rather difficult due to the rare occurrence of supernovae (typically on the order of one supernova per century in an average galaxy, Cappellaro 2003). The actual rates are measured in SN units (SNu), giving the number of supernovae per century per 10^{10} solar luminosities in the B band (usually abbreviated as $10^{10}\,\mathrm{L}_{\odot}^{B}$). Adopting $H_0 = 75\,\mathrm{km\ s^{-1}\,Mpc^{-1}}$, Cappellaro et al. (1999) find SNe Ia rates of 0.18 SNu (for early-type galaxies and early spirals) and 0.21 SNu (for late spirals), indicating that SNe Ia are equally common in galaxies of all morphological types. While core-collapse supernovae occur predominantly in the star-forming late-type galaxies, SNe Ia only show a slight preference for those hosts. However, there is some indication that the different sub-classes of Type Ia events prefer different morphological types with sub-luminous objects occurring predominantly in the old populations of early-type galaxies (Howell 2001, Gallagher et al. 2005).

2.2 Basic model

Taken together the observational evidence places strong constraints on the nature of SNe Ia, from which a broadly-accepted basic picture of these objects has emerged during the last decades. Details on the possible progenitors and the explosion mechanism itself, which are still under debate, are presented in Section 2.3 and 2.4, respectively.

The occurrence of SNe Ia in old and young environments directly indicates a connection with low mass stars ($M_\mathrm{i} < 8\,\mathrm{M}_{\odot}$), since more massive stars are too short-lived to occur in old environments. The rapid light curve evolution points to compact progenitor objects, which further must have lost their hydrogen and helium during the earlier evolution to explain the absence of lines of these elements in the spectra. Instead the occurrence of intermediate-mass elements and iron suggests nuclear processing of the material. Together with the work of Hoyle & Fowler (1960), who showed that thermonuclear burning in an electron-degenerate stellar core can lead to an explosion which eventually disrupts the star, this led to the conclusion that SNe Ia are thermonuclear explosions of degenerate material in White Dwarfs (WDs). Since isolated WDs form with masses below the Chandrasekhar limit ($M_\mathrm{Ch} \sim 1.38\,\mathrm{M}_{\odot}$ for a non-rotating carbon-oxygen WD) such objects are stable. Thus SNe Ia are believed to originate from interacting binary systems in order to introduce dynamics to the scenario such that an explosion might be triggered. The nature of the WD's companion in this system, however, is still under debate (see Section 2.3).

Truran et al. (1967) and Colgate & McKee (1969) refined this model by pointing out that the light curves of SNe Ia are powered by the radioactive decay of ^{56}Ni, which is synthesized during the explosion and decays by electron-capture to ^{56}Co with a half-life time of ~ 6.1 days. ^{56}Co in turn is unstable. It decays to the stable ^{56}Fe with a half-life time of ~ 77 days by electron capture (81%) or β^{+} decay (19%). The γ-photons arising from these decays interact with the ejecta by photo-electric absorption, Compton scattering and pair-production and are finally thermalized to ultraviolet, optical and infrared photons.

At early times the ejecta are sufficiently optically thick that the photon diffusion time is bigger than the time since the explosion and the radiation is trapped. As time passes, the optical depth of the ejecta and thus the diffusion time decrease continuously. Because the energy deposition by the radioactive burning products decreases exponentially with time, the light curves peak roughly when the diffusion time-scale becomes comparable to the expansion time-scale. Arnett (1982) has shown that at peak the bolometric luminosity of a supernova equals the instantaneous energy deposition by the radioactive decay of ^{56}Ni and ^{56}Co (Arnett's law). This has been used to derive ^{56}Ni masses (e.g. Stritzinger et al. 2006). However, carrying out more detailed simulations, Pinto & Eastman (2000a) have shown that this is only a first-order approximation. After the peak, the luminosity of the supernova exceeds the instantaneous energy deposition for a little while until the stored radiation has diffused out of the ejecta. Afterwards the photon diffusion time is so small that the radiation escapes freely and the luminosity follows the instantaneous energy deposition which at that times is dominated by the decay of the longer-lived ^{56}Co nucleus. This is found to be in excellent agreement with both photometric and spectroscopic observations (see above).

In this picture the light curve width-luminosity relation (Phillips 1993), characterized by the decline parameter $\Delta m_{15}\,(B)$, is explained by the amount of ^{56}Ni synthesized during the explosion: brighter events synthesize more ^{56}Ni, thus reaching higher peak luminosities (Arnett 1982). Since the light curve widths depend strongly on the opacity of the ejecta material, this also affects the light curve shapes, due to the large opacity associated with the iron-group elements. Thus brighter events decline more slowly owing to their increased amount of ^{56}Ni and SNe Ia – to a first-order approximation – form a one-parameter sequence in $M\left(^{56}\mathrm{Ni}\right)$.

However, there is spectroscopic diversity among SNe Ia of similar $\Delta m_{15}\,(B)$ values (e.g. Benetti et al. 2005). Whether this influences the peak luminosity and thus the cosmological measurements is not yet clear and needs to be investigated further. Especially a dependence on the mean metallicity, which has evolved over the cosmic history from zero to the present day value, could introduce a secular evolution of supernova properties leading to systematic errors in the cosmological measurements.

Mazzali et al. (2007) recently refined this one-parameter model analyzing a sample of SNe Ia. Assuming that all supernovae in the sample originate from carbon-oxygen WDs at the Chandrasekhar mass, their total ejecta mass should be constant. Mazzali et al. (2007) divided these ejecta – starting at the core – into radial zones dominated by stable iron-group elements (^{58}Ni, ^{54}Fe), radioactive ^{56}Ni, intermediate-mass elements and unburned material (C, O). The extension of the different regions in velocity space were derived from spectral analysis. Using this and assuming the density profile of the standard explosion model W7 (Nomoto et al. 1984), they obtained values for the mass enclosed within the different regions. This is illustrated in the so-called "Zorro"-plot (Figure 2.5), named for the shape of the plot.

The basic result of this analysis is that all SNe Ia contain similar amounts of burned material ($\sim 1\,\mathrm{M}_\odot$). Among the burning products the amounts of stable iron-group material seem to be constant as well ($\sim 0.2\,\mathrm{M}_\odot$), while the amount of ^{56}Ni synthesized during the explosion can vary from $\sim 0.1\,\mathrm{M}_\odot$ to almost $1\,\mathrm{M}_\odot$. Taken together with the finding that the light curve shape [i.e. $\Delta m_{15}\,(B)$] correlates more closely with the total iron-group mass than with the mass of ^{56}Ni, this suggests that the ratio of stable to unstable iron-group elements could be a second parameter

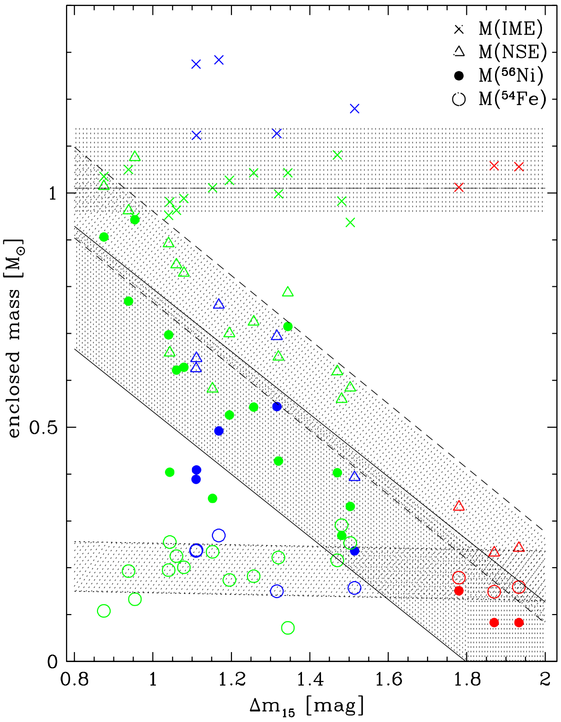

Figure 2.5: "Zorro"-diagram showing the distribution of the principal isotopic groups in a sample of SNe Ia (Mazzali et al. 2007). The mass enclosed by different burning products is plotted versus $\Delta m_{15}\,(B)$. For each supernova of the sample open circles indicate the mass of stable ^{54}Fe plus ^{58}Ni. Solid circles show the mass of ^{56}Ni and open triangles the sum of those two (i.e. the total iron-group mass). Crosses show the summed mass of iron-group and intermediate-mass elements, indicating the total mass burned. While the mass of stable iron-group elements (^{54}Fe and ^{58}Ni) is roughly constant, irrespective of luminosity, the ^{56}Ni mass correlates strongly with $\Delta m_{15}\,(B)$ and thus luminosity. The total mass burned is roughly constant. All the masses have been derived assuming the density profile of the W7 explosion model (Nomoto et al. 1984).

influencing the peak and width of the light curves. Since this is currently uncorrected in the cosmological measurements, this could be a source of systematic errors in the Hubble diagram if the typical ratio evolves on cosmological time scales.

2.3 Progenitor scenarios

In the previous section we discussed the basic picture that SNe Ia are thermonuclear explosions of degenerate material in interacting WDs as motivated by the observational data. While this is broadly accepted, the nature of the WD and the WD's companion are still debated and no progenitor system of a SN Ia has been identified so far. For a review see Branch et al. (1995) and Livio (2000).

Concerning the WD itself, three different chemical compositions, depending on the evolution of the progenitor star (Iben & Tutukov 1985), are possible: (i) pure helium WDs, (ii) carbon-oxygen (C/O) WDs and (iii) oxygen-neon-magnesium (O/Ne/Mg) WDs. Since helium WDs are completely burned to iron-group elements in a detonation when they reach $\sim 0.7\,\mathrm{M}_\odot$ (e.g. Woosley et al. 1986), their explosions cannot explain the observed spectra of SNe Ia and are thus ruled out as progenitors. Similarly it is unlikely that O/Ne/Mg WDs are the main producers of SNe Ia since their expected number is too small to explain the observed supernova rate (Livio & Truran 1992). Moreover, numerical simulations suggest that they are more likely to undergo accretion-induced collapse to a neutron star rather than a thermonuclear explosion when approaching the Chandrasekhar mass (Nomoto & Kondo 1991). Thus the most promising candidates are the C/O WDs.

Since WDs are inert objects, the dynamics needed to trigger a thermonuclear explosion must originate from a companion star. This could be either a normal main sequence or a red giant star [single degenerate (SD) scenario; Whelan & Iben 1973, Nomoto 1982] or another WD [double degenerate (DD) scenario; Iben & Tutukov 1984, Webbink 1984]. Within the SD scenario a further distinction is made concerning the ignition conditions. In the Chandrasekhar-mass models, the WD accretes hydrogen- or helium-rich matter until it nears the Chandrasekhar limit. Thereby its central density increases and its core heats up, leading to enhanced nuclear reaction rates and thus enhanced energy production. Since the equation-of-state of degenerate matter does not depend on the temperature, the WD does not expand and cool. Together with the strong temperature dependence of the nuclear reactions this leads to a thermonuclear runaway, eventually disrupting the WD (Arnett 1969, Woosley & Weaver 1986). An alternative way to trigger the thermonuclear explosion is provided by the sub-Chandrasekhar-mass models. There a WD below the Chandrasekhar limit accumulates a helium shell of $\sim 0.15\,\mathrm{M}_\odot$, leading to a helium detonation at the interface between the C/O core and the helium shell. The inward propagating detonation shock wave compresses the C/O core leading to a second detonation in the core (Woosley & Weaver 1994, Fink et al. 2007).

An attractive feature of the Chandrasekhar-mass models is that exploding at a well specified mass provides a natural explanation of the observed homogeneity of the SNe Ia class. Thus they are believed to be the progenitors of the bulk of spectroscopically normal SNe Ia (compare the "Zorro"-analysis in the previous section). However, they suffer from some shortcomings. In particular, it is questionable if they can account for the observed SNe Ia rate (e.g. Branch et al. 1995), since the parameter space in WD mass and accretion rate that allows a WD to stably accrete matter up to the Chandrasekhar mass is rather narrow (Nomoto 1982, see Figure 2.6). For small accretion rates hydrogen burning on top of the WD is unstable and leads to cyclic flashes or nova eruptions which cause a net mass loss. For high accretion rates the burning is stable, but the WD expands to red giant dimensions. Moreover, initially heavy WDs ($M \gtrsim 1.2\,\mathrm{M}_\odot$) are more likely to undergo accretion-induced collapse rather than a thermonuclear explosion, thus forming neutron stars and not SNe Ia (Nomoto & Kondo 1991).

In the SD scenario it is furthermore expected that hydrogen accretion would leave a footprint in the neighbourhood of the supernova. So far there was no convincing detection of circumstellar hydrogen around SNe Ia by radio observations (Livio 2000). However, Patat et al. (2007) found the Na I D doublet in SN 2006X to be variable which they attributed to changing properties in the circumstellar matter. Moreover, with the detection of the supersoft X-ray sources a class of possible progenitor objects was found in the last decades (see e.g. Kahabka & van den Heuvel 1997 for a review) and even a highly controversial claim for a possible Type Ia progenitor system was made for SN 2007on (Voss & Nelemans 2008). A follow-up study (Roelofs et al. 2008) revealed that this claim does not hold since there was a spatial offset between SN 2007on and the claimed supersoft

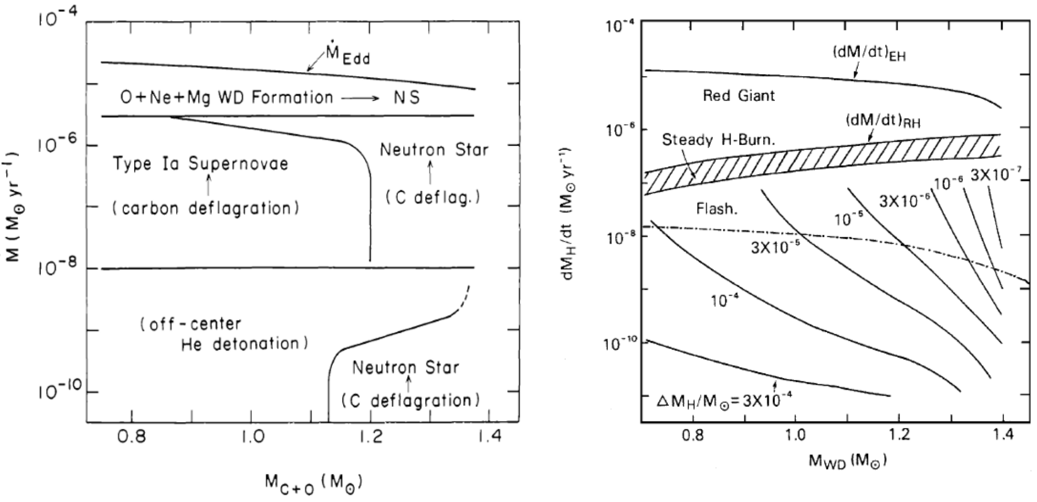

Figure 2.6: Left panel: Outcome of an accreting C/O WD depending on its initial mass and the accretion rate (Nomoto & Kondo, 1991). Right panel: Regime of steady hydrogen burning and thus stable accretion in a hydrogen-rich progenitor system depending on the initial WD mass and the accretion rate. Outside weak flashes (cyclic burning), strong flashes (novae, below the dash-dotted line) or common envelope phases occur, leading to mass losses and unstable accretion. The $\Delta M_{\rm H}$ values indicate envelope masses (for a given accretion rate) at which burning is ignited (Kahabka & van den Heuvel 1997).

X-ray progenitor signal. However, the method of searching for a correlation between supernova positions and archival supersoft X-ray sources might be successful for future SNe Ia.

The sub-Chandrasekhar-mass models, in contrast, could explain the observed supernova rates much more easily since less mass needs to be accreted by a WD which itself can be well below the Chandrasekhar limit (Livio 2000). However, there are indications that spectra and light curves produced by these models do not fit the observations well (Höflich & Khokhlov 1996, Nugent et al. 1997). Particularly the influence of the burning products of the helium detonation which are located at the highest velocities and consist mainly of iron-group elements could be problematic. However, this needs to be investigated further by self-consistent detailed models and is one of the applications of the code developed during this thesis (see Section 6.3).

In the DD scenario two orbiting C/O WDs coalesce due to the emission of gravitational waves. Population synthesis studies show that the rate of such mergers is comparable to the rate of SNe Ia (e.g. Branch et al. 1995, Ruiter et al. 2009), even though only a few DD systems which could merge within a Hubble time are known. Of these only one exceeds the Chandrasekhar mass (Livio 2000, Napiwotzki et al. 2004). Moreover, these systems naturally explain the (so far complete) absence of hydrogen in SN Ia spectra. However, it has remained unclear whether these mergers could really trigger a thermonuclear explosion leading to a SN Ia: numerical simulations (Benz et al. 1990, Motl et al. 2007, Yoon et al. 2007) have shown that the less massive WD is disrupted by tidal forces and forms an accretion disc around the more massive WD. Due to the high accretion rates from this disc, carbon ignites in the outer layers of the more massive WD (Saio & Nomoto 1998), incinerating the WD into oxygen, neon, and magnesium. This configuration is expected to collapse into a neutron star (Saio & Nomoto 1985), rather than making a SN Ia. Recently Pakmor et al. (2009) showed that dynamical mergers of WD binaries with a mass ratio close to one can avoid this fate and produce thermonuclear explosions. For their particular model we found good agreement with the subluminous 1991bg-like objects (see also Section 6.2). Since the parameter space of these models (i.e. the initial masses of the WDs and their exact ratio) is quite large, it is possible that these models could also contribute to other sub-types of the Ia class. In particular, such mergers are also promising candidates for explaining the recently discovered superluminous objects like SN 2003fg (Howell et al. 2006) since they can naturally explain their predicted masses above the Chandrasekhar limit. Detailed follow-up studies are required to investigate this.

Due to the different evolution of the progenitor systems in the DD and SD scenarios, the corresponding delay times, i.e. the time from progenitor formation until explosion, are also different. The mass accretion in the SD scenario happens via Roche-lobe overflow (e.g. Warner 1995). Since the less massive companion star does not fill its Roche lobe before ending its hydrogen core burning, the delay time in this scenario is basically determined by the life-time of the companion star. The following accretion phase is much shorter than the time-scale of the progenitor evolution and can be neglected. For the DD scenario the delay time is given by the sum of the main-sequence life-time of the less massive of the two progenitors plus the time-scale for merging due to gravitational wave emission. Thus it depends strongly on the initial separation of the WDs and can be substantial. This is of particular interest in the context of the claim that there are two different populations of Type Ia progenitors with different delay times (Mannucci et al. 2005, Scannapieco & Bildsten 2005, Mannucci et al. 2006).

2.4 Explosion mechanism

Although the outcome of explosion models depends sensitively on the initial conditions (e.g. Röpke et al. 2007, Sim et al. 2007), our knowledge about the ignition of the thermonuclear flame in different progenitor scenarios is still poor. Particularly whether the ignition occurs at the centre of the progenitor star, or off-centre and whether one or multiple spatial regions are ignited is still debated (e.g. Höflich & Stein 2002, Woosley et al. 2004, Kuhlen et al. 2006). This is mainly due to the great complexity of the processes involved (see Hillebrandt & Niemeyer 2000 for a discussion) which require multi-dimensional modelling over a wide range of length- and time-scales and pose enormous computational demands. Thus in current explosion models ignition is enforced artificially, typically based on some physically motivated assumptions. However, it remains an initial parameter.

In contrast, significant progress has been made in the modelling of the propagation of the thermonuclear flame through the progenitor star in recent years and it is now possible to solve this in three dimensions (e.g. Röpke et al. 2007; see Figure 2.7). In principle there are two hydrodynamical modes of flame propagation (Landau & Lifschitz 1991). One is mediated by thermal conduction in the degenerate electron gas and propagates subsonically (deflagration), the other is mediated by compressional heating due to shock waves, which propagate supersonically (detonation).

A pure carbon detonation which has been proposed in the past (Arnett 1969) as a possible explosion mechanism, is ruled out by the observation of intermediate-mass elements in SNe Ia spectra. Owing to the supersonic propagation of the detonation wave, the fuel ahead of the shock cannot expand

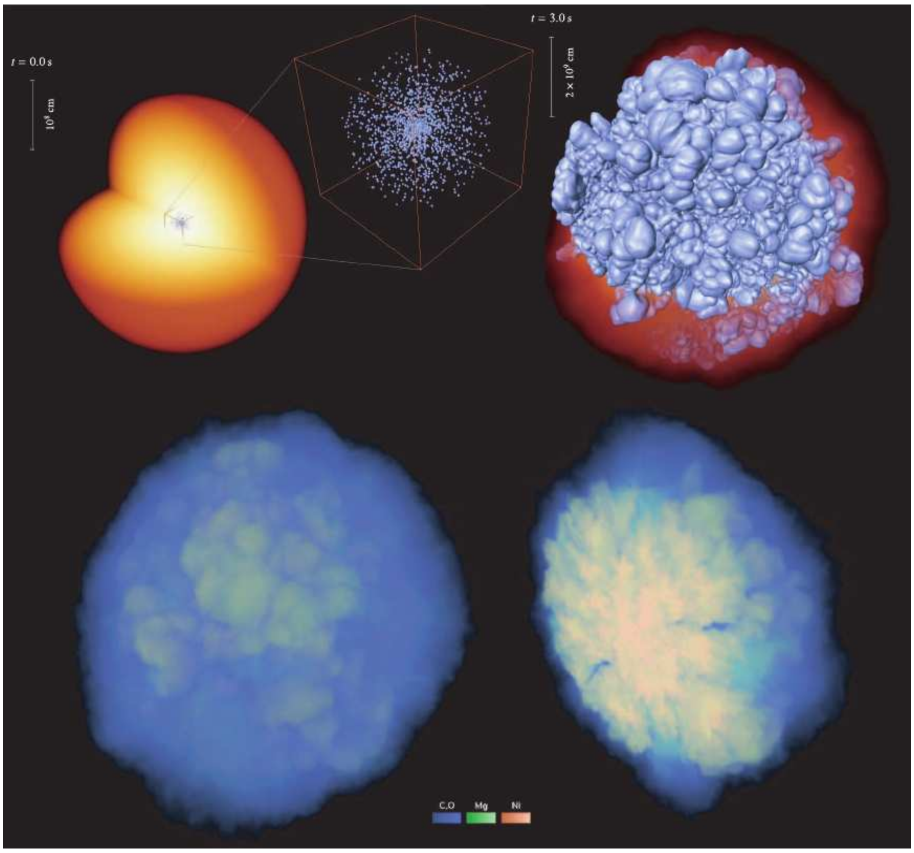

Figure 2.7: Structure of a 3D deflagration model (Röpke et al., 2007). The top panels show the initial setup (left) and the evolution of the flame front at three seconds after the explosion (right). The orange sphere illustrates the progenitor WD. The bottom panels show the composition of the ejecta at ten seconds after the explosion. The products of the mass fractions of carbon/oxygen, magnesium and nickel with density are volume rendered in different colours (left). The lower right panel shows a cut through the midplane of the simulation volume to illustrate the composition of the central parts.

in this case. Thus all the WD material is burned at the high densities of the progenitor star, resulting in an ejecta composition of almost pure iron-group elements. This does not occur for a carbon deflagration (Nomoto et al. 1976), since its burning front moves subsonically and rarefaction waves ahead of the flame are able to dilute the WD material. At these lower fuel densities the thermonuclear burning produces less massive elements.

In contrast, the pure deflagration model suffers from a different problem: the laminar flame propagation velocity is not large enough that the kinetic energy of the explosion suffices to unbind the WD against its gravitational force. However, turbulent motions can affect the flame propagation in the deflagration regime strongly. In the early 1D explosion models this intrinsically multi-dimensional effect could not be tackled directly. Instead, a parameterized flame propagation velocity was used, tuned such that the models were able to reproduce observational spectra and light curves. The W7 model of Nomoto et al. (1984) is the most well-known example of these models and is still widely used today. With increasing computational power and progress in numerical techniques during the 1990s, multi-dimensional simulations and thus a self-consistent treatment of the flame propagation became possible (e.g. Reinecke et al. 1999, Gamezo et al. 2003). These have shown that the burning is strongly enhanced by the turbulent interactions which lead to a wrinkling of the flame and thus an enlarged flame surface area (Niemeyer & Hillebrandt 1995). The main process behind this is the Rayleigh-Taylor instability, which develops during the flame propagation since the hot and light ashes of the burning products are created below the cold and dense fuel – a buoyancy unstable stratification. At the interface of the evolving mushroom-shaped bubbles, Kelvin-Helmholtz instabilities form due to the large viscosity. These lead to the formation of turbulent eddies which decay to smaller scales and form a turbulent cascade until they are dissipated at the Kolmogorov scale. The wide range of scales involved – from the WD radius of $\sim 1000\,\mathrm{km}$ down to ~ 1 mm for the Kolmogorov scale – makes it impossible to resolve the internal flame structure in numerical simulations. Instead, different flame modelling techniques [e.g. flame capturing (Khokhlov 1993) or flame tracking (Reinecke et al. 1999)] are used and the turbulent interactions are taken into account by a subgrid model technique (Schmidt et al. 2006a, Schmidt et al. 2006b), which determines the turbulent energy on unresolved scales based on conservation laws.

Three-dimensional deflagration models accounting for all this can unbind the WD and thus lead to “healthy” thermonuclear explosions (e.g. Reinecke et al. 2002). However, it is challenging to synthesize more than $\sim 0.4\,\mathrm{M}_\odot$ of ^{56}Ni (Röpke et al. 2006), which makes it difficult to explain the majority of the normal SNe Ia with this model. Furthermore the mixing of burned and unburned ejecta material due to the hydrodynamical instabilities seems to be too large compared to the observations (Röpke et al. 2007), which show a strong stratification.

One way to solve these problems is the combination of the deflagration and the detonation modes to the delayed detonation model (Khokhlov 1991). There the explosion starts as a deflagration, leaving the WD material time to expand, before a supersonic detonation triggers. By that time the fuel is sufficiently diluted that it does not burn completely to iron-group elements. At the same time the increased burning produces enough ^{56}Ni to account for normal SNe Ia and the detonation wave also suppresses the hydrodynamical mixing. Parameterized 1D explosion models (e.g. Höflich et al. 1995) using this approach have been quite successful in producing synthetic spectra and light curves which fit the observations. Furthermore the “transition density” at which the flame switches from the subsonic deflagration to the supersonic detonation mode in these simulations was found to correlate with the explosion strength (Höflich et al. 1995) and thus could explain the observed brightness sequence of SNe Ia. The physical mechanism behind the deflagration-to-detonation transition (DDT), however, is still unclear. Niemeyer & Woosley (1997) argued that if such a transition happens, it is most likely to occur when the turbulent interactions start to modify the internal structure of the deflagration flame. At this point a pure deflagration switches to the so-called distributed burning regime. While earlier the deflagration is driven by a contiguous flame front which can only be wrinkled or corrugated by the turbulent motions, afterwards turbulent eddies can distribute material out of the flame and thus disrupt the flame front.

Although this connection between the DDT and the onset of the distributed burning regime is currently only an assumption, it is physically motivated and provides a possibility to compare different simulations consistently to observational data. Röpke & Niemeyer (2007) used this approach to calculate full star explosion models in 3D and found that these can explain normal to bright SNe Ia. Recently, Kasen et al. (2009) have shown in a comprehensive study of 2D delayed-detonation models – combining hydrodynamical and radiative transfer simulations – that these models are able to reproduce the observational spread of normal SNe Ia. Depending on the strength of the initial deflagration phase, the WD material becomes diluted. Weak initial deflagrations lead to bright supernovae, since a lot of the fuel is burned at high densities during the subsequent detonation, producing large amounts of ^{56}Ni. Inversely, for a strong deflagration the pre-expansion of the fuel is quite effective and the detonation produces mainly intermediate-mass elements, leading to dimmer supernovae.

Another possibility for a deflagration-to-detonation transition was proposed by Plewa et al. (2004) with the gravitationally confined explosion scenario. There an almost centrally ignited deflagration leads to the formation of a buoyancy instable bubble which reaches the WD surface at supersonic velocities and then becomes confined by the gravitational force of the WD. This causes the material in the outer stellar layers to sweep around the stellar surface converging at the point opposite to the bubble breakout. Plewa et al. (2004) claimed that a detonation forms at the convergence point, which then propagates again through the already pre-expanded WD and incinerates the material which was left unburned by the initial deflagration. Kasen & Plewa (2005, 2007) have shown that synthetic spectra obtained from this model are in remarkably good agreement with spectra of normal SNe Ia. However, the synthetic light curves decline too fast and are somewhat too bright, due to the large amounts of ^{56}Ni produced in their particular model. Moreover, the observational display of the model depends, due to its significant large scale asymmetries, strongly on the line-of-sight under which it is observed. Finally, the ignition of the secondary detonation by the converging waves of stellar surface material is still under debate since numerical models of different research groups give different results (Plewa 2007, Röpke et al. 2007, Jordan et al. 2008).

In this chapter, we have summarized the current knowledge about thermonuclear supernovae to provide a thorough basis for future analysis. Before addressing the problem of radiative transfer in supernova ejecta directly, however, we will now give a short introduction to the theory of radiative transfer in the next chapter.

3 Basics of radiative transfer

In this chapter we give a brief introduction to the theory of radiation and radiative transfer following the discussion by Mihalas & Weibel Mihalas (1984) to provide the basics for the following parts of this thesis which deal mainly with simulating radiative transfer in supernova ejecta. More details may be found for instance in Mihalas (1978), Rybicki & Lightman (1979) or Castor (2004).

3.1 Description of the radiation field

Neglecting polarization (which we do not deal with in this work since spectropolarimetric data for SNe Ia are still rare and it requires deep observations with a very good signal-to-noise ratio to obtain reliable polarization spectra), in the macroscopic picture the radiation field is fully characterized by the **specific intensity** $I\left(\mathbf{x},t;\mathbf{n},\nu\right)$. It describes the amount of energy $\mathrm{d}E$ transported by radiation of frequencies $(\nu,\nu+\mathrm{d}\nu)$ across a surface element $\mathrm{d}S$ at position $\mathbf{x}$ into a solid angle $\mathrm{d}\omega$ around a direction $\mathbf{n}$ between times t and $t+\mathrm{d}t$. Thus

$$I_\nu = I\left(\mathbf{x},t;\mathbf{n},\nu\right) = \frac{\mathrm{d}E}{\mathrm{d}S\cos\vartheta\,\mathrm{d}\omega\,\mathrm{d}\nu\,\mathrm{d}t} \tag{3.1}$$

with ϑ being the angle between $\mathbf{n}$ and the normal to $\mathrm{d}S$. In the cgs system, commonly used in astrophysics, the units of I_ν are $\mathrm{erg\,cm^{-2}\,s^{-1}\,Hz^{-1}\,sterad^{-1}}$.

Averaging over solid angles yields the **mean intensity**

$$J_\nu = J\left(\mathbf{x},t;\nu\right) = \frac{1}{4\pi}\oint I\left(\mathbf{x},t;\mathbf{n},\nu\right)\mathrm{d}\omega. \tag{3.2}$$

This is also called the zeroth moment of the radiation field (with respect to $\mathbf{n}$). The mean intensity relates to the monochromatic radiation energy density E_ν via

$$E_\nu = E\left(\mathbf{x},t;\nu\right) = \frac{4\pi}{c}J_\nu \tag{3.3}$$

see e.g. Mihalas (1978).

In a similar way higher order moments of I_ν with respect to $\mathbf{n}$ are defined:

- The first moment or Eddington flux

  $$\mathbf{H}_\nu = \mathbf{H}\left(\mathbf{x},t;\nu\right) = \frac{1}{4\pi}\oint I\left(\mathbf{x},t;\mathbf{n},\nu\right)\mathbf{n}\,\mathrm{d}\omega \tag{3.4}$$

  relates to the monochromatic radiation flux $\mathbf{F}_\nu = \mathbf{F}\left(\mathbf{x},t;\nu\right) = 4\pi\mathbf{H}_\nu$ which gives the net rate of energy per unit frequency and unit time crossing a surface element $\mathrm{d}S$.

- The second moment

$$K_\nu = K(\mathbf{x}, t; \nu) = \frac{1}{4\pi} \oint I(\mathbf{x}, t; \mathbf{n}, \nu)\, \mathbf{n} \otimes \mathbf{n} \mathrm{d}\omega \tag{3.5}$$

is related to the monochromatic radiation pressure tensor $P_\nu = P(\mathbf{x}, t; \nu) = (4\pi/c)\, K_\nu$.

3.2 Radiation in thermodynamic equilibrium

In an enclosure of constant temperature the radiation field is in thermodynamic equilibrium, i.e. it is isotropic (i.e. $I_\nu = J_\nu$) and can be described by a unique distribution function

$$I_\nu = B_\nu(T_\mathrm{e}) = \frac{2h\nu^3}{c^2} \frac{1}{e^{h\nu/k_\mathrm{B}T_\mathrm{e}} - 1}, \tag{3.6}$$

(the **Planck function**), which depends only on the temperature T_e of the enclosed gas. Its derivation from Bose-Einstein quantum statistics can be found in many textbooks (e.g. Landau & Lifschitz 1987). A radiation field which follows Equation (3.6) is called black body radiation and the emitter a black body.

Due to its isotropy, the monochromatic radiation energy density of a black body radiation field follows from Equation (3.3) and Equation (3.6)

$$E^*_\nu(T_\mathrm{e}) = \frac{4\pi}{c} \cdot \frac{2h\nu^3}{c^2} \frac{1}{e^{h\nu/k_\mathrm{B}T_\mathrm{e}} - 1}. \tag{3.7}$$

Integrating over ν yields the **Stefan-Boltzmann law**

$$E^*(T_\mathrm{e}) = a_\mathrm{R} T_\mathrm{e}^4 \tag{3.8}$$

in which $a_\mathrm{R} = 8\pi^5 k_\mathrm{B}^4 / 15c^3h^3$. Comparing Equation (3.7) and Equation (3.8), we obtain the frequency integrated Planck function

$$B(T) = \frac{\sigma_\mathrm{R}}{\pi} T^4, \tag{3.9}$$

where $\sigma_\mathrm{R} = \frac{1}{4} a_\mathrm{R} c$ is the Stefan-Boltzmann constant.

In thermodynamic equilibrium, the same temperature T_e which characterizes the radiation field, also completely describes the matter state. The derivation of the governing equations, which are the Maxwellian velocity distribution, the Boltzmann excitation formula and the Saha ionization equation, can be found in standard textbooks (e.g. Landau & Lifschitz 1987).

The Maxwellian velocity distribution

$$f(v)\, \mathrm{d}v = \left(\frac{m}{2\pi k_\mathrm{B} T_\mathrm{e}}\right)^{3/2} \exp\left(\frac{-mv^2}{2k_\mathrm{B}T_\mathrm{e}}\right) 4\pi v^2 \mathrm{d}v \tag{3.10}$$

gives the probability that a particle of mass m has a velocity in $[v, v + dv]$ at T_e. The **Boltzmann excitation formula**

$$\frac{n_{u,j,k}}{n_{l,j,k}} = \frac{g_{u,j,k}}{g_{l,j,k}} \exp\left(-\frac{\varepsilon_{u,j,k} - \varepsilon_{l,j,k}}{k_\mathrm{B}T_\mathrm{e}}\right) \tag{3.11}$$

determines the ratio of the populations (i.e. number densities) between two levels u and l within ionization state j of element k. $g_{i,j,k}$ and $\varepsilon_{i,j,k}$ are statistical weights and total (i.e. ionization plus excitation) energies of level i of ion j of element k, respectively ($\varepsilon_{u,j,k} > \varepsilon_{l,j,k}$). The **Saha ionization equation**

$$\frac{N_{j,k}}{N_{j+1,k} n_e} = \frac{U_{j,k}}{U_{j+1,k}} \frac{C}{T_{\mathrm{e}}^{3/2}} \exp\left(\frac{\varepsilon_{0,j+1,k} - \varepsilon_{0,j,k}}{k_{\mathrm{B}} T_{\mathrm{e}}}\right) \tag{3.12}$$

describes the total population $N_{j,k} = \sum_i n_{i,j,k}$ of ionization state j of element k relative to that of the next ionization state $j+1$. Here, n_{e} is the number density of free electrons,

$$C = \frac{1}{2} \left(\frac{h^2}{2\pi m_{\mathrm{e}} k_{\mathrm{B}}}\right)^{3/2} \tag{3.13}$$

the Saha constant and

$$U_{j,k}\left(T_{\mathrm{e}}\right) = \sum_{i=1}^{\mathcal{N}_{\mathrm{L}}(j,k)} g_{i,j,k} \exp\left(-\frac{\varepsilon_{i,j,k}}{k_{\mathrm{B}} T_{\mathrm{e}}}\right) \tag{3.14}$$

the partition function of the corresponding ionization state. $\mathcal{N}_{\mathrm{L}}\left(j,k\right)$ is the number of atomic levels associated with ion j of element k. Note that $N_{j,k} = n_{0,j,k} U_{j,k}\left(T_{\mathrm{e}}\right)/g_{0,j,k}$. Furthermore it is convenient to define the Saha factor $\phi_{i,j,k}\left(T_{\mathrm{e}}\right)$

$$\begin{aligned} n_{i,j,k}^{*} &= n_{0,j+1,k} n_{\mathrm{e}} \frac{g_{i,j,k}}{g_{0,j+1,k}} \frac{C}{T_{\mathrm{e}}^{3/2}} \exp\left(\frac{\varepsilon_{0,j+1,k} - \varepsilon_{i,j,k}}{k_{\mathrm{B}} T_{\mathrm{e}}}\right) \\ &= n_{0,j+1,k} n_{\mathrm{e}} \phi_{i,j,k}\left(T_{\mathrm{e}}\right) \end{aligned} \tag{3.15}$$

3.3 Interaction of radiation and matter

A beam of radiation passing through a slab of matter may be altered owing to absorption or emission of photons by the matter. Macroscopically this is described by the opacity and the emissivity respectively.

The **opacity** $\chi_\nu = \chi\left(\mathbf{x}, t; \mathbf{n}, \nu\right)$ is defined such that the change in intensity $\mathrm{d}I^{\mathrm{abs}}\left(\mathbf{x}, t; \mathbf{n}, \nu\right)$ due to absorptions along a path element $\mathrm{d}l \cdot \mathbf{n}$ is given by

$$\mathrm{d}I^{\mathrm{abs}}\left(\mathbf{x}, t; \mathbf{n}, \nu\right) = -\chi_\nu\left(\mathbf{x}, t; \mathbf{n}, \nu\right) I_\nu\left(\mathbf{x}, t; \mathbf{n}, \nu\right) \mathrm{d}l. \tag{3.16}$$

Hence it has the dimensions of an inverse length which equals the mean free path of a photon in the material

$$\lambda_\nu = \frac{1}{\chi_\nu}. \tag{3.17}$$

The **emissivity** $\eta_\nu = \eta\left(\mathbf{x}, t; \mathbf{n}, \nu\right)$ gives the change in intensity $\mathrm{d}I^{\mathrm{em}}\left(\mathbf{x}, t; \mathbf{n}, \nu\right)$ due to emission along a path element $\mathrm{d}l \cdot \mathbf{n}$ and is given by

$$\mathrm{d}I^{\mathrm{em}}\left(\mathbf{x}, t; \mathbf{n}, \nu\right) = \eta_\nu\left(\mathbf{x}, t; \mathbf{n}, \nu\right) \mathrm{d}l. \tag{3.18}$$

In the cgs system its units are $\mathrm{erg\,cm^{-3}\,s^{-1}\,Hz^{-1}\,sterad^{-1}}$.

Microscopically a large number of different atomic processes can contribute to the total opacity and emissivity. Important for the conditions in supernova ejecta are the following:

- In **bound-free (bf) transitions** an electron, bound in an atomic state, absorbs a photon of sufficiently high energy that it escapes with finite kinetic energy to the continuum and the atom becomes ionized (photoionization, photo-electric effect). Thereby the incident photon is destroyed. If the plasma's particle distribution function is Maxwellian, the difference between the photon energy and the ionization threshold of the electron is ultimately transferred into thermal kinetic energy of the plasma by collisional interactions. For typical conditions in stellar atmospheres this is a good assumption, since the self-collision time for elastic collisions of electrons is much shorter than the time scale of radiative processes and the time between inelastic collisions (Mihalas & Weibel Mihalas 1984), which could perturb the equilibrium. Thus elastic collisions of electrons dominate and drive the particle distribution function to its Maxwellian value.

  The inverse process in which a free electron recombines to a bound atomic state (radiative recombination), releases the sum of the kinetic energy of the free electron plus the binding energy of the electron in form of a photon. If the absorbed electron originated from the thermal pool of the plasma, this transforms thermal kinetic energy to radiation energy.
- In **free-free (ff) transitions** a free electron moving in the electric field of a charged ion can absorb energy from a photon (free-free absorption). This alters the kinetic energy of the electron and thus transfers radiation energy into thermal kinetic energy of the plasma. Inversely, electrons moving freely in the electric field of charged ions, emit photons by Bremsstrahlung.
- In **bound-bound (bb) transitions** the absorption of a photon leads to a transition from a bound atomic state of lower energy $\varepsilon_{l,j,k}$ to another bound atomic state of higher energy $\varepsilon_{u,j,k}$. This "excited state" has several possibilities to de-excite. Among those (i) the emission of a photon of the same[1] energy as the absorbed photon $h\nu = \varepsilon_{u,j,k} - \varepsilon_{l,j,k}$, called resonance scattering, (ii) the emission of a photon by a transition to a different atomic level, thereby emitting a photon of different energy, called fluorescence and (iii) the inelastic collisions with another particle, thereby transferring the radiant energy of the incident photon into thermal kinetic energy of the plasma.
- **Scattering** of photons by free (Thomson limit valid for UV/optical radiation but Compton treatment required for higher energy photons) or bound (Rayleigh scattering) electrons.
- For photon energies above $2m_ec^2$ a photon in the electric field of an atomic nucleus can be converted into an electron-positron pair by **pair-production**.

Thus the total opacity and emissivity for a given frequency ν is a sum over the individual opacities of all contributing processes, which we discuss in Sections 3.3.2 and 3.3.3.

It is common to distinguish between "true" or "thermal" absorption and emission processes, which convert radiation energy into thermal kinetic energy of the plasma and scattering processes, in

---

[1] Owing to the finite energy width of bound atomic states, bound-bound transitions have a natural line width. Thus the energy of an emitted photon can be slightly different from the absorbed one. A similar effect can be caused by Doppler shifts due to the thermal motion of the plasma. This line broadening is expressed by the line profile ϕ_ν ($\int_0^\infty \phi_\nu \mathrm{d}\nu = 1$). In general a redistribution function, which describes the probability that a photon absorbed at frequency ν and direction $\mathbf{n}$ gets re-emitted at frequency ν' into direction $\mathbf{n}'$, accounts for this. Here we assume complete redistribution, i.e. isotropic emission randomly distributed over the line profile. For a detailed discussion see Mihalas (1978, Chapter 2.1 and 13).

which a photon changes its direction but no significant energy exchange between photon and plasma takes place (note, that even in pure scattering processes on free or bound electrons the energy of the scattered photon can be slightly different from the energy of the incident photon due to the thermal motions of the plasma). Thus

$$\chi_\nu = \kappa_\nu + \sigma_\nu, \tag{3.19}$$

with κ_ν being the true absorption coefficient and σ_ν the scattering coefficient and

$$\eta_\nu = \eta_\nu^{\text{thermal}} + \eta_\nu^{\text{scat}}. \tag{3.20}$$

Following the previous discussion, it is clear that bound-free and free-free transitions are thermal processes, while bound-bound transitions contribute to the thermal processes for case (iii) and to the scattering processes for case (i). In general, however, neither is exactly true for bound-bound transitions as we see from case (ii).

In static media and the fluid rest frame (quantities denoted with a prime) the opacity and the emissivity are usually isotropic

$$\chi'_\nu = \chi'\left(\mathbf{x}, t; \nu'\right) \tag{3.21}$$

$$\eta'_\nu = \eta'\left(\mathbf{x}, t; \nu'\right). \tag{3.22}$$

An exception is Compton scattering. In general, however, owing to the frequency dependence of the atomic processes, the opacity and the emissivity are angle dependent since a photon moving with frequency ν in direction $\mathbf{n}$ in the lab frame experiences a Doppler shift

$$\nu' = \nu\gamma\left(1 - \mathbf{n} \cdot \mathbf{v}/c\right) = \nu D \tag{3.23}$$

in the fluid rest frame. $\mathbf{v}$ is the velocity of the fluid relative to the lab frame and γ is the Lorentz factor

$$\gamma = \left(1 - \frac{v^2}{c^2}\right)^{-1/2}. \tag{3.24}$$

Similarly aberration alters the direction of a photon measured in different frames

$$\mathbf{n}' = \frac{\mathbf{n} - \gamma\frac{\mathbf{v}}{c}\left(1 - \frac{\gamma}{\gamma+1}\frac{\mathbf{n}.\mathbf{v}}{c}\right)}{\gamma\left(1 - \frac{\mathbf{n}.\mathbf{v}}{c}\right)}. \tag{3.25}$$

3.3.1 Local thermodynamic equilibrium

In thermodynamic equilibrium the energy absorbed by a matter element must equal the energy emitted by that matter element

$$\left(\eta_\nu^{\text{thermal}}\right)^* = \left(\kappa_\nu I_\nu\right)^* = \kappa_\nu^* B_\nu\left(T_{\text{e}}\right) \tag{3.26}$$

where we made use of Equation (3.6) and starred values refer to conditions of thermodynamic equilibrium. This is called the **Kirchhoff-Planck relation**.

Considering the photon destruction length $\lambda_{\text{d}}\left(\nu\right)$, which compared to the photon mean free path

$\lambda_{\rm mfp}(\nu)$ [given by Equation (3.17)] takes into account that a thermally emitted photon may, due to scattering processes, travel much farther than indicated by the photon mean free path [$\lambda_{\rm d}(\nu) > \lambda_{\rm mfp}(\nu)$], we identify two regimes. In the first regime the physical properties of a plasma change only slightly over a photon destruction length. Then Equation (3.26), evaluated using the local thermodynamic properties of the plasma

$$\left(\eta^{\rm thermal}(\mathbf{x}, t, \nu)\right)^* = \kappa^*(\mathbf{x}, t; \nu)\, B(\nu, T_{\rm e}(\mathbf{x}, t)), \tag{3.27}$$

becomes a valid approximation, called local thermodynamic equilibrium (LTE). In the microscopic picture this means that all local absorption and emission processes are in detailed balance, i.e. absorptions are exactly balanced by their corresponding inverse processes [see e.g. §84 of Mihalas & Weibel Mihalas (1984) for a detailed discussion of the microscopic requirements for LTE].

In the second regime, due to the non-local character of freely propagating radiation, as it occurs e.g. in dilute and hot media, this is no longer true and the conditions for LTE break down. In that case, called non-LTE (NLTE), the statistical equilibrium equations (see Section 3.4) must be solved without assuming detailed balance.

3.3.2 Bound-bound opacity

The interaction between radiation and a bound-bound transition connecting two atomic levels (l, j, k) and (u, j, k) with $\varepsilon_{l,j,k} < \varepsilon_{u,j,k}$ is described by the Einstein coefficients for photo-absorption ($B_{l,j,k\to u,j,k}$), spontaneous ($A_{l,j,k\leftarrow u,j,k}$) and stimulated ($B_{l,j,k\leftarrow u,j,k}$) emission, which are matter quantities determining the probability of the corresponding processes. In quantum mechanical calculations the transition cross-section $\alpha_{l,j,k\to u,j,k}$ is characterized by an oscillator strength $f_{l,j,k\to u,j,k}$ which relates to $B_{l,j,k\to u,j,k}$ via

$$\alpha_{l,j,k\to u,j,k} = \frac{\pi e^2}{m_{\rm e} c} f_{l,j,k\to u,j,k} = \frac{h\nu_{lu}}{4\pi} B_{l,j,k\to u,j,k}, \tag{3.28}$$

where e is the electron charge, $m_{\rm e}$ the electron mass and $h\nu_{lu} = \varepsilon_{u,j,k} - \varepsilon_{l,j,k}$ the energy difference between the two bound states. It is common to characterize the strength of a transition by its gf-value

$$gf = g_{l,j,k} f_{l,j,k\to u,j,k} = g_{u,j,k} f_{l,j,k\leftarrow u,j,k}, \tag{3.29}$$

where $g_{i,j,k}$ is the statistical weight of the corresponding atomic state.

Using the Einstein coefficients we find

$$a_\nu I_\nu = n_{l,j,k} \frac{B_{l,j,k\to u,j,k} h\nu_{lu}}{4\pi} \phi_\nu I_\nu \tag{3.30}$$

for the rate at which energy is removed from an incident beam of radiation. a_ν is the macroscopic line absorption coefficient, $n_{i,j,k}$ the number density of atomic state (i, j, k) and ϕ_ν the line profile. Assuming complete redistribution, the emissivities due to spontaneous and stimulated emission are given by

$$\eta_\nu^{\rm spont} = n_{u,j,k} \frac{A_{l,j,k\leftarrow u,j,k} h\nu_{lu}}{4\pi} \phi_\nu \tag{3.31}$$

and

$$\eta_\nu^{\mathrm{stim}} = n_{u,j,k} \frac{B_{l,j,k\leftarrow u,j,k} h\nu_{lu}}{4\pi} \phi_\nu I_\nu, \tag{3.32}$$

respectively. Treating stimulated emission as negative absorption the net line opacity and emissivity are

$$\chi_{l,j,k\rightarrow u,j,k}(\nu) = \left(n_{l,j,k} B_{l,j,k\rightarrow u,j,k} - n_{u,j,k} B_{l,j,k\leftarrow u,j,k}\right) \frac{h\nu_{lu}}{4\pi} \phi_\nu \tag{3.33}$$

and

$$\eta_{l,j,k\leftarrow u,j,k}(\nu) = n_{u,j,k} \frac{A_{l,j,k\leftarrow u,j,k} h\nu_{lu}}{4\pi} \phi_\nu. \tag{3.34}$$

Assuming thermodynamic equilibrium, detailed balance requires that each absorption process balances its inverse emission processes. Therefore Equation (3.30) - Equation (3.32) imply

$$\left(\frac{n_{l,j,k}}{n_{u,j,k}}\right)^* B_{l,j,k\rightarrow u,j,k} I_\nu^* = A_{l,j,k\leftarrow u,j,k} + B_{l,j,k\leftarrow u,j,k} I_\nu^*, \tag{3.35}$$

where starred terms mean values in thermodynamic equilibrium. Using the Planck function (Equation 3.6) and the Boltzmann formula (Equation 3.11) this yields

$$\frac{2h\nu_{lu}^3}{c^2}\left(\exp\left(\frac{h\nu_{lu}}{k_{\mathrm{B}}T_{\mathrm{e}}}\right) - 1\right)^{-1} = \frac{A_{l,j,k\leftarrow u,j,k}}{B_{l,j,k\leftarrow u,j,k}}\left(\frac{B_{l,j,k\rightarrow u,j,k} g_{l,j,k}}{B_{l,j,k\leftarrow u,j,k} g_{u,j,k}} \exp\left(\frac{h\nu_{lu}}{k_{\mathrm{B}}T_{\mathrm{e}}}\right) - 1\right)^{-1}. \tag{3.36}$$

Thus we find the following relations between the Einstein coefficients

$$g_{l,j,k} B_{l,j,k\rightarrow u,j,k} = g_{u,j,k} B_{l,j,k\leftarrow u,j,k} \tag{3.37}$$

$$A_{l,j,k\leftarrow u,j,k} = \frac{2h\nu_{lu}^3}{c^2} B_{l,j,k\leftarrow u,j,k}. \tag{3.38}$$

Despite invoking thermodynamic equilibrium for this derivation, these relations hold in general since the Einstein coefficients depend on matter properties only, as mentioned earlier.

Thus, using Equation (3.37) we can rewrite the line opacity as

$$\chi_{l,j,k\rightarrow u,j,k}(\nu) = n_{l,j,k} \frac{B_{l,j,k\rightarrow u,j,k} h\nu_{lu}}{4\pi}\left(1 - \frac{g_{l,j,k} n_{u,j,k}}{g_{u,j,k} n_{l,j,k}}\right)\phi_\nu. \tag{3.39}$$

3.3.3 Continuum opacities

Treating stimulated recombination as negative absorption, the opacity due to bound-free absorptions in the continuum connecting the bound state (i, j, k) to the continuum $(j + 1, k)$ is given by

$$\chi_{i,j,k\rightarrow j+1,k}(\nu) = \alpha_{i,j,k\rightarrow j+1,k}(\nu)\left(n_{i,j,k} - n_{i,j,k}^* e^{-h\nu/k_{\mathrm{B}}T_{\mathrm{e}}}\right) \tag{3.40}$$

where $\alpha_{i,j,k\rightarrow j+1,k}(\nu)$ is the corresponding photoionization cross-section and $n_{i,j,k}^*$ refers to the LTE number density of level (i, j, k), which can be calculated from the actual values of n_{e} and $n_{0,j+1,k}$ using the Saha factor (Equation 3.15). This yields

$$\chi_{i,j,k\rightarrow j+1,k}(\nu) = n_{i,j,k}\alpha_{i,j,k\rightarrow j+1,k}(\nu)\left(1 - \frac{n_{0,j+1,k}}{n_{i,j,k}}\left(\frac{n_{i,j,k}}{n_{0,j+1,k}}\right)^* e^{-h\nu/k_{\mathrm{B}}T_{\mathrm{e}}}\right), \tag{3.41}$$

where the term in brackets is the correction for stimulated emission. The emissivity due to spontaneous bound-free emission is given by

$$\eta_{i,j,k\leftarrow j+1,k}\left(\nu\right)=n^{*}_{i,j,k}\alpha_{i,j,k\rightarrow j+1,k}\left(\nu\right)\frac{2h\nu^{3}}{c^{2}}e^{-h\nu/k_{\mathrm{B}}T_{\mathrm{e}}} \tag{3.42}$$

From this and Equation (3.40) we see that spontaneous and stimulated bf-emission always occur at their LTE rate for the kinetic temperature T_{e}, since recombination always involves collisions between ions and electrons.

The photoionization cross-section $\alpha_{i,j,k\rightarrow j+1,k}\left(\nu\right)$ can be calculated quantum mechanically (see Mihalas 1978). In general it sets in at the threshold frequency $\nu_{i,j,k}=\left(\varepsilon_{0,j+1,k}-\varepsilon_{i,j,k}\right)/h$ of the continuum and then declines continuously. In the simple hydrogenic approximation this decline follows

$$\alpha_{i,j,k\rightarrow j+1,k}\left(\nu\right)=\alpha^{\mathrm{threshold}}_{i,j,k\rightarrow j+1,k}\cdot\left(\frac{\nu_{i,j,k}}{\nu}\right)^{3}. \tag{3.43}$$

For ions with a more complicated atomic structure than hydrogen, resonances interfere with the trend of a generally declining photoionization cross-section above the edge frequency. Tabulated values for quantum mechanically calculated photoionization cross-sections, taking these resonances into account are available from the opacity project[2] (Seaton 1995).

Similarly opacity and emissivity due to free-free absorptions in the field of an ion (j,k) with ionic charge $j-1$ are given by

$$\chi^{\mathrm{ff}}_{j,k}\left(\nu\right)=n_{\mathrm{e}}N_{j,k}\alpha^{\mathrm{ff}}_{j,k}\left(\nu,T_{\mathrm{e}}\right)\left(1-e^{-h\nu/k_{\mathrm{B}}T_{\mathrm{e}}}\right) \tag{3.44}$$

and

$$\eta^{\mathrm{ff}}_{j,k}\left(\nu\right)=n_{\mathrm{e}}N_{j,k}\alpha^{\mathrm{ff}}_{j,k}\left(\nu,T_{\mathrm{e}}\right)\frac{2h\nu^{3}}{c^{2}}e^{-h\nu/k_{B}T_{\mathrm{e}}}, \tag{3.45}$$

where

$$\alpha^{\mathrm{ff}}_{j,k}\left(\nu,T\right)=\frac{4e^{6}}{3hc}\left(\frac{2\pi}{3m_{\mathrm{e}}^{3}k_{\mathrm{B}}}\right)^{1/2}\frac{\left(j-1\right)^{2}}{T^{1/2}}\frac{g_{\mathrm{ff}}\left(j,k\right)}{\nu^{3}}. \tag{3.46}$$

In cgs units this becomes $\alpha^{\mathrm{ff}}_{j,k}\left(\nu,T\right)=3.69255\cdot10^{8}\cdot\left(j-1\right)^{2}g_{\mathrm{ff}}\left(j,k\right)T^{-1/2}\nu^{-3}$. The quantum mechanical Gaunt factor $g_{\mathrm{ff}}\left(j,k\right)$ can be calculated or obtained from look-up tables (see e.g. Mihalas 1978).

Scattering by free electrons contributes also to the continuum opacity. In the limit of low energy photons ($h\nu\ll m_{\mathrm{e}}c^{2}$) its cross-section is given by the frequency independent Thomson cross-section

$$\sigma_{\mathrm{Th}}=\frac{8\pi e^{4}}{3m_{\mathrm{e}}^{2}c^{4}}=6.65\cdot10^{-25}\,\mathrm{cm}^{2}. \tag{3.47}$$

Thus opacity and emissivity follow,

$$\chi_{\mathrm{Th}}=n_{\mathrm{e}}\sigma_{\mathrm{Th}} \tag{3.48}$$

and

$$\eta_{\mathrm{Th}}=\chi_{\mathrm{Th}}J_{\nu}, \tag{3.49}$$

in which we assumed that frequency changes due to Doppler shifts caused by the thermal motions

---

[2] See http://cdsweb.u-strasbg.fr/topbase/home.html.

of the plasma can be neglected (coherent scattering). Furthermore the dipole characteristic of the Thomson scattering was approximated by isotropic re-emission.

3.3.4 Interaction of γ-photons and matter

The relevant mechanisms for interactions of γ-photons with matter in supernova ejecta are Compton scattering, photo-electric absorption and pair-production for photons of energies above $2m_{\mathrm{e}}c^2$. The Compton cross-section σ_{C} can be derived from quantum electrodynamics. Neglecting the thermal motions of electrons in the cmf of the photon, this is given by the Klein-Nishina formula

$$\sigma_{\mathrm{C}} = \frac{3}{4}\sigma_{\mathrm{Th}} \left\{ \frac{1+x}{x^3} \left[\frac{2x\,(1+x)}{1+2x} - \ln{(1+2x)} \right] + \frac{1}{2x} \ln{(1+2x)} - \frac{1+3x}{(1+2x)^2} \right\} \tag{3.50}$$

(Rybicki & Lightman 1979), where $x = h\nu/m_{\mathrm{e}}c^2$. Due to their large energies, γ-rays can be Compton scattered by both free and bound electrons. Thus the total opacity for Compton scattering is

$$\chi_{\mathrm{C}} = n_{\mathrm{e}}^{\mathrm{tot}} \sigma_{\mathrm{C}}, \tag{3.51}$$

where $n_{\mathrm{e}}^{\mathrm{tot}}$ is the total number density of electrons. Since Compton scattering is not isotropic, the directional characteristic given by the differential cross-section should be taken into account when scattered photons are re-emitted.

For photo-electric absorption and pair production, we follow Ambwani & Sutherland (1988) and use parameterized cross-sections derived from Veigele (1973) which depend on the composition of the absorbing material in a simple manner. Thus the opacity due to photo-electric absorption is

$$\begin{aligned} \chi_{\gamma}^{\mathrm{bf}}(\nu) = {} & 1.16 \cdot 10^{-24} \mathrm{cm}^2 \left(\frac{h\nu}{100\,\mathrm{keV}} \right)^{-3.13} \frac{\rho}{m_{\mathrm{Si}}} (1 - X_{\mathrm{Fe-grp}}) \\ & + 25.7 \cdot 10^{-24}\,\mathrm{cm}^2 \left(\frac{h\nu}{100\,\mathrm{keV}} \right)^{-3.0} \frac{\rho}{m_{\mathrm{Fe}}} X_{\mathrm{Fe-grp}}, \end{aligned} \tag{3.52}$$

where the first term represents a typical cross-section for intermediate-mass elements (here normalized to the mass of the silicon atom m_{Si}) and the second term one for iron-group elements (normalized to the mass of the iron atom m_{Fe}). ρ is the local mass density and $X_{\mathrm{Fe-grp}}$ the local mass-fraction of iron-group elements. Similarly the adopted opacity due to pair-production is

$$\chi_{\gamma\gamma}(\nu) = \rho \left[\frac{Z_{\mathrm{Si}}^2}{m_{\mathrm{Si}}} (1 - X_{\mathrm{Fe-grp}}) + \frac{Z_{\mathrm{Fe}}^2}{m_{\mathrm{Fe}}} X_{\mathrm{Fe-grp}} \right] \cdot 1.0063 \left(\frac{h\nu}{1\,\mathrm{MeV}} - 1.022 \right) \cdot 10^{-27}\,\mathrm{cm}^2 \tag{3.53}$$

for photon energies in the range $1.022\,\mathrm{MeV} < h\nu < 1.5$ MeV and

$$\chi_{\gamma\gamma}(\nu) = \rho \left[\frac{Z_{\mathrm{Si}}^2}{m_{\mathrm{Si}}} (1 - X_{\mathrm{Fe-grp}}) + \frac{Z_{\mathrm{Fe}}^2}{m_{\mathrm{Fe}}} X_{\mathrm{Fe-grp}} \right] \left[0.0481 + 0.301 \left(\frac{h\nu}{1\,\mathrm{MeV}} - 1.5 \right) \right] \cdot 10^{-27}\,\mathrm{cm}^2 \tag{3.54}$$

above. Here Z_{Si} and Z_{Fe} denote the charge number of the silicon and iron nuclei, respectively.

3.4 Statistical equilibrium

The excitation and ionization state of a gas, described by the occupation numbers of the different atomic levels, in general depends on both collisional and radiative transitions between the atomic levels. Provided that elastic collisions between electrons happen so frequently that particles follow their equilibrium distribution given by the Maxwellian velocity distribution and collisional processes dominate in all transitions, the populations can be calculated using the Saha and Boltzmann equations described in Section 3.2 evaluated at the local kinetic temperature and density. Then LTE is a valid approximation.

In radiating astrophysical plasmas, however, this is not true due to their low densities. Thus radiative processes can drive the excitation and ionization state of the plasma away from its equilibrium value if the radiation field deviates from its equilibrium distribution (i.e. the Planck function). This is particularly the case in regions from which we see escaping radiation (e.g. stellar atmospheres) because the radiation field there is necessarily anisotropic (almost no radiation enters through the medium's outer boundary). Furthermore the radiation field in these low opacity environments originates mostly from scattering in deeper layers. Thus, even once thermally emitted radiation can have a different characteristic radiation temperature T_{R} than the local kinetic temperature T_{e}. In this case the statistical rate equations, describing the temporal change in the occupation numbers for each atomic level due to all contributing population and depopulation processes must be solved to derive the excitation and ionization state of the plasma.

3.4.1 Rate equations

The most general form of these equations is given by

$$\frac{\partial n_i}{\partial t} = \sum_{j \neq i} n_j P_{ji} - n_i \sum_{j \neq i} P_{ij} - \nabla \cdot (n_i \vec{v}) \,, \tag{3.55}$$

where we have a separate equation for all the atomic levels $i \in [1, L]$ in consideration. n_i is the number density of particles in atomic state i and P_{ij} the total rate coefficient denoting the probability of transitions from state i to state j per unit time. It has contributions from both radiative (r_{ij}) and collisional (c_{ij}) transitions

$$P_{ij} = r_{ij} + c_{ij}. \tag{3.56}$$

$\nabla \cdot (n_i \vec{v})$ accounts for changes due to advection. The summations run over all processes contributing to population and depopulation of state i, regardless if i and j belong to the same ionization state or not. Thus they include radiative and collisional excitation/deexcitation and ionization/recombination. Neglecting inelastic atomic collisions and molecular processes there are, however, no transitions between different chemical species.

In the stationary case ($\partial n_i / \partial t = 0$) the equation system (3.55) reduces to

$$\sum_{j \neq i} n_j P_{ji} - n_i \sum_{j \neq i} P_{ij} - \nabla \cdot (n_i \vec{v}) = 0 \qquad i \in [1, L] \,. \tag{3.57}$$

These are called the **statistical equilibrium equations**.

Considering e.g. the radiative recombination rate from Fe III to Fe II which, according to Shull & van Steenberg (1982), is given by $R = n_{\mathrm{e}} 1.02 \cdot 10^{-12} \left(T_{\mathrm{e}}/10^4\,\mathrm{K}\right)^{0{,}843}\,\mathrm{cm}^3\,\mathrm{s}^{-1}$, we obtain a recombination time of $\sim 10^3\,\mathrm{s}$ for typical values at maximum light of SNe Ia ($T_{\mathrm{e}} \sim 10\,000\,\mathrm{K}$, $n_{\mathrm{e}} \sim 10^9\,\mathrm{cm}^{-3}$, $t_{\max} \sim 20\,\mathrm{d}$). Compared to the time scale on which the flow properties change, which is proportional to the time since explosion ($\sim 2 \cdot 10^6\,\mathrm{s}$), the recombination time is negligible, although radiative recombination is a comparatively slow processes. Having radiative time scales which are much smaller than the typical time scales of the flow, the advection term may be neglected, yielding

$$\sum_{j \neq i} n_j P_{ji} - n_i \sum_{j \neq i} P_{ij} = 0 \qquad i \in [1, L]\,. \tag{3.58}$$

To solve this equation system which depends on the $L+2$ variables $(n_1, \dots, n_L, n_{\mathrm{e}}, N)$ with N being the total number density of particles, we need two additional equations. These are the equations describing the conservation of the particle number and charge

$$N = \sum_{i=1}^{L} n_i + n_{\mathrm{e}} \tag{3.59}$$

$$n_{\mathrm{e}} = \sum_{i=1}^{L} n_i q_i, \tag{3.60}$$

where q_i denotes the charge of the ionization state corresponding to level n_i. The equation system given by (3.58) - (3.60) is highly non-linear since the transition probabilities depend on n_e and via the radiation field also on the occupation numbers (see the corresponding expressions in the following sections). Thus their solution requires an iterative linearization scheme.

3.4.2 Radiative rates

The rates for bound-bound radiative transitions between two atomic levels (i, j, k) and (i', j, k) with $\varepsilon_{i,j,k} < \varepsilon_{i',j,k}$ are given by the Einstein coefficients

$$\begin{aligned} R_{i,j,k \to i',j,k} &= n_{i,j,k} r_{i,j,k \to i',j,k} \\ &= n_{i,j,k} B_{i,j,k \to i',j,k} \int \phi_\nu J_\nu \mathrm{d}\nu \end{aligned} \tag{3.61}$$

$$\begin{aligned} R_{i,j,k \leftarrow i',j,k} &= n_{i',j,k} r_{i,j,k \leftarrow i',j,k} \\ &= n_{i',j,k} \left(A_{i,j,k \leftarrow i',j,k} + B_{i,j,k \leftarrow i',j,k} \int \phi_\nu J_\nu \mathrm{d}\nu \right). \end{aligned} \tag{3.62}$$

Using Equation (3.28) and the line profile function ϕ_ν we can define the frequency-dependent line absorption cross-section

$$\alpha_{i,j,k \to i',j,k}(\nu) = \alpha_{i,j,k \to i',j,k} \phi_\nu = \frac{h\nu_{ii'}}{4\pi} B_{i,j,k \to i',j,k} \phi_\nu, \tag{3.63}$$

to rewrite Equations (3.61) and (3.62)

$$\begin{aligned} R_{i,j,k\to i',j,k} &= n_{i,j,k} r_{i,j,k\to i',j,k} \\ &= n_{i,j,k} 4\pi \int \frac{\alpha_{i,j,k\to i',j,k}(\nu)}{h\nu} J_\nu \mathrm{d}\nu \end{aligned} \tag{3.64}$$

$$\begin{aligned} R_{i,j,k\leftarrow i',j,k} &= n_{i',j,k} r_{i,j,k\leftarrow i',j,k} \\ &= n_{i,j,k} \left(\frac{n_{i,j,k}}{n_{i',j,k}}\right)^* 4\pi \int \frac{\alpha_{i,j,k\to i',j,k}(\nu)}{h\nu} \left(\frac{2h\nu^3}{c^2} + J_\nu\right) e^{-h\nu/k_\mathrm{B}T_\mathrm{e}} \mathrm{d}\nu, \end{aligned} \tag{3.65}$$

where we made use of the Einstein relations (Equations 3.37 and 3.38) for the downward rate and $\left(n_{i,j,k}/n_{i',j,k}\right)^*$ is the LTE population ratio of the corresponding levels given by the Boltzmann formula (Equation 3.11). The frequency dependent factors can be taken below the integral since the line profile varies much more rapidly than those terms.

The bound-free radiative rates take the same form. The only difference are the absorption cross-sections, which must be replaced by the photoionization cross-section. Thus for a continuum $(i,j,k) \to (j+1,k)$ with edge frequency $\nu_{i,j,k} = \left(\varepsilon_{0,j+1,k} - \varepsilon_{i,j,k}\right)/h$ the bound-free radiative rates are given by

$$\begin{aligned} R_{i,j,k\to j+1,k} &= n_{i,j,k} \gamma_{i,j,k} \\ &= n_{i,j,k} 4\pi \int_{\nu_{i,j,k}}^{\infty} \frac{\alpha_{i,j,k\to j+1,k}(\nu)}{h\nu} J_\nu \mathrm{d}\nu \end{aligned} \tag{3.66}$$

$$\begin{aligned} R_{i,j,k\leftarrow j+1,k} &= n_{0,j+1,k} r_{i,j,k\leftarrow j+1,k} \\ &= n_{0,j+1,k} \left(\frac{n_{i,j,k}}{n_{0,j+1,k}}\right)^* 4\pi \int_{\nu_{i,j,k}}^{\infty} \frac{\alpha_{i,j,k\to j+1,k}(\nu)}{h\nu} \left(\frac{2h\nu^3}{c^2} + J_\nu\right) e^{-h\nu/k_\mathrm{B}T_\mathrm{e}} \mathrm{d}\nu. \end{aligned} \tag{3.67}$$

where $\gamma_{i,j,k}$ is the rate coefficient for photoionization.

Splitting the latter equation into spontaneous and stimulated recombination we obtain

$$\begin{aligned} R^{\mathrm{spont}}_{i,j,k\leftarrow j+1,k} &= n_{0,j+1,k} n_\mathrm{e} \alpha^{\mathrm{spont}}_{i,j,k} \\ &= n_{0,j+1,k} n_e \phi_{i,j,k}(T_\mathrm{e}) 4\pi \int_{\nu_{i,j,k}}^{\infty} \frac{\alpha_{i,j,k\to j+1,k}(\nu)}{h\nu} \frac{2h\nu^3}{c^2} e^{-h\nu/k_\mathrm{B}T_\mathrm{e}} \mathrm{d}\nu \end{aligned} \tag{3.68}$$

$$\begin{aligned} R^{\mathrm{stim}}_{i,j,k\leftarrow j+1,k} &= n_{0,j+1,k} n_\mathrm{e} \alpha^{\mathrm{stim}}_{i,j,k} \\ &= n_{0,j+1,k} n_e \phi_{i,j,k}(T_\mathrm{e}) 4\pi \int_{\nu_{i,j,k}}^{\infty} \frac{\alpha_{i,j,k\to j+1,k}(\nu)}{h\nu} J_\nu e^{-h\nu/k_\mathrm{B}T_\mathrm{e}} \mathrm{d}\nu, \end{aligned} \tag{3.69}$$

where we made use of the Saha factor (Equation 3.15). Treating stimulated recombinations as negative photoionizations, the corrected photoionization rate is given by

$$\tilde{R}_{i,j,k\to j+1,k} = n_{i,j,k} \tilde{\gamma}_{i,j,k} = n_{i,j,k} \gamma_{i,j,k} - n_{0,j+1,k} n_\mathrm{e} \alpha^{\mathrm{stim}}_{i,j,k} \tag{3.70}$$

with the rate coefficient corrected for photoionization

$$\begin{aligned}\tilde{\gamma}_{i,j,k} &= \gamma_{i,j,k} - \frac{n_{0,j+1,k} n_{\mathrm{e}}}{n_{i,j,k}} \alpha^{\mathrm{stim}}_{i,j,k} \\ &= 4\pi \int_{\nu_{i,j,k}}^{\infty} \frac{\alpha_{i,j,k\to j+1,k}\left(\nu\right)}{h\nu} \left(1 - \frac{n_{0,j+1,k}}{n_{i,j,k}} \frac{n^{*}_{i,j,k}}{n^{*}_{0,j+1,k}} e^{-h\nu/k_{\mathrm{B}}T_{\mathrm{e}}}\right) J_{\nu} \mathrm{d}\nu. \end{aligned} \tag{3.71}$$

3.4.3 Collisional rates

Due to their small mass, electrons have higher velocities compared to the more massive ions. Thus electron collisions are more frequent and dominate the collisional rates. The collisional bound-bound upward rates are then given by

$$\begin{aligned} C_{i,j,k\to i',j,k} &= n_{i,j,k} c_{i,j,k\to i',j,k} \\ &= n_{i,j,k} n_{\mathrm{e}} \int_{v_0}^{\infty} \sigma_{i,j,k\to i',j,k}\left(v\right) f\left(v\right) \mathrm{d}v, \end{aligned} \tag{3.72}$$

where $\sigma_{i,j,k\to i',j,k}\left(v\right)$ is the cross-section for electron-induced collisional transitions between two atomic levels (i,j,k) and (i',j,k) $(\varepsilon_{i,j,k} < \varepsilon_{i',j,k})$, $f\left(v\right)$ the Maxwellian velocity distribution and v_0 a velocity such that the kinetic energy $\frac{1}{2} m_{\mathrm{e}} v_0^2$ equals the threshold energy of the transition. Replacing $\sigma_{i,j,k\to i',j,k}\left(v\right)$ with the collisional ionization cross-section $\sigma_{i,j,k\to j+1,k}\left(v\right)$ connecting the atomic level (i,j,k) to the continuum $(j+1,k)$ we find the collisional bound-free upward rate

$$\begin{aligned} C_{i,j,k\to j+1,k} &= n_{i,j,k} c_{i,j,k\to j+1,k} \\ &= n_{i,j,k} n_{\mathrm{e}} \int_{v_0}^{\infty} \sigma_{i,j,k\to j+1,k}\left(v\right) f\left(v\right) \mathrm{d}v, \end{aligned} \tag{3.73}$$

where now $\frac{1}{2} m_{\mathrm{e}} v_0^2$ corresponds to the ionization threshold of the considered continuum.

The downward rates follow from a detailed balance argument

$$n_{i',j,k} c_{i,j,k\leftarrow i',j,k} = n_{i',j,k} \left(\frac{n_{i,j,k}}{n_{i',j,k}}\right)^{*} c_{i,j,k\to i',j,k} \tag{3.74}$$

$$n_{0,j+,k} c_{i,j,k\leftarrow j+1,k} = n_{0,j+1,k} \left(\frac{n_{i,j,k}}{n_{0,j+1,k}}\right)^{*} c_{i,j,k\to j+1,k}. \tag{3.75}$$

The collisional cross-sections $\sigma_{i,j,k\to i',j,k}\left(v\right)$ and $\sigma_{i,j,k\to j+1,k}\left(v\right)$ can be calculated quantum mechanically, but are not well known in general. In this work we use very simple approximations, allowing the calculation of the collisional bound-bound rates for radiatively permitted transitions $(i,j,k) \to (i',j,k)$ from the oscillator strength $f_{ii'}$ (Equation 3.28)

$$c_{i,j,k\to i',j,k} = n_{\mathrm{e}} c_0 T^{1/2} 14.5 \left(\frac{I_{\mathrm{H}}}{h\nu_{ii'}}\right) f_{ii'} \frac{h\nu_{ii'}}{k_{\mathrm{B}} T_{\mathrm{e}}} e^{-h\nu_{ii'}/k_{\mathrm{B}}T_{\mathrm{e}}} \Gamma\left(\frac{h\nu_{ii'}}{k_{\mathrm{B}} T_{\mathrm{e}}}\right) \tag{3.76}$$

(van Regemorter approximation; Equation 5-75 of Mihalas 1978). Here, $c_0 = 5.46510^{-11}$ is a constant, $I_{\mathrm{H}} = 13.6\,\mathrm{eV}$ is the ionization potential of hydrogen and $h\nu_{ii'} = \varepsilon_{i',j,k} - \varepsilon_{i,j,k}$ is the corresponding transition energy.

$$\Gamma\left(x\right)=\max\left(\bar{g},0.276e^{x}E_{1}\left(x\right)\right) \tag{3.77}$$

is a function, which depends via

$$\bar{g}\sim\begin{cases}0.7 & \text{for transitions } \langle n,l\rangle\rightarrow\langle n,l'\rangle\\ 0.2 & \text{for transitions } \langle n,l\rangle\rightarrow\langle n',l'\rangle\end{cases} \tag{3.78}$$

on the type of transition and the exponential integral function $E_1\left(x\right)$.

Similarly the collisional bound-free rates for the continuum $(i,j,k)\rightarrow(j+1,k)$ with ionization threshold $h\nu_{i,j,k}=\varepsilon_{0,j+1,k}-\varepsilon_{i,j,k}$ are calculated from the corresponding photoionization cross-section $\alpha_{i,j,k\rightarrow j+1,k}\left(\nu_{i,j,k}\right)$

$$c_{i,j,k\rightarrow j+1,k}=n_{\mathrm{e}}\frac{1.55\cdot10^{13}}{T_{\mathrm{e}}^{1/2}}\bar{g}_{i}\frac{\alpha_{i,j,k\rightarrow j+1,k}\left(\nu_{i,j,k}\right)}{h\nu_{i,j,k}/k_{\mathrm{B}}T_{\mathrm{e}}}e^{-h\nu_{i,j,k}/k_{\mathrm{B}}T_{\mathrm{e}}} \tag{3.79}$$

where $\bar{g}_i$ equals 0.1, 0.2 or 0.3 if the charge on the ionization state of level i is 0, 1 or ≥ 2 (Seaton approximation; Equation 5-79 of Mihalas 1978).

3.5 Transfer equation

The change in specific intensity $\mathrm{d}I_\nu$ between $(\mathbf{x}+\mathrm{d}\mathbf{x},t+\mathrm{d}t)$ and $(\mathbf{x},t)$ along a ray element $\mathrm{d}\mathbf{s}=\mathrm{d}s\mathbf{n}$ in the laboratory frame is given by

$$\mathrm{d}I_{\nu}=I\left(\mathbf{x}+\mathrm{d}\mathbf{x},t+\mathrm{d}t;\mathbf{n},\nu\right)-I\left(\mathbf{x},t;\mathbf{n},\nu\right)=\left(\frac{1}{c}\frac{\partial}{\partial t}I_{\nu}+\frac{\partial}{\partial\mathbf{s}}I_{\nu}\right)\mathrm{d}s. \tag{3.80}$$

This must equal the change in intensity $\mathrm{d}I_\nu=\mathrm{d}I_\nu^{\mathrm{em}}-\mathrm{d}I_\nu^{\mathrm{abs}}$ during time $\mathrm{d}t$ due to absorption and emission by the matter along the ray element $\mathrm{d}\mathbf{s}$. Using Equations (3.16) and (3.18) we then find the transfer equation

$$\left(\frac{1}{c}\frac{\partial}{\partial t}+\frac{\partial}{\partial\mathbf{s}}\right)I\left(\mathbf{x},t;\mathbf{n},\nu\right)=\eta\left(\mathbf{x},t;\mathbf{n},\nu\right)-\chi\left(\mathbf{x},t;\mathbf{n},\nu\right)I\left(\mathbf{x},t;\mathbf{n},\nu\right). \tag{3.81}$$

In the stationary case this simplifies to

$$\frac{\partial}{\partial\mathbf{s}}I\left(\mathbf{x};\mathbf{n},\nu\right)=\eta\left(\mathbf{x};\mathbf{n},\nu\right)-\chi\left(\mathbf{x};\mathbf{n},\nu\right)I\left(\mathbf{x};\mathbf{n},\nu\right). \tag{3.82}$$

If opacity and emissivity are known this is an ordinary differential equation with **formal solution**

$$I\left(\mathbf{x};\mathbf{n},\nu\right)=\int_{0}^{s_{0}}\eta\left(\mathbf{x}-\mathbf{n}s;\mathbf{n},\nu\right)e^{-\int_{0}^{s}\chi(\mathbf{x}-\mathbf{n}s';\mathbf{n},\nu)ds'}ds+I\left(\mathbf{x}_{0};\mathbf{n},\nu\right)e^{-\int_{0}^{s_{0}}\chi(\mathbf{x}-\mathbf{n}s;\mathbf{n},\nu)ds}. \tag{3.83}$$

Thus the intensity of a beam of radiation, originating from point $\mathbf{x}$ into direction $\mathbf{n}$, is given by a summation of the emissivity along the path segment $\mathbf{x}-\mathbf{n}s$ between point $\mathbf{x}$ and a boundary at $\mathbf{x}_0 = \mathbf{x} - \mathbf{n}s_0$ ($s \in [0, s_0]$) attenuated by the integrated opacity of the intervening material. The second term accounts for the incident intensity at the boundary $I(\mathbf{x}_0; \mathbf{n}, \nu)$ attenuated by the material between the boundary and point $\mathbf{x}$.

Defining the **optical depth**

$$\tau_\nu(s_0) = \tau_\nu(0, s_0) = \int_0^{s_0} \chi(\mathbf{x} - \mathbf{n}s; \mathbf{n}, \nu)\, \mathrm{d}s \tag{3.84}$$

which gives the integrated opacity along a given path element, or according to Equation (3.17) inversely the number of photon mean free paths, Equation (3.83) can be rewritten as

$$I(\mathbf{x}; \mathbf{n}, \nu) = \int_0^{s_0} \eta(\mathbf{x} - \mathbf{n}s; \mathbf{n}, \nu)\, e^{-\tau_\nu(s)} \mathrm{d}s + I(\mathbf{x}_0; \mathbf{n}, \nu)\, e^{-\tau_\nu(s_0)}. \tag{3.85}$$

Due to scattering terms, however, the emissivity generally depends on the radiation field via the mean intensity J_ν, thus making Equations (3.81) and (3.82) integro-differential equations coupling together radiation from different directions. Furthermore, without using the LTE approximation, both emissivity and opacity depend on the radiation field via the excitation and ionization state of the plasma. Thus the solution of Equation (3.81) becomes a highly complex problem which has to be solved numerically by iterative schemes [for different solution strategies see e.g. Mihalas (1978) or Hubeny et al. (2003)]. We use a Monte Carlo method to solve the transfer problem which is outlined in Chapter 4.

In connection with the transfer equation it is common to define the **source function**

$$S(\mathbf{x}, t; \mathbf{n}, \nu) = \frac{\eta(\mathbf{x}, t; \mathbf{n}, \nu)}{\chi(\mathbf{x}, t; \mathbf{n}, \nu)}. \tag{3.86}$$

Together with the optical depth $d\tau_\nu = -\chi(\mathbf{x}, t; \mathbf{n}, \nu)\, \mathrm{d}s$ (the minus sign enters because, according to Equation (3.84), the optical depth increases while going back along the photon path) this allows us to rewrite Equation (3.82) as

$$\frac{\partial}{\partial \tau_\nu} I(\mathbf{x}; \mathbf{n}, \nu) = I_\nu - S_\nu. \tag{3.87}$$

Media in which energy transport is maintained by radiative processes only (i.e. neglecting heat conduction and convection), are said to be in **radiative equilibrium**. Then at each point $\mathbf{x}$

$$\int_\nu \mathrm{d}\nu \oint_{4\pi} \mathrm{d}\omega \left(\eta(\mathbf{x}, t; \mathbf{n}, \nu) - \chi(\mathbf{x}, t; \mathbf{n}, \nu)\, I(\mathbf{x}, t; \mathbf{n}, \nu)\right) = 0. \tag{3.88}$$

Having outlined the basic concepts of the theory of radiation in this chapter, we will now focus on the special case of radiative transfer in supernova ejecta and describe the code developed during this thesis to tackle that problem.

4 Implementation

In this chapter we give a short overview on Monte Carlo methods and the difficulties arising in the treatment of radiative transfer in supernovae due to their expanding ejecta. Then we present a detailed discussion of ARTIS the multi-dimensional Monte Carlo code to solve the time-dependent non-grey radiative transfer problem in chemically inhomogeneous models of supernova ejecta which was developed during this thesis on the basis of the grey code of Sim (2007). Aiming for an approximate NLTE treatment, we outline the derivation of the plasma conditions from the radiative transfer simulation. Finally some remarks concerning the parallelization of the code and the atomic data, required for the non-grey radiation treatment, are made. Parts of the discussion in Sections 4.3, 4.4 and 4.6 have already been published (Kromer & Sim 2009).

4.1 Monte Carlo radiative transfer

The Monte Carlo method is a probabilistic approach to solving the transfer equation (3.81) directly and has been widely applied in astrophysical radiative transfer (e.g. Auer 1968, Pozdniakov et al. 1983, Abbott & Lucy 1985, Mazzali & Lucy 1993, Long & Knigge 2002, Ercolano et al. 2003). However, it is not restricted to radiative transfer simulations. In fact it is widely used in the numerical sciences, e.g. for general statistical problems, hardware simulation, numerical integration and in particle physics simulations (for a historical review on the development of Monte Carlo techniques see Metropolis 1987). In the astrophysical context other application areas are e.g. hierarchical structure formation or population synthesis.

The basic concept of a Monte Carlo radiative transfer code is to track photons (or energy packets representing a bunch of identical photons), emitted randomly by sampling an emissivity η_ν, through a simulation volume until they interact with matter or leave the volume. Thereby the optical depth along the photon path is accumulated and used to determine randomly whether an interaction occurs. In an interaction the incident photon is destroyed and a new photon may be emitted randomly according to the probability distribution of the interaction process. The escaping photons are used to obtain synthetic spectra while weighted sums of the photons in a given volume element, or better – since that reduces the statistical noise – weighted sums of the path length for all photons that passed through that volume element during a given time span, can be used to estimate properties of the radiation field.

Compared to other iterative radiative transfer techniques (see e.g. Mihalas 1978 or Hubeny et al. 2003), the Monte Carlo method is quite simple. Thus Monte Carlo codes are relatively easy to develop and less likely to suffer from numerical problems (Auer 2003). Because the method does not rely on a specific geometry, Monte Carlo codes are also readily extended to multi-dimensional problems (see e.g. Long & Knigge 2002, Ercolano et al. 2003, Kasen et al. 2006 and Maeda et al.

2006). Furthermore Doppler and aberration effects are easily taken into account when photons are tracked via quanta, thus making Monte Carlo methods particularly suited to model astrophysical radiative transfer in moving media [e.g. Abbott & Lucy (1985) and Lucy & Abbott (1993) for winds of massive stars and Mazzali & Lucy (1993) for the expanding envelopes of supernovae]. The photon propagation itself is carried out in the rest frame of the observer, where it is described most easily. Interactions between photons and matter, however, depend on the atomic processes discussed in Section 3.3 and are thus most naturally described in the local co-moving frame of the fluid. Hence the photon is transformed to the co-moving frame to calculate opacities, which are then transformed back to the rest frame for use in the transfer calculation. Similarly emissions of photons after photon-matter interactions are treated in the co-moving frame, making the emission of a photon a two step procedure: first the frequency and direction of the photon in the cmf are sampled, then the photon is transformed to the rest frame for propagation.

The main disadvantage of Monte Carlo codes, compared to codes based on traditional methods, are the enormous needs of computational power to obtain results of sufficient signal-to-noise ratio. Due to their probabilistic nature this requires a large number of photons to be tracked (the signal-to-noise ratio improves with the square root of the number of simulated photons). Especially in optically thick regions, where photons are trapped, this becomes very expensive. However, since energy packets can be propagated independently of each other, Monte Carlo codes are easy to parallelize and show a good scaling behaviour. Thus they become more and more attractive, with the increasing availability of massively parallel super-computers – especially since other methods do not show such favorable scaling behaviour.

The key tool in all Monte Carlo simulations is the random sampling of a probability distribution function. If a process has the probability density function (PDF) $p\left(x\right)$, the probability to find a random value x_r in the interval $[x_0, x_1]$ is given by

$$\mathcal{P}\left(x_0 \leq x_\mathrm{r} \leq x_1\right) = \int_{x_0}^{x_1} p\left(x'\right) \mathrm{d}x'$$

and the cumulative probability distribution function (CDF) by

$$P\left(x\right) = \int_{x_\mathrm{min}}^{x} p\left(x'\right) \mathrm{d}x'. \tag{4.1}$$

Since the total probability of a process must be one, $P\left(x_\mathrm{max}\right) = 1$. Thus

$$z = \int_{x_\mathrm{min}}^{x} p\left(x'\right) \mathrm{d}x', \tag{4.2}$$

specifies a particular value x for a randomly selected value z distributed uniformly on $[0, 1]$. This has to be drawn from a random number generator. Since computational random number generators are only able to produce sequences of pseudo random numbers, determined by the numerical algorithm in use and an initial seed, particular care has to be taken that the random number generator in use produces sufficiently long sequences of independent random numbers. In this work we use the `gsl_rng_ran3` algorithm of the GNU Scientific Library (GSL)[1]. For a discussion on random number generators see e.g. Press et al. (1992).

---

[1] Available at http://www.gnu.org/software/gsl/.

For a discrete CDF $P(x) = \sum_i p(x_i)$, which occurs for example in the random selection of a particular atomic transition, Equation (4.2) can be solved by performing a search over the contributing processes. For continuous CDFs Equation (4.2) may be inverted analytically in simple cases. Calculating how far a photon travels before it interacts with matter, for example, is such a case. Recalling from Equation (3.84) that the optical depth τ is a measure of the number of photon mean free paths, the probability that a photon travels an amount τ without interacting is given by $e^{-\tau}$. Inversely, it will undergo an interaction with probability $1 - e^{-\tau}$. Thus we may sample

$$z = 1 - e^{-\tau_\mathrm{r}}, \qquad z \in [0,1[\tag{4.3}$$

to get a random optical depth τ_r to the next interaction of a photon packet. Inverting Equation (4.3) yields

$$\tau_\mathrm{r} = -\ln(1-z)\,. \tag{4.4}$$

Changing z to $z' \in]0,1]$ this can be rewritten as

$$\tau_\mathrm{r} = -\ln(z') \tag{4.5}$$

since the logarithm covers the same range of values for $1-z$ and z if $z \in [0,1]$. The physical distance corresponding to τ_r follows then from Equation (3.84).

If Equation (4.2) cannot be inverted analytically the rejection method may be used. Thereby a random value $x \in [x_\mathrm{min}, x_\mathrm{max}]$ is chosen. If $p(x)$ is smaller than a second random value $\xi \in [0, p_\mathrm{max}]$, x is selected. Otherwise a new pair of random numbers (x, ξ) is chosen until the selection criterion is fulfilled.

4.2 Homologous expansion, Sobolev approximation

Since supernovae ejecta are expanding, a full treatment of the radiative transfer problem would require a solution of the radiative transfer equation coupled to the equations of hydrodynamics (see e.g. Mihalas & Weibel Mihalas 1984). This is a highly complex problem, which is computationally still too demanding to solve. However, simulations show that the ejecta of SNe Ia are in free expansion, i.e. their kinetic energy density dominates the gravitational and internal energy densities, less than a minute after the explosion (e.g. Röpke 2005). In this limit the evolution of the ejecta at a particular position $\mathbf{r} = r\hat{\mathbf{r}}$ can be described by

$$\mathbf{r} = v\,(t - t_\mathrm{fs})\,\hat{\mathbf{r}} + \mathbf{r}_\mathrm{fs}, \tag{4.6}$$

where v is the velocity, t is the time since explosion, t_fs the time when the free-streaming sets in and $\mathbf{r}_\mathrm{fs}$ the position at this time. Since the ejecta are sufficiently optically thick prior to t_fs that no radiation will escape, the radiative transfer problem then decouples from the hydrodynamic evolution of the ejecta, thereby significantly simplifying the problem.

Simulations of the radiative transfer problem must set in when the optical depth in the ejecta drops sufficiently that photons start to escape. This occurs typically at $\sim 1\,\mathrm{d}$ after the explosion. Since then $t \gg t_\mathrm{fs}$ and the ejecta will have expanded sufficiently that we can neglect $\mathbf{r}_\mathrm{fs}$, it is possible to describe the further evolution of the ejecta assuming **homologous expansion**

$$\mathbf{r} = vt\hat{\mathbf{r}}. \tag{4.7}$$

As consequence of this simple velocity law the co-moving frame frequency ν' of photons is constantly redshifting on their way through the ejecta. To see this, we differentiate the Doppler formula (3.23) along the photon path

$$\frac{\mathrm{d}\nu'}{\mathrm{d}s} = -\frac{\nu}{c}\frac{\mathrm{d}}{\mathrm{d}s}\mathbf{n}.\mathbf{v} = -\frac{\nu}{c}\frac{\mathrm{d}v_s}{\mathrm{d}s}. \tag{4.8}$$

With Equation (4.7) this yields

$$\frac{\mathrm{d}\nu'}{\mathrm{d}s} = -\frac{\nu}{ct} < 0. \tag{4.9}$$

Rewriting Equation (4.8) as

$$\Delta s = \left| -\frac{c}{\nu_{lu}} \frac{\Delta\nu'}{\mathrm{d}v_s/ds} \right| \tag{4.10}$$

we find a simple estimate of the region Δs in which a photon can come into resonance with a particular atomic line $(l, j, k) \rightarrow (u, j, k)$ $(h\nu_{lu} = \varepsilon_{u,j,k} - \varepsilon_{l,j,k})$. Assuming that the line width $\Delta\nu'$ is only due to Doppler broadening

$$\Delta\nu' = \nu_{lu}\frac{v_{\mathrm{th}}}{c} \tag{4.11}$$

with v_{th} being the velocity of particles in the ejecta due to their thermal motions. Approximating the velocity gradient by $\mathrm{d}v_s/\mathrm{d}s \approx v_0/l_0$, where v_0 and l_0 are the characteristic velocity and length on which the macroscopic quantities of the ejecta vary, this yields

$$\Delta s = \frac{v_{\mathrm{th}}}{v_0} l_0. \tag{4.12}$$

Since the thermal velocity in supernova ejecta (typically $v_{\mathrm{th}} \sim 5\,\mathrm{km\,s^{-1}}$) is much smaller than v_0 (typical expansion velocities in supernova envelopes reach up to $\sim 30\,000\,\mathrm{km\,s^{-1}}$), the interaction region Δs is much smaller than the characteristic length on which the macroscopic properties of the ejecta vary $\Delta s \ll l_0$. In this limit we can assume that the interaction is confined to the resonance point at which $\nu'(s) = \nu_{lu}$. Then the line profile can be approximated by the δ-function

$$\phi(\nu') = \delta(\nu' - \nu_{lu}). \tag{4.13}$$

This so-called **Sobolev approximation** [Sobolev (1957), Castor (1970); for a discussion see e.g. Mihalas (1978) or Lamers & Cassinelli (1999)], facilitates a large simplification of the line transport problem, since line interactions become purely local processes.

Recall from Equation (3.39) that the opacity in a bound-bound transition is

$$\chi_{l,j,k\rightarrow u,j,k}(\nu) = n_{l,j,k}\frac{B_{l,j,k\rightarrow u,j,k}h\nu_{lu}}{4\pi}\left(1 - \frac{g_{l,j,k}n_{u,j,k}}{g_{u,j,k}n_{l,j,k}}\right)\phi(\nu). \tag{4.14}$$

The optical depth a photon accumulates on its path due to this opacity is then, following Equation

(3.84), given by

$$\begin{aligned}\tau_{lu}\left(s_0\right) &= n_{l,j,k}\frac{B_{l,j,k\rightarrow u,j,k}h\nu_{lu}}{4\pi}\left(1-\frac{g_{l,j,k}n_{u,j,k}}{g_{u,j,k}n_{l,j,k}}\right)\int_0^{s_0}\phi\left(\nu'\left(s\right)\right)\mathrm{d}s.\\ &= n_{l,j,k}\frac{B_{l,j,k\rightarrow u,j,k}h\nu_{lu}}{4\pi}\left(1-\frac{g_{l,j,k}n_{u,j,k}}{g_{u,j,k}n_{l,j,k}}\right)\int_{\nu'(s=0)}^{\nu'(s=s_0)}\phi\left(\nu'\right)\frac{\mathrm{d}s}{\mathrm{d}\nu'}\mathrm{d}\nu'. \end{aligned} \tag{4.15}$$

Using the Sobolev approximation this becomes

$$\tau^{\mathrm{S}}_{lu}\left(s_0\right) = n_{l,j,k}\frac{B_{l,j,k\rightarrow u,j,k}h\nu_{lu}}{4\pi}\left(1-\frac{g_{l,j,k}n_{u,j,k}}{g_{u,j,k}n_{l,j,k}}\right)\left(\frac{\mathrm{d}s}{\mathrm{d}\nu'}\right)_{\nu_{lu}}\begin{cases}0 & \nu_{lu}\notin\left[\nu'\left(0\right),\nu'\left(s_0\right)\right]\\ -1 & \nu_{lu}\in\left[\nu'\left(0\right),\nu'\left(s_0\right)\right]\end{cases} \tag{4.16}$$

Finally, using Equation (4.9), we find the Sobolev optical depth for a bound-bound transition in an homologous flow

$$\tau^{\mathrm{S}}_{lu} = n_{l,j,k}\frac{B_{l,j,k\rightarrow u,j,k}hct}{4\pi}\left(1-\frac{g_{l,j,k}n_{u,j,k}}{g_{u,j,k}n_{l,j,k}}\right). \tag{4.17}$$

Compared to Equation (4.15) this is now a purely local expression which is moreover independent of direction and any other properties of the incoming photon. Thus a photon propagating through the ejecta encounters the full optical depth of a line with which it comes in resonance at a single point. If the photon is not absorbed in the line, it will never encounter the line again due to the continuous red-shifting and escapes. A photon scattered in the line escapes with probability

$$\beta_{lu} = \frac{1}{\tau^{\mathrm{S}}_{lu}}\left(1-e^{-\tau^{\mathrm{S}}_{lu}}\right). \tag{4.18}$$

This, of course, is a major simplification compared to a treatment in which the overlapping line profiles of a multitude of atomic line transitions are taken into account which also affects the radiative bound-bound transition rates. Generally given by Equations (3.61) and (3.62), those simplify to

$$R^{\mathrm{S}}_{l,j,k\rightarrow u,j,k} = n_{l,j,k}\beta_{lu}B_{l,j,k\rightarrow u,j,k}J_{lu} \tag{4.19}$$

$$R^{\mathrm{S}}_{l,j,k\leftarrow u,j,k} = n_{u,j,k}\beta_{lu}\left(A_{l,j,k\leftarrow u,j,k}+B_{l,j,k\leftarrow u,j,k}J_{lu}\right) \tag{4.20}$$

in the Sobolev limit. Here J_{lu} denotes the mean intensity at the far blue wing of the transition $(l,j,k)\rightarrow(u,j,k)$. Treating stimulated emission as negative absorption this becomes

$$\tilde{R}^{\mathrm{S}}_{l,j,k\rightarrow u,j,k} = \left(n_{l,j,k}B_{l,j,k\rightarrow u,j,k}-n_{u,j,k}B_{l,j,k\leftarrow u,j,k}\right)\beta_{lu}J_{lu} \tag{4.21}$$

$$\tilde{R}^{\mathrm{S}}_{l,j,k\leftarrow u,j,k} = n_{u,j,k}\beta_{lu}A_{l,j,k\leftarrow u,j,k}. \tag{4.22}$$

Looking at the derivation above, the Sobolev approximation is strictly only valid if $\phi\left(\nu'\right) = \delta\left(\nu'-\nu_{lu}\right)$. In Nature, in contrast, the resonance region will always have a finite width. We have argued, however, that as long as this resonance region is smaller than the typical scale on which the ejecta properties change, the Sobolev approximation is expected to be valid. But if lines are densely packed in frequency space, as it is e.g. the case in the UV region for the iron-group elements, their line profiles may overlap even in high velocity gradient environments, thus challenging the Sobolev approximation (Baron et al. 1996): coming into resonance with two strong lines, closely neighboured in frequency space, a Sobolev treatment prevents photons to come into resonance with the redder of the two lines if they are absorbed in the bluer one. In reality, however, both lines would have the chance to absorb the photon if their line profiles overlap. If this effect is really significant remains to be shown in calculations directly comparing a Sobolev treatment and a non-Sobolev treatment for realistic models since the majority of transitions with overlapping line profiles will be weak.

Moreover, the unphysical (δ-function shaped) line profiles assumed for the Sobolev approximation will induce artificially sharp edges of absorption and emission profiles in synthetic spectra. For supernovae, however, this is not a problem since line features are typically blended and the scales on which this becomes relevant are smaller than the thermal velocity ($v_{\mathrm{th}} \sim 5\,\mathrm{km\,s^{-1}}$) and thus negligible (the resolution of current hydrodynamical models or radiative transfer simulations reach at best a cell size of $\sim 20\,\mathrm{km\,s^{-1}}$). Although our method could be generalized, the Sobolev approximation is a fundamental assumption of the presented code for computational reasons. Dropping it, would cause the assumption of strictly local line interactions to break down and require us to sample over all line profiles which contribute to a given frequency.

4.3 Outline of the code

In the following we outline the operation of the code with reference to the flow chart shown in Figure 4.1 and discuss the relevant physical processes. The basic transfer calculations are carried out in the observer rest frame (rf, quantities always denoted unprimed) so that an energy packet's trajectory at time t is described by its position $\mathbf{r}(t)$ and direction $\mathbf{n}(t)$. For interactions with matter we transform to the local co-moving frame of the ejecta (cmf, quantities denoted with prime).

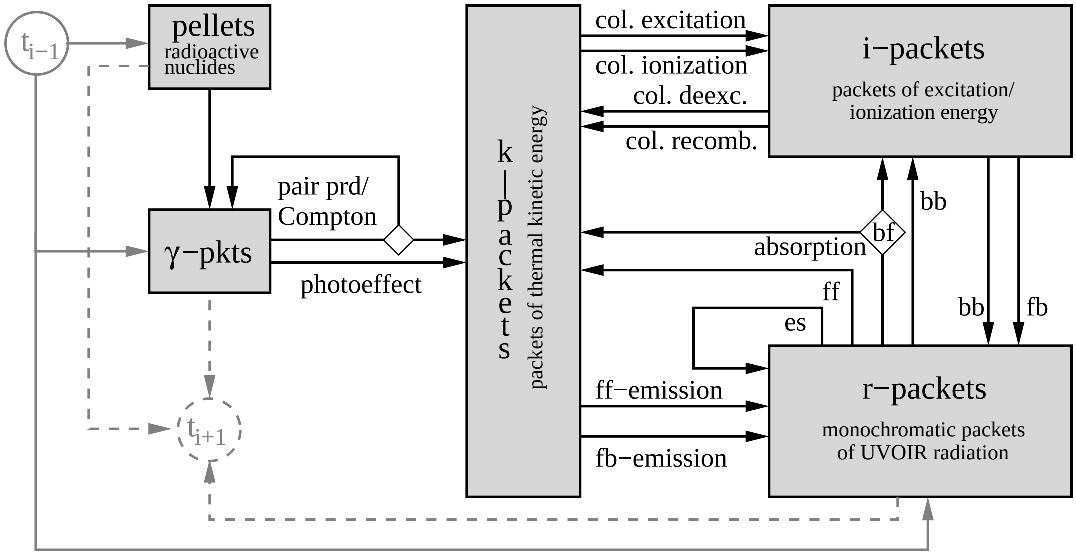

Figure 4.1: Flow chart outlining the mode of operation of the code. For discussion see text.

4.3.1 Setting up the computational domain

To avoid any symmetry assumptions and keep the code simple, we map the explosion ejecta to a 3D Cartesian grid with origin at the centre-of-mass of the supernova and containing I^3 cubic cells. The grid expands with time to follow the evolution of the ejecta. Physical variables are assumed not to vary spatially within the grid cells. As input we take densities $\rho_i(t)$, velocities $v_i(t)$ and composition $X_{i,k}(t)$ from explosion models specified for the phase of homologous expansion and map these for a time t_0 onto the grid. t_0 and all time specifications in the following indicate the time since explosion, unless otherwise noted.

We then follow the expansion of the ejecta for N time steps up to time t_N by expanding the individual grid cells continuously. The time steps (t_n,t_{n+1}) are spaced logarithmically and thermodynamic quantities in a cell such as densities, temperatures and atom/ion populations are kept fixed during a time step n at the value they have for $t_{n+0.5}$.

4.3.2 Energy deposition

In addition to the radioactive decays of ^{56}Ni → ^{56}Co and ^{56}Co → ^{56}Fe, which are the primary sources of energy in SNe Ia (Truran et al. 1967, Colgate & McKee 1969) and power their light curves, we also take into account energy released by the decay sequences ^{52}Fe → ^{52}Mn → ^{52}Cr and ^{48}Cr → ^{48}V → ^{48}Ti. For other radioactive nuclei as e.g. ^{44}Ti, ^{57}Ni and ^{57}Co the amounts synthesized during the explosion are much smaller than $M_{^{56}\mathrm{Ni}}$ (e.g. Travaglio et al. 2004). Thus they can be neglected at early times when the decays of ^{56}Ni and ^{56}Co power the light curves. However, at late times ^{57}Co and ^{44}Ti will become important due to their larger decay times.

Out of the total energies, $E_{^{56}\mathrm{Ni}}$, $E_{^{56}\mathrm{Co}}$, $E_{^{52}\mathrm{Fe}}$, $E_{^{52}\mathrm{Mn}}$, $E_{^{48}\mathrm{Cr}}$ and $E_{^{48}\mathrm{V}}$ emitted per decay of ^{56}Ni, ^{56}Co, ^{52}Fe, ^{52}Mn, ^{48}Cr and ^{48}V we determine the total γ-ray energy emitted in the decay chain for $t \rightarrow \infty$

$$E_{\mathrm{tot}} = (E_{^{56}\mathrm{Ni}} + E_{^{56}\mathrm{Co}})\frac{M_{^{56}\mathrm{Ni}}}{m_{^{56}\mathrm{Ni}}} + (E_{^{52}\mathrm{Fe}} + E_{^{52}\mathrm{Mn}})\frac{M_{^{52}\mathrm{Fe}}}{m_{^{52}\mathrm{Fe}}} + (E_{^{48}\mathrm{Cr}} + E_{^{48}\mathrm{V}})\frac{M_{^{48}\mathrm{Cr}}}{m_{^{48}\mathrm{Cr}}}. \tag{4.23}$$

$M_{^{56}\mathrm{Ni}}$ ($M_{^{52}\mathrm{Fe}}$, $M_{^{48}\mathrm{Cr}}$) is the initial mass of ^{56}Ni (^{52}Fe, ^{48}Cr) synthesized in the explosion and $m_{^{56}\mathrm{Ni}}$ ($m_{^{52}\mathrm{Fe}}$, $m_{^{48}\mathrm{Cr}}$) the mass of the ^{56}Ni (^{52}Fe, ^{48}Cr) atom.

Following Lucy (2005), this energy is quantized into $\mathcal{N} = E_{\mathrm{tot}}/\epsilon_0$ identical indivisible energy packets of cmf energy $\epsilon' = \epsilon_0$ which we call "pellets" in the following. Compared to using Nature's quantization of radiation this has two major advantages: first it keeps the code simple as packet histories can be followed one-by-one, avoiding the need to follow multiple packets in e.g. recombination cascades. Second it ensures rapid convergence to an accurate temperature stratification by implicitly imposing the constraint of energy conservation (radiative equilibrium) in the co-moving frame (Lucy 1999a).

The pellets are distributed on the grid according to the initial distribution of ^{56}Ni, ^{52}Fe and ^{48}Cr and follow the homologous expansion until they decay. Decay times are sampled in a three step process. First one of the included decay sequences is chosen randomly according to the amount of energy deposited in the different sequences. Then, if the ^{56}Ni chain was chosen the pellet is assigned to represent either a ^{56}Ni or ^{56}Co decay [with probability $E_{^{56}\mathrm{Ni}}/\left(E_{^{56}\mathrm{Ni}}+E_{^{56}\mathrm{Co}}\right)$ and $E_{^{56}\mathrm{Co}}/\left(E_{^{56}\mathrm{Ni}}+E_{^{56}\mathrm{Co}}\right)$ respectively]. Finally an appropriate decay time is sampled

$$t_{\mathrm{decay}}\left(^{56}\mathrm{Ni}\right)=-\tau\left(^{56}\mathrm{Ni}\right)\log\left(z\right) \tag{4.24}$$

$$t_{\mathrm{decay}}\left(^{56}\mathrm{Co}\right)=-\tau\left(^{56}\mathrm{Ni}\right)\log\left(z_1\right)-\tau\left(^{56}\mathrm{Co}\right)\log\left(z_2\right) \tag{4.25}$$

from the mean life times of the ^{56}Ni [$\tau\left(^{56}\mathrm{Ni}\right)=8.80\,\mathrm{d}$] and ^{56}Co [$\tau\left(^{56}\mathrm{Co}\right)=113.7\,\mathrm{d}$] nuclei. The ^{52}Fe [$\tau\left(^{52}\mathrm{Fe}\right)=0.4974\,\mathrm{d}$, $\tau\left(^{52}\mathrm{Mn}\right)=0.02114\,\mathrm{d}$] and ^{48}Cr [$\tau\left(^{48}\mathrm{Cr}\right)=1.296\,\mathrm{d}$, $\tau\left(^{48}\mathrm{V}\right)=23.04\,\mathrm{d}$] chains are treated analogously.

Upon decay, a pellet transforms to a single γ-packet representing a bundle of monochromatic γ-radiation of cmf energy $\epsilon'=\epsilon_0$ and photon energy $E'_\gamma=h\nu$'. Positrons released during β^+-decays are assumed to annihilate in situ following Ambwani & Sutherland (1988) and Lucy (2005). Assuming further that their kinetic energy is radiated at softer energies during preceding deceleration processes, the annihilation gives rise to the emission of two γ-ray photons at 0.511 MeV in the cmf. The cmf photon energy E'_γ of the γ-packets is randomly sampled from the relative probabilities of the γ-lines (including the annihilation line due to positron emission) in the appropriate decay of the selected decay sequence. The γ-packet's direction ($\mathbf{n}'$) in the cmf is sampled randomly assuming isotropic emission

$$\mathbf{n}'=\left(\sin\theta\cos\phi,\sin\theta\sin\phi,\cos\theta\right) \tag{4.26}$$

with $\cos\theta=1-2z_1$ and $\phi=2\pi z_2$. To start the γ-packet's propagation we transform $\mathbf{n}'$ into the rf using the aberration formula (3.25). Rest frame energy and rf photon energy of the packet are given by the Doppler formula (3.23)

$$\epsilon=\epsilon'/D \tag{4.27}$$

$$E_\gamma=E'_\gamma/D. \tag{4.28}$$

Owing to the comparatively short life times of ^{52}Fe and ^{52}Mn, these nuclei have already decayed to their daughter nuclei when we start the radiative transfer simulation at ~ 1 day. Since the ejecta at these early times are almost opaque for γ-rays, the γ-packets released by the ^{52}Fe decay chain will be thermalized rapidly. Therefore we do not follow the propagation of the γ-packets released by the ^{52}Fe decay chain, but immediately convert their energy to thermal kinetic energy. In the framework of this code, this is described by a transformation of the pellet into a so-called k-packet of equal cmf energy. The treatment of k-packets is described in Section 4.3.4.

4.3.3 Propagation of γ-packets

The γ-packets are propagated through the ejecta in the rest frame of the grid until either (i) they leave the grid, (ii) the current time step finishes or (iii) they interact with matter. To determine which event occurs, we calculate how far a packet can travel along its trajectory until it reaches the grid boundary (d_{g}) and how far it can travel along this trajectory during the remaining time of the active time step (d_{t}). These distances are then compared to the distance d_{i} to the next interaction with matter.

Following Equation (4.5) d_{i} is calculated from a randomly sampled optical depth $\tau_{\mathrm{r}}=-\ln z$ with

$z \in]0,1]$, by inverting $\tau_{\mathrm{r}} = \chi_\gamma^{\mathrm{tot}} d_{\mathrm{i}}$. Here $\chi_\gamma^{\mathrm{tot}}$ is the total opacity on γ-photons which can be calculated by summing $\left(\chi_\gamma^{\mathrm{tot}}(\nu')\right)' = \left(\chi_{\mathrm{C}}(\nu')\right)' + \left(\chi_\gamma^{\mathrm{bf}}(\nu')\right)' + \left(\chi_{\gamma\gamma}(\nu')\right)'$ the individual contributions of Compton scattering (Equation 3.51), photoelectric absorption (Equation 3.52) and pair-production (Equations 3.53 and 3.54). Since these expressions are only valid in the cmf, we must transfer them to the rf $\chi_\gamma^{\mathrm{tot}}(\nu) = \left(\chi_\gamma^{\mathrm{tot}}(\nu')\right)'(1 - \mathbf{n} \boldsymbol{.} \mathbf{v}/c)$ to calculate d_{i}.

From the three events, we select the one which occurs first, i.e. the one which has the shortest corresponding distance (d_{g}, d_{t}, d_{i}). In the first case the γ-packet is flagged inactive and the calculation proceeds to the next active packet. In the second case we save the rf data string ($\mathbf{r}$, t, $\mathbf{n}$, ϵ, E_γ) for the following time step and continue with the next active packet.

For the third case we randomly sample the rf absorption coefficients χ_{C}, $\chi_\gamma^{\mathrm{bf}}$, $\chi_{\gamma\gamma}$ to determine which of the included processes caused the event. In the case of a photoelectric absorption, the energy of the γ-packet – in principle carried away by a non-thermal electron – is assumed to thermalize instantaneously and is deposited as thermal kinetic energy. In the framework of this code, this is described by a transformation of the γ-packet into a k-packet of equal cmf energy. The treatment of k-packets is described in Section 4.3.4.

Since our energy packets are indivisible, the treatment of Compton scattering and pair production, where physically the photon energy is distributed to two particles, is slightly more complex. A γ-photon, which in the cmf was Compton scattered by an angle θ relative to its original direction, continues with reduced energy $E'_{\gamma\mathrm{f}} = E'_{\gamma\mathrm{i}}/f$, where

$$f = 1 + \frac{E'_\gamma}{m_{\mathrm{e}}c^2}(1 - \cos\theta)\,. \tag{4.29}$$

The remaining energy is carried away by a Compton electron. Following Lucy (2005), we force γ-packets in Compton scattering to either scatter (with probability $1/f$) and continue as γ-packets or transform the incident packets into non-thermal e^--packets (in both cases the cmf energy of the incident packet is conserved). Since the final energy of a scattered photon is related to the scattering angle by Equation (4.29), the corresponding probabilities can be sampled from the partial cross-section.

If a γ-packet was scattered its cmf photon energy is reduced $E'_{\gamma\mathrm{f}} = E'_{\gamma\mathrm{i}}/f$ and the new direction in the cmf is selected such that $\mathbf{n}'_{\mathrm{i}} \boldsymbol{.} \mathbf{n}'_{\mathrm{f}} = \cos\theta$ and $\phi = 2\pi z$ (measured relative to the polar direction $\mathbf{n}'_{\mathrm{i}}$). Before continuing the packet's propagation through the grid, the cmf quantities $\left(\mathbf{n}'_{\mathrm{f}}, \epsilon', E'_{\gamma\mathrm{f}}\right)$ are transformed to the rf $(\mathbf{n}, \epsilon, E_\gamma)$ using the aberration (3.25) and Doppler (3.23) formulae, respectively. e^--packets are assumed to thermalize and are instantaneously transformed into k-packets.

In pair productions we either create e^+- or e^--packets. For an incident γ-packet of cmf photon energy E'_γ a fraction of $2m_{\mathrm{e}}c^2/E'_\gamma$ (represented by the e^+-packets) is released in form of γ-rays when the positron annihilates. Assuming in situ annihilation, the e^+-packets are instantaneously converted to γ-packets which are emitted isotropically (Equation 4.26) in the local cmf and conserve the cmf energy of the incident photon. Representing now a bundle of γ-photons due to annihilation their new cmf photon energy is $E'_\gamma = 0.511\,\mathrm{MeV}$. To continue the packet's propagation through the grid, the cmf quantities are again transformed to the rf using the aberration (3.25) and Doppler (3.23) formulae, respectively. The remaining part $(1 - 2m_{\mathrm{e}}c^2/E'_\gamma)$ of the energy of an incident photon, representing the kinetic energy of the electrons and positrons, is converted to e^--packets. Assuming again that these thermalize immediately, this energy goes directly to the thermal pool, i.e. k-packets.

4.3.4 Treatment of thermal kinetic energy

Neglecting energy storage in the ejecta gas, thermal kinetic energy converts instantaneously (i.e. without propagating) into ultraviolet-optical-infrared (UVOIR) radiation. This happens either directly via continuum emission by free-free or free-bound processes or indirectly by collisional excitations/ionizations of the gas and subsequent radiative deexcitations/recombinations (see Section 3.3). In our framework, this means either transforming a k-packet into an r-packet – representing a monochromatic energy packet of UVOIR radiation (for details see Section 4.3.6) – or into a packet of atomic internal energy, which we call i-packets. Details of the latter will be discussed in the next section.

Which of the processes happens depends on the cooling rate associated with the particular process and is sampled randomly from the total cooling rate

$$\mathcal{C} = \sum_{k=1}^{\mathcal{N}_\mathrm{E}} \sum_{j=1}^{\mathcal{N}_\mathrm{I}(k)} \mathcal{C}^\mathrm{ff}_{j,k} + \sum_{k=1}^{\mathcal{N}_\mathrm{E}} \sum_{j=1}^{\mathcal{N}_\mathrm{I}(k)-1} \sum_{i=1}^{\mathcal{N}_\mathrm{L}(j,k)} \left(\mathcal{C}^\mathrm{fb,sp}_{i,j,k \leftarrow j+1,k} + \mathcal{C}^\mathrm{ion}_{i,j,k \rightarrow j+1,k} + \sum_{i'=i+1}^{\mathcal{N}_\mathrm{L}(j,k)} \mathcal{C}^\mathrm{exc}_{i,j,k \rightarrow i',j,k} \right), \tag{4.30}$$

where $\mathcal{N}_\mathrm{E}$ is the number of included elements, $\mathcal{N}_\mathrm{I}(k)$ the number of ionization stages available for element k and $\mathcal{N}_\mathrm{L}(j,k)$ the number of atomic levels associated with a given ion (j,k). The highest ionization state included for each element, is only considered as a closure, which is needed to solve for the ionization balance. Thus it has only one associated level and we do not loose contributions from collisional excitation by terminating the second j-sum at $\mathcal{N}_\mathrm{I}(k) - 1$.

The free-free cooling rate is given by

$$\mathcal{C}^\mathrm{ff}_{j,k} = C_0 q^2_{j,k} T_\mathrm{e}^{1/2} N_{j,k} n_\mathrm{e}, \tag{4.31}$$

where $q_{j,k}$ is the charge of ion (j,k) and C_0 a constant which is given by $1.426\,10^{-27}$ in cgs units (Osterbrock 1974). For the collisional processes we find the cooling rates by multiplying the transition rates (3.72) and (3.73) with the energy transfer in the corresponding transitions

$$\mathcal{C}^\mathrm{ion}_{i,j,k \rightarrow j+1,k} = n_{i,j,k} c_{i,j,k \rightarrow j+1,k} \left(\varepsilon_{0,j+1,k} - \varepsilon_{i,j,k} \right) \tag{4.32}$$

$$\mathcal{C}^\mathrm{exc}_{i,j,k \rightarrow i',j,k} = n_{i,j,k} c_{i,j,k \rightarrow i',j,k} \left(\varepsilon_{i',j,k} - \varepsilon_{i,j,k} \right). \tag{4.33}$$

$c_{i,j,k \rightarrow j+1,k}$ and $c_{i,j,k \rightarrow i',j,k}$ are thereby calculated in the Seaton (Equation 3.79) and van Regemorter approximation (Equation 3.76), respectively.

For the free-bound cooling rate we consider only spontaneous recombination since stimulated recombination is treated as negative photoionization and, as such, is taken into account in the creation of k-packets. Using Equation (3.68) the rate at which ionization energy is spontaneously converted to radiant energy in a given fb-transition $(i,j,k) \leftarrow (j+1,k)$ is described by $h\nu_{i,j,k} N_{j+1,k} n_\mathrm{e} \alpha^\mathrm{spont}_{i,j,k}$ $(h\nu_{i,j,k} = \varepsilon_{0,j+1,k} - \varepsilon_{i,j,k})$. The rate at which thermal and ionization energy is converted to radiant energy in the corresponding transition is similarly given by

$$h\nu_{i,j,k}N_{j+1,k}n_{\mathrm{e}}\alpha_{i,j,k}^{\mathrm{E,spont}} = h\nu_{i,j,k}N_{j+1,k}n_{\mathrm{e}}\phi_{i,j,k}\left(T_{\mathrm{e}}\right)4\pi\int_{\nu_{i,j,k}}^{\infty}\frac{\alpha_{i,j,k\rightarrow j+1,k}\left(\nu\right)}{h\nu_{i,j,k}}\frac{2h\nu^{3}}{c^{2}}e^{-h\nu/k_{\mathrm{B}}T_{\mathrm{e}}}\mathrm{d}\nu. \tag{4.34}$$

Thus the cooling rate, i.e. the rate at which thermal energy is converted to radiant energy, is

$$\mathcal{C}_{i,j,k\leftarrow j+1,k}^{\mathrm{fb,sp}} = N_{j+1,k}n_{\mathrm{e}}\left(\alpha_{i,j,k}^{\mathrm{E,spont}} - \alpha_{i,j,k}^{\mathrm{spont}}\right)\left(\varepsilon_{0,j+1,k} - \varepsilon_{i,j,k}\right). \tag{4.35}$$

From sampling the cooling rates, we know if a collisional process happened, free-free emission was selected or in which free-bound continuum (specified by level i of ion j of element k) an emission occurred. In the first case the packet is converted to an i-packet, whose macro-atom state (see Section 4.3.5) is set to the target level of the excitation/ionization. In the second and third cases the packet is converted to an r-packet which is emitted isotropically (Equation 4.26) in the cmf. In any case the cmf energy ϵ' of the packet is conserved.

To specify the emitted r-packet fully, we must also determine the r-packet photon frequency. In the cmf this can be derived by sampling the emissivity of the corresponding process. Thus for free-free emission the cmf frequency ν' is determined from

$$\int_{\nu'}^{\infty}\left(\eta_{j,k}^{\mathrm{ff}}(\nu)\right)'\mathrm{d}\nu = z\int_{0}^{\infty}\left(\eta_{j,k}^{\mathrm{ff}}(\nu)\right)'\mathrm{d}\nu \tag{4.36}$$

where $\left(\eta_{j,k}^{\mathrm{ff}}\right)'$ is given by Equation (3.45) and z a random number in $]0,1[$. For free-bound emission we use

$$\int_{\nu'}^{\infty}\left(\eta_{i,j,k}^{\mathrm{fb}}(\nu)\right)'\mathrm{d}\nu = z\int_{\nu_{i,j,k}}^{\infty}\left(\eta_{i,j,k}^{\mathrm{fb}}(\nu)\right)'\mathrm{d}\nu \tag{4.37}$$

where z is a random number in $]0,1]$ and $\nu_{i,j,k}$ is the edge frequency of the continuum. The emissivity $\left(\eta_{i,j,k}^{\mathrm{fb}}(\nu)\right)'$ for spontaneous recombination by that continuum is given by Equation (3.42). Before continuing the photon propagation through the grid, the cmf quantities $(\mathbf{n}', \epsilon', \nu')$ are transformed to the rf $(\mathbf{n}, \epsilon, \nu)$ using the aberration (3.25) and Doppler (3.23) formulae, respectively.

In principle we want to only release thermal energy when transforming a k-packet to an r-packet. However, in emitting a bound-free photon at frequency ν, a fraction $\nu_{i,j,k}/\nu$ of the packet energy is drawn from the ionization/excitation energy pool. The machinery described in the next section ensures that this is balanced by the amount of thermal energy which is released by recombination processes in our treatment of atomic internal energy (see also Lucy 2003).

4.3.5 Treatment of atomic internal energy

We treat atomic internal energy using the macro-atom approach of Lucy (2002, 2003). The idea behind this approach is to describe the interactions between matter and energy packets by a set of rules that asymptotically recovers the emissivity of a gas in statistical equilibrium – thus allowing for a fully general treatment of radiation/matter interactions in statistical equilibrium, including true absorption, scattering and fluorescence. For Monte Carlo methods this is an improvement over earlier work in both 1D and 3D, which either used the assumption of pure resonance scattering (e.g. Mazzali & Lucy 1993), a downward branching scheme (Lucy 1999b, Kasen et al. 2006) or an approximate source function (Kasen et al. 2006) derived in the equivalent two-level atom formalism (see e.g. Mihalas 1978).

Since we want to keep the concept of indivisible energy packets also for the atomic internal energy (*i*-packets), in deriving such a set of rules we need to think about the matter in a finite volume element being in a discrete state, which corresponds to one of the atomic states of all the elements included in the simulation. Thereby we effectively quantize the matter into "macro-atoms". Such a macro-atom is activated to a particular macro-atom state i [now used as a shorthand note for a fully specified state $i = (l, j, k)$] by the absorption of a packet of kinetic (*k*-packet) or radiation energy (*r*-packet). Not taking into account energy storage in the ejecta gas, it may then instantaneously undergo multiple internal transitions to connected states i' without emitting an energy packet before it deactivates by emitting a packet of thermal kinetic (*k*-packet) or radiation energy (*r*-packet), thereby conserving the cmf energy of the incident packet (Figure 4.2).

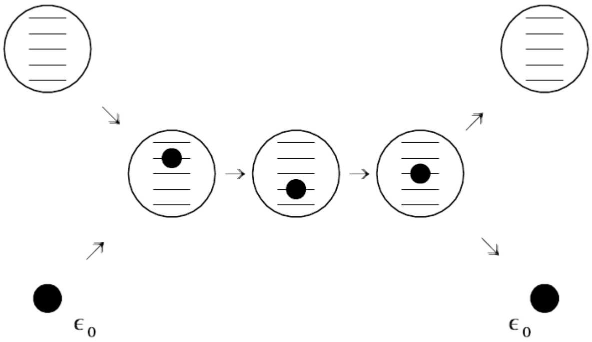

Figure 4.2: Schematic illustration of the macro-atom formalism (from Lucy 2002): an incident packet of energy ϵ_0 (either a k- or r-packet) activates a macro-atom into a particular internal state i, which corresponds to an energy level of one of the atomic species in the simulation. It may then undergo several (here two) internal transitions ("jumps") to other states i' without absorbing or emitting an energy packet according to a set of rules (macro-atom transition probabilities, Lucy 2002) which enforce statistical equilibrium. By emitting an energy packet of the same cmf-energy ϵ_0, the active macro-atom deactivates either collisionally (*k*-packet) or radiatively (*r*-packet). In the second case a photon frequency corresponding to the selected deactivation process must be chosen.

Lucy (2002) has shown that in statistical equilibrium the rate per unit volume at which a particular atomic level i with total energy ε_i (i.e. ionization plus excitation) looses energy is given by

$$\dot{E}_i^{\mathrm{tot}} = \dot{E}_i^{\mathrm{R}} + \dot{E}_i^{\mathrm{C}} + \dot{E}_i^{\mathrm{int,down}} + \dot{E}_i^{\mathrm{int,up}}, \tag{4.38}$$

where the four terms on the right hand side denote energy losses due to radiative deactivation $[\dot{E}_i^{\mathrm{R}} = \sum_{l<i} R_{il}\,(\varepsilon_i - \varepsilon_l)]$, collisional deactivation $[\dot{E}_i^{\mathrm{C}} = \sum_{l<i} C_{il}\,(\varepsilon_i - \varepsilon_l)]$ and jumps to lower $[\dot{E}_i^{\mathrm{int,down}} = \sum_{l<i} (R_{il} + C_{il})\,\varepsilon_l]$ and higher lying $[\dot{E}_i^{\mathrm{int,up}} = \sum_{u>i} (R_{iu} + C_{iu})\,\varepsilon_i]$ atomic levels. R_{ij} and C_{ij} denote the corresponding radiative and collisional rates, respectively. Thus to recover statistical equilibrium, an ensemble of active macro-atoms must undergo deactivations and internal jumps with probabilities

- $p_i^{\mathrm{R}} = \dot{E}_i^{\mathrm{R}} / \dot{E}_i^{\mathrm{tot}}$ for radiative deactivations,
- $p_i^{\mathrm{C}} = \dot{E}_i^{\mathrm{C}} / \dot{E}_i^{\mathrm{tot}}$ for collisional deactivations,

- $p^{\text{int,down}} = \dot{E}_i^{\text{int,down}} / \dot{E}_i^{\text{tot}}$ for internal downward transitions and
- $p^{\text{int,up}} = \dot{E}_i^{\text{int,up}} / \dot{E}_i^{\text{tot}}$ for internal upward transitions.

In contrast to atomic transition probabilities, which are pure matter properties, these probabilities depend on the state of the plasma in the volume element under consideration and thus on the ambient radiation field.

Neglecting auto-ionization and non-thermal processes[2], the transition rates needed to fully specify these probabilities are given by collisional bound-bound and bound-free rates and their radiative counter parts. The collisional upward rates are taken from Equations (3.72) and (3.73), using cross-sections calculated in the van Regemorter (Equation 3.76) and Seaton (Equation 3.79) approximations, respectively. Their downward rates follow from detailed balancing (Section 3.3.1).

In radiative transitions we treat stimulated emission as negative absorption. Since the transition probabilities must be positive definite, this requires that no population inversions (i.e. $g_l n_u > g_u n_l$, for $\varepsilon_u > \varepsilon_l$) occur due to stimulated emission. This is not expected for the typical conditions in supernova ejecta. Note further that our excitation treatment (Section 4.4.2) explicitly prevents population inversions within a particular ionization state. The bound-free rates are then given by Equations (3.70) and (3.68). The corresponding expressions for bound-bound rates in the Sobolev approximation are Equations (4.21) and (4.22). Thus we find the following probabilities for a particular process

- radiative deexcitation

$$p^{\mathrm{R}}_{l,j,k\leftarrow i,j,k} = \tilde{R}^{\mathrm{S}}_{l,j,k\leftarrow i,j,k} \left(\varepsilon_{i,j,k} - \varepsilon_{l,j,k}\right) / \dot{E}_i^{\text{tot}} \tag{4.39}$$

- radiative recombination

$$p^{\mathrm{R}}_{l,j-1,k\leftarrow j,k} = R^{\text{spont}}_{l,j-1,k\leftarrow j,k} \left(\varepsilon_{0,j,k} - \varepsilon_{l,j-1,k}\right) / \dot{E}_i^{\text{tot}} \tag{4.40}$$

- collisional deexcitation

$$p^{\mathrm{C}}_{l,j,k\leftarrow i,j,k} = C_{l,j,k\leftarrow i,j,k} \left(\varepsilon_{i,j,k} - \varepsilon_{l,j,k}\right) / \dot{E}_i^{\text{tot}} \tag{4.41}$$

- collisional recombination

$$p^{\mathrm{C}}_{l,j-1,k\leftarrow j,k} = C_{l,j-1,k\leftarrow j,k} \left(\varepsilon_{0,j,k} - \varepsilon_{l,j-1,k}\right) / \dot{E}_i^{\text{tot}} \tag{4.42}$$

- internal downward jump within the current ionization state

$$p^{\text{int,down}}_{l,j,k\leftarrow i,j,k} = \left(\tilde{R}^{\mathrm{S}}_{l,j,k\leftarrow i,j,k} + C_{l,j,k\leftarrow i,j,k}\right) \varepsilon_{l,j,k} / \dot{E}_i^{\text{tot}} \tag{4.43}$$

- internal downward jump to the lower ionization state

$$p^{\text{int,down}}_{l,j-1,k\leftarrow j,k} = \left(R^{\text{spont}}_{l,j-1,k\leftarrow j,k} + C_{l,j-1,k\leftarrow j,k}\right) \varepsilon_{l,j-1,k} / \dot{E}_i^{\text{tot}} \tag{4.44}$$

---

[2] Non-thermal excitations by fast electrons and γ-rays and auto-ionizations are not currently taken into account but the method could be extended to include them in due course.

- internal upward jump within the current ionization state

$$p^{\mathrm{int,up}}_{i,j,k\to u,j,k} = \left(\tilde{R}^{\mathrm{S}}_{i,j,k\to u,j,k} + C_{i,j,k\to u,j,k}\right)\varepsilon_{i,j,k}/\dot{E}^{\mathrm{tot}}_{i} \tag{4.45}$$

- internal upward jump to a higher ionization state

$$p^{\mathrm{int,up}}_{i,j,k\to j+1,k} = \left(\tilde{R}_{i,j,k\to j+1,k} + C_{i,j,k\to j+1,k}\right)\varepsilon_{i,j,k}/\dot{E}^{\mathrm{tot}}_{i} \tag{4.46}$$

Whenever a packet is converted to atomic internal energy (i-packet), by either collisional excitation/ionization (represented by a k-packet to i-packet transition, see Section 4.3.4) or photoexcitation/ionization (represented by an r-packet to i-packet transition see Section 4.3.6) we assign it to a particular macro-atom state (i, j, k) which is determined by the particular excitation/ionization which led to the creation of the i-packet. Then, by sampling the probabilities (4.39)-(4.46), we randomly select one of all the possible transitions which connect the current macro-atom state to other states or which allow the macro-atom to deactivate, i.e. transform the internal atomic energy back to either thermal kinetic (k-packet) or radiative (r-packet) energy. If a macro-atom internal jump is selected, we reset the i-packet's macro-atom state and continue this procedure until we select a deactivating process.

In the case of a collisional deactivation the i-packet is just transformed into a k-packet. In case of radiative deexcitation/recombination we transform the i-packet into an r-packet and emit it isotropically ($\mathbf{n}'$) in the cmf (Equation 4.26). Finally we need to assign a photon frequency ν' to the r-packet. For a radiative deexcitation this is given by the frequency of the associated line transition. In the case of a radiative recombination, we again sample the emissivity for the free-bound emission (Equation 4.37). Note that we thereby emit both ionization and thermal energy, as in the case of free-bound cooling.

Before continuing the photon propagation through the grid, the cmf quantities $(\mathbf{n}', \epsilon', \nu')$ are transformed to the rf $(\mathbf{n}, \epsilon, \nu)$ using the aberration (3.25) and Doppler (3.23) formulae, respectively.

4.3.6 Propagation of UVOIR radiation

r-packets representing monochromatic energy packets of UVOIR radiation are propagated through the ejecta from their first emission by any of the above processes until (i) they leave the grid, (ii) the current time step finishes or (iii) they interact with matter. In the zeroth time step we also have radiation which comes from pellets which decayed at $t_\gamma < t_0$ at position $\mathbf{r}_\gamma$. We assume that the ejecta are optically thick at these early times such that the radiation is trapped and LTE is a good approximation. Therefore we emit these packets isotropically in the cmf at the position $\mathbf{r}_\gamma t_0/t_\gamma$ the pellets would have at t_0 (assuming homologous expansion) and assign them reduced cmf energies ($\epsilon' = \epsilon_0 t_\gamma/t_0$) to account for the expansion work done on the ejecta before t_0. The cmf photon frequencies of these packets are sampled according to a black-body distribution at the local kinetic temperature T_e. To start their propagation through the grid, the cmf quantities $(\mathbf{n}', \epsilon', \nu')$ are transformed to the rf $(\mathbf{n}, \epsilon, \nu)$ using the aberration (3.25) and Doppler (3.23) formulae, respectively.

We follow the packets along their trajectory until they are stopped by the first event which occurs. For (i) and (ii) this is a simple geometrical problem. For case (iii) it requires calculating the distance to a randomly sampled optical depth $\tau_\mathrm{r} = -\ln z$ with $z \in]0,1]$, as described by Mazzali & Lucy (1993). First the trajectory point $\mathbf{r}^*$ at which the photon comes into resonance with the next spectral line of the line list is found in the Sobolev approximation (Equation 4.17). Then the continuum optical depth $\tau^*_\mathrm{cont} = \chi_\mathrm{cont}\,|\mathbf{r}^* - \mathbf{r}|$ accumulated up to that point is determined. Therefore we calculate the continuum opacity $\chi^{'}_\mathrm{cont}(\nu')$ in the cmf from the contributions of electron scattering, free-free absorption and bound-free absorption corrected for stimulated emission given by Equations (3.48), (3.44) and (3.41)

$$\begin{aligned}\chi^{'}_\mathrm{cont}(\nu') &= \chi'_\mathrm{Th} + \sum_{k=1}^{\mathcal{N}_\mathrm{E}} \sum_{j=2}^{\mathcal{N}_\mathrm{I}(k)} \left(\chi^\mathrm{ff}_{j,k}(\nu')\right)' + \sum_{k=1}^{\mathcal{N}_\mathrm{E}} \sum_{j=1}^{\mathcal{N}_\mathrm{I}(k)-1} \sum_{i=1}^{\mathcal{N}_\mathrm{L}(j,k)} \left(\chi^\mathrm{bf}_{i,j,k\to j+1,k}(\nu')\right)' \\ &= \chi'_\mathrm{Th} + \chi'_\mathrm{ff} + \chi^{'}_\mathrm{bf}\end{aligned} \tag{4.47}$$

and transform it back to the rf $\chi_\mathrm{cont}(\nu) = \chi^{'}_\mathrm{cont}(\nu')\,(1 - \mathbf{n} \cdot \mathbf{v}/c)$. If the continuum optical depth is bigger than the random optical depth ($\tau^*_\mathrm{cont} > \tau_\mathrm{r}$), the travelled distance $\mathrm{d}s$ is calculated from $\chi_\mathrm{cont}\mathrm{d}s = \tau_\mathrm{r}$ and a continuum absorption occurs. If the sum of continuum and line optical depth is bigger than the random optical depth, $\mathrm{d}s$ is given by the distance to the resonance point $|\mathbf{r}^* - \mathbf{r}|$ and a line event occurs. Otherwise we calculate the distance to the next spectral line with which the photon comes into resonance and repeat the procedure. This is illustrated in Figure 4.3.

According to the chosen event, the packet properties are now updated. For case (i), the r-packet is flagged inactive and we proceed to the next active packet. For case (ii), we save the actual rf data string ($\mathbf{r}$, t, $\mathbf{n}$, ϵ, ν) for the following time step and continue with the next active packet. For case (iii), we change the packet type according to the process which terminated the packet flight. For a line absorption, we convert the r-packet into an i-packet and set it to the corresponding macro-atom target state and the macro-atom machinery (Section 4.3.5) determines its fate.

For a continuum event, we first decide whether it was Thomson scattering, free-free absorption or bound-free absorption by randomly sampling their rf absorption coefficients χ_Th, χ_ff, χ_bf. Thomson scattering, which we assume to be coherent and isotropic, changes neither the packet type, nor the cmf frequency of the packet. Thus, Thomson scattering amounts to isotropic re-emission of the r-packet in the local cmf. Before continuing the packet's propagation through the grid, the cmf quantities $(\mathbf{n}', \epsilon', \nu')$ are transformed to the rf $(\mathbf{n}, \epsilon, \nu)$ using the aberration (3.25) and Doppler (3.23) formulae, respectively.

Free-free absorption transforms the absorbed radiative energy completely into thermal kinetic energy, i.e. converts the r-packet into a k-packet. Bound-free absorption is more complicated since it contributes both to atomic internal energy and thermal kinetic energy. After randomly selecting one specific continuum according to its absorption coefficient, we follow Lucy (2003) in forcing a conversion to either a single k- or i-packet. For an r-packet absorbed with frequency ν by a continuum with edge frequency $\nu_{i,j,k}$, a fraction $\nu_{i,j,k}/\nu$ of its energy is converted to atomic internal energy and the rest to thermal kinetic energy. To account for this, we convert the packet to an i-packet with probability $\nu_{i,j,k}/\nu$, setting it to the corresponding macro-atom state, and to a k-packet otherwise.

To speed up the calculations, we introduced an optional initial grey approximation in the code. Controlled by two input parameters $\tau_\mathrm{grey,min}$ and N_grey, the propagation of UVOIR radiation in cells

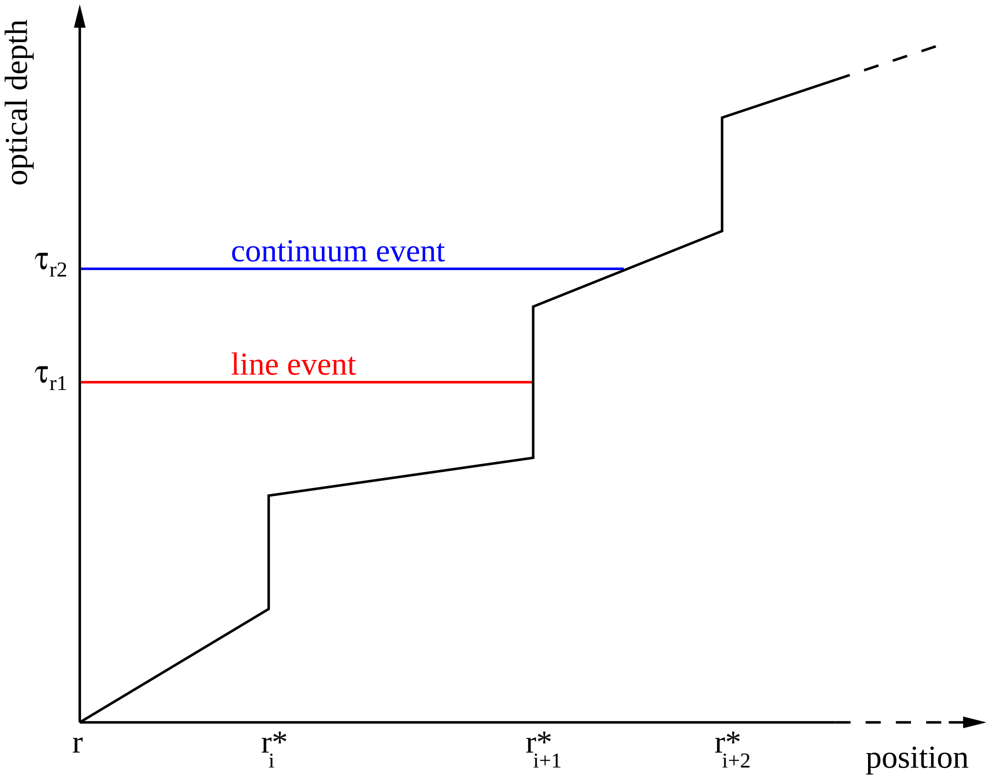

Figure 4.3: Illustration of the selection of the next photon absorption from a randomly sampled optical depth τ_r: whereas the continuum optical depth grows constantly while a photon travels through the supernova ejecta, in the Sobolev approximation the total optical depth of a particular atomic line is encountered at a specific resonance point $\mathbf{r}^*$. Owing to the continuous redshift in the expanding ejecta, the photon comes into resonance with all the included lines one-by-one at the resonance points $\mathbf{r}_1^*$, $\mathbf{r}_2^*, \ldots$ For a randomly drawn optical depth τ_r the next absorption happens then in the process, which causes the accumulated optical depth (accounting for continuum and line opacities along the photon path) to outrange τ_r for the first time. Thus, for the situation shown in the figure, a line event happens if τ_r1 was selected since the accumulated optical depth outranges τ_r1 for the first time at a resonance point. If τ_r2 was selected, the accumulated optical depth excels τ_r2 for the first time between two resonance points due to continuum opacity. Thus a continuum event is selected.

which have a grey optical depth $\tau_\mathrm{grey} > \tau_\mathrm{grey,min}$ is performed using only a grey opacity treatment. If τ_grey falls below $\tau_\mathrm{grey,min}$, and for all time steps later than N_grey, we switch to the non-grey treatment. Currently there are two implementations of this using either Thomson scattering as the grey opacity or a parameterized grey opacity $\kappa_\mathrm{grey} = 0.1 \cdot (0.9 X_\mathrm{Fe-grp} + 0.1)\ \mathrm{cm^2\,g^{-1}}$ following Mazzali & Podsiadlowski (2006), which roughly accounts for the composition in a cell by using the local iron-group mass fraction $X_\mathrm{Fe-grp}$. In the case of Thomson scattering we use the Thomson optical depth of a grid cell to decide if a cell is to be treated in the grey approximation or not. In the case of the parameterized grey opacity the distance along the photons trajectory from the cells midpoint to the surface of the simulation volume is multiplied by the local grey opacity to derive $\tau_\mathrm{grey,min}$. This speeds up the initial phase of a calculation by a factor of ~ 10, since much of the ejecta are still rather dense and photons cannot propagate. With a good selection of $\tau_\mathrm{grey,min}$ and N_grey the differences in spectra and light curves from a fully non-grey calculation are negligible (Figure 4.4).

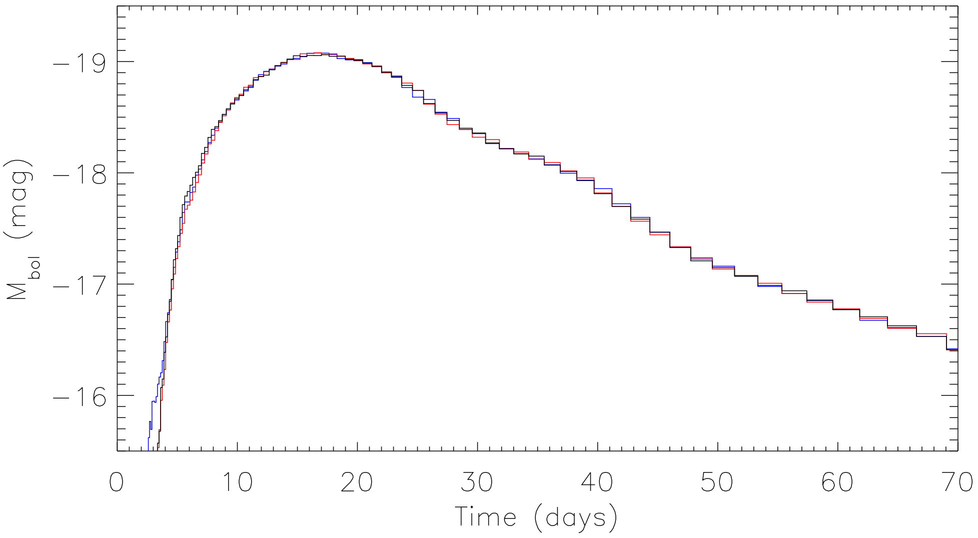

Figure 4.4: Bolometric light curve of a simulation without the initial grey approximation (black) compared to simulations which made use of the different grey approximations. For the blue curve the local Thomson optical depth with $\tau_{\mathrm{grey,min}} = 15$ and $N_{\mathrm{grey}} = 30$ was used to decide whether a cell stays grey. For the red curve the optical depth to the surface of the simulation volume calculated from the parameterized grey opacity was used as criterion ($\tau_{\mathrm{grey,min}} = 1000$ and $N_{\mathrm{grey}} = 30$). Baring Monte Carlo noise, the light curves are identical after 10 days. The Thomson parameterization leads to a slight enhancement of packets escaping at early times ($t < 4\,\mathrm{d}$). Compared to the runtime of the non-grey calculation, the one using the parameterized grey opacity is faster by about a factor two. The Thomson parameterization yields only a speed-up of 10%. For more complicated input models than the parameterized 1D model W7 (see Section 5.1) shown here, the number of photon packets propagated by each processor is (unlike here) typically smaller than the number of grid cells. Then differences in the cell properties lead to work imbalances in the parallelization at early times. The grey approximation strongly helps in reducing those, giving speed-up factors of ~ 10 in this case.

4.3.7 Extraction of spectra and light curves

When the simulation has finished, we extract the spectral evolution by binning the escaping r-packets in frequency, time and direction of escape, accounting for light travel-time effects. Colour light curves are extracted from the spectral evolution by integrating the spectra over the appropriate filter functions (Bessell & Brett 1988, Bessell 1990). UVOIR bolometric light curves are extracted by binning the escaping r-packets by time and angle. Similarly γ-ray spectra and light curves can be obtained from the γ-packets.

Recording Monte Carlo estimators for the source function in each grid cell and formally solving the radiative transfer equation (3.81) with these source functions to extract spectra and light curves along different rays would substantially reduce the Monte Carlo noise (formal integral method of Lucy 1999b). However, the need to store line and continuum source functions in all grid cells for all lines and continua included in the simulation (typically $10^5 \ldots 10^7$, in reality even more) causes the simulation memory requirements to be so high that this method becomes computationally prohibitive, even with current state-of-the-art super-computers for 3D grids. Requiring the storage of a double (8 bytes) for each line source function, this schemes consumes about 76 Megabytes per grid cell. Thus, we would need more than 72 000 Terabytes to hold this data in memory for a high resolution 3D grid of 1000^3 cells! Even on a modestly sized grid of 50^3 cells we would still require more than 9 Terabytes. In contrast, present day machines with a memory of 2 Gigabytes per core are already considered well-equipped. Therefore all results presented here have been obtained using the direct binning approach. For a comment on a possible distributed memory architecture of the code see Section 4.5.

4.4 Plasma conditions

To calculate opacities we need to know atomic level populations which in turn depend on the radiation field. In principle, these could be extracted exactly out of our simulation, but it is computationally restrictive to record the complete set of level-by-level radiative rates for every grid cell which would be required to do this. Therefore we use an approximate model for the radiation field and for excitation and ionization conditions. Two different descriptions have been implemented in our code. The first parameterizes the ionization balance in a simple one-temperature description using the Saha formula. This is less demanding of computational resources but also less accurate than our second which treats ionization in detail and simultaneously solves the thermal balance equation.

4.4.1 Radiation field models

Following Lucy (2003), the zeroth moment (Equation 3.2) of the radiation field in a grid cell can be reconstructed from the Monte Carlo packets using the estimator

$$J_\nu \mathrm{d}\nu = \frac{1}{4\pi \Delta t V} \sum_{\mathrm{d}\nu} \epsilon'_\nu \mathrm{d}s \tag{4.48}$$

where Δt is the length of the time step, V the grid cell volume, ds the trajectory length within the grid cell and $\epsilon_\nu^{\mathrm{cmf}}$ the packet energy in the cmf. The summation runs over all trajectory segments ds in V for which the packet frequency $\nu \in [\nu, \nu + \mathrm{d}\nu]$ during the time step.

As discussed above, we do not use this general description directly but parameterize the radiation field. For the simple one-temperature description of ionization, the radiation field is parameterized as a black body,

$$J_\nu = B_\nu \left(T_\mathrm{J}\right) \tag{4.49}$$

at a temperature T_J corresponding to the local energy density of the radiation field [$B_\nu(T)$ is the Planck function (3.6)]. The parameter T_J can be extracted by equating the frequency integrated estimator $\langle J \rangle \equiv \int_0^\infty J_\nu \, \mathrm{d}\nu$ (where J_ν is given by Equation 4.48) with the Stefan-Boltzmann law (Equation 3.8)

$$T_\mathrm{J} = \left(\pi \left\langle J \right\rangle / \sigma\right)^{1/4}. \tag{4.50}$$

In our simple ionization treatment, we also equate the kinetic temperature $T_\mathrm{e} = T_\mathrm{J}$.

For the detailed ionization treatment we parameterize the radiation field using a nebular approximation

$$J_\nu = W B_\nu \left(T_\mathrm{R}\right), \tag{4.51}$$

with the radiation temperature T_R and the dilution factor W as parameters. T_R is chosen such that the mean-intensity weighted mean frequency of the radiation field $\langle\nu\rangle \equiv \int_0^\infty \nu J_\nu \,\mathrm{d}\nu / \int_0^\infty J_\nu \,\mathrm{d}\nu$ matches that of a blackbody at T_R. Following Mazzali & Lucy (1993) T_R and W can be extracted from $\langle J\rangle$ and $\langle\nu\rangle$ by

$$W = \frac{\pi \langle J\rangle}{\sigma T_\mathrm{R}^4} \qquad \text{and} \qquad T_\mathrm{R} = \frac{h \langle\nu\rangle}{x k_\mathrm{B}} \tag{4.52}$$

with $x = 360 \cdot \zeta\left(5\right)/\pi^4$ and $\zeta\left(x\right)$ being Riemann's ζ-function. T_J remains defined as in the simple ionization treatment (implying $T_\mathrm{J} = W^{1/4} T_\mathrm{R}$ from Equation 4.50).

4.4.2 Excitation and ionization

Independent of the ionization description used, we apply the Boltzmann formula evaluated at T_J

$$\frac{n_{i,j,k}}{n_{0,j,k}} = \frac{g_{i,j,k}}{g_{0,j,k}} \exp\left(-\frac{\varepsilon_{i,j,k} - \varepsilon_{0,j,k}}{k_\mathrm{B} T_\mathrm{J}}\right) \tag{4.53}$$

to calculate the population $n_{i,j,k}$ of a level i of ion j of element k relative to the ion ground state population $n_{0,j,k}$. $g_{i,j,k}$ and $\varepsilon_{i,j,k}$ are statistical weights and energies of the corresponding levels.

Assuming ionization equilibrium in a radiation dominated environment[3], we require

$$\sum_{i=0}^{\mathcal{N}_\mathrm{L}(j,k)} n_{i,j,k} \gamma_{i,j,k} = n_e N_{j+1,k} \sum_{i=0}^{\mathcal{N}_\mathrm{L}(j,k)} \left(\alpha_{i,j,k}^\mathrm{sp} + \alpha_{i,j,k}^\mathrm{st}\right) \tag{4.54}$$

where $\mathcal{N}_\mathrm{L}\left(j,k\right)$ is the number of levels associated with ion j of element k, and n_e the density of free electrons. $\gamma_{i,j,k}$ denotes the photoionization rate coefficient from a bound level $\left(i,j,k\right)$ given by Equation (3.66) and $\alpha_{i,j,k}^\mathrm{sp}$ is the rate coefficient for spontaneous recombination from the $\left(j+1\right)$-th ion to the bound state $\left(i,j,k\right)$ given by Equation (3.68). In our simple one-temperature ionization treatment this reduces to the Saha equation (3.12).

Treating stimulated recombination as negative absorption and defining

$$\Gamma_{j,k} \equiv \sum_{i=0}^{\mathcal{N}_{j,k}} \frac{n_{i,j,k} \tilde{\gamma}_{i,j,k}}{n_{0,j,k}} \qquad \text{and} \qquad A_{j,k}^\mathrm{sp} \equiv \sum_{i=0}^{\mathcal{N}_{j,k}} \alpha_{i,j,k}^\mathrm{sp}, \tag{4.55}$$

where $\tilde{\gamma}_{i,j,k}$ is given by Equation (3.71), we obtain the following ionization formula for the detailed ionization treatment from Equation (4.54)

$$\frac{N_{j,k}}{N_{j+1,k} n_\mathrm{e}} = \frac{A_{j,k}^\mathrm{sp}}{\Gamma_{j,k}} \cdot \frac{U_{j,k}\left(T_\mathrm{J}\right)}{g_{0,j,k}}. \tag{4.56}$$

---

[3] Currently we consider only photoionization and radiative recombination. Temperatures in the recombination zones of iron-group elements are sufficiently low that dielectronic recombination (calculated according to Shull & van Steenberg 1982) is small compared to radiative recombination. However we note that in high temperature environments it may become important, especially for intermediate-mass elements. For more detailed studies our treatment could readily be extended to incorporate additional ionization/recombination processes (including dielectronic recombination and non-thermal ionization).

$U_{j,k}\left(T_\mathrm{J}\right)$ is the partition function Equation (3.14). Since $\alpha^\mathrm{sp}_{i,j,k}$ does not depend directly on the radiation field, we calculate $A_{j,k}$ by summing all the $\alpha^\mathrm{sp}_{i,j,k}$ of the ion (j,k) evaluated at the local kinetic temperature T_e.

In contrast, the photoionization rate coefficients $\tilde{\gamma}_{i,j,k}$ (Equation 3.71) depend directly on the radiation field. Thus, following Lucy (2003), for most accurate results they should be determined from volume-based Monte Carlo estimators

$$\begin{aligned}\tilde{\gamma}_{i,j,k} &= 4\pi \int_{\nu_{i,j,k}}^{\infty} \frac{\alpha_{i,j,k\to j+1,k}\left(\nu\right)}{h\nu}\left(1-\frac{n_{0,j+1,k}}{n_{i,j,k}}\frac{n^*_{i,j,k}}{n^*_{0,j+1,k}}e^{-h\nu/k_\mathrm{B}T_\mathrm{e}}\right)J_\nu \mathrm{d}\nu \\ &= \frac{1}{\Delta t V}\sum_{\nu'>\nu_{i,j,k}} \frac{\epsilon_\nu^{'}}{h\nu'}\alpha_{i,j,k\to j+1,k}\left(\nu'\right)\left(1-\frac{n_{0,j+1,k}}{n_{i,j,k}}\frac{n^*_{i,j,k}}{n^*_{0,j+1,k}}e^{-h\nu'/k_\mathrm{B}T_\mathrm{e}}\right)\mathrm{d}s \qquad (4.57)\end{aligned}$$

where we made use of Equation (4.48). However, we cannot afford to store $\tilde{\gamma}_{i,j,k}$ for each bound-free continuum in every grid cell since it would consume too much memory. Instead we derive $\tilde{\gamma}^*_{i,j,k}$ from an integration of the radiation field model (Equation 4.51) using the local values of T_R and W. Estimated in this way $\tilde{\gamma}^*_{i,j,k}$ is expected to be reliable for bound-free absorptions which lie around the peak of the radiation field. However, the radiation field model is inadequate at very blue frequencies where the spectrum is systematically affected by bound-free edges. Thus to track the effect of absorption continua on the radiation field, we record estimators $\tilde{\gamma}_{0,j,k}$ for the photoionization rate coefficient of the ground level continua and use them to derive renormalization coefficients $\zeta_{0,j,k}=\tilde{\gamma}_{0,j,k}/\tilde{\gamma}^*_{0,j,k}$. To obtain the $\tilde{\gamma}_{i,j,k}$-values in $\Gamma_{j,k}$ of Equation 4.55 we renormalize all the integrated photoionization rate coefficients via

$$\tilde{\gamma}_{i,j,k}=\zeta_{0,j',k'}\tilde{\gamma}^*_{i,j,k}, \qquad (4.58)$$

where we take the $\zeta_{0,j',k'}$-value from the ground level continuum which lies closest in edge frequency to the considered continuum [i.e. the one for level (i,j,k)]. For continua redder than the reddest ground level continuum, ζ is set to one. The same renormalization is also applied during the calculation of the transition rates for the macro-atom transition probabilities described in Section 4.3.5.

For the zeroth time step, and also for cells treated in our initial grey approximation (see Section 4.3.6), we use the simple ionization treatment. We also assume that at all times prior to our zeroth time step the ejecta are sufficiently optically thick, that all the radiation is trapped. Thus we calculate initial temperatures $T_{\mathrm{e},0}=T_{\mathrm{R},0}=T_{\mathrm{J},0}$ for each grid cell from the energy released by the decay of ^{56}Ni in the cell prior to the midpoint of the zeroth time step. Since the trapping is not really perfect, it takes a few (typically ~ 5) time steps until the propagation of the energy packets washes out the effect of this boundary condition on temperatures and level/ion populations.

In practice this boundary condition primarily effects calculations using the detailed ionization description. In this case, it is more important to have accurate level populations as errors can feed back to the thermal balance calculation. Thus we typically do the first ~ 10 time steps of a calculation in the simple ionization treatment to obtain reliable initial conditions for the detailed ionization treatment at all later times. Since our simple ionization treatment reproduces LTE

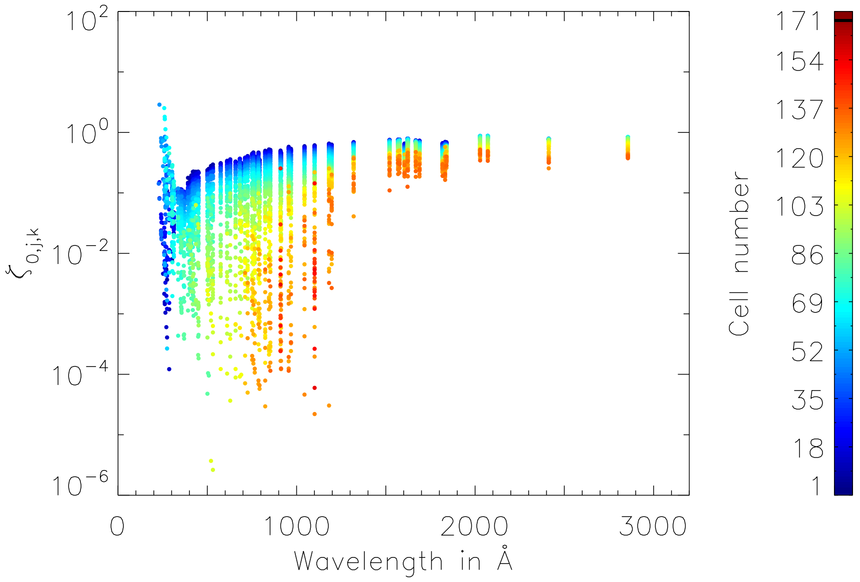

Figure 4.5: Renormalization factors $\zeta_{0,j,k}$ for the photoionization rate coefficients for a typical SN Ia explosion model (W7, see Section 5.1) around maximum light. The figure shows the $\zeta_{0,j,k}$-values vs. edge wavelength of the corresponding ground level continuum. Differently coloured dots represent different cells from inside out (dark blue to dark red, W7 is a 1D model). In general line blocking dilutes the radiation field more strongly in the blue. Thus the reduction of the photoionization rate increases from red to blue edges. Since the radiation field in the outer layers originates from deeper cells, they are more strongly affected by absorption processes leading to a larger reduction of the photoionization rate. Note that we do not include lines for the highest ionization state considered in the model (here fourfold ionized). Thus the line opacity close to the bluest edges decreases. This can be seen in a few cells where the photoionization rates is increased ($\zeta_{0,j,k} > 1$) for the bluest edges. These are the cells which have the highest ^{56}Ni mass fractions of the model and thus the locally bluest radiation field.

conditions we expect it to be a good approximation at early times when optical depths are high.

4.4.3 Thermal balance

In the detailed ionization description, we also solve for the local kinetic temperature T_e in a grid cell by balancing the local cooling ($\mathcal{C}$) and heating ($\mathcal{H}$) rates. Including cooling by free-free and free-bound emission, collisional ionization/excitation and adiabatic expansion the total cooling rate is given by

$$\mathcal{C} = \sum_{k=1}^{\mathcal{N}_\mathrm{E}} \sum_{j=1}^{\mathcal{N}_\mathrm{I}(k)} \mathcal{C}^{\mathrm{ff}}_{j,k} + \sum_{k=1}^{\mathcal{N}_\mathrm{E}} \sum_{j=1}^{\mathcal{N}_\mathrm{I}(k)-1} \sum_{i=1}^{\mathcal{N}_\mathrm{L}(j,k)-1} \left(\mathcal{C}^{\mathrm{fb,sp}}_{i,j,k\leftarrow j+1,k} + \mathcal{C}^{\mathrm{ion}}_{i,j,k\rightarrow j+1,k} + \sum_{i'=i+1}^{\mathcal{N}_\mathrm{L}(j,k)} \mathcal{C}^{\mathrm{exc}}_{i,j,k\rightarrow i',j,k} \right) + \mathcal{C}^{\mathrm{ad}}, \tag{4.59}$$

where the particular contributions are defined in Equations (4.31), (4.35), (4.32) and (4.33), respectively. The adiabatic cooling rate in a grid cell of volume V is

$$\mathcal{C}^{\mathrm{ad}} = \frac{p}{V} \frac{\partial V}{\partial t} \tag{4.60}$$

where p is the gas pressure

$$p = N k_{\mathrm{B}} T_{\mathrm{e}} \tag{4.61}$$

and $N = \sum_k^{\mathcal{N}_{\mathrm{E}}} \sum_j^{\mathcal{N}_{\mathrm{I}}(k)} N_{j,k} + n_{\mathrm{e}}$. Since these cooling rates do not depend on the radiation field directly, they are calculated from the current set of level populations and T_{e}.

In contrast, the total heating rate $\mathcal{H}$, which is given by the sum of heating due to γ-ray depositions, free-free and bound-free absorptions and collisional deexcitation/recombination

$$\mathcal{H} = \mathcal{H}^{\gamma} + \mathcal{H}^{\mathrm{ff}} + \mathcal{H}^{\mathrm{bf}} + \mathcal{H}^{\mathrm{deexc}} + \mathcal{H}^{\mathrm{recomb}}, \tag{4.62}$$

contains with $\mathcal{H}^{\gamma}$, $\mathcal{H}^{\mathrm{ff}}$ and $\mathcal{H}^{\mathrm{bf}}$ contributions which depend directly on the radiation field. Following Lucy (2003, 2005), we use volume-based Monte Carlo estimators derived from the previous time step to determine those rates.

For γ-ray heating such an estimator is given by

$$\mathcal{H}^{\gamma} = \frac{1}{\Delta t V} \sum_{\gamma-\mathrm{paths}} \left(\kappa_{\gamma}^{\mathrm{tot}}\left(\nu'\right)\right)' \epsilon \left(1 - 2\mathbf{n} \cdot \mathbf{v}/c\right) \mathrm{d}s \tag{4.63}$$

according to Lucy (2005), where $\left(\kappa_{\gamma}^{\mathrm{tot}}\left(\nu'\right)\right)'$ is the cmf opacity due to true absorption of γ-photons, i.e. neglecting those photons which are really scattered by Compton scattering and not converted to electrons. The summation runs over all γ-packets with path segments in V during Δt.

The heating due to free-free absorptions is given by

$$\mathcal{H}^{\mathrm{ff}} = 4\pi \int_0^{\infty} \left(\chi^{\mathrm{ff}}\left(\nu'\right)\right)' J\left(\nu'\right) \mathrm{d}\nu'. \tag{4.64}$$

Using Equation (4.48) this yields the estimator

$$\mathcal{H}^{\mathrm{ff}} = \frac{1}{\Delta t V} \sum_{r-\mathrm{paths}} \epsilon_{\nu}' \left(\chi^{\mathrm{ff}}\left(\nu'\right)\right)' \mathrm{d}s \tag{4.65}$$

where the summation runs over all r-packets with path segments in V during Δt.

Treating stimulated recombination as negative photoabsorption, the heating by bound-free absorptions is given by

$$\begin{aligned}\mathcal{H}^{bf} &= \sum_{k=1}^{\mathcal{N}_{\mathrm{E}}} \sum_{j=1}^{\mathcal{N}_{\mathrm{I}}(k)-1} \sum_{i=1}^{\mathcal{N}_{\mathrm{L}}(j,k)} n_{i,j,k} \left[\left(\gamma_{i,j,k}^{\mathrm{E}} - \gamma_{i,j,k}\right) - \frac{n_{0,j+1,k} n_{\mathrm{e}}}{n_{i,j,k}} \left(\alpha_{i,j,k}^{\mathrm{stim,E}} - \alpha_{i,j,k}^{\mathrm{stim}}\right)\right] \left(\varepsilon_{0,j+1,k} - \varepsilon_{i,j,k}\right) \\ &= \sum_{k=1}^{\mathcal{N}_{\mathrm{E}}} \sum_{j=1}^{\mathcal{N}_{\mathrm{I}}(k)-1} \sum_{i=1}^{\mathcal{N}_{\mathrm{L}}(j,k)} n_{i,j,k} h_{i,j,k}^{\mathrm{bf}},\end{aligned} \tag{4.66}$$

where $\gamma_{i,j,k}$ and $\alpha_{i,j,k}^{\mathrm{stim}}$ are the rate coefficients for photoionization and stimulated recombinations defined in Equations (3.66) and (3.69), respectively. $\gamma_{i,j,k}^{\mathrm{E}}$ and $\alpha_{i,j,k}^{\mathrm{stim,E}}$ describe similarly to $\alpha_{i,j,k}^{\mathrm{spont,E}}$ [defined in Equation (4.34)] the rate at which radiation energy is converted to both thermal and ionization energy and are given by

$$\gamma^{\mathrm{E}}_{i,j,k} = n_{i,j,k} 4\pi \int_{\nu_{i,j,k}}^{\infty} \frac{\alpha_{i,j,k\to j+1,k}\left(\nu\right)}{h\nu_{i,j,k}} J_\nu \mathrm{d}\nu \tag{4.67}$$

$$\alpha^{\mathrm{stim,E}}_{i,j,k} = \phi_{i,j,k}\left(T_{\mathrm{e}}\right) 4\pi \int_{\nu_{i,j,k}}^{\infty} \frac{\alpha_{i,j,k\to j+1,k}\left(\nu\right)}{h\nu_{i,j,k}} J_\nu e^{-h\nu/k_{\mathrm{B}}T_{\mathrm{e}}} \mathrm{d}\nu. \tag{4.68}$$

Using again Equation (4.48) we thus find

$$\begin{aligned} h^{\mathrm{bf}}_{i,j,k} &= 4\pi \int_{\nu_{i,j,k}}^{\infty} \alpha_{i,j,k\to j+1,k}\left(\nu\right) \left(1 - \frac{\nu_{i,j,k}}{\nu}\right) \left(1 - \frac{n_{0,j+1,k}}{n_{i,j,k}} \frac{n^*_{i,j,k}}{n^*_{0,j+1,k}} e^{-h\nu/k_{\mathrm{B}}T_{\mathrm{e}}}\right) J_\nu \mathrm{d}\nu \\ &= \frac{1}{\Delta t V} \sum_{\nu' > \nu_{i,j,k}} \epsilon'_\nu \alpha_{i,j,k\to j+1,k}\left(\nu'\right) \left(1 - \frac{\nu_{i,j,k}}{\nu}\right) \left(1 - \frac{n_{0,j+1,k}}{n_{i,j,k}} \frac{n^*_{i,j,k}}{n^*_{0,j+1,k}} e^{-h\nu'/k_{\mathrm{B}}T_{\mathrm{e}}}\right) \mathrm{d}s \end{aligned} \tag{4.69}$$

Since, for computational reasons, we cannot afford to store a bound-free heating estimator for each continuum in every grid cell, the values for $h^{\mathrm{bf}}_{i,j,k}$ are not obtained directly from Monte Carlo estimators but from an integration of the radiation field model (Equation 4.51) using the local values of T_{R} and W yielding $h^{\mathrm{bf},*}_{i,j,k}$. As for the photoionization rate coefficients (Section 4.4.2), we then use estimators $h^{\mathrm{bf}}_{0,j,k}$ for the bound-free heating coefficient of the ground level continua to derive renormalization coefficients $\xi_{0,j,k} = h^{\mathrm{bf}}_{0,j,k}/h^{\mathrm{bf},*}_{0,j,k}$. These are used to calculate the bound-free heating coefficients

$$h^{\mathrm{bf}}_{i,j,k} = \xi_{0,j',k'} h^{\mathrm{bf},*}_{i,j,k} \tag{4.70}$$

where we again take the $\xi_{0,j',k'}$ which lies closest in frequency to the considered continuum [i.e. the one for level (i,j,k)] to track the effect of absorption continua on the radiation field. Continua which are redder than the reddest ground-level continuum are not renormalized.

Estimates for the heating by collisional deexcitation/recombination are obtained by summing the cmf energies ϵ' of packets which contributed to the corresponding processes in each cell.

Balancing the heating and cooling rates on a temperature interval $[T_{\mathrm{min}}, T_{\mathrm{max}}]$ with $T_{\mathrm{min}} = 3500\,\mathrm{K}$ and $T_{\mathrm{max}} = 1.4 \cdot 10^5\,\mathrm{K}$ in our simulations, leads to a new value of T_{e}. For cells in which the heating and cooling rates cannot be balanced on this interval, T_{e} is set to the upper/lower boundary value if the heating/cooling rates dominate. The same temperature limits apply to T_{J} and T_{R}. T_{max} is chosen such that it will be only reached at the very earliest times in the inner iron-rich core where the opacity is so high that the radiation is trapped. T_{min} will be reached at late times but only in layers which are sufficiently optically thin that they have no strong influence on the spectrum formation.

To speed up the calculations, the rate coefficients for spontaneous recombination (Equation 3.68), photoionization (Equation 3.71), bound-free cooling (Equation 4.35) and bound-free heating (Equation 4.66) are precalculated for a grid on this temperature interval and interpolations on the precalculated values are used at runtime.

Assuming that time steps are short enough and the radiation field does not depend strongly on the evolution of T_{e} we use the value obtained for T_{e} and the same Monte Carlo estimators as before to re-solve for the populations and then for thermal balance again. Repeating this iteratively we reach a converged solution for T_e and the ionization state (see Figure 4.6). This iteration can be extended to an outer loop in which the Monte Carlo simulation is also repeated. Kasen et al. (2006, Section 3.4) showed that, even from crude initial conditions, such an iteration converges very rapidly. By using short time steps and initial thermodynamic quantities from the previous time step, we found that such an outer iteration of the Monte Carlo experiment does not affect the results strongly. Thus we do not iterate on the Monte Carlo simulation for each time step in the simulations described below (however the option to do so remains in the code see Figure 4.6).

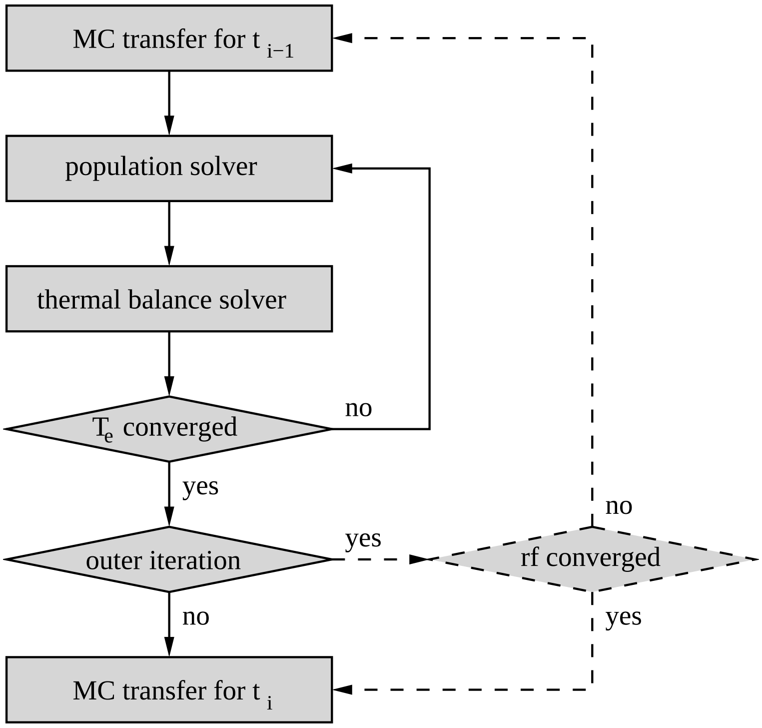

Figure 4.6: Schematic view of the thermal balance calculation. If desired an outer iteration over the Monte Carlo radiative transfer can be carried out to obtain a more converged radiation field for each time step.

4.5 Parallelization

Since propagating an individual energy packet does not depend on the propagation of the other energy packets, a Monte Carlo transfer simulation can be parallelized by distributing the propagation of bunches of packets to a multitude of processors, each of them performing its own Monte Carlo experiment. This “fully replicative” approach should scale perfectly because in the simplest case of a time-independent problem there is no need of communication between the different processors at runtime.

For a time-dependent problem, where the physical properties of the grid cells have to be updated, the situation is more complex. On a distributed memory machine each processor works on its own copy of the complete simulation grid. Thus the estimates for the radiation field in each grid cell recorded during the propagation phase, must be communicated between the different processors after the packet propagation of each time step. To speed up the subsequent update of the grid properties (i.e. the solution of the coupled thermal and ionization balance equations), it is then useful to distribute this calculation to different processors as well. This introduces another need for communicating the properties of all cells among all processors after the update of the grid properties has finished.

In our code we use the Message Passing Interface[4] (MPI) to realize such a parallelization scheme. Employing only collective communication routines between subsequent time steps it retains an almost perfect scaling behaviour, if no significant work imbalance between the individual tasks occurs during the packet propagation phase (Figure 4.7).

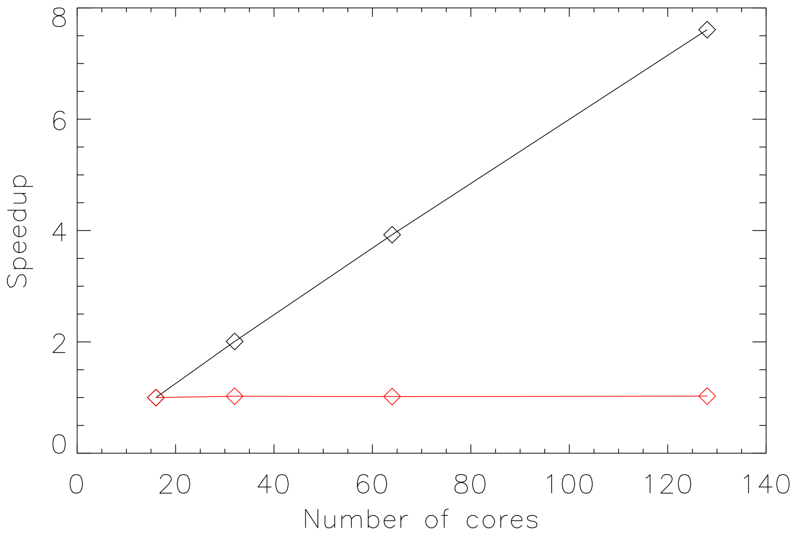

Figure 4.7: Scaling behaviour of the MPI parallelization of our code for a run of the W7 model (see Section 5.1). The black diamonds show the speed-up factor in a strong-scaling test, i.e. propagating a given number of packets on an increasing number of cores. For the number of cores tested (16,32,64,128) the scaling is almost perfect. The red diamonds show the speed-up factor in a weak-scaling, i.e. each core propagates a given number of packets such that by increasing the number of cores the problem size increases. Again the scaling is almost perfect, showing no slow-down. Actually in this test we find even a slight speed-up because updating the grid properties is becoming more parallel with the increasing number of cores.

Despite its favourable scaling behaviour, this fully replicative approach has some shortcomings, especially if it comes to the calculation of 3D models. To adequately resolve these models, grid sizes of $\sim 100^3$ are required. Since we need to store the ion populations and all the temperatures and estimators mentioned in the previous section for each grid cell, such a calculation requires $\sim 10^8 \ldots 10^9$ floating point variables to be held in memory. Owing to the need to hold a copy of this data on each processor, the full replication approach poses great demands on the memory available per processor (~ 8 Gigabytes).

Typically computers share a part of their main memory among a few processors (all those processors together are referred to as a node, while the individual processors are then called cores). Thus a hybrid parallelization scheme, in which all cores of a node share the same simulation grid, can help

---

[4] See http://www.mcs.anl.gov/research/projects/mpi/.

to reduce the memory consumption. Due to the memory sharing, however, we must make sure that if two or more cores of a single node simultaneously propagate packets in the same grid cell they do not access the memory position associated with that grid cell at the same time (race condition). This requires simultaneous memory access to be blocked and thus causes the scaling to suffer. In our code we use OpenMP[5] to implement a shared memory parallelization of the packet propagation and update grid phase below the global fully replicative MPI parallelization.

Since current developments in super-computing favour the use of systems with many small independent nodes with less shared memory (e.g. IBMs BlueGene architecture), for the future one might consider a parallelization approach involving a distribution of the grid to different nodes, rather than distributing the energy packets, to make best use of the available distributed memory. In this, so called domain-decompositioned approach, each node would then treat the propagation on the part of the grid it is responsible for and packets are communicated between the nodes. Obviously this requires considerably more communication than the fully replicative approach and thus will show a significantly worse scaling behaviour.

4.6 Atomic data

The most important opacity source in supernova envelopes is the wealth of bound-bound line transitions associated with the iron-group elements synthesized by the thermonuclear explosion. Thus an extensive line list which covers all the important species is needed. We restrict our atomic data to the lowest five ionization stages of elements up to Zn, neglecting H, Li, Be and B. To study the sensitivity to the choice of atomic data, we use two datasets which are based on the $\sim 5 \cdot 10^5$ lines of Kurucz & Bell (1995) (CD23) and the more modern theoretical atomic data computed by Kurucz (2006)[6] which are far more comprehensive but still not complete. For example this dataset contains $\sim 3.5 \cdot 10^7$ lines associated with the important second and third ions of Fe, Co and Ni compared to only $\sim 1.2 \cdot 10^5$ in CD23.

Since it is computationally too demanding to use all of the lines in a dataset, when constructing model atoms we apply cuts in $\log(gf)$ to reduce the number of lines. From the comprehensive dataset we take only the lines of Fe II, Fe III, Co II, Co III, Ni II and Ni III, the most important species in the spectrum forming region, and continue to use the data of CD23 for all the other species and remaining ions of Fe, Co and Ni. In this way, we created a set of model atoms (summarized in Table 4.1) which are used in the following calculations.

Bound-free cross sections are obtained from the fits by Verner & Yakovlev (1995) or Verner et al. (1996) where available. A hydrogenic approximation is adopted for excited configurations.

Having discussed the physics simulated by ARTIS in detail, we now apply it to simply-parameterized test models to verify its operation.

---

[5] See http://openmp.org/wp/.

[6] Available at http://kurucz.harvard.edu/atoms.html.

Table 4.1: Atomic data sets used in the calculations. Source A is Kurucz & Bell (1995), Source B Kurucz (2006).

Model name	Source	log(gf)	Levels	Lines (total)
cd23_gf-2	A	-2	18237	$1.4 \cdot 10^5$
cd23_gf-3	A	-3	18815	$2.5 \cdot 10^5$
cd23_gf-5	A	-5	19472	$4.1 \cdot 10^5$
cd23_gf-20	A	-20	21100	$4.7 \cdot 10^5$
big_gf-3	B (Fe II–III)	-3	41829	$3.5 \cdot 10^6$
	B (Co II–III)	-3	31816	
	B (Ni II–III)	-3	24853	
	A (other)	-3	16616	
big_gf-4	B (Fe II–III)	-4	47141	$8.2 \cdot 10^6$
	B (Co II–III)	-4	36442	
	B (Ni II–III)	-4	28022	
	A (other)	-4	17523	

5 Two simple test cases

To test the code developed during this thesis, we calculate model spectra and light curves for two simply-parameterized test cases in this chapter and compare them to results from earlier studies using other codes. Furthermore we discuss the basic effects of the different ionization treatments included in the code, the influence of completeness of atomic data and how line-of-sight effects affect the observable properties of multi-dimensional models. This chapter has already been published (Kromer & Sim 2009).

5.1 The parameterized 1D deflagration model W7

As a first test we calculate the spectral evolution for the one-dimensional deflagration model W7 (Nomoto et al. 1984, Thielemann et al. 1986) which has already been investigated in several other radiative transfer studies (Jeffery et al. 1992, Höflich 1995, Nugent et al. 1997, Lentz et al. 2001, Salvo et al. 2001, Baron et al. 2006, Kasen et al. 2006) and is found to be in good overall agreement with observations.

Our calculations use $5 \cdot 10^6$ energy packets to follow the spectral evolution over 100 time steps from 2 to 80 days after explosion [$\Delta \ln(t) \sim 0.037$] and were performed on a 50^3 grid using the cd23_gf-5 model atom (see Table 4.1 for details) with our detailed ionization treatment. The first 10 time steps have been calculated in the simple ionization treatment to obtain reliable initial values (see the discussion in Section 4.4.2). To save computational time we make use of our initial grey approximation employing the Thomson parameterization with $\tau_{\mathrm{grey,min}} = 15$ and $N_{\mathrm{grey}} = 40$ (see Section 4.3.6).

Figure 5.1 shows the 2500 to 10 000 Å spectra for 15, 22 and 44 days after explosion, corresponding to -5, +2 and +24 days relative to B-band maximum. The colour coding shows the element associated with the last line emission of escaping photons, giving an indication of the elements responsible for spectral features (absorption features of individually strong lines can be identified in the plot from their associated P-Cygni emission). The contribution of photons which escaped after a bound-free or free-free emission to the total flux is negligible ($< 10^{-3}$) and not shown. The most striking individual features are the Ca II NIR triplet ($\lambda\lambda 8498, 8542, 8662$) and the characteristic Si II doublet ($\lambda\lambda 6347, 6371$) which is clearly visible around maximum light. While the outer layers, which are dominated by intermediate-mass elements, are optically thick, the spectra are dominated by these elements. Around maximum light the outer layers become optically thin and the spectra start to be dominated by iron-group elements which completely take over at later times. Only individual strong lines of the intermediate-mass elements (e.g. the Ca II NIR triplet) persist.

Overplotted with our synthetic spectra are observations of SN 1994D (Patat et al. 1996) for the corresponding epochs. Given that the W7 model has not been tuned to any particular supernova, the agreement of our model spectra with the observed ones is good. We reproduce the main spectral features, e.g. the Si II doublet and the Ca II NIR triplet, as well as the overall flux distribution allowing for extinction effects. However there are obvious differences: at early times our model spectra have a strong excess in the UV flux below 4000 Å where Fe II, Fe III, Co III and Co IV dominate the spectrum formation. At late times we obtain emission in Fe II at ∼ 6050 Å where the data shows an absorption feature. Model spectra calculated for W7 by Kasen et al. (2006) show the same discrepancies compared to SN 1994D. This could be an indication that some details of the explosion model would need to be changed to obtain better agreement with SN 1994D.

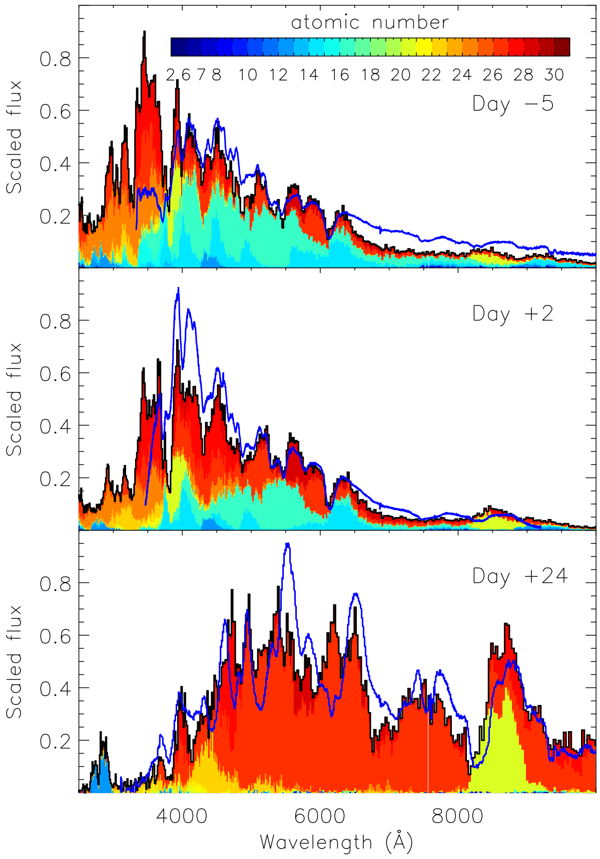

Figure 5.1: Spectra for the W7 explosion model at 5 days before and 2 and 24 days after maximum light in *B* band (from top to bottom) calculated using the detailed ionization description and atomic dataset cd23_gf-5. Overplotted in blue are the observed spectra of SN 1994D for comparison (no redshift and extinction corrections have been applied). The colour coding shows the element associated with the last line emission of escaping photons. Atomic numbers in the colour legend are associated with the colour right to the number centre.

5.1.1 Simple versus detailed ionization treatment

In the following we investigate how the two different ionization treatments (see Section 4.4.2) which are implemented in our code affect the spectral evolution of a given explosion model. Therefore we also followed the spectral evolution of the W7 model using the cd23_gf-5 atomic data from 2 to 80 days after the explosion using the simple ionization treatment.

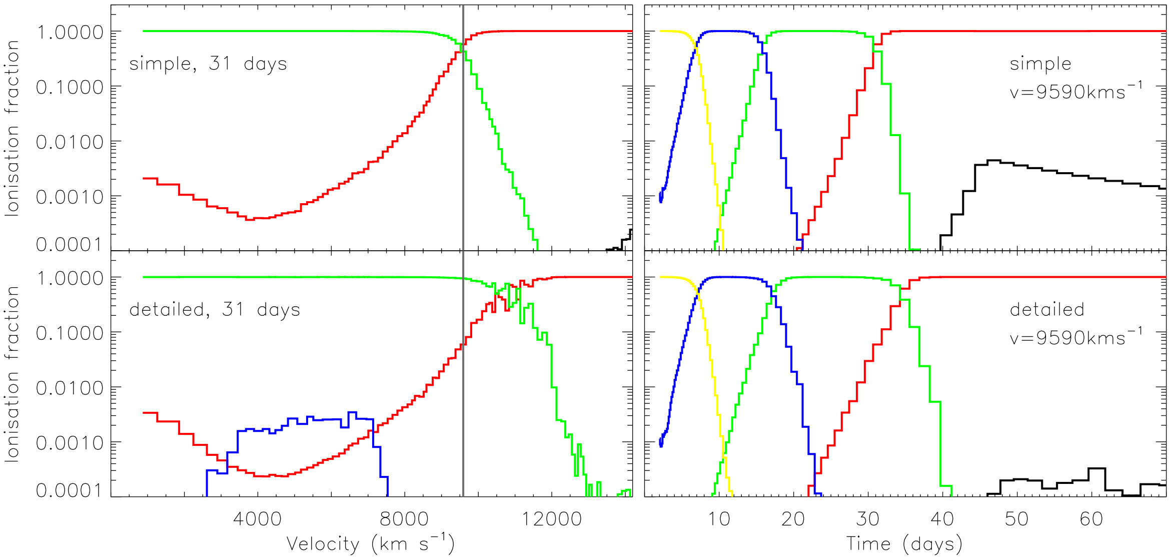

Figure 5.2: The left panels show the radial ionization structure of iron in the W7 explosion model at 31 days after the explosion obtained with the simple (top) and detailed ionization treatment (bottom) and model atom cd23_gf-5. Black/red/green/blue/yellow lines represent Fe I/II/III/IV/V. The outer layers of the model, which consist only of unburned material and extend up to 22 800 km s^{-1}, are not shown. The right panels show the time evolution of the iron ionization structure at a velocity of 9590 km s^{-1} (indicated by the grey vertical line in the left panels) from 2 to 70 days for the two different ionization treatments.

Since differences in the spectral evolution must originate from the different ionization treatment, we compare ionization fractions from our different simulations in Figure 5.2. We focus on iron since the iron-group elements, which have similar ionization structure to each other, dominate the spectra for the relevant epochs. The left panels of Figure 5.2 show the ionization fractions as a function of radial velocity at 31 days after the explosion for the simple and detailed ionization treatment. The right panels show the same ionization fractions as a function of time at a radial velocity of 9590 km s^{-1}, which is marked by the grey vertical line in the left panels. This is the velocity at which the iron-group mass fraction of the ejecta drops to 0.5 and thus is around the outer velocity of the iron-rich inner core.

From the left panels we see that, using the detailed ionization treatment, the ejecta are more highly ionized at higher radial velocities. The right panels show that, with the detailed ionization treatment, the ejecta also stay more highly ionized for a longer time at a given radius and never recombine as fully as with the simple ionization treatment at late times. In the simple ionization treatment, the ionization is determined only by the energy density of the radiation field calculated from the r-packets. In the detailed ionization treatment, the frequency distribution of the calculated radiation field has an important effect. $T_{\mathrm{R}} > T_{\mathrm{J}}$ and $W < 1$ (see Equations 6 – 8) with T_{R} and W departing more strongly from T_{J} and 1, respectively, with increasing time and decreasing ejecta density and opacity. Thus, there tend to be more high-energy ionizing photons than suggested by the radiation field model of the simple ionization treatment. This gives rise to higher ionization states, particularly for later times. This is illustrated in Figure 5.3 which shows the time evolution of the radiation temperature T_{R} and the temperature T_{J} corresponding to the energy density of the radiation field at a radial velocity of 9590 km s^{-1}. While $T_{\rm J}$ drops similarly for the simple and detailed ionization treatment, $T_{\rm R}$ for the detailed ionization treatment stays significantly hotter from 20 days on.

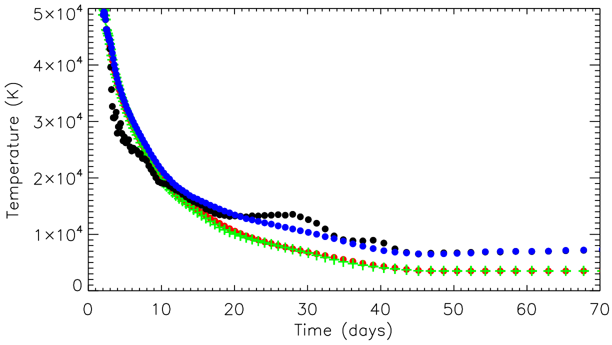

Figure 5.3: Temperature evolution at a radial velocity of 9590 km s^{-1} i.e. at the outer edge of the iron-rich core. The green crosses show $T_{\rm J}$ in the simple ionization treatment. The circles are the three temperatures used in the detailed ionization treatment and show the kinetic temperature $T_{\rm e}$ (black), the radiation temperature $T_{\rm R}$ (blue) and $T_{\rm J}$ (red). At around 45 days, $T_{\rm J}$ hits the lower temperature boundary of 3500 K and is not allowed to drop further.

$T_{\rm e}$ shows a similar decline and stays somewhat below $T_{\rm R}$ up to about maximum light (note that at very early times, prior to $\sim$ 10 days, this region is dominated by Fe V for which line transitions were not included – this likely explains the less complete coupling of $T_{\rm e}$ to the radiation field at these early epochs). Afterwards γ-ray heating dominates the total heating rate and controls the kinetic temperature. Although the γ-ray heating decreases smoothly with time, $T_{\rm e}$ shows distinct changes. These arise when recombination from one dominant ion to the next occurs and the contributing cooling processes change abruptly. In order to retain the balance between the heating and cooling rates then $T_{\rm e}$ must change rapidly.

Figure 5.4 illustrates the radial temperature distribution at 31 days after the explosion. $T_{\rm J}$ for the two different ionization treatments shows no strong difference. However $T_{\rm R}$ in the detailed ionization treatment differs strongly from $T_{\rm J}$ over the entire ejecta, indicating that the radiation field is bluer and more dilute that would be implied by our radiation field model in the simple ionization treatment. The kinetic temperature is mainly controlled by γ-ray heating which dominates over the other heating rates outside $\sim$ 2500 km s^{-1} and varies only gradually with velocity, declining outwards. This leads to $T_{\rm e} > T_{\rm R}$. Around recombination fronts the contributing cooling processes change abruptly. This means that $T_{\rm e}$ has to change rapidly in such regions in order that the heating rate remains balanced by the total cooling rate and leads to the rapid decline in $T_{\rm e}$ between 8000 and 10 000 km/s where the recombination from Fe III to Fe II happens (compare Figure 5.2). The vertical lines show the mean radii of last scattering for packets which had their last scattering at $\sim$ 31 days. Because of line blocking the optical depths are biggest in the UV and blue and the different bands probe deeper into the ejecta in a sequence from blue to red. An exception is the mean radius of last scattering in the I band which lies at $\sim$ 8500 km s^{-1}, between the R and V bands. This is because the I band has significant contribution from the Ca II NIR triplet which forms outside the iron-rich core.

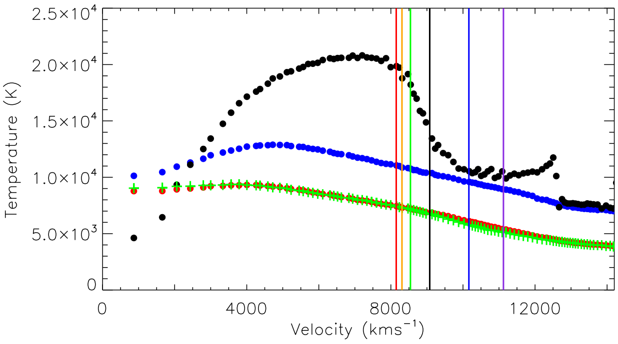

Figure 5.4: Radial temperature distribution at 31 days after the explosion. The outer layers of the model, which consist only of unburned material and extend up to 22 800 km s^{-1}, are not shown. The green crosses show T_{J} in the simple ionization treatment. The circles are the three temperatures used in the detailed ionization treatment and show the kinetic temperature T_{e} in black, the radiation temperature T_{R} in blue and T_{J} in red. The black/violet/blue/green/red/orange vertical lines show the mean radii of last scattering in bolometric/U/B/V/R/I light. The sharp drop in T_{e} around 12 500 km s^{-1} is associated with a strong change in composition in the W7 model. The iron-group abundance abruptly drops at this point and intermediate-mass elements dominate.

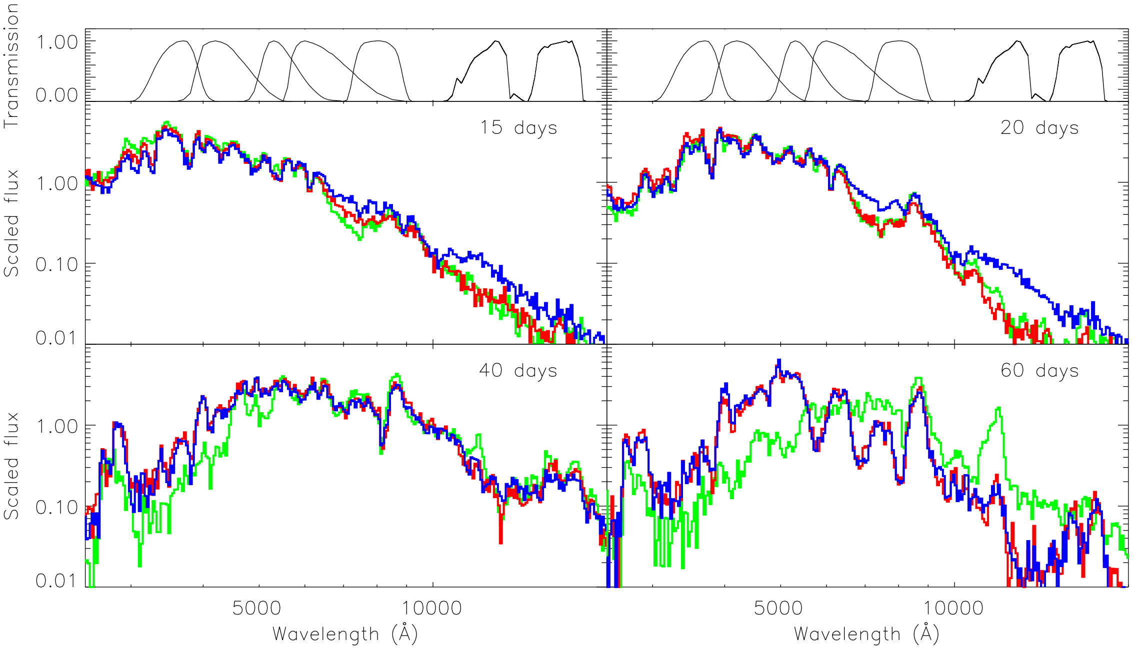

Figure 5.5: Spectra for the W7 explosion model at 15, 20, 40 and 60 days after the explosion, respectively. The green and red lines were calculated with the cd23_gf-5 atomic dataset using the simple and detailed ionization treatment, respectively. The blue line was calculated with the big_gf-4 atomic dataset and the detailed ionization treatment. The top panels show (from left to right) the normalized U,B,V,R,I,J and H passbands of Bessell (1990) and Bessell & Brett (1988).

That the ejecta stay more ionized for longer in the detailed ionization description has a direct influence on the spectra at late times. This is illustrated in Figure 5.5 which shows spectra for 15, 20, 40 and 60 days after the explosion for the simple and detailed ionization treatments. While there are no differences up to about maximum light in B band at 20 days, the spectra calculated using the detailed ionization treatment are significantly bluer at late times. This is because they still have more Fe II contribution relative to Fe I than the spectra using the simple ionization treatment (Fe II has bluer lines). The simple ionization treatment shifts more flux into the red and NIR leading to a strong Fe I emission feature at 60 days which is not seen in observations.

The same effect influences the broad band light curves calculated using the simple and detailed ionization treatment which are shown in Figure 5.6. The band passes of Bessell (1990) and Bessell & Brett (1988) are shown in the top panel of Figure 5.5 to clarify the following discussion. Like the spectra, the light curves are rather similar before maximum light in B band at $\sim$ 20 days, with slight differences in the NIR bands. After maximum light there are strong differences. The U, B and V light curves calculated using the simple ionization treatment fade much quicker than those using the detailed ionization treatment. In contrast, R, I, J, H and K stay brighter with J showing a third maximum which is associated with the appearance of the strong Fe I emission feature in the bottom right panel of Figure 5.5 at about 60 days.

Of particular interest is the R band which shows a clear secondary maximum using the detailed ionization treatment but only a slight plateau using the simple ionization treatment. As pointed out by Kasen (2006), the secondary maximum forms when the zone in which doubly ionized iron-group elements recombine hits the inner iron-rich core. It is then that the redistribution of flux from the UV and blue part of the spectrum into the red and NIR by fluorescence is most effective. This argumentation is confirmed and explains the differences in the R-band light curve between the simple and the detailed ionization treatment. In the right panels of Figure 5.2, which shows the ionization fractions of iron as a function of time at the outer edge of the iron-rich inner core, we see that for the simple ionization treatment (top panel) the transition from Fe III to Fe II happens at $\sim$ 33 days while it occurs at $\sim$ 36 days in the detailed ionization treatment. These times correspond to the times of the secondary maximum of the R-band light curve in Figure 5.6. Thus, with the simple ionization treatment, the secondary maximum is blended in the first peak such that it is not clearly evident in the light curves.

Taking into account all the effects which have been discussed in this section we conclude that a detailed treatment of ionization, consistent with the properties of the radiation field, has an important influence and is needed to obtain reliable broad-band light curves and spectra after maximum light. In particular, we note that the colour evolution obtained from calculations using a simple LTE description of ionization is subject to strong uncertainties.

5.1.2 Influence of atomic data

As already mentioned, the vast number of line transitions associated with the iron-group elements are the main contributors to the opacity. Furthermore the lines provide an efficient way to redistribute radiation from the ultraviolet and blue part of the spectrum into the red and NIR by fluorescence (Pinto & Eastman 2000b). This is illustrated in Figure 5.7 which shows, for 20 days after explosion, the wavelength at which escaping photon packets were emitted versus the wavelength at which the same packets had been last absorbed prior to escape (using atomic dataset cd23_gf-5 and the detailed ionization treatment). It shows that many absorptions in the UV are followed by emission in the red and NIR, but also that the reverse process happens too (see discussion by

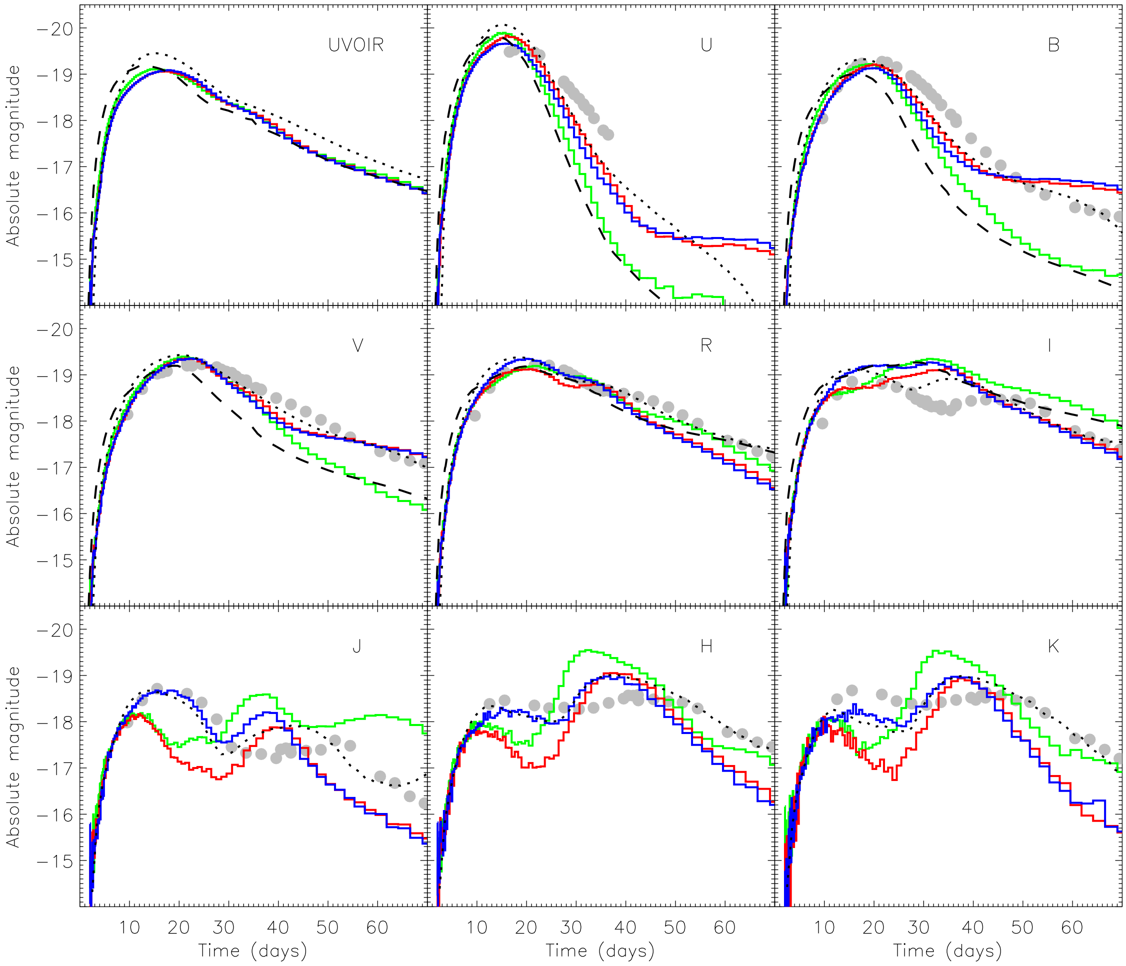

Figure 5.6: UVOIR bolometric and U,B,V,R,I,J,H,K light curves for the W7 explosion model. The green/red lines are the light curves obtained with the simple/detailed ionization treatment and atomic dataset cd23_gf-5. The blue lines are calculated with the detailed ionization treatment and atomic dataset big_gf-4. The small fluctuations e.g. in the U light curve of the simple ionization treatment and the NIR light curves are due to Monte Carlo noise. For comparison observations of SN 2001el (Krisciunas et al. 2003) are overplotted as grey circles assuming a distance modulus of 31.54 and the reddening law of Cardelli et al. (1989) with $A_V = 0.5$ and $R_V = 3.1$. Furthermore W7 light curves obtained with the Monte Carlo radiative transfer code SEDONA (Kasen priv. comm.; UVOIR,U,B,V,R,I,J,H,K dotted lines) and the radiation hydrodynamics code STELLA (Sorokina priv. comm.; UVOIR,U,B,V,R,I dashed lines) are shown.

Mazzali 2000, Sauer et al. 2008). From the colour coding we see that the iron-group elements are most effective in this redistribution.

Figure 5.8 shows the redistribution at 35 days after the explosion with escaping photon packets binned into a wavelength grid, and indicating how many packets escaped in a bin by its grey shade. Here individual strong lines become visible. The dark dots at $\lambda_{\rm out} \sim 8600\,\text{Å}$ are associated with emission in the Ca II NIR triplet which results from absorption in the Ca II H and K lines at $\lambda_{\rm in} \sim 4000\,\text{Å}$ as well as from resonance scattering in the NIR triplet itself. In a similar way the Si II doublet at $\sim 6355\,\text{Å}$ shows up as a resonance line and in fluorescence with photons absorbed at $\sim 4000\,\text{Å}$. This underlines that a fully detailed treatment of line formation is needed to make

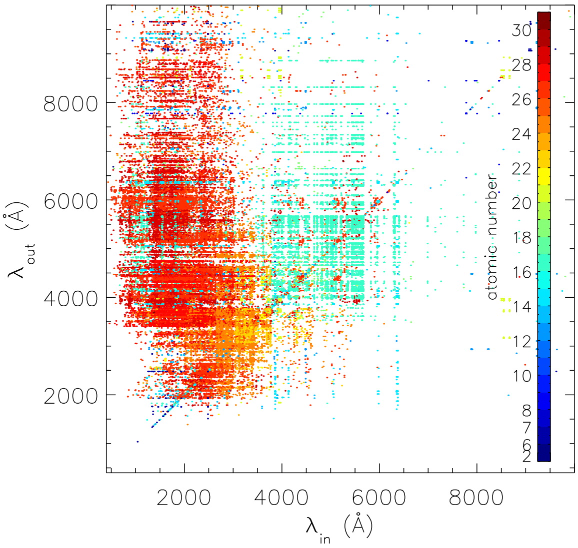

Figure 5.7: Wavelength redistribution in the last line transition of photon packets which escaped at 20 days after the explosion. Each point displays the wavelength of an escaping photon packet versus the wavelength at which the same packet had been absorbed immediately before emission. Thereby a single point can represent multiple photon packets which have undergone the same absorption and emission processes before they escaped. Points on the diagonal line are photon packets which last undergone resonance scattering. Points above (below) that line have been redistributed into the red (blue) by fluorescence (reverse fluorescence). The colour coding shows by which element an escaping photon was last emitted (atomic numbers refer to the colour on top of the number centre) thus indicating that the iron-group elements are most efficient in redistributing flux into the red by fluorescence. The data were extracted from our W7 calculation using the detailed ionization treatment and the cd23_gf-5 model atom.

reliable predictions of individual spectral features and to a lesser extent also for the broad-band light curves. Especially the I-band light curve will be affected since it has a strong contribution from the Ca II NIR triplet (see top panels of Figure 5.5).

To simulate this redistribution properly an atomic dataset as complete as possible is desirable. Unfortunately the simulations become more and more expensive for bigger atomic datasets and the atomic data is not completely known. Thus in the following we study the effect of incomplete atomic data by using datasets of different completeness to calculate the spectral evolution of W7.

We started with the line list of Kurucz & Bell (1995) and tried to reproduce the results of the previous section using atomic datasets with cuts of -2 and -3 in $\log(gf)$ compared to -5 which was used so far (see Table 4.1 for details on the atomic data). The light curves obtained with the -2 cut differ strongly from the previous ones, indicating that lines weaker than -2 in $\log(gf)$ play an important role. With the -3 cut, the light curves in the optical bands are almost identical but there are still some minor differences in the NIR bands. Going further to a -20 cut does not change the results compared to the -5 cut. So the cd23_gf-5 atomic dataset, which was used above, is sufficient to simulate the redistribution which is possible within the line list of Kurucz & Bell (1995).

However, this line list, with its meagre total of $\sim 5 \cdot 10^5$ lines, contains only a tiny fraction of the

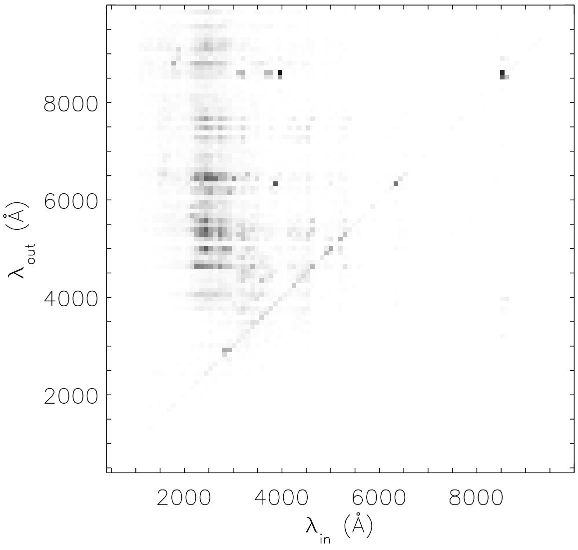

Figure 5.8: Wavelength redistribution in the last line transition of photon packets which escaped at 35 days after the explosion. The escaping photon packets have been binned into a wavelength grid. The shade of a grid point indicates how many photon packets escaped in this bin (the darker the more packets escaped). Points on the diagonal line are photon packets which last underwent resonance scattering. Points above (below) that line have been redistributed into the red (blue) by fluorescence (reverse fluorescence). The dark dots at $\lambda_{\text{out}} \sim 8600\,\text{Å}$ and $\sim 6300\,\text{Å}$ show the flux redistribution from the Ca II H and K lines into the Ca II NIR triplet and in Si II respectively. The data were extracted from our W7 calculation using the detailed ionization treatment and the cd23_gf-5 model atom.

millions of lines expected of the iron-group elements. As many of these lines are associated with transitions amongst highly excited levels, this line list lacks especially lines in the red and NIR parts of the spectrum. It was pointed out by Kasen et al. (2006) and Kasen (2006) that these missing lines are crucial to obtain light curves in good agreement with observations, especially in the NIR. To study this, we use atomic dataset big_gf-4 (for details see Table 4.1 and Section 4.6) which includes atomic data for Fe II, Fe III, Co II, Co III, Ni II and Ni III from more modern theoretical computations, increasing the number of lines by a factor of ~ 20 compared to the cd23_gf-5 atomic dataset.

The bolometric and broad-band light curves obtained for the W7 model using the detailed ionization treatment and atomic dataset big_gf-4 are shown by the blue line in Figure 5.6. UVOIR bolometric and the U, B and V light curves are not strongly affected. In contrast, the enhanced redistribution of flux from the UV and blue to the red and NIR at early times, which can be seen comparing the red and blue curves in the top panels of Figure 5.5, increases the first peak in the R, I, J, H and K bands and causes strong differences for $t \lesssim 40$ days. As a consequence of this redistribution, the U- and B-band light curves using the big_gf-4 atomic dataset are slightly dimmer between ~ 10 and ~ 40 days than those using the cd23_gf-5 atomic dataset. At later times, the light curves are very similar.

The increase in the magnitude of the primary peak in the NIR brings the model light curves to better agreement with observations. The distinct secondary maximum which is present in the R-band light curve using the cd23_gf-5 atomic dataset changes – as it is observed – to a shoulder using atomic dataset big_gf-4. However it occurs too early compared to the observations and especially the H and K bands show systematic differences from the observations having secondary peaks brighter than their primary peaks. This could be due to a further lack of atomic data, which might increase the redistribution into the H and K bands. However, calculations with the big_gf-3 atomic dataset (see Table 4.1), which has fewer lines by a factor of ~ 2, do not show significant differences around the first peaks, suggesting that very weak lines are not critical in this. It is possible, however, that the atomic data set in use is still not complete in terms of lines stronger than a -4 cut in $\log(gf)$ – which we cannot exclude – or that more iron-group elements or ions should be included from the comprehensive atomic data set (Kurucz 2006). However memory limitations and computational costs become a severe issue if the atomic data are to be significantly expanded and we note that the small abundances of the other iron-group elements suggest that they are less likely to have a major effect. Alternatively, the explosion model itself may be at fault. In particular in a model where the recombination front from doubly to singly ionized material hits the iron-rich inner core later, the secondary maxima would be dimmer and in better agreement with observations.

5.1.3 Comparison with other codes

We now compare our bolometric and broad-band light curves with those obtained with other radiative transfer codes for the W7 model. We start with the light curves from the multi-energy group radiation hydrodynamics code STELLA (Blinnikov et al. 2006) which treats the line opacity in the expansion opacity formalism (Karp et al. 1977, Friend & Castor 1983, Eastman & Pinto 1993). E. Sorokina (priv. comm.) provided us with bolometric, U, B, V, R and I light curves calculated with an updated version of this code using a line list of $\sim 1.6 \cdot 10^5$ lines. In this approach, matter is treated in LTE and redistribution is modeled using an approximate source function. The light curves are shown in Figure 5.6: aside from having earlier peaks, even in bolometric light, these light curves are very similar to our light curves calculated in the simple ionization treatment with atomic dataset cd23_gf-5. This is not surprising since our simple ionization description is appropriate for LTE and the atomic data sets are of comparable size. The obvious difference around the first peak in the I band, which is dominated by the Ca II NIR triplet, is most likely due to our more complete treatment of fluorescence. Compared to our detailed ionization treatment the same remarks as made in Section 5.1.1 apply.

We also show light curves obtained with the 3D Monte Carlo radiative transfer code SEDONA (Kasen et al. 2006). SEDONA uses the expansion opacity formalism but is capable of treating fluorescence with a more sophisticated approximation for a subset of lines using a downward-branching scheme. When a photon is absorbed by a line treated in the expansion opacity formalism a two-level atom (TLA) approximation is used and the photon undergoes coherent scattering with probability $1-\epsilon$. Otherwise it is absorbed and re-emitted at a wavelength sampled from the local thermal emissivity, thus representing both true absorption and fluorescence. In principle ϵ is a unique parameter for each line, however SEDONA usually uses a common value for all lines (see Kasen et al. 2006 for a discussion). Matter is treated in LTE with the local kinetic temperature being derived from balancing the thermal emissivity with the energy deposition by γ-ray heating and photon absorption recorded during the Monte Carlo simulations. The light curves shown in Figure 5.6 were provided by D. Kasen (priv. comm.) and use a line list of $\sim 10^7$ lines treated in the TLA approximation.

The light curves are in good agreement with our calculations using the big_gf-4 atomic dataset up to maximum light. After maximum light some differences manifest. The SEDONA U and B light curves after 50 days decline faster than ours – this may be because of recombination to the neutral state, which is responsible for the relatively rapid decay of the U and B light curves obtained with our simple ionization treatment (see Section 5.1.1). Note that, despite using LTE conditions to describe the matter state, the SEDONA light curves do not fade as quickly after maximum light as those obtained with STELLA or with our simple ionization treatment (which is equivalent to treating matter in LTE). This is likely to be due to the different manner in which the kinetic temperature is computed by the different codes.

The V-band light curves are almost identical. In the NIR light curves we get remarkably similar results up to ~ 40 days. Afterwards, the SEDONA light curves stay brighter. Since we have seen in Section 5.1.1 that a more complete recombination leads to an increased redistribution of flux into the red and NIR by Fe I and Co I this is presumably due to a more complete recombination compared to our calculation. The strong differences in the I-band light curve are most likely due to the different treatment of line formation. The flux in the I band is dominated by the Ca II NIR triplet for which the SEDONA light curves shown here assume pure scattering ($\epsilon = 0$; see the discussion in Kasen 2006), while we treat the line formation in full detail.

5.2 An ellipsoidal toy model

In this section we use an ellipsoidal toy model to demonstrate the multi-dimensional capabilities of the code and to illustrate the basic effects which large-scale ejecta asymmetries introduce in spectra and light curves. Large-scale asymmetries in the ejecta of SNe Ia are suggested both by observed polarimetry (see Wang & Wheeler 2008 for a review) as well as by theoretical explosion models [e.g. from an off-centre ignition condition (Röpke et al. 2007), a deflagration to detonation transition (Röpke & Niemeyer 2007) or in the gravitationally confined explosion scenario (Plewa et al. 2004)]. We stress that the toy model we employ here is extremely simple and has a much stronger asphericity than the observations or theoretical arguments suggest. However, it is a useful test case for our code which clearly identifies the sense of the effects acting on the spectra and light curves.

5.2.1 The model

Taking the total mass and composition of the W7 model and assuming homologous expansion, we constructed a simple ellipsoidal toy model assuming rotational symmetry about the z-axis. The maximum velocities along the x- and y-axes are set to be only half the maximum velocity ($v_z^{\max} = 27\,500\,\mathrm{km\,s^{-1}}$) along the z-axis, thus giving an axis-ratio of 1:1:2. Within the model, ellipsoidal surfaces are taken as surfaces of constant density and we adopt a density profile

$$\rho(v) \propto \exp\left(\sqrt{v_\mathrm{r}^2 + \left(\frac{v_\mathrm{z}}{2}\right)^2} / v_0\right) \tag{5.1}$$

in cylindrical polar coordinates and $v_0 = 2750\,\mathrm{km\,s^{-1}}$. We assume a stratified composition with three zones. The innermost zone contains all the iron-group material (Sc to Zn) and is surrounded by a zone of intermediate-mass elements (F to Ca). The outermost zone contains the unburned material (He,C,N,O). Inside each zone the relative abundances are homogeneous and kept fixed at their W7 values.

We mapped this model to a 64^3 grid and followed the propagation of $3.2 \cdot 10^7$ energy packets over 100 time steps from 2 to 80 days after the explosion, using the cd23_gf-5 atomic dataset and the detailed ionization treatment. The first 10 time steps have been calculated in the simple ionization treatment to get reliable initial values (see the discussion in Section 4.4.2). To save computational time we make use of our initial grey approximation employing the Thomson parameterization ($\tau_{\mathrm{grey,min}} = 15$, $N_{\mathrm{grey}} = 40$; see Section 4.3.6). Spectra and light curves were obtained by binning the escaping packets in 10 equal solid-angle bins centred around the z-axis.

5.2.2 Spectral evolution

In Figure 5.9 we compare the 2500 to 10 000 Å spectra along the major and minor axes with an angle averaged spectrum for 15 (around maximum light in B band), 25 and 40 days after explosion. In the absorption trough of the P-Cygni feature of the Ca II NIR triplet one clearly sees the different velocity extent along the different axes: viewed down the major axis, the escaping photons see a velocity field twice as large compared to the minor axes such that the absorption troughs extend farther into the blue. In general the spectra along the minor axes show much sharper features than those along the major axis, where the higher velocities cause stronger blending.

Furthermore the total flux observed along the minor axis is larger. This can be understood by a simple geometrical argument. Viewed down the minor axis the cross-section surface of our ellipsoid is twice as big as seen down the major axis. For an opaque ellipsoid of uniform surface brightness, we would expect the same ratio for the flux (i.e. $\Delta M_{\mathrm{geom}} \approx -0.75$ in magnitudes). However, additional effects come into play such that the flux difference between major and minor axis depends on wavelength and time as discussed below.

5.2.3 Broad-band light curves

The broad-band light curves are shown in Figure 5.10. As expected, the light curves observed along the minor axes are always brighter than those observed along the major axis. The viewing-angle effect is always strongest in the bluer bands and after maximum light becomes weaker with time in V and redder bands (see Table 5.1) as the ejecta become optically thin in these parts of the spectrum.

In the U and B bands, which stay optically thick throughout our calculation, this effect remains significant until the latest times of our simulation and the difference $\Delta M = M_{\mathrm{minor}} - M_{\mathrm{major}}$ is even bigger than one would expect from the simple geometrical argument (which would imply $\Delta M_{\mathrm{geom}} \approx -0.75$; see above). This is simply because we do not have an opaque ellipsoid of uniform surface brightness. In fact, Figure 5.11 – which illustrates the region of last emission (RLE) of selected bands at different times – shows that the U-band RLE is concentrated around

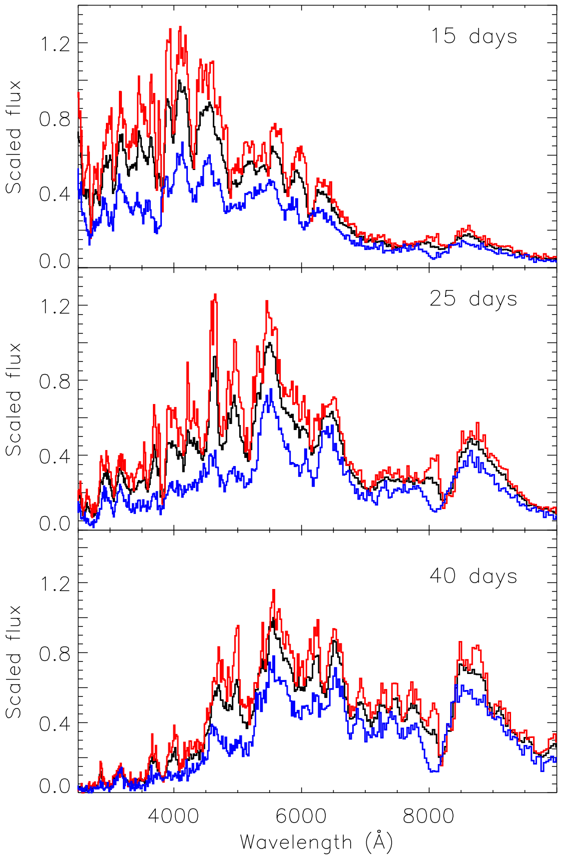

Figure 5.9: Spectra for the ellipsoidal toy model at 15, 25 and 40 days after the explosion (from top to bottom). Blue/red lines are for viewing down the major/minor axis. The black line shows an angle-averaged spectrum for comparison.

Table 5.1: $\Delta M = M_{\rm minor} - M_{\rm major}$ for selected bands in the ellipsoidal model at different times after explosion.

t	15d	22d	29d	35d	42d	49d
$\Delta M(U)$	-0.93	-1.01	-0.92	-0.80	-0.70	-0.87
$\Delta M(V)$	-0.52	-0.65	-0.54	-0.48	-0.45	-0.46
$\Delta M(I)$	-0.42	-0.41	-0.35	-0.36	-0.34	-0.23
$\Delta M(H)$	-0.38	-0.24	-0.22	-0.27	-0.27	-0.19

the equatorial plane which acts to amplify the geometrical effect (as long as the ejecta are optically thick, the direction of escape tends to be peaked normal to the contours of constant density). This concentration is a consequence of the large number of highly optically thick iron-group lines in the UV: U-band photons are more strongly trapped than photons in other bands and therefore tend to preferentially leak out along the equatorial plane where the velocity swept out is smallest.

In contrast, the RLE of V and redder bands do not show a strong enhancement around the equatorial plane. The V-band RLE around maximum light is nearly ellipsoidal, making ΔM close to $\Delta M_{\rm geom}$. At later times, the emission becomes more isotropic as the ejecta become optically thinner (in Figure 5.11 the whole ellipsoid contributes to the RLE) and ΔM decreases. For the I and H band, in which ΔM is always less than $\Delta M_{\rm geom}$, the ejecta are already becoming optically thin around

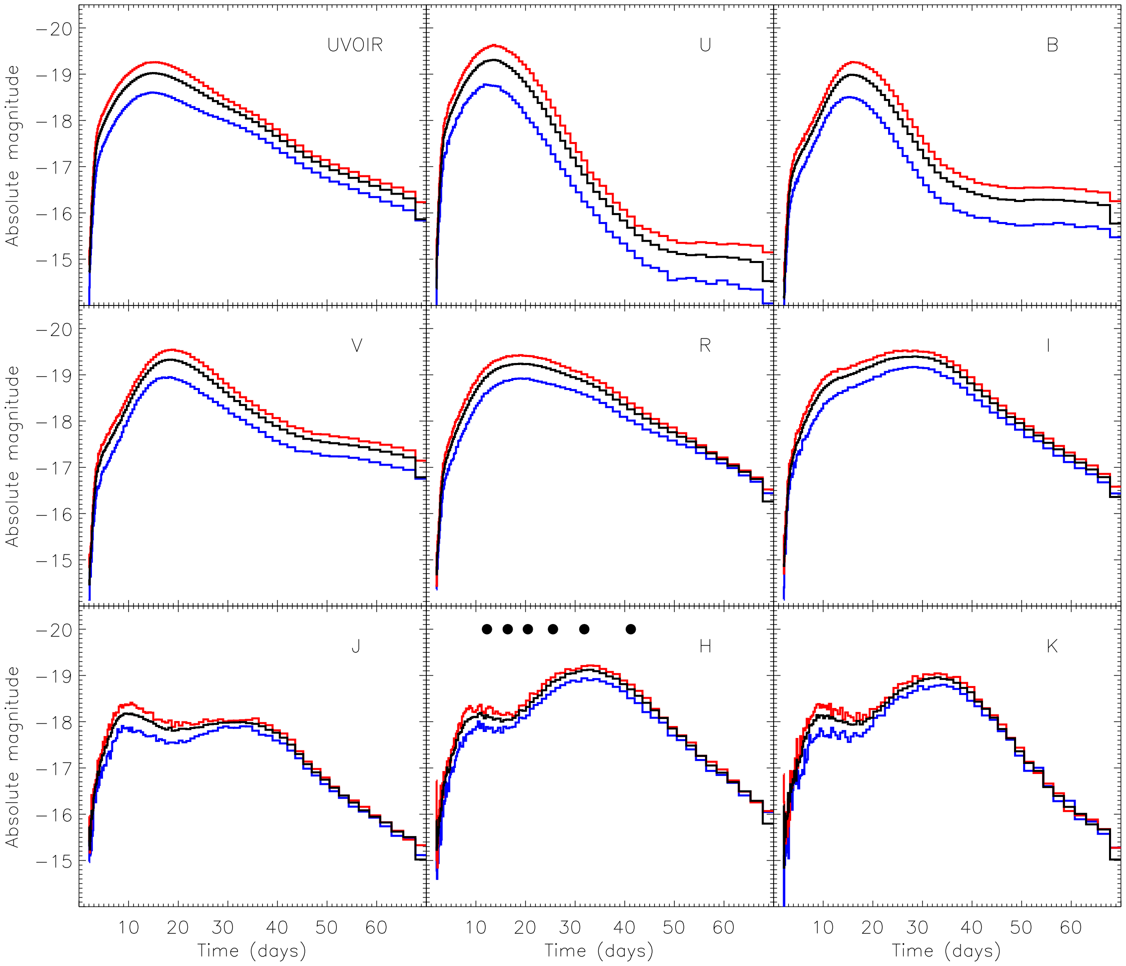

Figure 5.10: UVOIR bolometric and U,B,V,R,I,J,H,K light curves for the ellipsoidal toy model. The blue/red lines are the light curves obtained along the major/minor axis. The black line shows an angle-averaged light curve for comparison. The filled circles in the H-band panel indicate the times for which snapshots of the ionization state of iron are shown in Figure 5.12.

maximum light.

The H-band RLE shows a slight enhancement towards the polar regions around maximum light. This is related to the reduced U-band emission in these regions. The high optical depths for blue and UV photons mean that fluorescence redistributes flux into the NIR where optical depths are lower such that the radiation can escape.

In general the NIR light curves are least viewing-angle dependent, supporting the use of NIR light curves for cosmological distance measurements since less intrinsic scatter would be expected if geometry effects have any role in the observed properties of SNe Ia. However, more detailed studies are needed to investigate this.

The light curves observed along the major axis peak slightly earlier than those observed along the minor axes (see Table 5.2). Furthermore light curves observed along the major axis decline more slowly than those observed along the minor axes (compare the Δm_{15} values in Table 5.2). A similar effect was already found in a study using a grey version of our code by Sim (2007), and we note that it is opposite to the sense of the observed light curve width-luminosity relation.

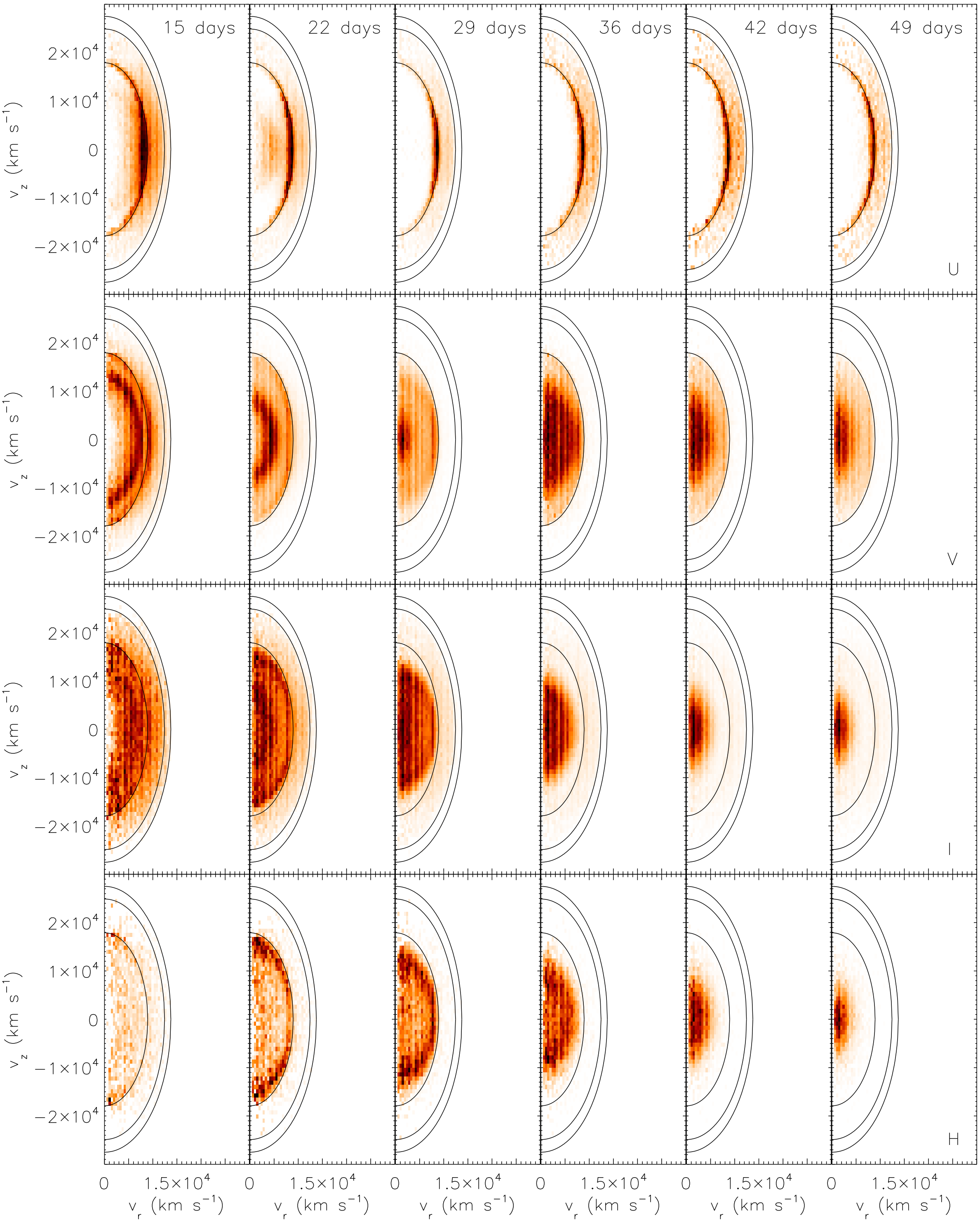

Figure 5.11: Region of last emission for selected bands (U, V, I, H from top to bottom) and different times (from left to right). Dark regions contribute most to the flux escaping in the band. The solid lines indicate the three zones of different composition, with Sc to Zn in the centre surrounded by F to Ca and finally He, C, N and O in the outer zone. The model is symmetric under rotation about the z-axis.

Table 5.2: Peak times and Δm_{15} for selected bands in the ellipsoidal model.

	$t_{\rm max}^{\rm major}$ (d)	$t_{\rm max}^{\rm minor}$ (d)	$\Delta m_{15}^{\rm major}$	$\Delta m_{15}^{\rm minor}$
UVOIR	14.7	15.8	-0.6	-0.9
U	11.8	13.7	-1.7	-1.9
B	15.2	15.8	-1.7	-1.8
V	18.3	19.0	-0.9	-1.1
R	19.0	19.0	-0.5	-0.6

The plot showing the regions of last emission in Figure 5.11 also traces the stratified composition of our model. The U and I bands – which have non-negligible contributions of Ca due to the Ca II H and K lines in U and the Ca II NIR triplet in I – show significant emission from the zone of intermediate-mass elements. In contrast, the RLE in the V and H bands – which are dominated by iron-group elements – is concentrated towards the iron-rich inner core.

5.2.4 Secondary maximum in the NIR bands

As discussed by Kasen (2006), the secondary maximum in the NIR bands forms when the inner iron-rich core recombines from doubly ionized iron-group elements to the singly ionized state. With the singly ionized state becoming dominant, the number of optically thick lines in the blue increases, thus blocking blue radiation very effectively and making the redistribution of flux from the UV and blue part of the spectrum into the red and NIR by fluorescence very effective. Here we discuss this effect for the H-band light curve and show the ionization fractions of Fe II–IV (which we use as a proxy for all iron-group elements) in Figure 5.12 for selected times from near the first peak ($\sim$ 10 days after explosion) to well after the second peak in the H band ($\sim$ 32 days after explosion, compare Figure 5.10).

Around the first peak the iron-rich core consists predominantly of Fe IV. In the very centre there is still a contribution of Fe V (not shown in Figure 5.12) and at the outer edge there is a small region which has already recombined to Fe III. As time passes the ejecta cool and the Fe IV region recedes. At the same time the Fe III region extends further in and a contribution of Fe II starts to build up around the outsides. Recombination occurs first at the poles since they see the least amount of ionizing radiation (compare Figure 5.11). The secondary maximum in the H band occurs at $\sim$ 32 days when the Fe II region first forms a complete elliptical ring (Figure 5.12). This is the point at which the opportunity for fluorescence is maximal. Note that although the ionization fractions vary with position, the NIR bands are sufficiently optically thin that the NIR flux is approximately angle-independent at these epochs (this is apparent from Figure 5.11 where the full ellipsoid is bright). At late times the recombination front moves inwards as the light curves fade until only a small Fe III core remains at the end of our simulation.

Comparing the two different lines-of-sight in Figure 5.10, we see that the local minimum between the first and secondary maximum in the H-band light curve along the polar axis occurs slightly earlier ($\sim$ 15 days) than along the equatorial axes ($\sim$ 18 days). This follows from the earlier recombination from Fe III to Fe II in polar lobes which gives an earlier increase in the redistribution of flux from the UV and blue into the red and NIR.

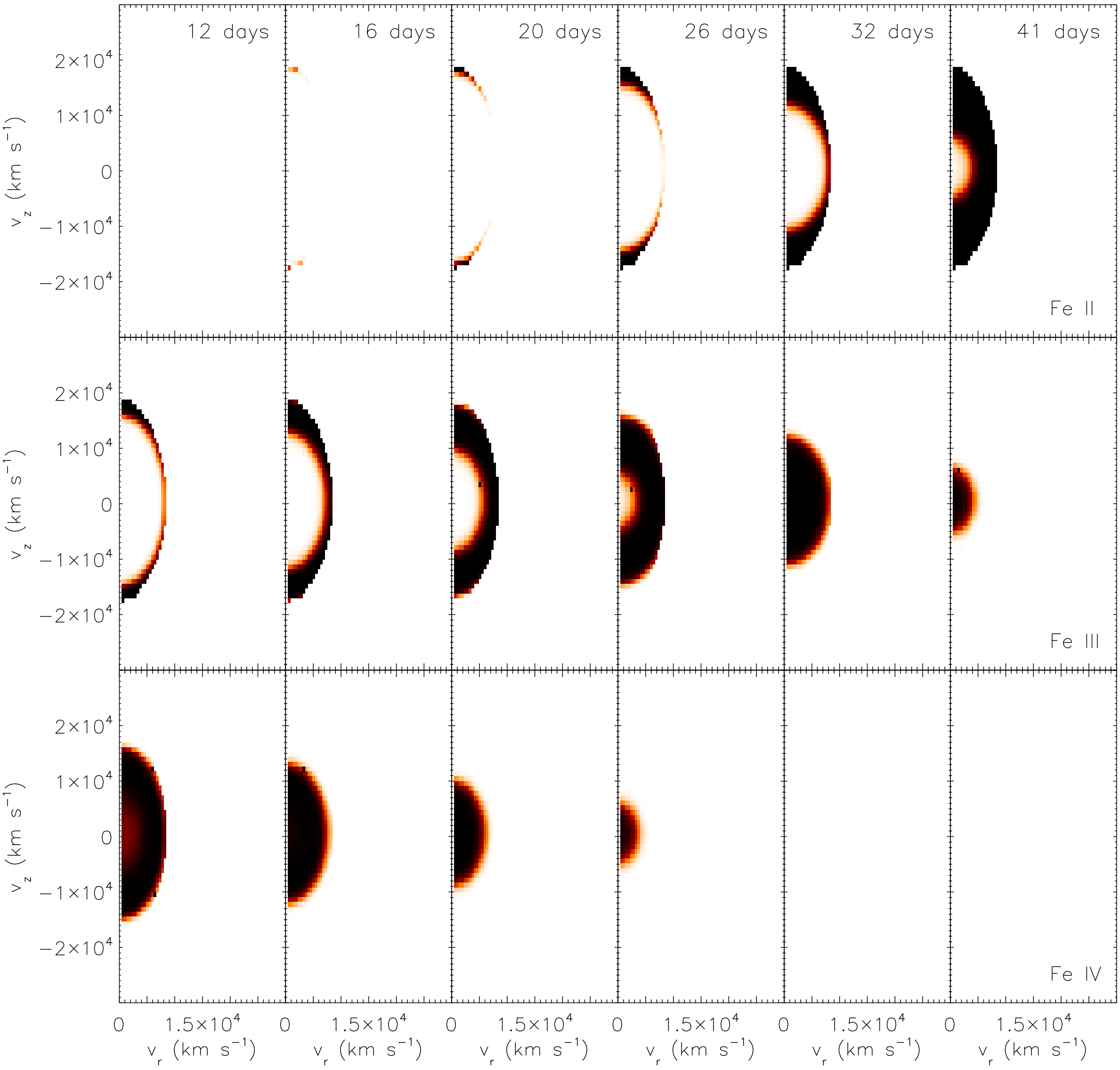

Figure 5.12: Ionization fractions of Fe II, Fe III and Fe IV (from top to bottom) for selected times (from left to right). The corresponding times are marked with filled circles in the *H* band panel of Figure 5.10. Black regions have an ionization fraction of 1. Lower ionization fractions are shown in lighter reddish colours down to white (0) on a linear scale.

Having studied the parameterized 1D deflagration model W7 (Nomoto et al. 1984) we verified the operation of the code and studied the influence of our different prescriptions of the plasma state. Moreover, we quantified basic effects of non-spherical geometry using a toy model. Now, we apply the code to more sophisticated multi-dimensional explosion models.

6 Application to hydrodynamic explosion models

In this chapter we apply our code to derive synthetic observables for hydrodynamical simulations of different explosion models which have been carried out within the supernova group at MPA. Thus we discuss the outcome of different explosion mechanisms (Section 2.4) and progenitor scenarios (Section 2.3) and compare them with observational data. Parts of the discussion in Section 6.2 have been submitted for publication (Pakmor et al. 2009).

6.1 Comparing a deflagration to the faint end of delayed detonations

In Section 2.2 we presented the basic model of SNe Ia as inferred from the observational data. However, progenitor systems and the explosion mechanism are still debated. While the prompt detonation model (Arnett 1969) was ruled out early on due to its lack of intermediate-mass elements, which are responsible for prominent features in observed SNe Ia, there was a long discussion whether the majority of normal SNe Ia originate from the pure deflagration or delayed detonation mechanisms, as discussed in Section 2.4.

Both mechanisms suffer from their own problems. Early deflagration models in 1D and 2D produced too little kinetic energy by nuclear burning, thus failing to gravitationally unbind the WD. With the progress in theoretical modelling in the last decade, however, it was shown that pure deflagration models in 3D are able to disrupt a WD due to turbulence effects – though the total kinetic energy released during the nuclear burning is still small ($0.6 \cdot 10^{51}$ erg, e.g. Röpke et al. 2006) compared to standard SN Ia models ($1.3 \cdot 10^{51}$ erg, Nomoto et al. 1984) . Therefore we believe now that pure deflagrations are unlikely to account for normal or bright SNe Ia. However they might account for some of the fainter objects.

While the energy release is sufficient for delayed detonation models, the transition from the initial deflagration phase to a detonation is still not understood theoretically. However, transitions between different hydrodynamical regimes of turbulent combustion might provide the physical conditions to trigger this transition (Niemeyer & Woosley 1997). From simulations using such an approach to model the deflagration-to-detonation transition it was inferred that the delayed detonation model might account for the majority of SNe Ia (Mazzali et al. 2007, Kasen et al. 2009). Synthesizing 0.3 to $1.1\,\mathrm{M}_\odot$ of ^{56}Ni, the only objects out of reach for this scenario are the really subluminous 1991bg-like objects, for which ^{56}Ni masses of $\sim 0.1\,\mathrm{M}_\odot$ were inferred observationally (Stritzinger et al. 2006).

To assess these conclusions we compare here the outcome of the two different explosion mechanisms and confront them with observations. Therefore we calculate synthetic observables for one of the faintest of the 2D delayed detonation models of Kasen et al. (2009) and a recently completed fully

3D model of a deflagration (Röpke, priv. comm.). Since both models produce similar amounts of ^{56}Ni ($\sim 0.3\,\mathrm{M}_\odot$), this should be a reasonable comparison of signatures of the explosion mechanism. However, we note that the delayed detonation model will suffer from some uncertainty, since first a 2D treatment of turbulence, which is an intrinsically 3D effect, can only be approximate and second the physics of the deflagration-to-detonation transition is still poorly understood (see Section 2.4).

The radiative transfer in both models was simulated over 111 time steps from 2 to 120 days after the explosion, yielding a width of $\Delta \ln(t) = 0.037$ for the individual time steps. Using our detailed ionization treatment and the cd23_gf-5 atomic data set, we propagated $20 \cdot 10^6$ packets for the delayed detonation model and $4 \cdot 10^6$ packets for the deflagration model. To speed up the initial phase of the calculation we made use of our initial grey approximation (Section 4.3.6) employing the Thomson parameterization for the delayed detonation model ($\tau_{\mathrm{grey,min}} = 15$, $N_{\mathrm{grey}} = 40$) and the parameterized grey opacity for the deflagration model ($\tau_{\mathrm{grey,min}} = 400$, $N_{\mathrm{grey}} = 30$). The first ten time steps were treated in LTE.

For the delayed detonation model, we took the tracer particles from the hydrodynamics simulation, which was extended up to the phase of homologous expansion, and mapped their final density structure to a 80×160 grid. Together with the nucleosynthesis yields from a post-processing calculation as described by Travaglio et al. (2004), this yields the input model. For the radiative transfer simulation this 2D model is re-mapped to a 3D Cartesian grid of size 100^3 which co-expands with the ejecta. For the 3D deflagration model, we mapped the final density structure of the hydrodynamics simulation and the nucleosynthesis yields to a 25^3 grid. Due to this low resolution the calculation for the deflagration model is still preliminary. Based on our experience with other models, however, we conclude that this most likely causes quantitative but no qualitative differences. Thus a qualitative comparison between the two models, which is the scope of this section, will be possible.

The low resolution of the 3D model is mainly due to the enormous amount of runtime a higher resolved simulation would require. This scales with the number of physically different cells in a calculation, since we need to increase the number of simulated packets to obtain a sufficient signal-to-noise ratio in the estimates for the radiation field quantities in each grid cell. Although the 2D delayed detonation model is carried out on a much higher resolved 3D grid compared to the deflagration, the number of physically different cells is smaller even for our current low resolution (12 800 different cells for the delayed detonation model vs. 15 625 for the deflagration). For a 100^3 version of the 3D model the difference increases by about two orders of magnitude. Such a simulation is feasible but very expensive. The delayed-detonation model ran for four days on 8192 cores of the BlueGene/P system at the Rechenzentrum Garching (RZG) of the Max-Planck-Gesellschaft. Thus a comparable run of the 3D model would be at least ten times more expensive. Although this is finally achievable, we only want to perform such a calculation once for a carefully selected set of models. Having currently only one up-to-date 3D hydro model of a deflagration available, this state has not yet been reached.

A plot illustrating the different composition structure of the delayed detonation and deflagration models is shown in Figure 6.1. The most obvious difference between the two models is their different extent in velocity space ($37\,125\,\mathrm{km\,s^{-1}}$ for the delayed detonation model vs. $14\,950\,\mathrm{km\,s^{-1}}$ for the deflagration model). This is a result of the different degree to which nuclear burning takes place

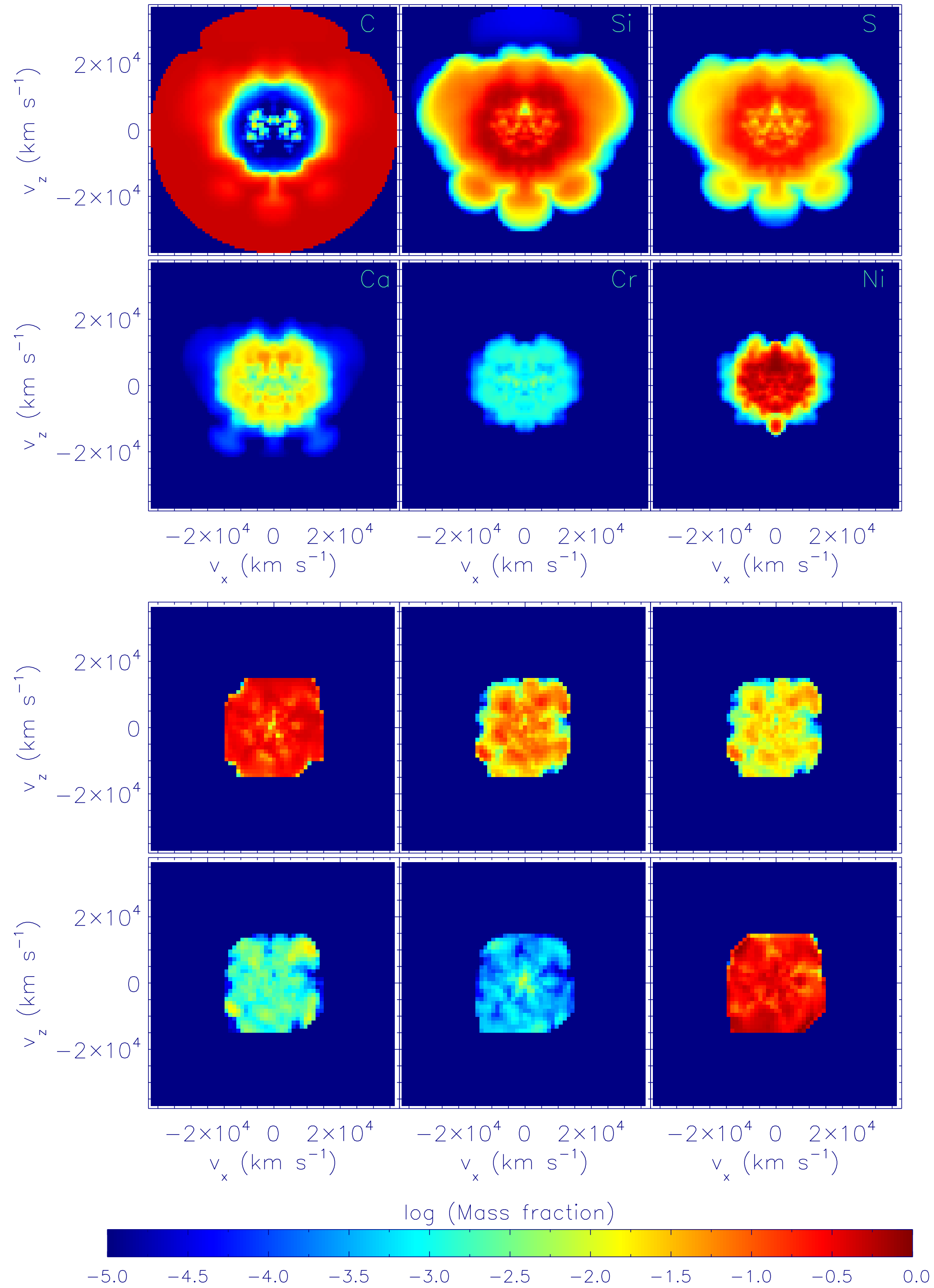

Figure 6.1: Comparison of the final composition structure of the delayed detonation (top) and the pure deflagration model (bottom). Shown are slices along the midplane of the simulation volume. The delayed detonation model is radially symmetric about the z-axis. The individual panels show the mass fractions of C, Si, S, Ca, Cr and Ni (from top left to bottom right, respectively).

in the models. While both produce similar amounts of iron-group material, the delayed detonation produces much more intermediate-mass elements than the deflagration model where a large part of the carbon-oxygen fuel is left unburned (Table 6.1). Thus, less energy is released during the burning phase and the kinetic energy of the ejecta is lower. Moreover, realizing that iron-group material is distributed up to the highest velocities for the deflagration model, we see that mixing by hydrodynamical instabilities is more effective in this model. This is also visible in the composition structure of the other elements. While showing a layered structure in the delayed detonation model, the deflagration model is characterized by small scale "blobby" features which are distributed over the entire velocity space of the model.

Table 6.1: Nucleosynthesis yields of the delayed detonation and deflagration model. Given are the total masses per species in units of the solar mass. The total mass in both models equals the Chandrasekhar limit.

	delayed detonation	deflagration
He	$1.1 \cdot 10^{-3}$	$1.8 \cdot 10^{-4}$
Li	$3.5 \cdot 10^{-18}$	0
Be	$1.3 \cdot 10^{-20}$	0
B	$9.6 \cdot 10^{-13}$	0
C	$1.3 \cdot 10^{-2}$	$3.2 \cdot 10^{-1}$
N	$5.2 \cdot 10^{-7}$	$8.3 \cdot 10^{-6}$
O	$1.9 \cdot 10^{-1}$	$4.0 \cdot 10^{-1}$
F	$1.5 \cdot 10^{-9}$	0
Ne	$7.1 \cdot 10^{-3}$	$3.1 \cdot 10^{-2}$
Na	$1.6 \cdot 10^{-4}$	$2.7 \cdot 10^{-4}$
Mg	$2.5 \cdot 10^{-2}$	$1.8 \cdot 10^{-2}$
Al	$1.5 \cdot 10^{-3}$	$1.2 \cdot 10^{-3}$
Si	$3.8 \cdot 10^{-1}$	$8.0 \cdot 10^{-2}$
P	$7.0 \cdot 10^{-4}$	$4.3 \cdot 10^{-4}$
S	$1.6 \cdot 10^{-1}$	$2.6 \cdot 10^{-2}$
Cl	$2.1 \cdot 10^{-4}$	$7.5 \cdot 10^{-5}$
Ar	$2.4 \cdot 10^{-2}$	$3.9 \cdot 10^{-3}$
K	$1.6 \cdot 10^{-4}$	$2.4 \cdot 10^{-5}$
Ca	$1.5 \cdot 10^{-2}$	$2.8 \cdot 10^{-3}$
Sc	$1.1 \cdot 10^{-7}$	$6.3 \cdot 10^{-13}$
Ti	$4.2 \cdot 10^{-5}$	$6.8 \cdot 10^{-6}$
V	$8.4 \cdot 10^{-6}$	$1.6 \cdot 10^{-6}$
Cr	$1.6 \cdot 10^{-3}$	$1.1 \cdot 10^{-3}$
Mn	$8.6 \cdot 10^{-4}$	$6.7 \cdot 10^{-4}$
Fe	$1.3 \cdot 10^{-1}$	$1.3 \cdot 10^{-1}$
Co	$6.2 \cdot 10^{-3}$	$9.2 \cdot 10^{-3}$
Ni	$4.5 \cdot 10^{-1}$	$3.9 \cdot 10^{-1}$
Cu	$6.8 \cdot 10^{-4}$	$8.8 \cdot 10^{-5}$
Zn	$1.3 \cdot 10^{-3}$	$1.5 \cdot 10^{-4}$

6.1.1 Spectral evolution

To start our discussion of the two models, we compare their spectral evolution at three epochs shown in Figure 6.2 and 6.3, respectively. Again we make use of the additional information which the escaping Monte Carlo packets provide on their last interaction (not counting electron scattering) before leaving the grid. The region below the synthetic spectrum is colour coded to indicate the fraction of escaping quanta in each wavelength bin which were last emitted by line transitions of a particular element. Similarly, the coloured regions above the spectra indicate which elements were last responsible for removing quanta from the wavelength bin (either by absorption or scattering/fluorescence). First we note that the early spectrum (five days before B-band maximum) of the deflagration model is significantly bluer in terms of the colour of the radiation field. Moreover, it looks almost like a featureless continuum rather than a Type Ia spectrum. This is still true at five days after maximum, though to a lesser extent and the spectra of the two models become more similar at later times.

Our colour coding largely helps us understanding the origin of these differences. For the deflagration model the iron-group elements (indicated by red and yellowish colours) contribute significantly to the emerging flux at all times, while this is only true for late times in the delayed detonation model. This is due to the strong mixing in the deflagration model which distributes iron-group elements up to the outermost layers (compare Figure 6.1). As a result the wealth of densely-spaced lines associated with the iron-group elements in the blue wavelength range can be seen directly at early times when the ejecta are still hot. This explains both the blue character of the radiation field and the continuum like shape.

Another difference concerns the lack of strong absorption features of intermediate-mass elements in the deflagration model (there is almost no absorption in the characteristic Si II doublet at $\lambda\lambda 6347, 6371$). In contrast, we see strong contributions from unburned material (carbon and oxygen, dark blue colours), which are neither present in the delayed detonation model nor in the spectra of normal SNe Ia. Although this might be related to the mixing to some extent, it is mainly a consequence of the different nucleosynthesis yields of the two models (Table 6.1). While the iron-group yields are comparable, silicon and sulphur are about a factor 5 less abundant in the deflagration model and carbon is ~ 20 times more abundant.

Leaving more material unburned, the energy release of the deflagration model is much smaller compared to the delayed detonation model. This clearly shows up in the different velocity extent of the models in Figure 6.1 and can also be seen in the different line shifts of absorption features in the spectra. Thus we find the blue edge of the absorption trough associated with the Ca II NIR triplet (gf-weighted mean 8549 Å) for the spectra 20 days after B-band maximum at 8000 Å for the delayed detonation model (indicating a velocity of $\sim 19\,260\,\mathrm{km\,s^{-1}}$), while it occurs at 8200 Å ($\sim 12\,250\,\mathrm{km\,s^{-1}}$) for the deflagration model. In contrast, the features associated with the iron-group elements appear at similar wavelengths. In the delayed detonation model iron-group elements occur only in the core which has about the same extent in velocity space as the full deflagration model (Figure 6.1). Thus the similar line velocities are not surprising.

6.1.2 Broad-band light curves

As a next step we compare the broad-band light curves of the two models in Figure 6.4. There we show light curves as seen from ten equally-sized solid-angle bins with respect to the polar (z) axis. Each polar bin averages over ten azimuth bins. First we note, that the deflagration model is generally dimmer than the delayed detonation model and its light curves rise somewhat faster (14 days compared to 17.5 days for the angle-averaged B-band light curves). The lower peak magnitudes of the deflagration model are due to the slightly lower amount of ^{56}Ni synthesized in that model ($0.313\,\mathrm{M}_\odot$ vs. $0.342\,\mathrm{M}_\odot$). The faster rise is due to the strong mixing in the deflagration model,

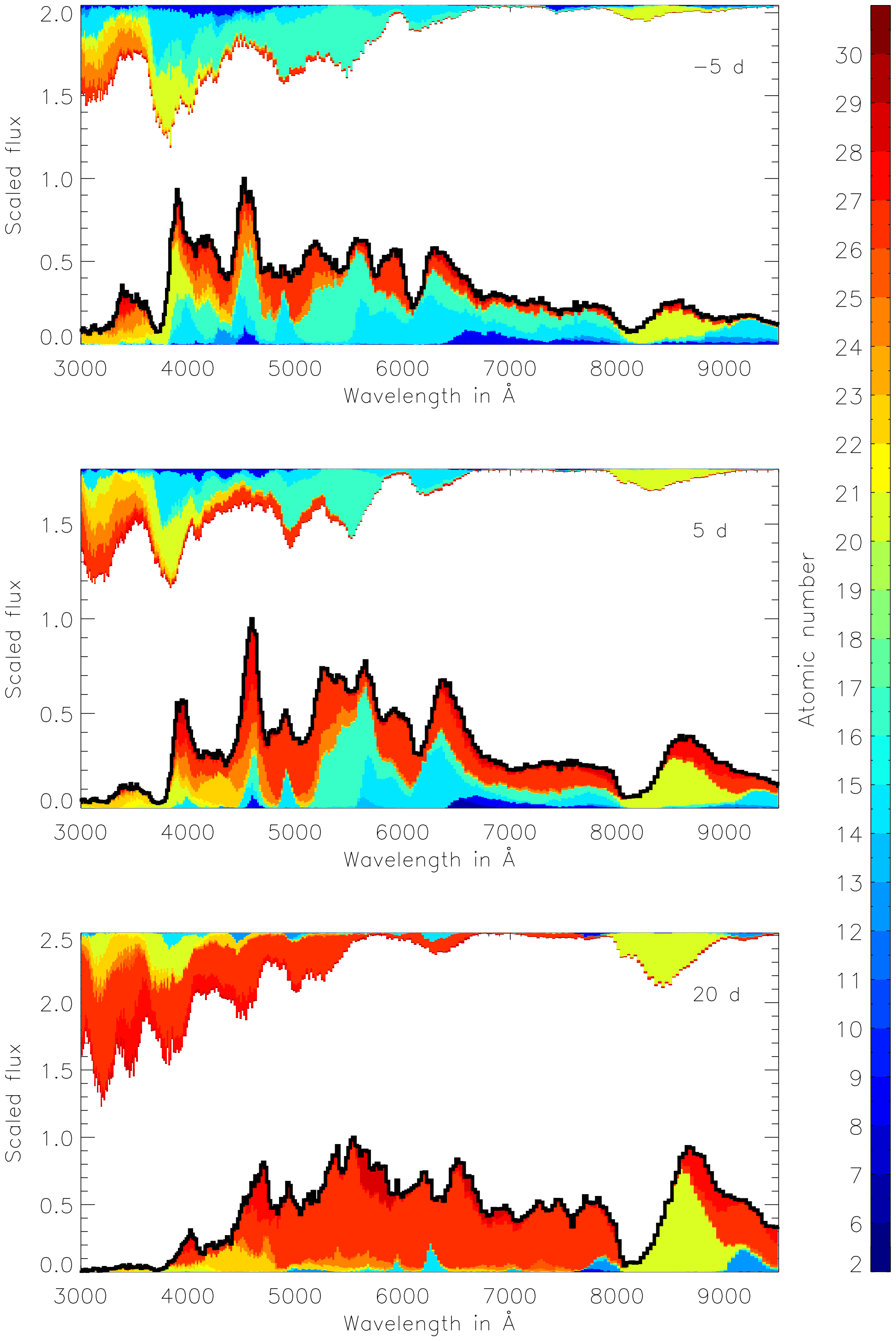

Figure 6.2: Angle-averaged synthetic spectrum (thick black line) for the delayed detonation model at −5 (top panel), 5 (middle panel) and 20 days (bottom panel) relative to B-band maximum. The colour coding indicates the element(s) responsible for both bound-bound emission and absorption of quanta in the Monte Carlo simulation. The region below the synthetic spectrum is colour coded to indicate the fraction of escaping quanta in each wavelength bin which last interacted with a particular element (the associated atomic numbers are illustrated in the colour bar). Similarly, the coloured regions above the spectra indicate which elements were last responsible for removing quanta from the wavelength bin (either by absorption or scattering/fluorescence).

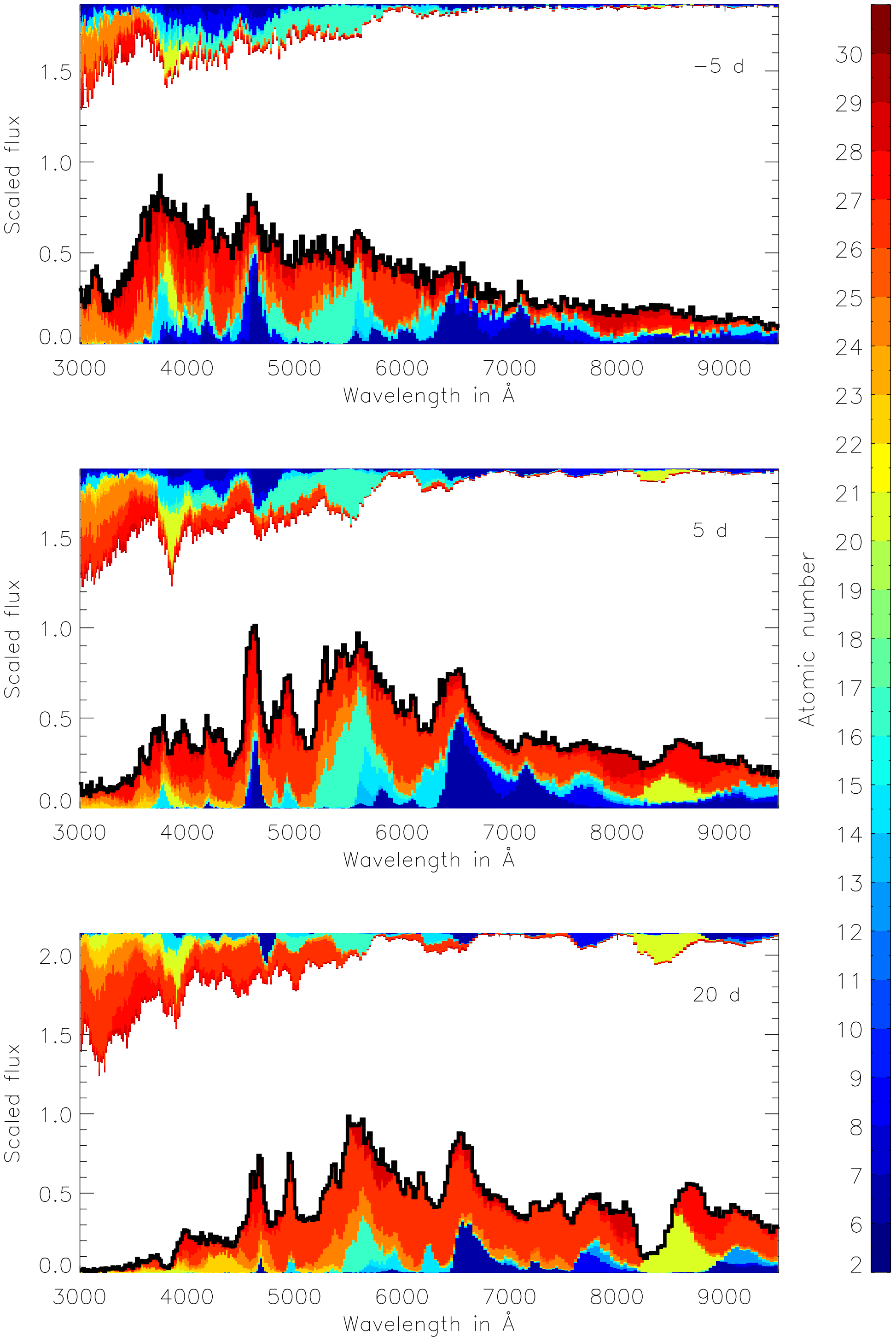

Figure 6.3: Angle-averaged synthetic spectrum (thick black line) for the deflagration model at −5 (top panel), 5 (middle panel) and 20 days (bottom panel) relative to B-band maximum. For an explanation of the colour coding see the caption of Figure 6.2. The strong carbon emissions are balanced by absorptions at shorter wavelengths.

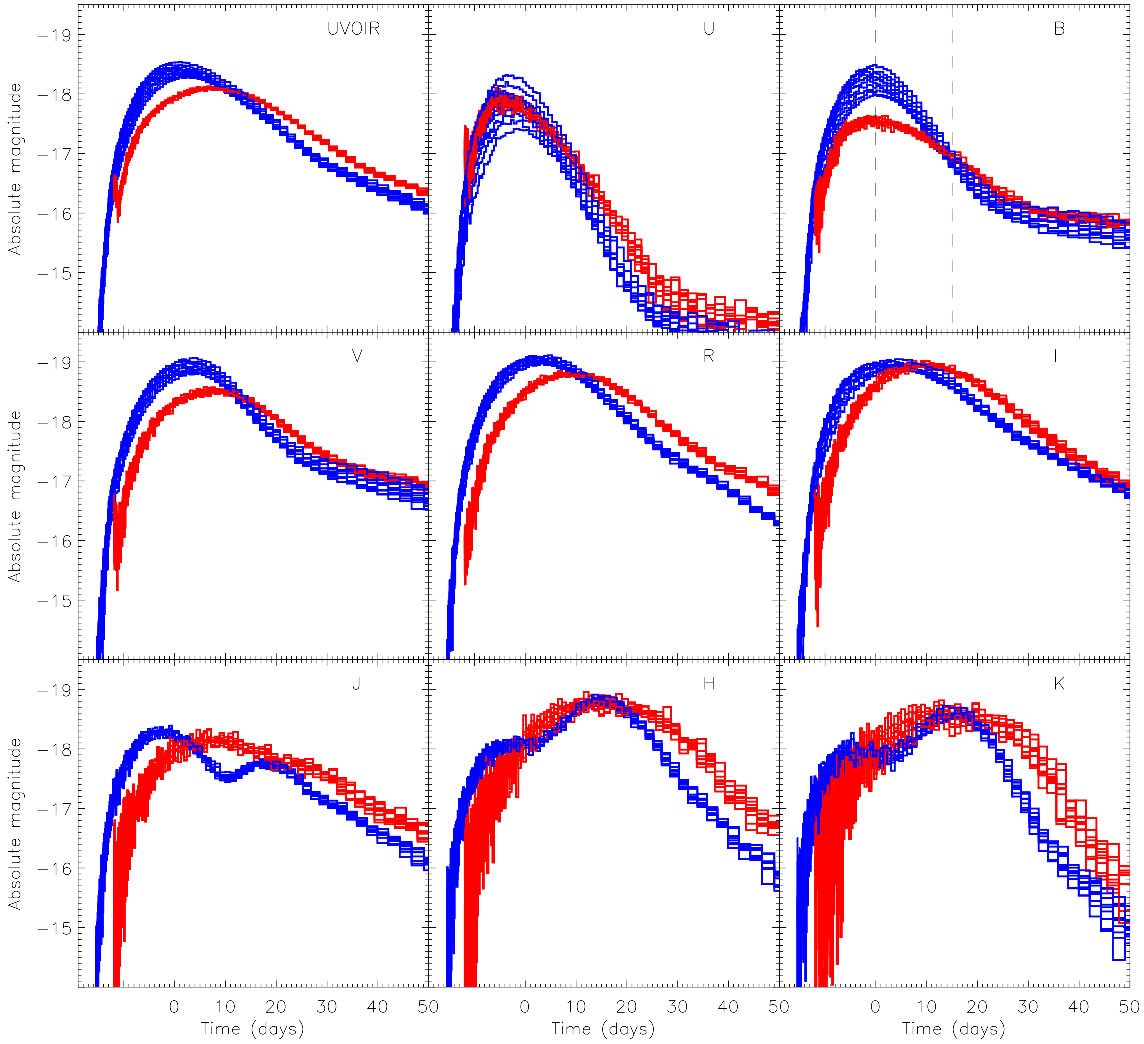

Figure 6.4: Comparison of the broad-band light curves derived for the delayed detonation model (blue) and the deflagration model (red). The ten lines in each panel correspond to the light curves seen from ten equally-sized solid-angle bins in the polar angle θ. Each polar bin averages over ten azimuth angle bins. The different panels correspond to the different broad-band filters as indicated. For the B band we show vertical lines at maximum and 15 days after to indicate $\Delta m_{15}\,(B)$. The small scale fluctuations of the light curves are due to Monte Carlo noise. Due to the lower number of packets this becomes particularly visible for the deflagration model.

which distributes ^{56}Ni up to the outermost layers (Figure 6.1). Thus decay energy is deposited not only in the core but also below the surface and it becomes easier for radiation to escape at early times. Together with our initial grey approximation this leads to the initial spike visible in the UVOIR, U and V light curves for the deflagration model in Figure 6.4. However, the amount of energy which escapes in that spike is very small and does not influence the later behaviour of the light curves significantly.

Concerning the decline of the light curves, the deflagration model [$\Delta m_{15}\,(B) \sim 0.5$] is much slower than the typical values in SNe Ia. Even the slowest decliners which are about two magnitudes brighter than our model, decline significantly faster [$\Delta m_{15}\,(B) \sim 0.65$ SN 2009dc, Yamanaka et al. 2009; $\Delta m_{15}\,(B) \sim 0.69$ SN 2006gz, Hicken et al. 2007]. This is most likely another consequence of the strong mixing in the deflagration model. Distributing iron-group elements up to the highest velocities leads to higher opacities in the outer layers which are usually dominated by intermediate-mass elements. Thus radiation originating from deeper layers is trapped for longer. In contrast, the delayed detonation model covers the range of spectroscopically normal SNe Ia [$\Delta m_{15}(B) \sim 1..1.5$]. However its peak magnitudes are too faint and its spectral behaviour does not fit to spectroscopically normal SNe Ia (see next section).

Looking at the UVOIR bolometric and U, B, V, R and I light curves, it becomes obvious that the spread due to asymmetries of the model is larger in the delayed detonation model than in the deflagration model ($\sim 1\,\mathrm{mag}$ vs. $\sim 0.4\,\mathrm{mag}$ at U-band maximum). We do not discuss the J, H, and K light curves here, since they suffer from large Monte Carlo noise particularly for the deflagration model. This makes it impossible to derive the actual scatter from the current simulation in these bands. Increasing the number of simulated packets will solve this problem. However, we did not want to do this with the current version of the model which is still preliminary for the reasons discussed at the beginning of this section.

Finding a larger spread in the light curves of the delayed detonation model is somewhat surprising. Since the turbulent mixing in deflagrations is much stronger than in delayed detonations (leading to the “blobby” structure seen in Figure 6.1) one would have expected that the deflagration model is more sensitive to geometry effects. Instead, it turns out that the turbulent mixing which occurs at rather small angular scales does not affect the observational display strongly, while the deflagration-to-detonation transition can introduce asymmetries on the largest scales in the delayed detonation model (Figure 6.1) which are observable. In both models the (initial) deflagration is ignited stochastically in several sparks distributed isotropically in a spherical bubble around the centre-of-mass of the progenitor WD. In general, asymmetric ignition conditions would provide an additional way to produce large scale asymmetries of the ejecta which give rise to observable effects (Sim et al. 2007).

A peculiarity of the light curves of the deflagration model concerns their peaking behaviour. While normal SNe Ia and the delayed detonation model show double peaked light curves in the NIR bands with first peaks before B-band maximum, the deflagration model shows singly peaked NIR light curves which peak well after B-band maximum. Moreover the V-, R- and I-band peaks of the deflagration model appear significantly later compared to B-band maximum than in the delayed detonation model.

This is related to the different rise times in the two models. Taking ~ 17.5 days to B band maximum for the delayed detonation model, the ejecta have already cooled sufficiently that the iron-rich core starts to recombine from Fe IV to Fe III around B-band maximum at its outer layers (Figure 6.5). As pointed out by Kasen (2006), the redistribution of flux from the UV and blue part of the spectrum into the red and NIR by fluorescence is particularly effective in such recombination regions. Since the opacity is generally less in the NIR this redistributed radiation can escape easily leading to an increased flux in these bands (see the bottom panels of Figure 6.5 which show the energy emitted in the J band during the corresponding time step and where the escaping photons have last interacted with a line). A secondary increase in the energy escaping in the J band occurs when the iron-rich core starts to recombine from Fe III to Fe II around 20 days after B-band maximum. This leads to the pronounced secondary maximum in the J-band light curve of the delayed detonation model at

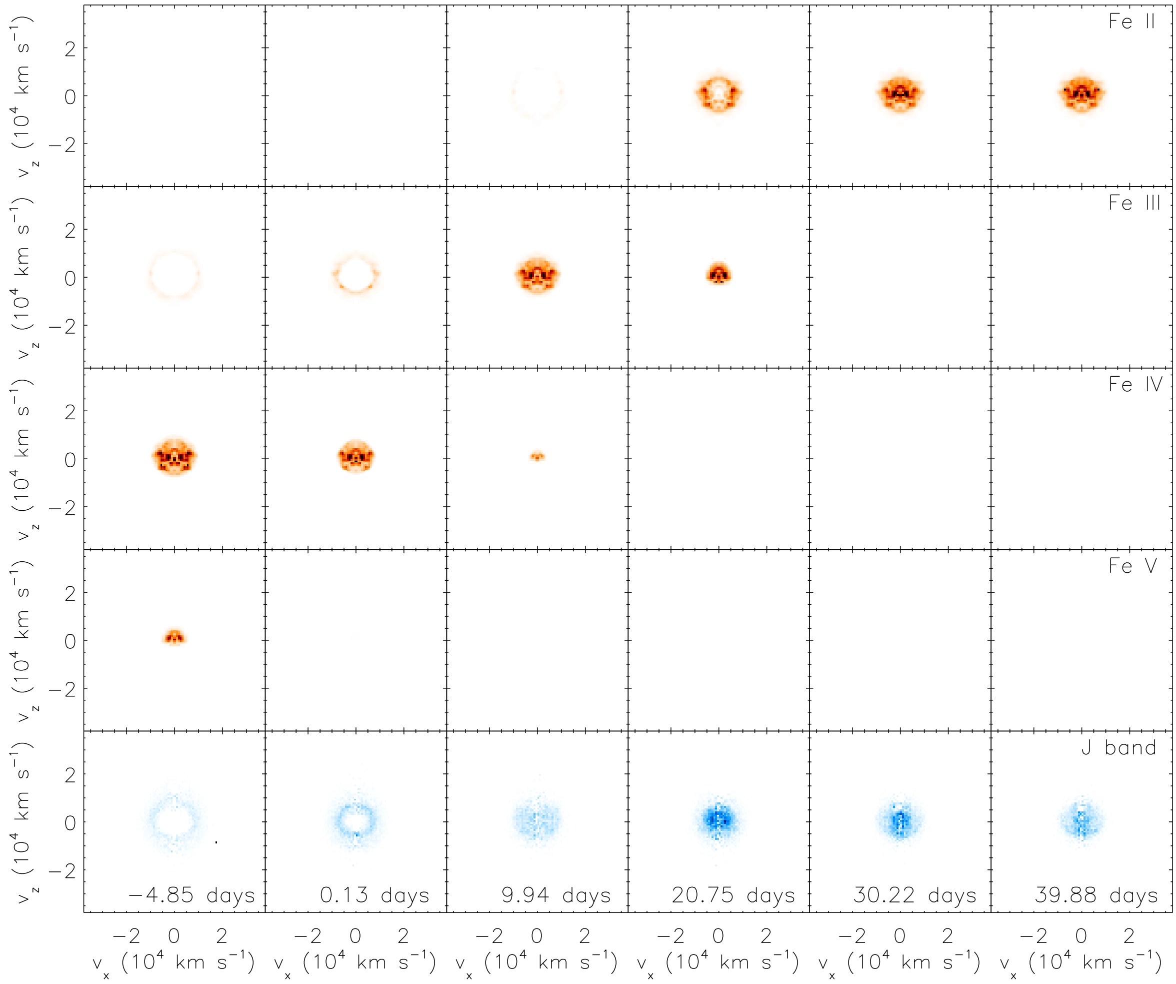

Figure 6.5: Snapshots (from left to right) showing the total population numbers of Fe II, III, IV and V (top four panels in reddish colours, darker regions have higher population) and the *J*-band regions of last emission (bottom panels in bluish colours) in the delayed detonation model at different times as indicated in the bottom panels. The model is rotationally symmetric about the *z*-axis. Iron never recombines fully during the time span considered in our simulations. The colour coding of the regions of last emission indicates the energy escaping from a grid cell during the corresponding time step.

this time.

In contrast, the deflagration model is still dominated by Fe V and Fe IV (Figure 6.6) at *B*-band maximum, which occurs ~ 3.5 days earlier than in the delayed detonation model due to the mixing of ^{56}Ni rich material up to the outermost layers (see the discussion at the beginning of this section). Accordingly the energy escaping in the *J* band is still negligible. The recombination from Fe IV to Fe III sets in at ~ 10 days after *B*-band maximum which is also about the time at which the *J*-band light curve reaches its maximum. When the subsequent recombination from Fe III to Fe II occurs at ~ 30 days after *B*-band maximum, most of the radioactive nuclides powering the light curve have already decayed, such that the enhanced energy escape does not lead to a distinct secondary maximum in the *J* band. However, there is a slight indication of a shoulder at that time. The later recombination with respect to *B*-band maximum is also the origin of the delayed maxima in the *V*, *R* and *I* bands.

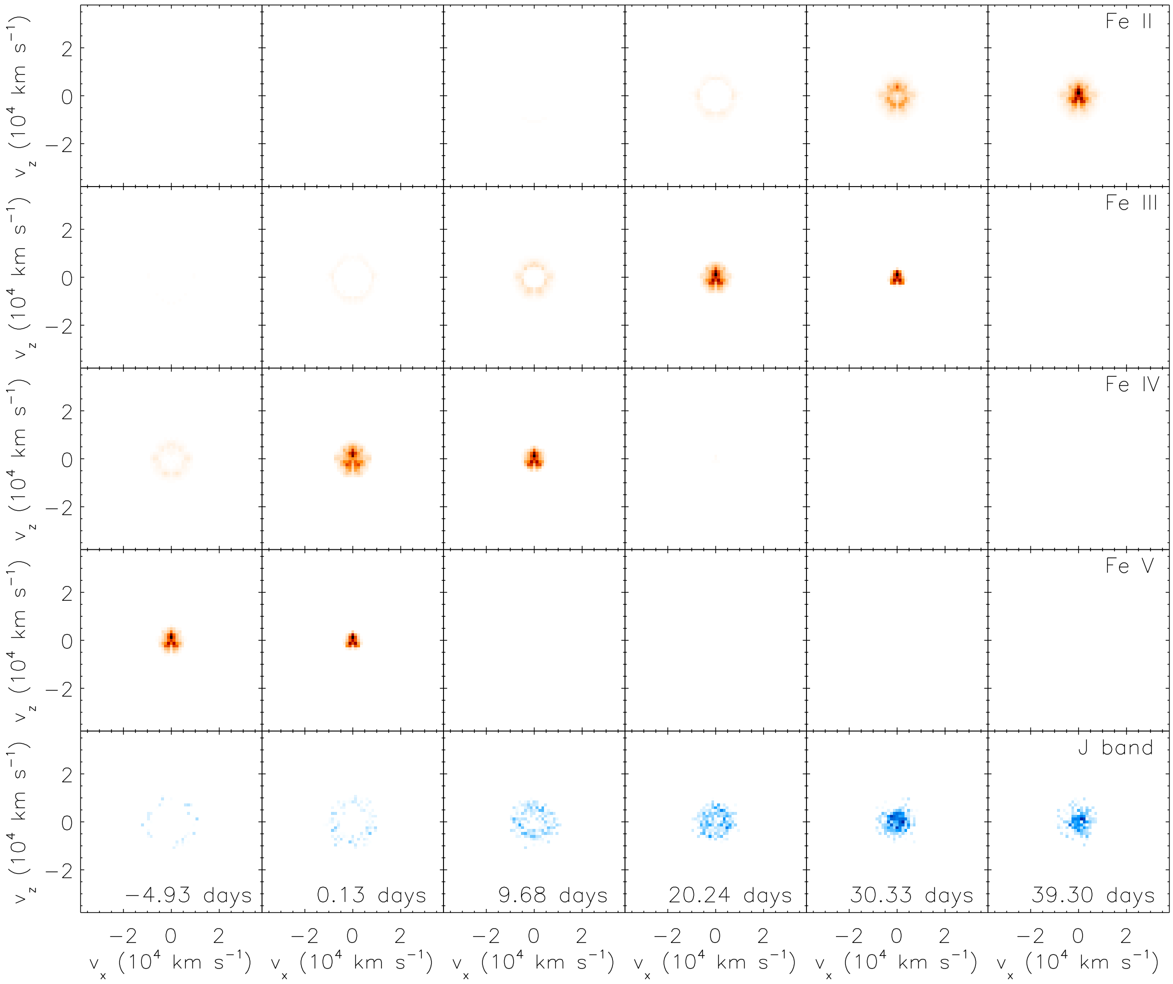

Figure 6.6: Snapshots (from left to right) showing the total population numbers of Fe II, III, IV and V (top four panels in reddish colours, darker regions have higher population) and the J-band regions of last emission (bottom panels in bluish colours) in the x-z plane of the deflagration model at different times as indicated in the bottom panels. Iron never recombines fully during the time span considered in our simulations. The colour coding of the regions of last emission indicates the energy escaping from a grid cell during the corresponding time step.

6.1.3 Comparison to observations

In the following we compare the synthetic observables derived for the deflagration and delayed detonation model to the observations. Starting with photometrical data we show angle-averaged bolometric and U, B, V, R and I light curves in Figure 6.7. Due to the rather low peak luminosities we overplotted a sample of supernovae ranging from the subluminous 1991bg-like events, represented by SN 2005bl in the Figure, to SN 2004eo which is representative for the faint end of the spectroscopically normal SNe Ia. Though not a perfect fit, the V and R light curves of the delayed detonation model match SN 2004eo quite well, although they lack the secondary maximum in the I band. In the U and B band the discrepancy is even worse, indicating a significantly redder colour of our model than SN 2004eo. We note, however, that with a $\Delta m_{15}(B) \sim 1.5$ the delayed detonation model is closest to SN 2004eo.

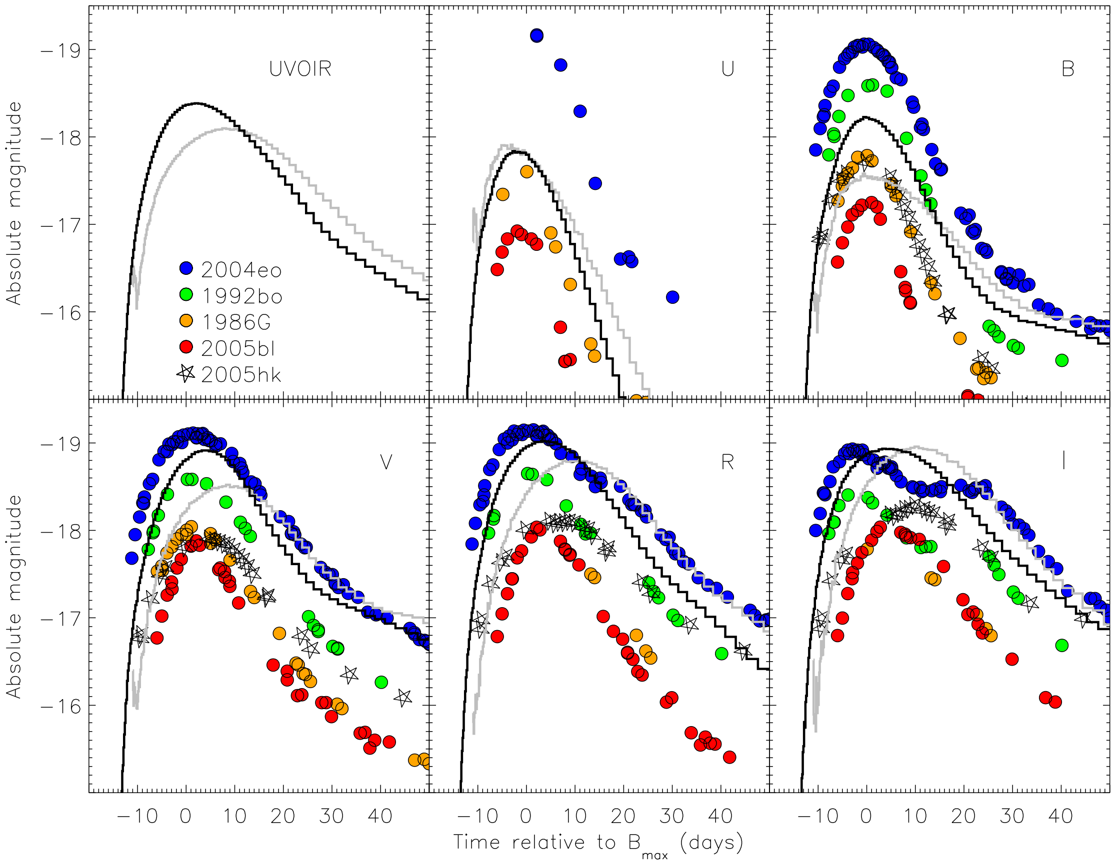

Figure 6.7: Comparing angle-averaged bolometric and U,B,V,R,I light curves of the deflagration (grey line) and delayed detonation model (black line) to a sample of different SNe Ia. Starting with SN 2004eo [$\Delta m_{15}\,(B) = 1.46$] which is representative for the faint end of spectroscopically normal SNe Ia, the supernovae indicated by the filled circles form a sequence of increasing $\Delta m_{15}\,(B)$ (SN 1992bo 1.69, SN 1986G 1.81, SN 2005bl 1.93) and thus decreasing peak luminosity. SN 2005hk [$\Delta m_{15}\,(B) = 1.56$, indicated by the open stars] was associated with a pure deflagration by Phillips et al. (2007).

On the faint end of the shown supernovae, SN 2005bl is clearly too dim in all bands compared to the delayed detonation model, thus ruling the model out as a possible explanation for the 1991bg-like events. Of course this was expected, since the 1991bg-like objects are usually associated with much lower amounts of ^{56}Ni ($\sim 0.1\,\mathrm{M}_\odot$, Stritzinger et al. 2006) than in both our models. Supernovae 1986G and 1992bo, which are bracketted in $\Delta m_{15}\,(B)$ by SN 2005bl and SN 2004eo, have about the right U- and B-band peak magnitudes, while they are too dim in V, R and I. However, they decline too fast compared to the delayed detonation model. Although in detail our model provides no perfect match to any of the supernovae discussed here, its general properties are promising.

For the deflagration model basically all problems mentioned for the delayed detonation model apply as well. However, they are somewhat more severe and especially the very slow decline [$\Delta m_{15}\,(B) \sim 0.6$] matches no observed faint SN Ia. Another problem with this model concerns the comparably large offset of the maxima in the V, R and I bands relative to the B-band maximum. Interestingly a similar trend, although weaker in R and I is observed for SN 2005hk, which Phillips et al. (2007) attributed to a pure deflagration due to its spectral evolution. The same was claimed for SN 2002cx (Li et al. 2003, Branch et al. 2004, Jha et al. 2006) which has similar properties as

SN 2005hk.

To assess this question we show a comparison of the spectral evolution of the delayed detonation and the deflagration model with observed spectra of SN 2005hk for the corresponding epochs in Figure 6.8. Although neither of the two models provide a perfect fit, the deflagration model does quite well. At early times the quasi-continuum of the deflagration model discussed in Section 6.1.1 is remarkably similar to what is observed for SN 2005hk, which shows no prominent Si II line up to maximum light. In contrast the delayed detonation model shows a spectrum which is characterized by strong absorption features of intermediate-mass elements (e.g. Si II $\lambda\lambda 6347, 6371$ and $\lambda\lambda 5958, 5979$; S II $\lambda\lambda 5468, 5612, 5654$; Ca II H & K lines, NIR triplet). Interestingly at 15 days after B-band maximum both models are quite similar to SN 2005hk. However, the deflagration model still does better due to its lower velocities. This becomes particularly obvious for the Ca II NIR triplet, which is clearly too blue-shifted in the delayed detonation model where the blue edge of this absorption trough extends to $\sim 8000\,\text{Å}$ (corresponding to a velocity of $19\,260\,\mathrm{km\,s^{-1}}$). For the deflagration model, in contrast, it extends only to $\sim 8200\,\text{Å}$ ($12\,250\,\mathrm{km\,s^{-1}}$) which is much better compared to the observed value of $\sim 8300\,\text{Å}$ ($8740\,\mathrm{km\,s^{-1}}$). At later times the models are more similar to each other than earlier on as discussed in Section 6.1.1 and both share some similarity with the observations. However, the details are not correct.

For comparison we contrast the delayed detonation and the deflagration model in Figure 6.9 with SN 1986G, which is one of the faint supernovae used for the light curve comparison but more normal than SN 2005hk. Here, in contrast to the comparison with SN 2005hk, the situation is somewhat inverted. Up to maximum light the delayed detonation model with all its absorption features of intermediate-mass elements provides a good fit to SN 1986G, while the lack of these features in the deflagration model rules it out as a possible explanation for SN 1986G. After maximum light, where the iron-core dominates, the models are more similar and both are comparable to SN 1986G to some extent. However the agreement is clearly worse than before maximum light in the delayed detonation model.

Interestingly, in the spectral range shown in Figure 6.9, the deflagration model seems to do better after maximum light than the delayed detonation model. This suggests that the iron-core of the delayed detonation model, which is basically formed by the initial deflagration phase, is a worse representation of SN 1986G than the pure deflagration model. Whether this is a result of the different ignition conditions and/or the simplified hydrodynamics treatment of the delayed detonation model in 2D is not clear. However, differences arising from the simplified 2D hydrodynamics treatment are visible in Figure 6.1. The iron core of the delayed detonation model shows a shell like enhancement in the nickel abundance on the northern hemisphere. This could be the result of either an unphysically fast growth of Rayleigh-Taylor plumes on large scales which is observed in 2D simulations or non-perfectly symmetric ignition conditions which again tend to introduce large scale asymmetries in 2D simulations. To conclude we note that a delayed detonation with an iron-core similar to the pure deflagration model [which has with $\sim 15\,000\,\mathrm{km\,s^{-1}}$ almost the same extent in velocity space than the the delayed detonation model ($v_{\max} = 14\,950\,\mathrm{km\,s^{-1}}$), see Figure 6.1] will match SN 1986G better than the current delayed detonation model. However, in the delayed detonation model it will never be possible to retain comparable amounts of unburned material in the core as in the pure deflagration model since those are burned in the detonation phase.

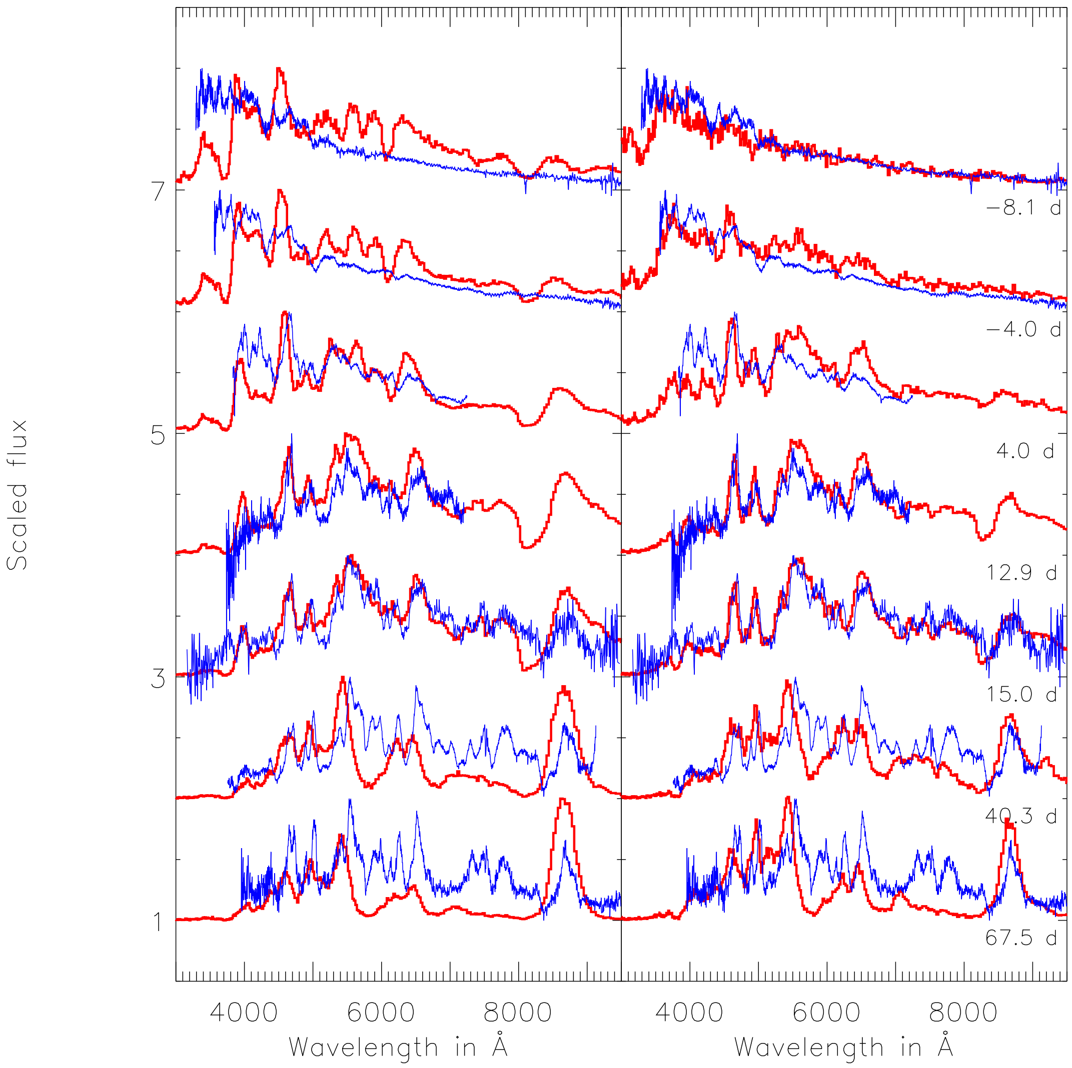

Figure 6.8: Comparison of synthetic spectra (red lines) of the delayed detonation (left panel) and deflagration model (right panel) with the spectral evolution of SN 2005hk (blue lines). The corresponding epochs indicated in the right panel are relative to B-band maximum. The observational spectra have been corrected for the redshift of the host galaxy, but no reddening correction was applied.

It is difficult to derive a statement for the outer layers at late times, since the observationally covered wavelength range for SN 1986G at these times is largely dominated by the iron-group elements. However, realizing that the absorption due to the Ca II H & K lines of the delayed detonation model matches the observational data quite well at early times, it can be deduced that the velocity extent in calcium is too low in the deflagration model. Inverting this statement, we would predict that the blue-shift of the Ca II NIR triplet absorption trough of the deflagration model (see Figure 6.6 and right panel of Figure 6.8) is too low compared to 1986G-like supernovae.

Finally we note that the problems of both models to fit the light curves of observed SNe Ia (see Figure 6.7 and the accompanying discussion) persist, even though some of the shown synthetic spectra fit the observations remarkably well. This is a result of the normalization applied in the spectrum comparison which hides the problem of absolute flux.

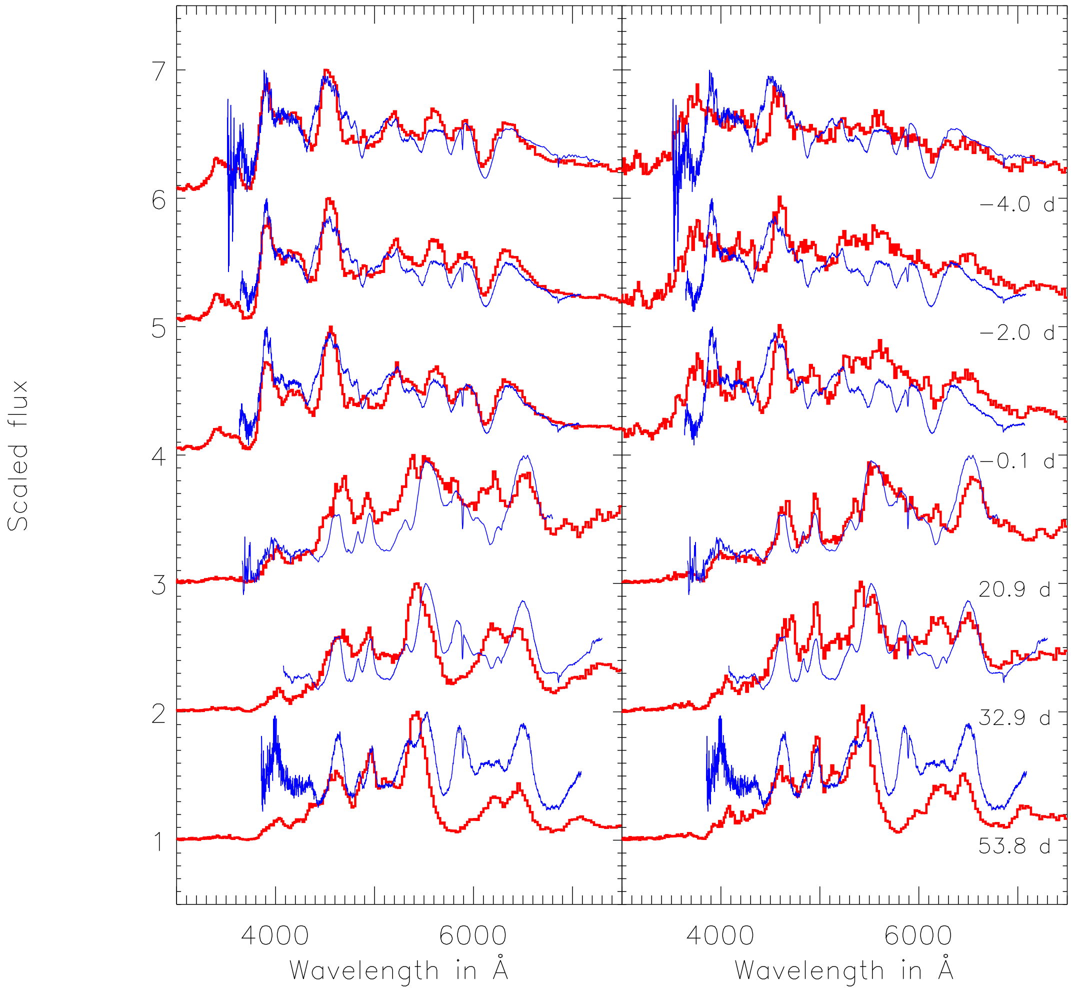

Figure 6.9: Comparison of synthetic spectra (red lines) of the delayed detonation (left panel) and deflagration model (right panel) with the spectral evolution of SN 1986G (blue lines). The corresponding epochs indicated in the right panel are relative to B-band maximum. The observational spectra have been corrected for both host galaxy redshift and reddening.

6.2 SN 2005bl and the class of 1991bg like objects

Although models have been proposed for normal and bright SNe Ia, there is a well-observed subclass of intrinsically faint SNe Ia that has eluded theoretical explanation. These supernovae, with SN 1991bg as a prototypical event, are characterized by peak magnitudes of $M_B \sim -17$ in the B band (pointing to ^{56}Ni masses of $0.1\,\mathrm{M}_\odot$, Stritzinger et al. 2006) and have to be understood in order to theoretically capture the full range of SN Ia diversity. Interestingly, a recent analysis of the spectral evolution of SN 2005bl (Hachinger et al. 2009), which is representative of the 1991bg-like SNe Ia, showed that both iron-group elements and silicon are abundant over a wide range of radii extending as close to the centre of the ejecta as is accessible observationally. In contrast, in normal SNe Ia the core of the ejecta consists predominantly of iron-group elements which is surrounded by a silicon-rich layer (e.g. Stehle et al. 2005, Mazzali et al. 2007, Mazzali et al. 2008). Since it is hard to imagine an explosion scenario in which hydrodynamic processes alone account for such a strong mixing of silicon and iron-group elements as observed in SN 2005bl, this difference in the characteristic chemical structures points to a different burning regime realized in the 1991bg-like objects.

Incomplete silicon burning is a natural way of producing a mixture of iron-group elements and silicon. It occurs in low-density carbon-oxygen fuel for a narrow window in ash temperatures (Thielemann et al. 1986). Burning significant amounts of stellar material in this regime therefore requires a shallow density profile of the exploding object. Moreover, supersonic propagation of the burning front is required to avoid pre-expansion of the material.

Recent studies of a dynamical merger of two equal-mass WDs by Pakmor et al. (2009) showed that both these conditions are satisfied in such an event. For a particular progenitor system containing two WDs of $0.89\,\mathrm{M}_\odot$ and central density $1.4 \cdot 10^7\,\mathrm{g\,cm^{-3}}$ they obtained an explosion during which only $0.12\,\mathrm{M}_\odot$ of ^{56}Ni have been synthesized. The final ejecta structure is remarkably similar to that inferred by (Hachinger et al. 2009, see Figure 6.10) for SN 2005bl from spectral analysis using the abundance tomography method (Stehle et al. 2005).

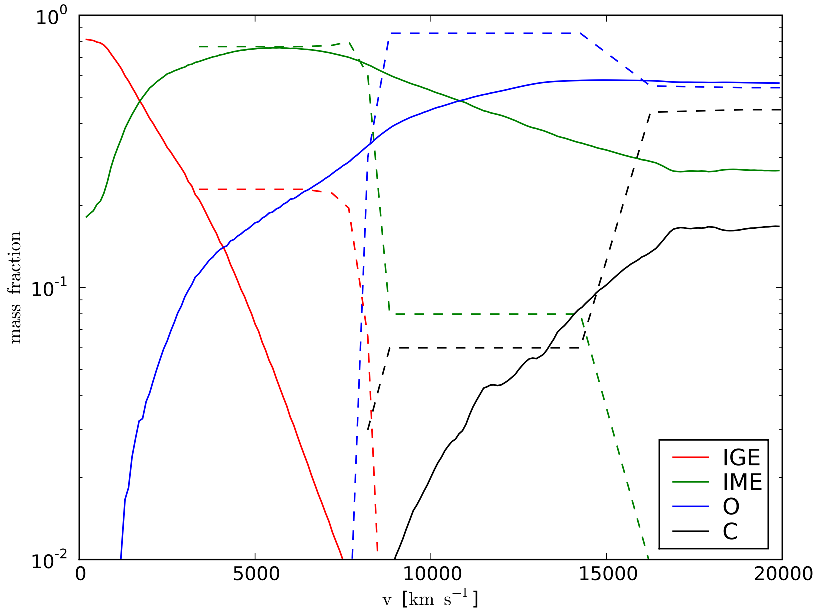

Figure 6.10: Radial abundance stratification of SN 2005bl compared to a model for a merger of two WDs of $0.89\,\mathrm{M}_\odot$ (courtesy: R. Pakmor).

6.2.1 Broad-band light curves

To quantitatively test this model against observations, we followed the radiative transfer through the ejecta to obtain synthetic spectra and light curves. For that purpose we mapped the final density and composition structure of the hydrodynamics simulation, which was extended up to the phase of homologous expansion ($t = 100\,\mathrm{s}$), to a 50^3 Cartesian grid. With a terminal velocity of $24\,980\,\mathrm{km\,s^{-1}}$ this yields a cell size of $\sim 1000\,\mathrm{km\,s^{-1}}$ which is less than the resolution in velocity space of our spectra (using our logarithmic wavelength bins with a size of $\sim 20\,\text{Å}$ at $5000\,\text{Å}$ we yield a resolution of $1200\,\mathrm{km\,s^{-1}}$). Moreover, comparison runs on a 25^3 grid showed no qualitative

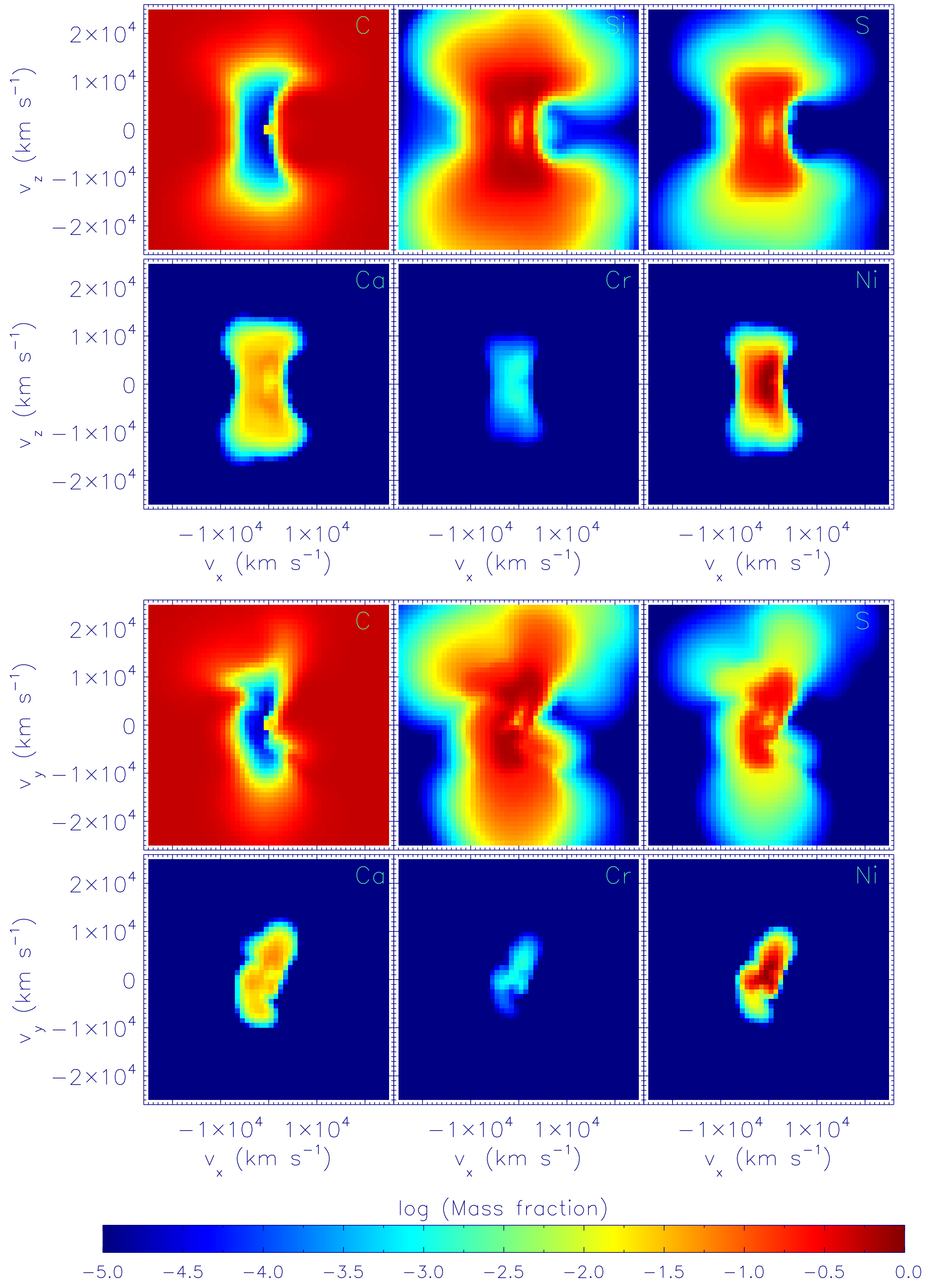

Figure 6.11: Final composition structure of the Pakmor et al. (2009) merger model in midplane slices parallel (top panels) and perpendicular (bottom panels) to the rotation axis of the progenitor system. The individual panels show the mass fractions of C, Si, S, Ca, Cr and Ni (from top left to bottom right, respectively).

differences in the light curves indicating that the main features of the model are resolved. The top and bottom panels of Figure 6.11 show the final composition structure for selected elements along the x-z and x-y planes of the simulation volume, respectively. The latter is perpendicular to the rotation axis of the progenitor system.

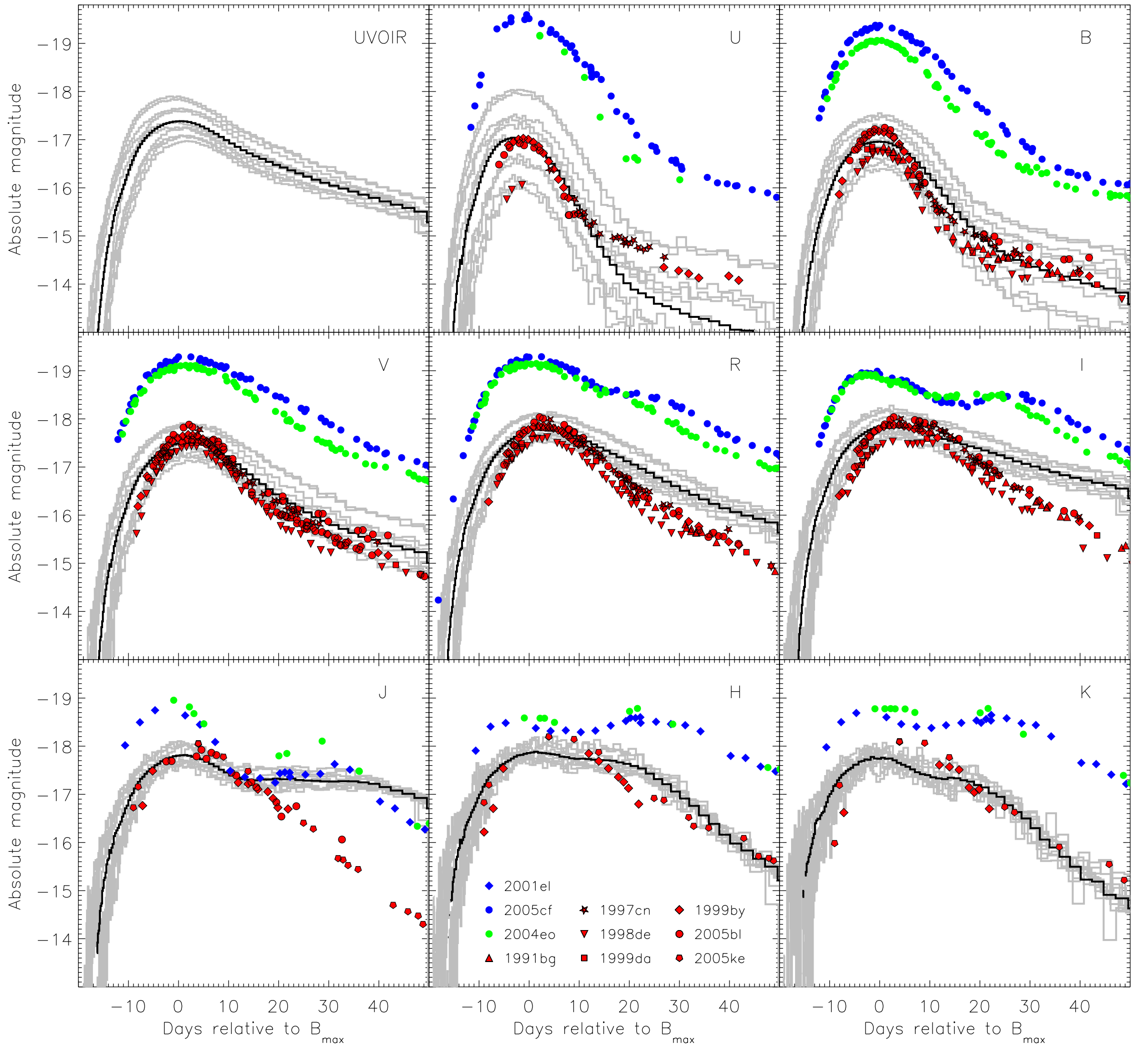

Figure 6.12: Synthetic light curves for the merger model compared to a sample of 1991bg-like objects (red, Taubenberger et al. 2008). The black line shows the angle-averaged light curve, the grey lines are light curves observed along ten different lines-of-sight. These have been chosen from 100 equally-sized solid-angle bins to indicate the full scatter in brightness arising from the asymmetries in the model. For comparison observations of bright (2001el, Krisciunas et al. 2003; 2005cf, Pastorello et al. 2007b) and faint (2004eo, Pastorello et al. 2007a) normal SNe Ia are shown. The panels correspond to the different broad-band filters as indicated.

The Monte Carlo simulation contains $51.2 \cdot 10^6$ packets and extends over 100 time steps from 2 to 80 days after explosion. The first 30 time steps ($t \lesssim 6\,\mathrm{d}$) are treated in LTE and make use of our initial grey approximation with the parameterized grey opacity and $\tau_{\mathrm{grey,min}} = 450$ (Section 4.3.6). The light curves obtained from this simulation are shown in Figure 6.12 and compared to the observational sample of 1991bg-like objects. The grey histograms correspond to ten different lines-of-sight, which have been selected from 100 equally-sized solid-angle bins to indicate the full scatter in brightness arising from the asymmetries in the model. The black line is the angle-averaged light curve. The overall agreement between the model and the observational sample is remarkably good. Owing to the small amount of ^{56}Ni synthesized during the explosion, the model naturally predicts the small absolute magnitudes of 1991bg-like objects (typically $M_{\mathrm{max}}\,(B) \sim -17\,\mathrm{mag}$) compared

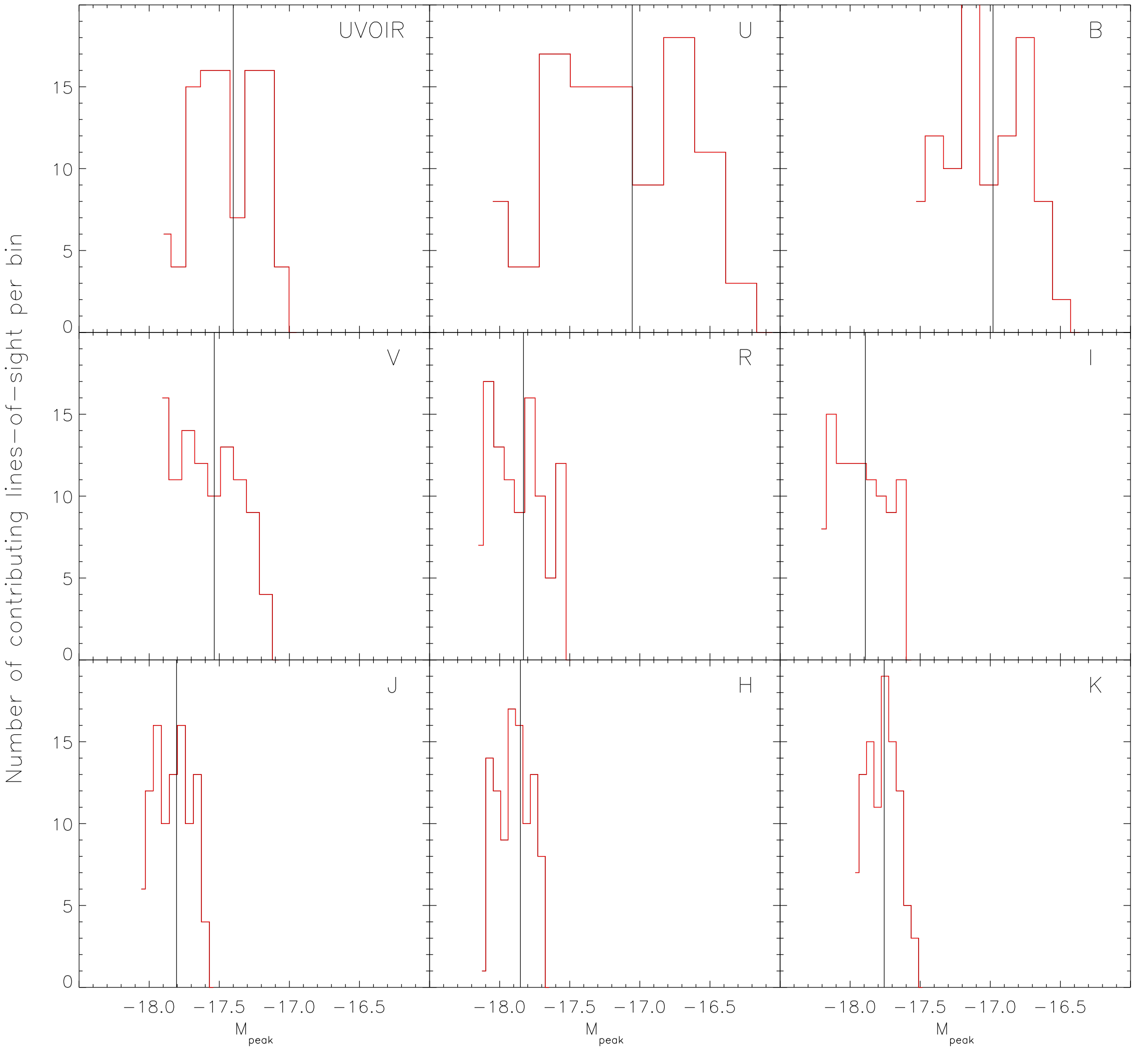

Figure 6.13: Histograms showing the distribution of peak magnitudes of the merger model over the different lines-of-sight. The panels correspond to the different broad-band filters as indicated. For each filter we distributed the different lines-of-sight to ten equally-sized bins, which cover the full range in peak magnitudes of the corresponding band.

to normal SNe Ia (typically $M_{\mathrm{max}}\,(B) \sim -19\,\mathrm{mag}$). Moreover, our model reproduces the peculiar colours of 1991bg-like objects at maximum light and does not show secondary maxima in R and redder bands. This is another peculiarity in which the 1991bg-like objects differ from normal SNe Ia.

The scatter owing to asymmetries in the model reaches from almost two magnitudes in the U band to ~ 0.5 magnitudes in the K band, decreasing continuously from bluer to redder bands. The distribution of peak magnitudes is shown in the histograms of Figure 6.13, which illustrate how many lines-of-sight contribute to a bin of given peak magnitude. This supports the conclusion drawn from the ellipsoidal model (Section 5.2), that the NIR bands are less sensitive to geometry effects, while U and B are very sensitive. Thus, if geometry effects due to asymmetric explosions are going to play a role for the scatter in the SN Ia Hubble diagram, their use for cosmological measurements might reduce the errors. Interestingly, Krisciunas et al. (2004) and Wood-Vasey et al. (2008) conclude from observational studies, which significantly extended the available NIR data of SNe Ia light curves, that SNe Ia are excellent standard candles in the NIR, even without correction for optical light-curve shape. This was already suggested by Elias et al. (1981, 1985).

A minor difficulty with the interpretation of Monte Carlo simulations is posed by statistical noise. This becomes a particular problem here when comparing the viewing angle-dependent NIR light curves, where the signal-to-noise ratio is poorest. To investigate the statistical significance of the scatter of the line-of-sight dependent light curves relative to the angle-averaged light curve, we did a Kolmogorov-Smirnov test (e.g. Press et al. 1992) to check if this scatter follows a normal distribution. Therefore we separated the simulation packets into two parts (of 25 million packets each) and extracted line-of-sight dependent light curves [$L_X\left(t_i\right)$, $L'_X\left(t_i\right)$; where X denotes a broad-band filter] for both of them. The difference $L_X\left(t_i\right)-L'_X\left(t_i\right)$ between the data points of these light curves results from Monte Carlo noise. We can use this to estimate the standard deviation of the simulation data. Taking into account that we use all simulation packets for the Kolmogorov-Smirnov test and the two sets of packets are statistically independent, we find $\sigma_X\left(t_i\right) = \left|L_X\left(t_i\right) - L'_X\left(t_i\right)\right| / \sqrt{2}$. Table 6.2 shows the fit-parameters thus derived for maximum light.

Table 6.2: Goodness-of-fit parameters for a Kolmogorov-Smirnov test probing the distribution of peak magnitudes in the different bands against a normal distribution around the corresponding angle-averaged light curves. For a significance level of 5%, the assumption of normal distribution has to be rejected for fit parameters greater than 0.136.

UVOIR	U	B	V	R	I	J	H	K
0.470	0.446	0.464	0.451	0450	0.386	0.282	0.206	0.083

For a significance level of 5% the critical value above which the hypothesis of normal distribution around the angle-averaged light curve has to be rejected is 0.136. Hence the scatter in the UVOIR bolometric and U to J light curves is due to line-of-sight effects and not attributable to Monte Carlo noise. The K band scatter, however, is compatible with random noise around the angle-averaged light curve. The H band is a marginal case.

Although our model light curves decline faster [for the angle-averaged light curve we find $\langle\Delta m_{15}\left(B\right)\rangle \sim 1.4$] than the light curves of normal SNe Ia [$\Delta m_{15}\left(B\right) \sim 1.1$], their evolution is not fast enough to reproduce the rapid decline [$\Delta m_{15}\left(B\right) \gtrsim 1.8$] of the 1991bg-like events. Even the line-of-sight with the fastest declining light curve [$\Delta m_{15}\left(B\right) \sim 1.75$] decays too slowly. This is illustrated in the top panels of Figure 6.14, which shows the B-band light curves along 100 different lines-of-sight compared to the observational sample of 1991bg-like objects (left) and the corresponding light curve width-luminosity relations in the $\Delta m_{15}\left(B\right)$-$M_{\mathrm{max}}\left(B\right)$ plane (right).

This slow decline could be a general problem of the proposed scenario, in which the ejecta mass ($1.78\,\mathrm{M}_\odot$) exceeds the Chandrasekhar mass. A large mass, and thus opacity, is expected to produce slow light curves. However, the most important contribution to the opacity comes from the iron-group elements, which contribute only little ($\sim 0.126\,\mathrm{M}_\odot$) to the total mass of our model. Furthermore we note, that LTE calculations of the same model generally show a steeper decline. Though the LTE approximation is certainly bad after maximum light (compare Section 5.1.1), it may be possible that the model light curves would decline faster, if we treat the non-LTE physics in more detail. Particularly the inclusion of dielectronic recombination (Section 4.4.2) could be important. Since the time at which the ejecta material recombines (which happens earlier in an

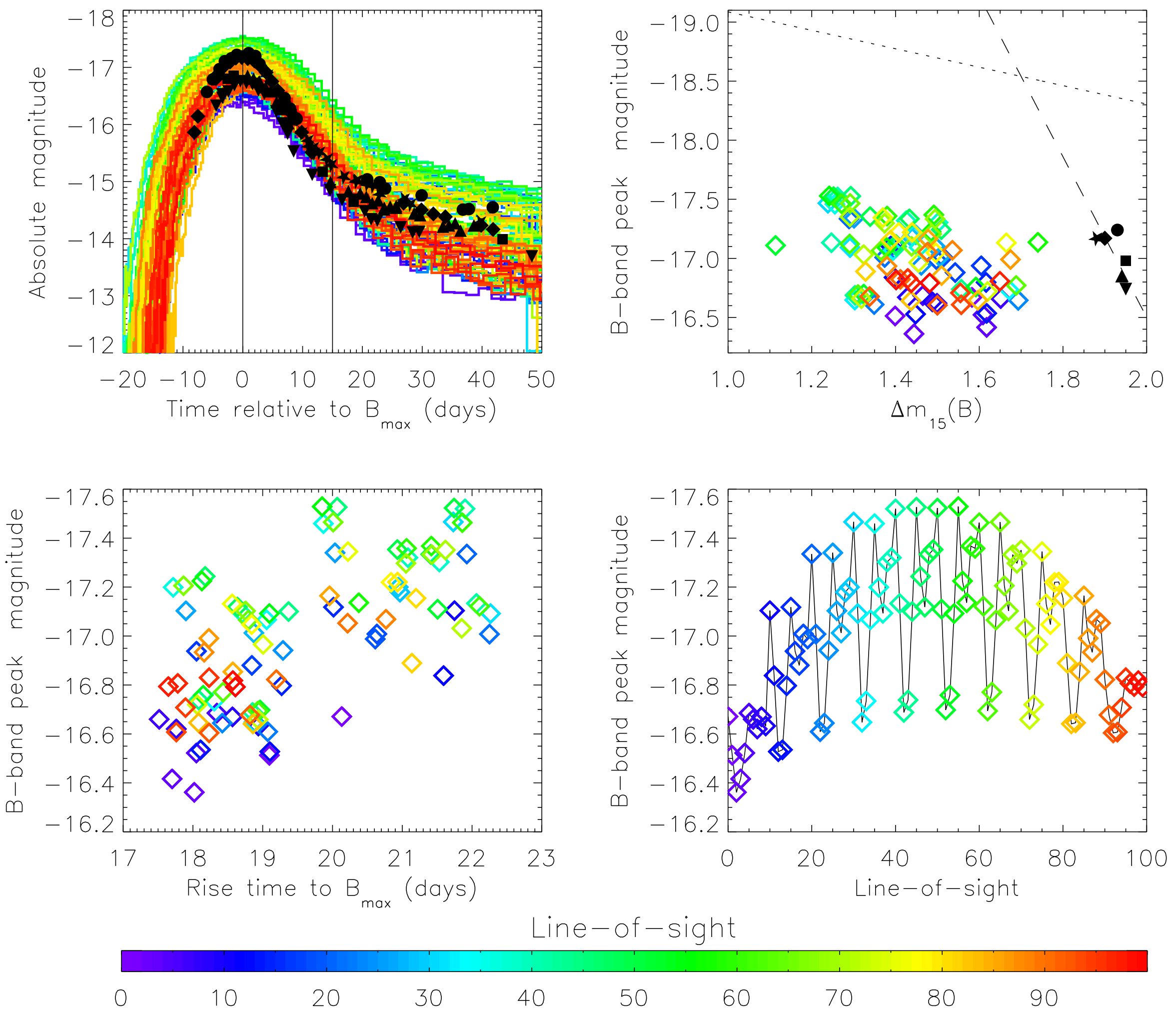

Figure 6.14: Diversity of the B-band light curve of the merger model due to geometry effects. The upper left panel shows the B-band light curves as seen from the 100 equally-spaced solid-angle bins by a colour coding. Overplotted is the observational sample of 1991bg-like objects in black (for a legend of the different objects see Figure 6.12). The upper right panel shows the B-band peak magnitudes vs. $\Delta m_{15}\,(B)$ along the different lines-of-sight and for the observational sample of 1991bg-like objects, using the same colour coding. The dashed line corresponds to the fit to the observational data given by Taubenberger et al. (2008) for objects with $\Delta m_{15}\,(B) \geq 1.69$. For comparison the dotted line shows the fit of Hamuy et al. (1996) for objects with a $\Delta m_{15}\,(B) \leq 1.69$. The lower left panel illustrates the relation between the rise time and the peak magnitude along the different lines-of-sight. The lower right panel shows B-band peak magnitude vs. line-of-sight.

LTE simulation, see Section 5.1.1) is the most important difference between the LTE and non-LTE treatment, an increased NLTE recombination rate might make the light curves decline faster. This should be investigated in future work. The approximate solution of the excitation state in our NLTE treatment could be another problem at later times. However, it is also possible that uncertainties in the nucleosynthesis results play a role and/or details in the explosion model itself.

From the bottom left panel of Figure 6.14 we see that brighter light curves tend to have longer rise times. This is in contrast to what is expected from Arnett's law, which relates the ^{56}Ni mass to the bolometric peak luminosity. Assuming that at maximum light the luminosity balances the instantaneous energy deposition by the radioactive nuclides of the ^{56}Ni decay sequence, the peak luminosity would decrease with increasing rise time. However, this result depends on the assumption of spherical symmetry, which is clearly not the case in our model. In general, the rise time of the light curves of the merger model (the average rise time to B-band maximum is $\sim 19.44\,\mathrm{d}$) is comparable to the rise times of normal SNe Ia for which Conley et al. (2006) derived 18 to 20 days. In contrast, 1991bg-like objects are expected to rise faster than normal SNe Ia. Thus Garnavich et al. (2004) derive a rise time of $13.9^{+1.2}_{-1.1}\,\mathrm{d}$ for the subluminous SN 1999by. Taubenberger et al. (2008) noted that this value should only be regarded as a lower limit to the rise time of SN 1999by. From a spectral analysis of SN 2005bl, they argue that the nickel in 1991bg like objects is confined to the very centre of the supernovae, such that the assumption that the luminosity of a supernova increases with t^2 (Riess et al. 1999) which is the basis of the analysis of Garnavich et al. (2004), might break down at very early times. From their analysis of SN 2005bl they find a rise time between 14 and 22 days. Taking this parameter range our model does quite well, however it contains no line-of-sight with a rise time below 17 days. This is most likely due to the large ejecta mass compared to Chandrasekhar mass models.

The bottom right panel of Figure 6.14 highlights the geometry effects, by plotting B-band peak magnitude for various lines-of-sight ordered by polar (θ) and azimuth (ϕ) angle. Being split into ten different θ-bins, with again each bin containing ten ϕ-bins, we see that the model appears brighter from equatorial lines-of-sight than from polar ones. Comparing this with the top panels of Figure 6.11, it is clear that this is due to the larger apparent surface area of the central nickel bubble from these lines-of-sight (as it was the case in the ellipsoidal model, Section 5.2). The overlying modulation in azimuthal lines-of-sight is due to a similar effect caused by the asymmetry in the rotation plane of the progenitor system (bottom panels of Figure 6.11).

Another problem concerns the colour evolution at later times ($t > 20\,\mathrm{d}$ after B-band maximum). There the I and J model light curves, and to a lesser extent also the R light curve, are systematically too bright compared to the data (Figure 6.12), while the U-band light curve becomes too faint. Looking at the spectra (see next section), the brightness of the R, I and J band can be attributed to the strong Ca II NIR triplet (contributing to R and I) and another Ca II line at $\lambda 11839, 11959$ ($5\mathrm{s}\,^2\mathrm{S}_{1/2} - 5\mathrm{p}\,^2\mathrm{P}_{3/2}$, $5\mathrm{s}\,^2\mathrm{S}_{1/2} - 5\mathrm{p}\,^2\mathrm{P}_{1/2}$). However, it is not clear whether this calcium domination at late times hints to an over-abundance of calcium in the nucleosynthesis yields of the explosion model, or might be related to shortcomings in our radiative transfer treatment. Especially the simplified treatment of collisional excitation in the van Regemorter approximation (Section 3.4.3), which makes use of the oscillator strength of permitted radiative dipole transitions to calculate the transition probabilities, could overestimate the calcium contribution since calcium has strong dipole transitions. Extending the treatment of collisional interactions with more detailed atomic data will help to address this question in the future.

6.2.2 Spectral evolution

Figure 6.15 shows synthetic spectra of the merger model for -5, 5 and 20 days relative to B-band maximum, which are compared to the observational data of Taubenberger et al. (2008) for the 1991bg-like SN 2005bl. The model reproduces the overall flux distribution remarkably well. Due

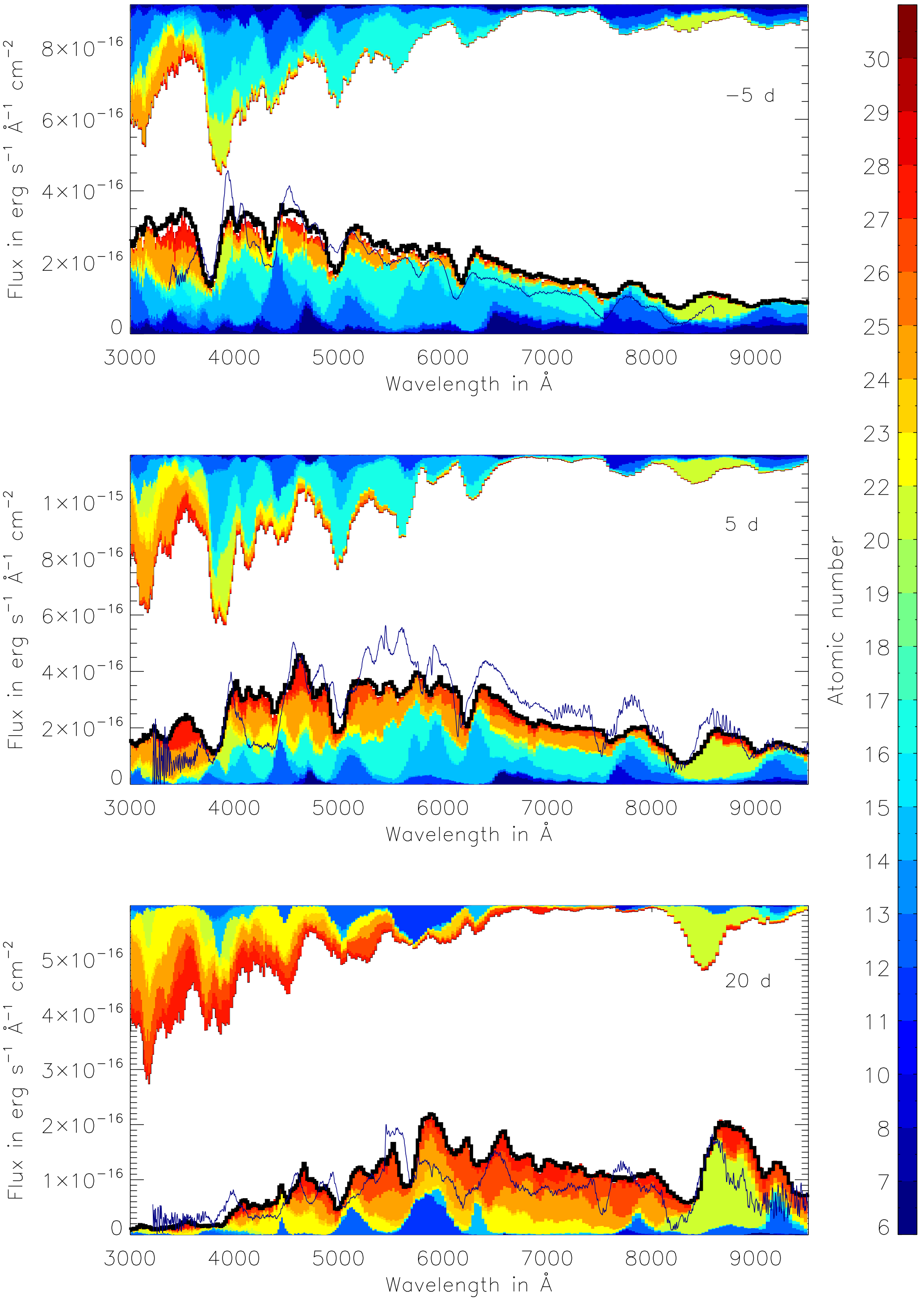

Figure 6.15: Angle-averaged synthetic spectrum (thick black line) for the merger model at −5 (top panel), 5 (middle panel) and 20 days (bottom panel) relative to B-band maximum compared to the corresponding epoch of SN 2005bl (dark blue). The colour coding indicates the element(s) responsible for both bound-bound emission and absorption of quanta in the Monte Carlo simulation. The region below the synthetic spectrum is colour coded to indicate the fraction of escaping quanta in each wavelength bin which last interacted with a particular element (the associated atomic numbers are illustrated in the colour bar). Similarly, the coloured regions above the spectra indicate which elements were last responsible for removing quanta from the wavelength bin (either by absorption or scattering/fluorescence).

to the low ejecta velocities the characteristic P-Cygni absorption features of Si II are only weakly blue-shifted. Compared to normal SNe Ia this is also true for SN 2005bl and the class of 1991bg-like objects. However, the merger model produces even smaller blue shifts. After maximum light the difference in the blue shifts and thus the different velocities in the model and the data become more visible: while for the Ca II H & K lines and the NIR triplet the velocities at -5 days agree quite well, the blue shift of the calcium absorption features in the model at 5 days is smaller than that in the observations. This increases at later times. As in the data the W-shaped S II lines at $\lambda\lambda 5468, 5612, 5654$ are comparably weak in the model spectra. However, for the spectrum at 5 days after maximum there is an obvious difference in this region between the model and the data.

Another difference concerns the characteristic Ti II absorption trough for 1991bg-like objects between 4000 and 4400 Å. While this is fully developed in the 5 days spectrum of SN 2005bl there is only a slight indication in the model spectrum. This disagrees with the common notion (Mazzali et al. 1997), that the strong Ti II absorption in 1991bg-like objects is mainly due to ionization effects. Compared to standard models, the temperature and ionization in the merger model are quite low, thus indicating that the Ti II absorption might be due to a real titanium abundance enhancement in 1991bg-like objects (see also Taubenberger et al. 2008). Currently the total mass of titanium in the model is only $\sim 1.11 \cdot 10^{-5}\,\mathrm{M}_\odot$. This corresponds to a mass fraction of $\sim 6 \cdot 10^{-6}$ compared to a value of $\sim 10^{-3}$ which was inferred for the spectrum forming layers of SN 2005bl by spectral analysis (Taubenberger et al. 2008). Moreover, titanium is about a factor 30 less abundant in our model than chromium. This is more than the relative difference in solar abundances of titanium and chromium and in contrast to earlier observational work, which suggests that titanium and chromium should have comparable abundances in SNe Ia (e.g. Stehle et al. 2005, Taubenberger et al. 2008). Determining the exact yields and spatial distribution of trace elements during the burning, however, poses a challenge to the nucleosynthesis simulations, which depend very sensitively on the burning temperature and the nuclear reaction rates. Both of these are somewhat uncertain: the temperatures, due to numerical difficulties in resolving the burning front and the rates since they are not well known. Due to the large number of titanium lines between 4000 and 4400 Å, however, a small increase in the titanium mass within the uncertainties of the nucleosynthesis could already help in making the absorption more pronounced.

Since we studied only one particular realization of the proposed merger scenario slightly different initial conditions might also help. The important parameters here are, the total mass of the progenitor system, the mass ratio $q = M_2/M_1$ of the WDs and their composition. Since we want to keep the peak magnitudes of our model which agree quite well with the 1991bg-like objects, the amount of ^{56}Ni synthesized during the explosion should not be changed significantly by different initial conditions. Thus the total mass of the progenitor system cannot change largely. However, the mass ratio of the two WDs (currently $q = 1$) may be changed within a range of at least $q = 0.9 \ldots 1.0$ (Pakmor et al. 2009). Moreover, the initial composition of the WDs is important. Being currently pure carbon-oxygen WDs, these have a metallicity of zero. A non-zero metallicity would increase the neutron fraction and thus influence the nucleosynthesis yields.

The O I $\lambda\lambda 7772, 7774, 7775$ feature is particularly strong in the 1991bg-like objects. Although we find a significant contribution of this feature in the synthetic spectra at early time it is much too weak compared to SN 2005bl after maximum light. Moreover, its blue-shift is too weak compared to the data indicating that oxygen generally occurs at too low velocities. This was already expected from the abundance tomography result of SN 2005bl. Comparing Figure 6.10 we see that the oxygen mass fraction below 8000 km s^{-1} in our model is significantly larger than inferred for SN 2005bl, while there is a slight under-abundance between 8000 and 15 000 km s^{-1}. In the outermost layers the agreement is excellent. Another feature which 1991bg-like objects develop well after maximum light is the Na I D doublet ($\lambda\lambda5890, 5896$, $3s\,^2S_{1/2} - 3p\,^2P_{3/2}$, $3s\,^2S_{1/2} - 3p\,^2P_{1/2}$). This can be clearly identified at ~ 5700 Å in the synthetic spectrum at 20 days after B-band maximum shown in the bottom panel of Figure 6.15 and becomes more prominent with time. In contrast to all other prominent absorption features, the blue-shift of the Na I D doublet is somewhat too large in the synthetic spectra, indicating that sodium is distributed at too large velocities in the merger model.

Figure 6.16 shows the complete spectroscopic coverage of the photospheric phase of SN 2005bl according to Taubenberger et al. (2008). For comparison we overplotted synthetic spectra of the merger model for the corresponding epochs. The red histograms show the angle-averaged spectra (of which we already discussed a subset in Figure 6.15) and the grey histograms indicate the spread due to asymmetries in the model. These spectra were extracted along 25 different lines-of-sight, each corresponding to an equally-sized solid-angle bin. While spectra seen along some lines-of-sight are in better agreement with the overall flux distribution of SN 2005bl than the angle-averaged spectrum (which was already indicated by the light curve analysis), the velocity offset between the model and the data remains a general problem as in the angle-averaged case. Although there are some lines-of-sight where, due to the large asymmetries of our merger model (Figure 6.11), the blue-shift of the line features is larger than observed in SN 2005bl (see Figure 6.17), it is too weak for most of the lines-of-sight. In particular, the velocities in the characteristic Si II doublet ($\lambda\lambda6347, 6371$) are too low. Moreover, there is no line-of-sight for which all three line features (Si II $\lambda\lambda6347, 6371$, O I $\lambda\lambda7772, 7774, 7775$ and Ca II $\lambda\lambda8498, 8542, 8662$) considered in Figure 6.17 compare equally-well to the observations.

Similarly we find no line-of-sight which is able to reproduce the strong Ti II absorption trough between 4000 and 4400 Å typical for 1991bg-like objects. This further confirms the conclusion drawn above, that the titanium abundance of our particular merger model is too small. For implications see the discussion above.

At the two latest available epochs ($t > 20$ d after B-band maximum) the calcium problem (discussed with the light curves) becomes obvious: the emission feature of the Ca II NIR triplet is much too strong compared to the data. Since the Ca II NIR triplet contributes to both, the R- and I-band filters, the corresponding light curves are too bright at late epochs. Possible reasons have already been discussed with the light curves (Section 6.2.1).

6.2.3 Ejecta asymmetries

Howell et al. (2001) found that SN 1999by, another member of the 1991bg-like family, has an overall level of polarization of $\sim 0.3\% \ldots 0.8\%$ which is unusually large for a SN Ia. Typically the continuum polarization observed in SNe Ia is $\lesssim 0.3\%$, while the line polarization can be much larger (Wang & Wheeler 2008). Since we observe the supernova ejecta as an (unresolved) point source and electric field vectors of photons undergoing electron scattering end up having a preferred direction, the polarization signal can be used as a tool to study the ejecta asymmetries. For totally spherical symmetric ejecta there is no preferred direction and all electric field vectors cancel exactly, resulting

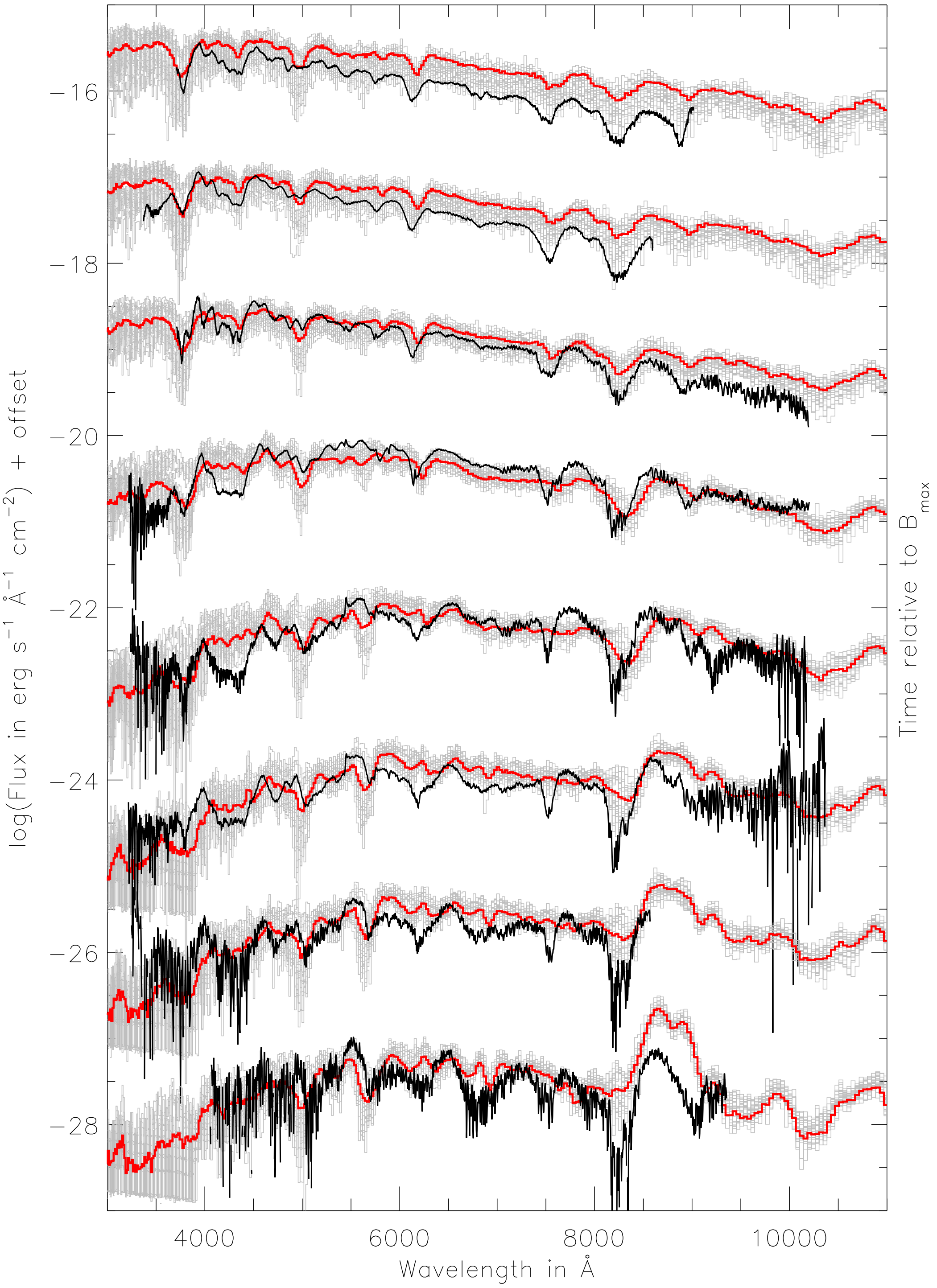

Figure 6.16: Angle-averaged spectral evolution of the merger model (red line) compared to SN 2005bl (black) for different epochs. The grey lines show model spectra as seen from 25 different equally-sized solid-angle bins to indicate the scatter resulting from the model asymmetries.

in zero polarization. Similarly line scattering leads to polarization, since its angular redistribution is not complete. However, the effect is usually weaker than that of electron scattering. Moreover, redistribution of flux by fluorescence in lines can weaken underlying continuum polarization due to electron scattering.

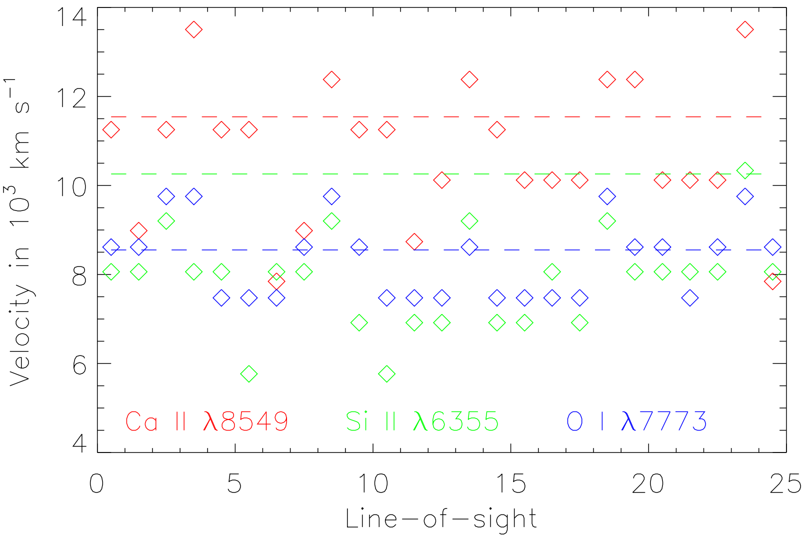

Figure 6.17: Line velocities inferred from the merger model at three days before B-band maximum for Si II $\lambda\lambda 6347, 6371$, O I $\lambda\lambda 7772, 7774, 7775$ and Ca II $\lambda\lambda 8498, 8542, 8662$ as seen from 25 different equally-sized solid-angle bins [coloured symbols as indicated; the wavelengths give the $\log(gf)$-weighted means of the corresponding features]. For comparison the values derived for SN 2005bl at the corresponding epoch are shown as dashed lines.

Given the comparably large amount of continuum polarization in SN 1999by Howell et al. (2001) concluded that the ejecta of SN 1999by are significantly more asymmetric than the ejecta of normal SNe Ia. Comparing their data to flux and polarization spectra of parameterized explosion models of ellipsoidal geometry, they find that a model of $\sim 20\%$ asphericity accounts best for SN 1999by when seen equator-on. They attribute this asymmetry to either a rapid rotation of the progenitor WD in the delayed detonation scenario or a possible WD merger as progenitor system and speculate that the 1991bg-like objects thus originate from different progenitors than the normal SNe Ia.

This would make it particularly interesting to study polarization spectra resulting from our merger model. However, our radiative transfer treatment does not include polarization so far. Thus we cannot address the question of polarization in the merger model directly. Instead, we have to restrict the discussion to the asymmetries of the compositional structure of the ejecta (Figure 6.11) and the shapes of the regions where photons are last emitted before escaping the ejecta. These can be extracted from our radiative transfer simulation as we did it for the ellipsoidal toy model (Section 5.2) and are shown in Figure 6.18 for the different bands at maximum light.

From these we infer an asphericity of $\sim 25\% \ldots 50\%$ for our model in the (x,z)-plane (the progenitor system orbited around the z-axis). Since we do not find strong differences in the properties of our flux spectra for different lines-of-sight, the model does not need to be observed equator-on to reproduce 1991bg-like objects but might be seen from a different direction, where the degree of asymmetry is less. Thus we find the asphericity of our model to be consistent with the value obtained by Howell et al. (2001) for SN 1999by.

Besides the large-scale asymmetry Howell et al. (2001) identify another difference between SN 1999by and more normal SNe Ia which affects the polarization properties. They argue that in normal SNe

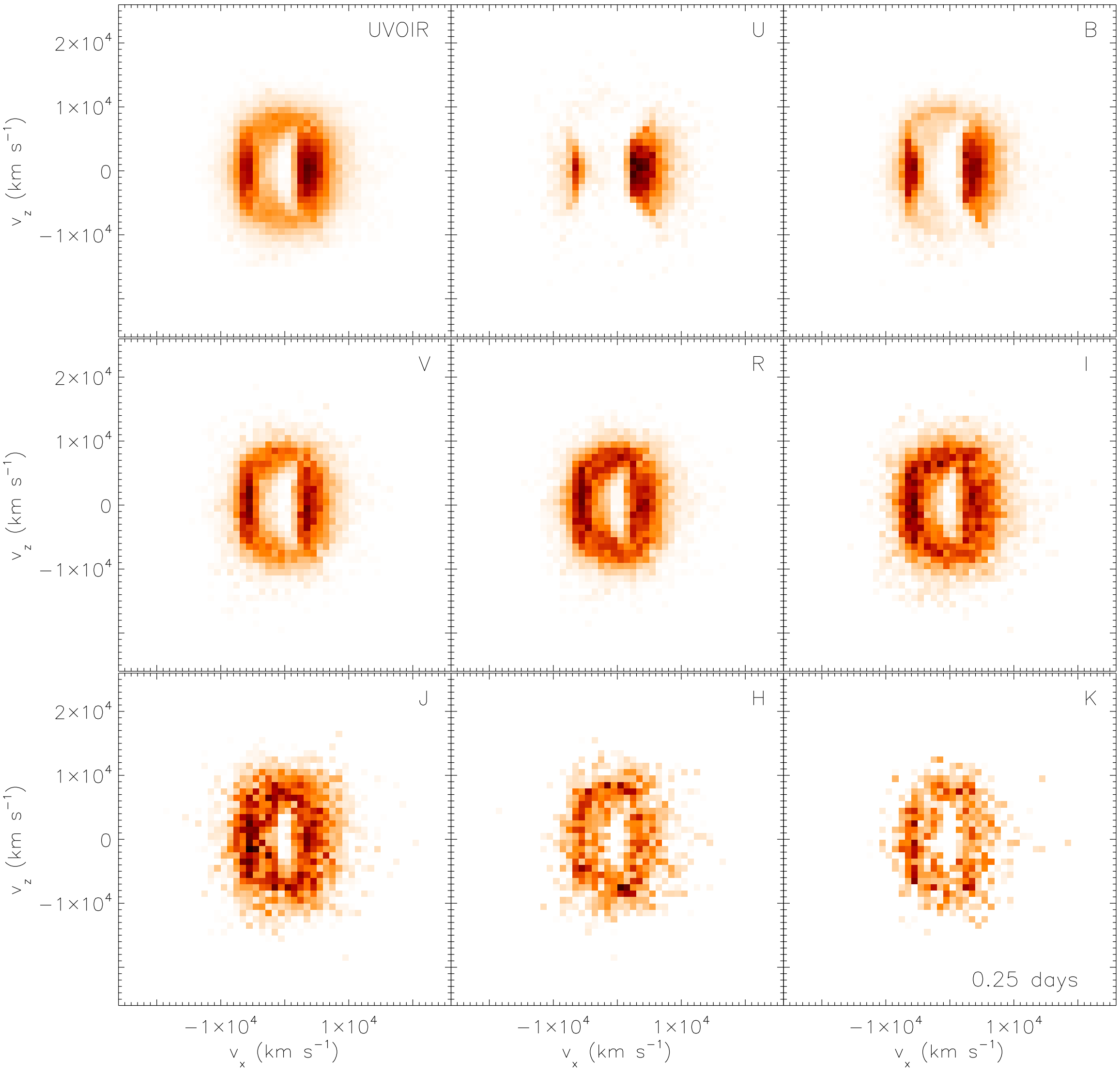

Figure 6.18: Slice through the merger model along the (x,z)-plane indicating the region of last emission for the different broad-band filters around maximum light in B band. Dark regions indicate strong emission. At that time the emission still originates from layers outside the iron-rich core which is located at the whitish half-moon shaped region in the middle (compare Figure 6.11).

Ia the amount of continuum polarization at maximum light is less since their photospheres have already receded to the iron-rich inner core, which is comparably larger in normal SNe Ia than in 1991bg-like objects. In contrast, the photospheres of 1991bg-like objects remain in the layers dominated by intermediate-mass elements at maximum light. Thus maximum light spectra of normal SNe Ia are more strongly affected by the wealth of lines associated with the iron-group elements leading to an increased influence of line polarization (the number of lines associated with the intermediate-mass elements is much less). Since line polarization tends to depolarize previous continuum polarization resulting from electron scattering, this would explain the lower amount of continuum polarization observed in normal SNe Ia.

Comparing the regions of last emission in our merger model (Figure 6.18) and the ellipsoidal toy model discussed in Section 5.2 (Figure 5.11), we confirm the different locations of the photospheres with respect to the iron core. Lacking a treatment of polarization in our radiative transfer code, however, we are currently not able to study the influence of this on the polarization spectra. This must be addressed by future work after extending the code. If a comparison of our merger model with an ellipsoidal toy model of similar asphericity then shows a significantly larger degree of continuum polarization in the merger model than in the ellipsoidal toy model, the argumentation of Howell et al. (2001) would be supported. As a consequence one could then argue further that for a fixed degree of asymmetry the degree of continuum polarization increases for supernovae with decreasing ^{56}Ni mass since this is a proxy for the amount of iron-group material synthesized during the explosion and therefore for the size of the iron-core.

6.3 Sub-Chandrasekhar-mass models – an alternative route to 1991bg-like objects?

In addition to the double degenerate scenario, sub-Chandrasekhar-mass models have been discussed as an alternative explanation for 1991bg-like objects. There an initial detonation in an accreted helium shell on top of a carbon-oxygen WD triggers a secondary detonation in the WD core (see Section 2.3). Due to their low progenitor mass, sub-Chandrasekhar-mass models could provide a natural explanation for both the low inferred ^{56}Ni masses and the fast light curve evolution of 1991bg-like objects.

Possible progenitor systems for sub-Chandrasekhar-mass models are AM CVn stars. These are rapidly orbiting ($P \lesssim 65\,\mathrm{min}$) cataclysmic variable stars in which a WD accretes matter from a helium star or helium WD [typical accretion rates are $\dot{M} = 10^{-13} \ldots 10^{-5}\,\mathrm{M}_\odot\,\mathrm{yr}^{-1}$; see e.g. Nelemans (2005) for an overview]. Bildsten et al. (2007) have shown that the helium accretion in these systems can lead to dynamical burning and possibly a detonation triggers. Based on the minimum shell masses derived by Bildsten et al. (2007) for such detonations, Fink et al. (2009) presented 2D hydrodynamical simulations for a set of models covering different WD shell-mass combinations. They focused on the question whether the shell detonations trigger a secondary detonation of the WD core as found by previous work (Fink et al. 2007). For their model sequence with WDs of masses from $M_\mathrm{WD} = 0.810$ to $1.385\,\mathrm{M}_\odot$ and helium shell-masses from $M_\mathrm{He} = 0.126$ to $0.0035\,\mathrm{M}_\odot$, they found the triggering of this secondary detonation to be robust.

In the models of Fink et al. (2009) the initial helium detonation was ignited in a single point at the north pole. From there the helium detonation wave sweeps around the WD core until it converges at the south pole. At the same time a shock wave propagates through the core, which converges in a point off-centre where the secondary core detonation is triggered. Due to the low densities in the shell, the burning does not reach nuclear statistical equilibrium, yielding instead mainly the lighter iron-group elements like titanium and chromium and some intermediate-mass elements. Moreover a large fraction of helium remains unburned (Figure 6.19). The core detonation yields a mixture of iron-group and intermediate-mass elements depending on the core density, which is determined by the WD mass.

Producing $0.171\,\mathrm{M}_\odot$ of ^{56}Ni, their least massive model ($M_\mathrm{WD} = 0.810\,\mathrm{M}_\odot$, $M_\mathrm{He} = 0.126\,\mathrm{M}_\odot$) comes close to the amount of ^{56}Ni inferred for the 1991bg-like objects (for a summary of the nucleosynthesis yields of the most abundant species see Table 6.3). Thus we derived synthetic observables for this

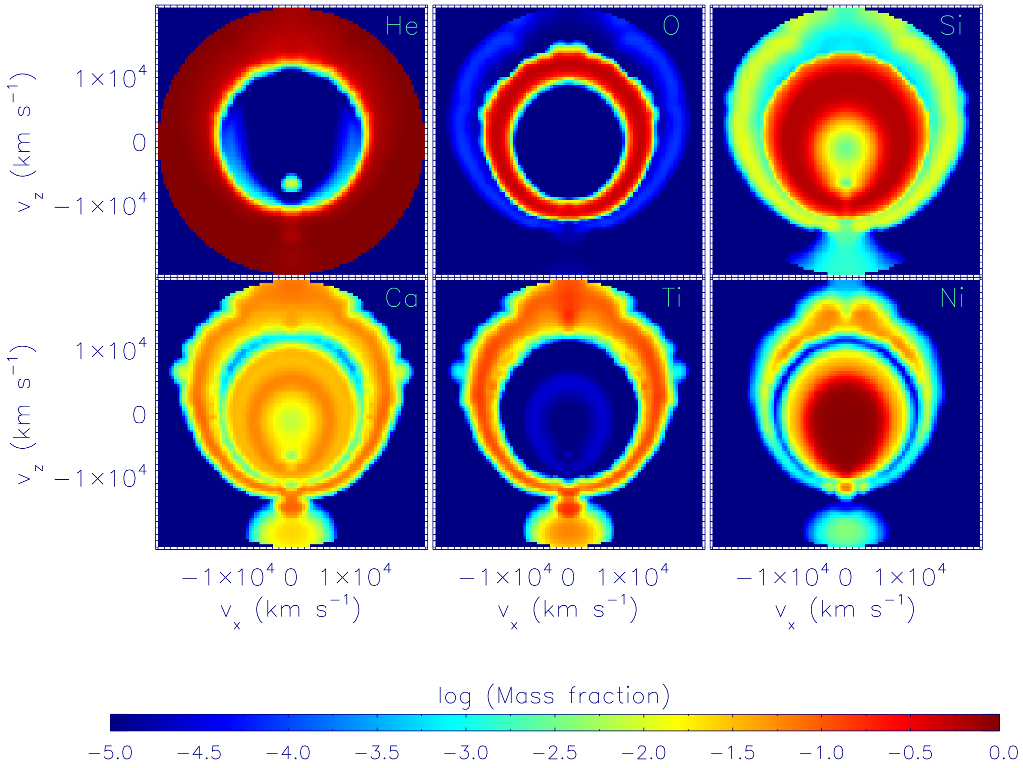

Figure 6.19: Final composition structure of the sub-Chandrasekhar-mass model. The individual panels show the mass fractions of He, O, Si, Ca, Ti and Ni (from top left to bottom right, respectively). The model is radially symmetric about the z-axis.

Table 6.3: Nucleosynthesis yields of selected species for the sub-Chandrasekhar-mass model. Given are the total masses per species in units of the solar mass.

	Core detonation	Shell detonation	Full model
He	$5.79 \cdot 10^{-6}$	$8.29 \cdot 10^{-2}$	$8.29 \cdot 10^{-2}$
O	$1.38 \cdot 10^{-1}$	$2.89 \cdot 10^{-6}$	$1.38 \cdot 10^{-1}$
Na	$1.80 \cdot 10^{-5}$	$2.65 \cdot 10^{-11}$	$1.80 \cdot 10^{-5}$
Si	$2.66 \cdot 10^{-1}$	$4.86 \cdot 10^{-4}$	$2.66 \cdot 10^{-1}$
S	$1.28 \cdot 10^{-1}$	$2.20 \cdot 10^{-3}$	$1.30 \cdot 10^{-1}$
Ca	$2.00 \cdot 10^{-2}$	$4.67 \cdot 10^{-3}$	$2.47 \cdot 10^{-2}$
Ti	$7.24 \cdot 10^{-6}$	$7.93 \cdot 10^{-3}$	$7.93 \cdot 10^{-3}$
Cr	$3.92 \cdot 10^{-4}$	$1.13 \cdot 10^{-2}$	$1.17 \cdot 10^{-2}$
Fe	$8.12 \cdot 10^{-3}$	$7.89 \cdot 10^{-3}$	$1.60 \cdot 10^{-2}$
Ni	$1.71 \cdot 10^{-1}$	$8.78 \cdot 10^{-4}$	$1.72 \cdot 10^{-1}$
Other	$7.85 \cdot 10^{-2}$	$7.80 \cdot 10^{-3}$	$8.63 \cdot 10^{-2}$
Total	$8.10 \cdot 10^{-1}$	$1.26 \cdot 10^{-1}$	$9.36 \cdot 10^{-1}$

model and compare them to the observational sample of 1991bg-like objects and contrast them to the result of the merger model presented in Section 6.2. To do this, we took the tracer particles from the hydrodynamics simulation, which was extended up to the phase of homologous expansion, and mapped their final density structure to a 80 × 160 grid. Together with the nucleosynthesis yields from a post-processing calculation as described by Travaglio et al. (2004), this yields the input model (see Figure 6.19 for the compositional structure). For the radiative transfer simulation this 2D model is re-mapped to a 3D Cartesian grid of size 100^3 which co-expands with the ejecta.

We then follow the radiative transfer over 111 time steps from 2 to 120 days after the explosion, yielding a width of $\Delta \ln(t) = 0.037$ for the individual time steps. Using our detailed ionization treatment and the cd23_gf-5 atomic data set, we simulated the propagation of $20 \cdot 10^6$ packets. To speed up the initial phase of the calculation we made use of our initial grey approximation (Section 4.3.6) employing the parameterized grey opacity ($\tau_{\mathrm{grey,min}} = 400$, $N_{\mathrm{grey}} = 30$). The first ten time steps were treated in LTE.

6.3.1 Broad-band light curves

Figure 6.20 shows the synthetic light curves obtained for this model from our radiative transfer simulation. While some lines-of-sight reach about the right peak magnitudes in the B and V bands compared to the sample of 1991bg-like objects, some of the redder bands (R,I,J and H) are generally too bright. The V and R bands tend to show a pronounced shoulder after B-band maximum which for some lines-of-sight is even the brightest point in these bands. Although the peak magnitude in the K band matches quite well, it shows a secondary maximum which is not observed in 1991bg-like objects. However, we note that the observational coverage there is not good.

The initial spikes of our light curves which are particularly prominent in the bolometric and U and B curves are a result of the peculiar nucleosynthesis in this type of model. Due to the helium shell detonation radioactive material occurs up to the outermost layers where the densities are very low. Thus energy deposited by decaying radioactive isotopes will escape immediately, leading to increased luminosities at early times. This correlation between the distribution of radioactive isotopes and the initial brightness of the light curves can also be seen in the dependence of the initial spikes on the various lines-of-sight. Observing the supernova from the northern hemisphere, where more of the shell material was burned and distributed to higher velocities (Figure 6.19), the initial luminosities are brighter. A second effect which contributes to the fast rise of the luminosity in this model is the special composition of the outer layers, where incomplete burning produces significantly more of the short-lived radioactive isotopes ^{48}Cr and ^{52}Fe [$M_{\mathrm{shell}}\left(^{48}\mathrm{Cr}\right) = 1.12 \cdot 10^{-2}\,\mathrm{M}_\odot$, $M_{\mathrm{shell}}\left(^{52}\mathrm{Fe}\right) = 7.6 \cdot 10^{-3}\,\mathrm{M}_\odot$] than of the longer-lived ^{56}Ni [$M_{\mathrm{shell}}\left(^{56}\mathrm{Ni}\right) = 8.4 \cdot 10^{-4}\,\mathrm{M}_\odot$]. This leads to a fast energy release.

We note that our initial grey approximation also plays a role here, making it easier to escape for radiation at early times. But even without this approximation there will be an increased flux at the very early times, however, not as sharply peaked. The exact shape of the light curves at early epochs will be addressed in future work by performing additional simulations which start significantly earlier than the current one and make no use of the initial grey approximation. Ultimately the initially high luminosities of this model will be a constraint to rule it out if photometric data for 1991bg-like objects at sufficiently early times become available and show no initial spikes. The currently available data set, however, does not cover epochs early enough to do so. Due to its origin close to the surface the initially escaping radiation will not be fully thermalized such that the initial spikes might be detectable as UV or X-ray flashes as well if those models are realized in Nature.

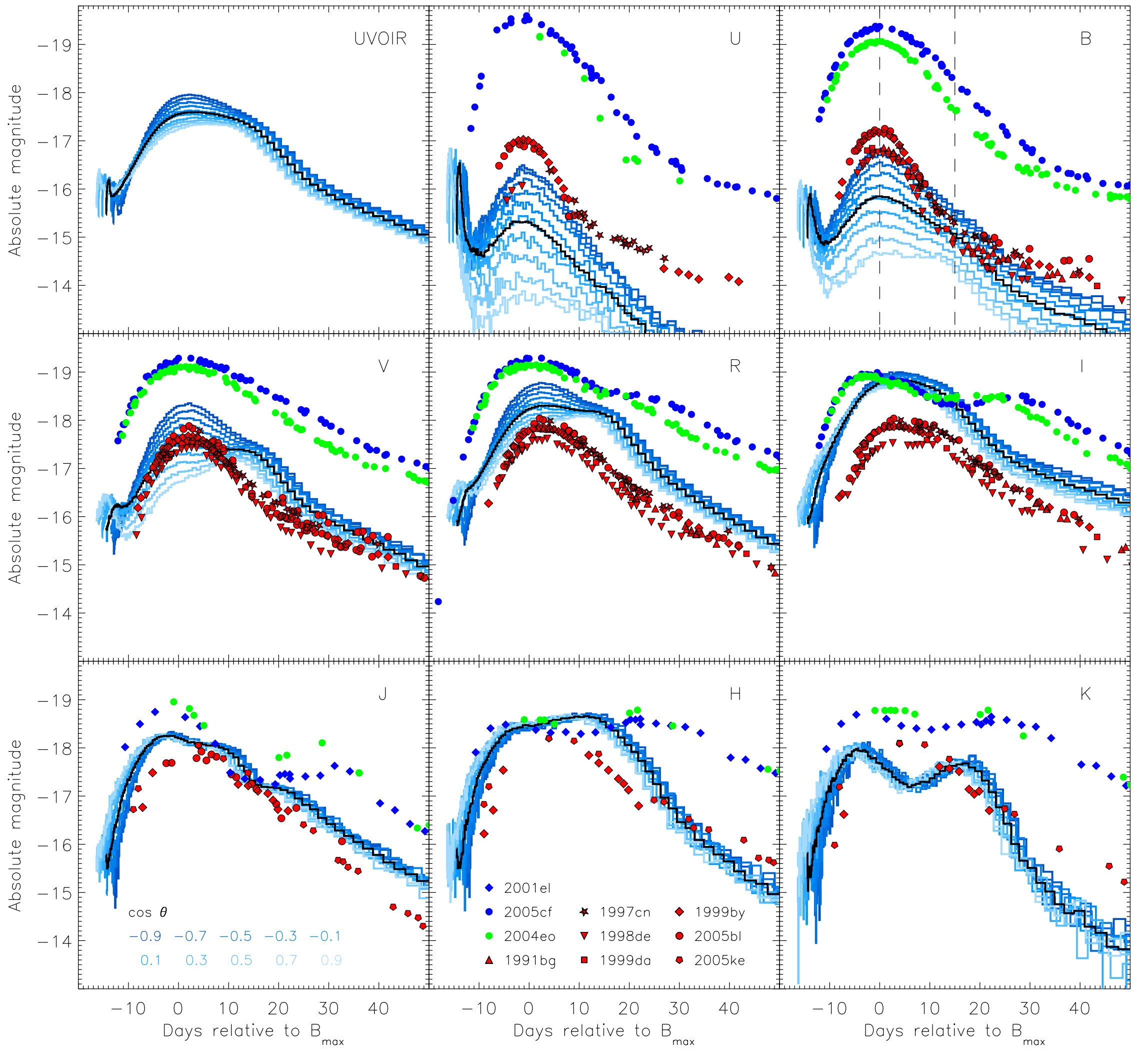

Figure 6.20: Synthetic light curves for the sub-Chandrasekhar-mass model compared to a sample of 1991bg-like objects (red, Taubenberger et al. 2008). The black line shows the angle-averaged light curve. The bluish lines are light curves observed along ten different lines-of-sight in polar angle θ as indicated by the colour coded labels in the lower left panel. Each represents an equally-sized solid-angle bin in $\cos\theta$ (the model is rotationally symmetric about the polar axis). For comparison observations of bright (2001el, Krisciunas et al. 2003; 2005cf, Pastorello et al. 2007b) and faint (2004eo, Pastorello et al. 2007a) normal SNe Ia are shown. The panels correspond to the different broad-band filters as indicated. For the B band vertical lines at maximum light and 15 days thereafter help to identify $\Delta m_{15}\,(B)$.

Neglecting these initial spikes, our light curves rise significantly faster $t_{\rm max}\,(B) \sim 14\,\rm d$ than those of normal SNe Ia [$t_{\rm max}\,(B) \sim 18\ldots20\,\rm d$; Riess et al. (1999), Conley et al. (2006)]. This is most likely due to their lower total mass compared to Chandrasekhar-mass models and would still be in agreement with the observed properties of 1991bg-like objects. However, despite this low mass, their decline is too slow compared to the 1991bg-like objects. The average value for $\Delta m_{15}\,(B)$ is ~ 0.8 and even the fastest line-of-sight yields only ~ 1.3 compared to ~ 1.9 for 1991bg-like objects. Curiously these $\Delta m_{15}\,(B)$-values are actually *smaller* than those observed in our merger model which has a mass significantly above the Chandrasekhar limit ($1.78\,\rm M_\odot$). This is a result of the peculiar shell composition of this model (see Section 6.3.3).

Another problem concerns the colours of the model. Already at maximum light these are much too red compared to the 1991bg-like objects and this persists until the end of our simulation. Moreover, the scatter owing to asymmetries in the model is huge. It reaches from ~ 3 magnitudes in the U band over ~ 2 magnitudes in B, V and R to almost none in the NIR bands (the observed spread there is on the level of the Monte Carlo noise). This strong scatter, which also significantly affects the light curve shape, poses an additional problem for the model since all light curves shapes should occur in Nature if this model was realized. We will discuss the origin of this large scatter in Section 6.3.3.

Summarizing all this, our sub-Chandrasekhar-mass model does much worse when compared to the 1991bg-like objects than the merger model discussed in Section 6.2. Moreover, it matches none of the currently observed SNe Ia particularly well due to its very red colours and peculiar light curve shapes.

6.3.2 Spectral evolution

Figure 6.21 shows the spectral evolution of our sub-Chandrasekhar-mass model compared to the complete spectroscopic coverage of the photospheric phase of SN 2005bl according to Taubenberger et al. (2008). The red histograms show the angle-averaged spectra. The bluish histograms show spectra as seen from the ten equally-sized solid-angle bins in $\cos\theta$ already used for the light curve plots. The overall trend of too red colours compared to 1991bg-like objects which we inferred from the light curves is also obvious here. Moreover, this model lacks the strong Si II features ($\lambda\lambda 5958, 5979$; $\lambda\lambda 6347, 6371$) observed in 1991bg-like objects since there is an insufficient amount of silicon in the outer layers (see Table 6.3) while the total amount of silicon produced in the model is comparable to that of normal SNe Ia. Similarly, basically all oxygen originates from the core detonation such that the O I feature at $\lambda\lambda 7772, 7774, 7775$ is also too weak. In contrast, the Ca II NIR triplet has about the right strength (calcium is the only intermediate-mass element of which a significant amount is synthesized in the initial helium shell, Figure 6.19). However, its absorption trough extends too far to the blue compared to SN 2005bl for all epochs, thus indicating that the calcium is located at too high velocities. The Na I D doublet ($\lambda\lambda 5890, 5896$), observed in late time spectra of 1991bg-like objects, is completely lacking.

Compared to the merger model, there is only one point in which the sub-Chandrasekhar-mass model reproduces SN 2005bl better than the merger model does (Figure 6.16). This is the characteristic Ti II absorption trough between 4000 and 4400 Å which is very pronounced in the sub-Chandrasekhar-mass model due to the titanium produced in the helium shell ($7.93 \cdot 10^{-3}\,\mathrm{M}_\odot$; for comparison the merger models has only $1.11 \cdot 10^{-5}\,\mathrm{M}_\odot$ of titanium). This further strengthens the conclusion drawn in Section 6.2.2 that the strong Ti II absorption in the spectra of 1991bg-like events might be associated with a real real titanium abundance enhancement in these objects compared to standard models.

Concerning the viewing-angle dependence, lines-of-sight from the southern hemisphere are preferred for modelling 1991bg-like objects. This preference is based on both the overall flux distribution which is also reflected in the light curves and the individual spectroscopic features. These are

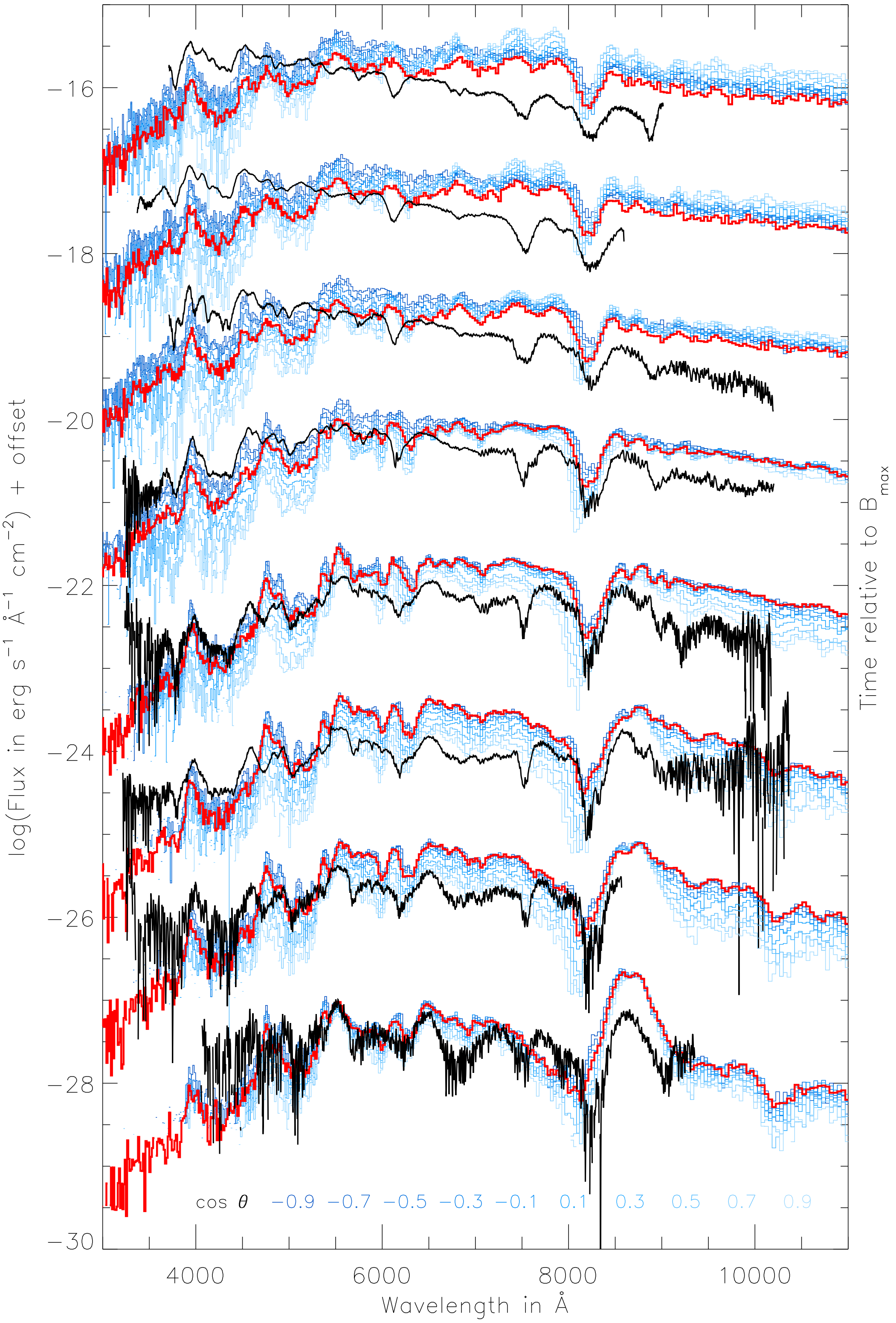

Figure 6.21: Angle-averaged spectral evolution of the sub-Chandrasekhar-mass model (red line) compared to SN 2005bl (black) for different epochs. The bluish lines show model spectra as seen from 10 equally-sized solid-angle bins in $\cos\theta$ to indicate the scatter resulting from the model asymmetries.

slightly more promising when seen from the southern hemisphere, since the helium detonation produced less iron-group elements there (Figure 6.19) such that the shielding of the inner core (see next section) is somewhat weaker and features from intermediate-mass elements are slightly stronger. Note again the problem that the other lines-of-sight should be realized as well in Nature.

6.3.3 Understanding the asymmetry effects

Due to the single-point ignition our model shows strong ejecta asymmetries (Figure 6.19) which can be divided into two main categories. First, the helium shell material shows a spatial gradient in the abundance of iron-group elements which decreases from the northern hemisphere, where the burning started, to the southern hemisphere. Second, the ignition point of the secondary core detonation is offset by ∼ 20% of the maximum velocity (20 960 km s^{-1}) of the model due to the off-centre convergence of the shock waves of the helium detonation which sweeps around the core. Sim et al. (2007) have shown that such an off-centre ignition can lead to significant viewing angle-effects in observable properties of SNe Ia. To investigate the extent to which the scatter observed in the light curves of our sub-Chandrasekhar-mass model (Figure 6.20) is due to the one or the other of these effects, we constructed a toy model which contains only the material which results from the secondary core detonation. The composition structure of this model is shown in Figure 6.22.

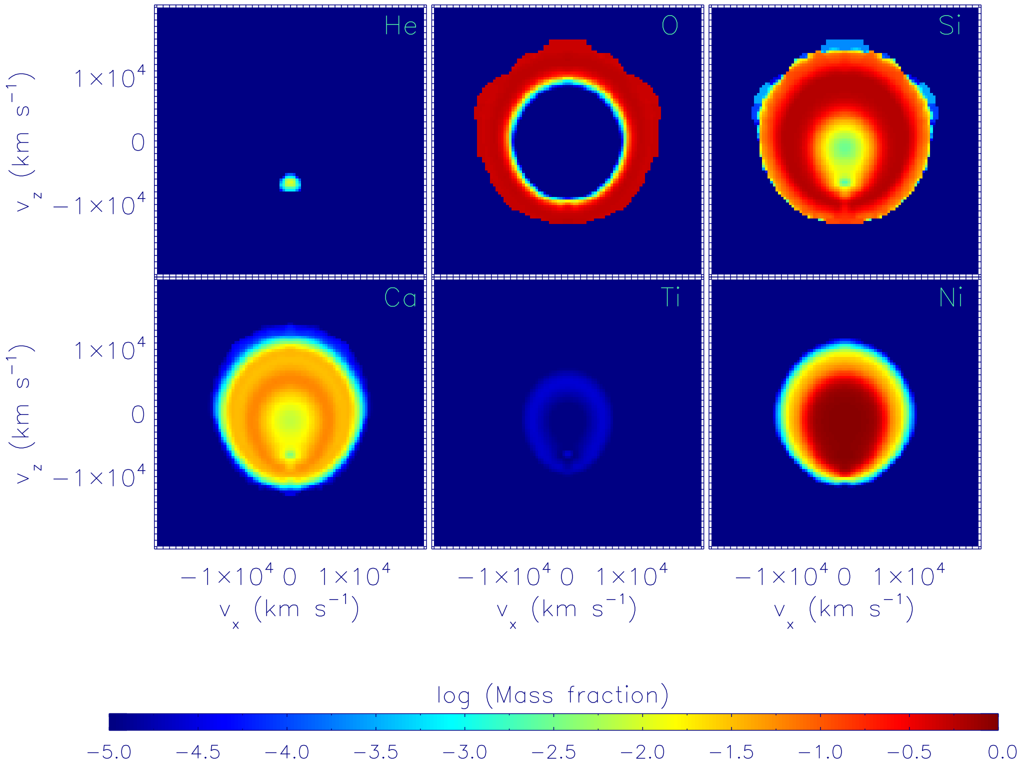

Figure 6.22: Composition structure of the sub-Chandrasekhar-mass model after removing the helium shell material. The individual panels show the mass fractions of He, O, Si, Ca, Ti and Ni (from top left to bottom right, respectively). The model is radially symmetric about the z-axis.

The light curves obtained for this toy model are shown in Figure 6.23. First we note that there are no initial spikes in these models as it was the case for the light curves of the full model (Figure 6.20). This is because there are no radioactive isotopes close to the surface of the toy model.

Moreover, the scatter in the light curves of the toy model is small compared to the light curves of the full model (Figure 6.20). It reaches at most $\sim 1\,\mathrm{mag}$ in U and $\sim 0.5\,\mathrm{mag}$ in B band around maximum light. For the other bands it is negligible. This makes clear, that the compositional asymmetry of the helium shell material is the main origin for the scatter observed in the full model. It becomes so strong since the incomplete burning in the helium shell produces relatively large amounts of iron-group material, in particular chromium and titanium (Table 6.3). Having a wealth of strong lines in the UV and blue wavelength range, titanium is very efficient in blocking radiation in these bands and redistributing it to longer wavelengths. Thus the emerging radiation is very sensitive to a spatial gradient in the titanium abundance as we find it in the full model between the northern and the southern hemisphere (Figure 6.19).

Comparing the angle-averaged light curves of Figure 6.20 and Figure 6.23, we see moreover that this line blocking and flux redistribution by the helium shell material is also responsible for the peculiar light curve shapes of our sub-Chandrasekhar-mass model which decline very slowly and show extremely red colours. Since the helium shell material is the only part in which the outcome of our sub-Chandrasekhar-mass model differs significantly from other explosion models (the core detonation material yields a rather normal abundance stratification with a bubble of iron-group elements in the centre enclosed by a shell of intermediate-mass elements and unburned material), it is not surprising that it is responsible for the observed peculiarities. However, our findings differ from earlier studies of sub-Chandrasekhar-mass models by Höflich & Khokhlov (1996). They concluded that processed helium shell material causes the light curves of these models to be too blue compared to observed SNe Ia.

The same effect also affects the spectroscopic features of our sub-Chandrasekhar-mass model. To highlight this we compare the maximum light spectra for the full model and the toy model in Figure 6.24. While the toy model is rather similar to the spectra of normal SNe Ia showing all the characteristic lines of intermediate-mass elements typical for SNe Ia, the full model is totally dominated by titanium and chromium. These block almost all the flux below 5000 Å and redistribute it to longer wavelengths, which can be clearly seen via our colour coding in the plots. Located outside of most of the intermediate-mass elements, this redistribution hides almost all the characteristic absorption features of intermediate-mass elements. Thus the maximum light spectrum of the full model shown in Figure 6.24 shows only a very weak feature of the Si II doublet at $\lambda\lambda 6347, 6371$. The only strong feature of intermediate-mass elements which is present in this spectrum is the Ca II NIR triplet [calcium is the only intermediate-mass element of which a significant amount ($4.67 \cdot 10^{-3}\,\mathrm{M}_\odot$) is synthesized in the initial helium shell]. Finally we note that despite the large amount of unburned helium ($8.29 \cdot 10^{-2}\,\mathrm{M}_\odot$) which is left in the initial helium shell we do not see prominent helium features in our synthetic spectra. This could be related to the lack of a treatment of non-thermal excitation and ionization in our code. We note, however, that Nugent et al. (1997) in a simulation including non-thermal effects for a sub-Chandrasekhar-mass model with an even more massive helium shell ($0.2\,\mathrm{M}_\odot$) also found no strong evidence of helium lines.

Summarizing these results we conclude that it will be difficult to find good agreement between the sub-Chandrasekhar-mass models of Fink et al. (2009) and normal SNe Ia, especially since these are

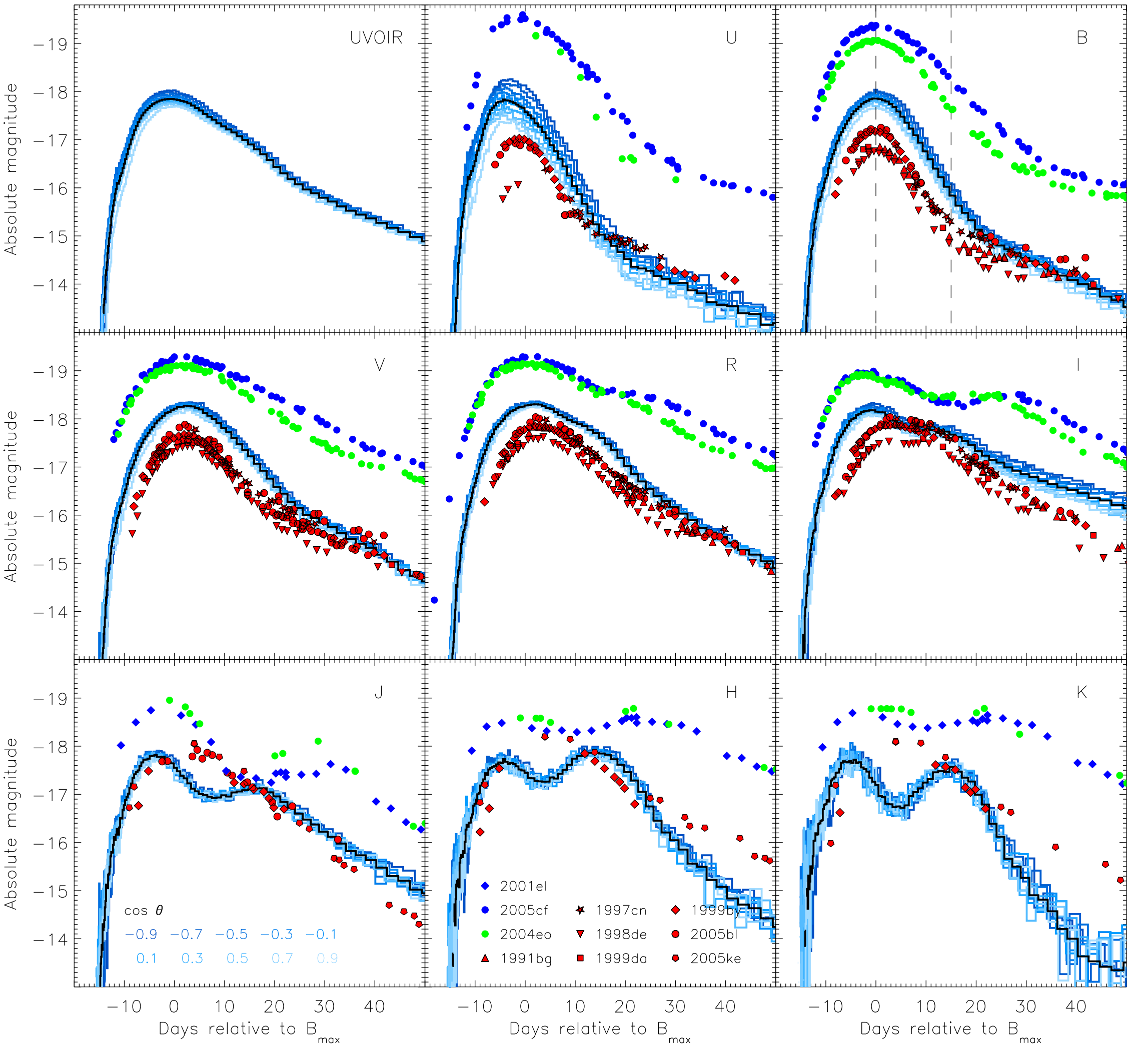

Figure 6.23: Synthetic light curves for the toy model for which the material from the helium shell was stripped from the sub-Chandrasekhar-mass model. For comparison we show the same sample of objects as in Figure 6.20. The black line shows the angle-averaged light curve. The bluish lines are light curves observed along ten different lines-of-sight in polar angle θ as indicated by the colour coded labels in the lower left panel. Each represents an equally-sized solid-angle bin in $\cos\theta$ (the model is rotationally symmetric about the polar axis). The panels correspond to the different broad-band filters as indicated. For the B band vertical lines at maximum light and 15 days thereafter help to identify $\Delta m_{15}(B)$.

already models of minimum shell-masses. We note that other models of the sequence of Fink et al. (2009) with a different WD shell-mass ratio might do slightly better, since the minimum shell-mass decreases for more massive WDs. In contrast, however, the density of the WD itself increases thereby leading to a more complete degree of burning and less intermediate-mass elements which again poses a challenge when compared to the observations. To draw final conclusions on this we need to investigate all models of this sequence in detail which is left for future work. Approaching the Chandrasekhar limit, however, these models will share the same fate as the Chandrasekhar mass pure detonation model which is known to incinerate almost the entire WD to nuclear statistical equilibrium (Arnett 1969) and thus has been ruled out observationally.

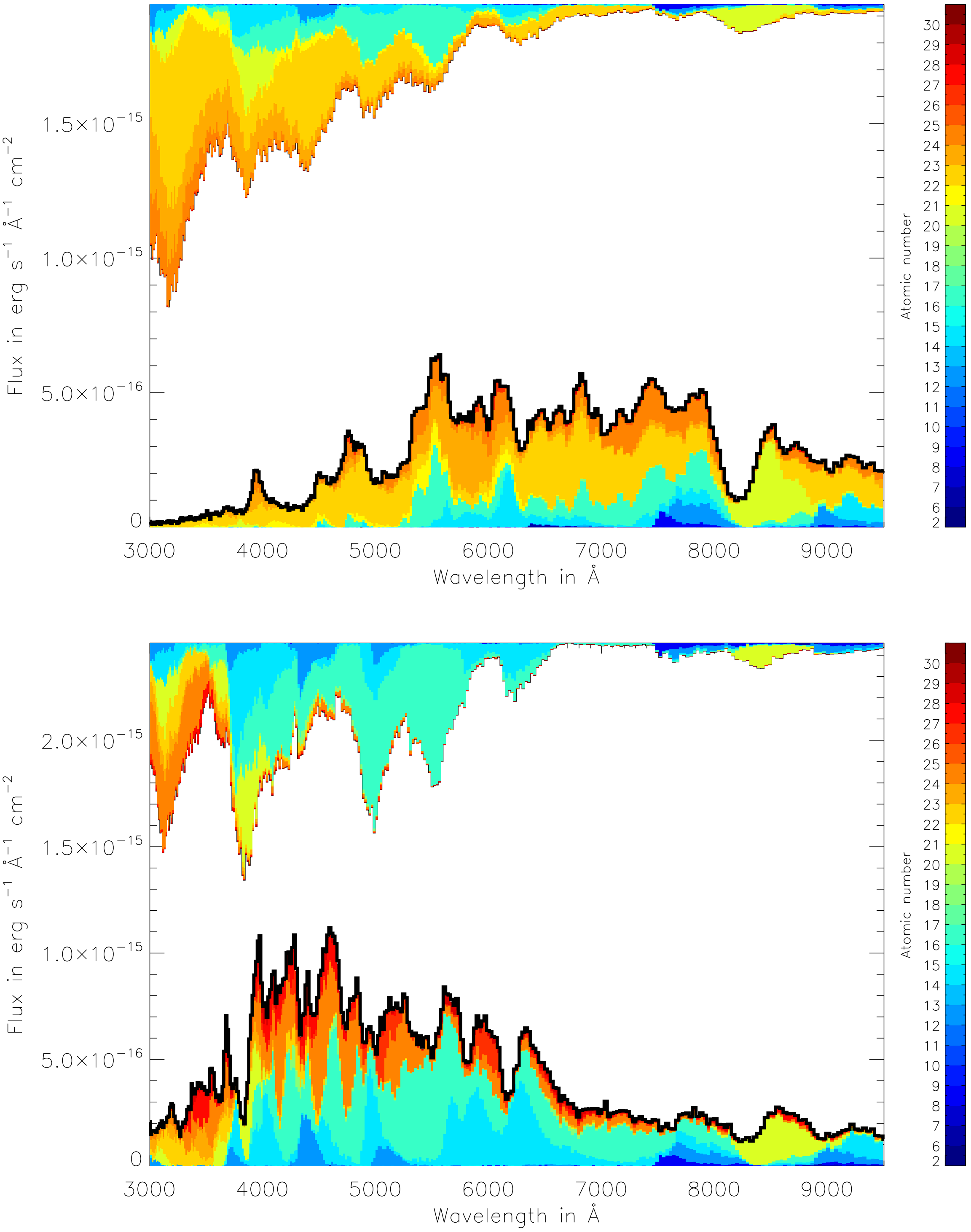

Figure 6.24: Angle-averaged maximum light spectrum (thick black line) of the sub-Chandrasekhar-mass model (top) compared to a toy model for which the material from the helium shell was removed (bottom). The colour coding indicates the element(s) responsible for both bound-bound emission and absorption of quanta in the Monte Carlo simulation. The region below the synthetic spectrum is colour coded to indicate the fraction of escaping quanta in each wavelength bin which last interacted with a particular element (the associated atomic numbers are illustrated in the colour bar). Similarly, the coloured regions above the spectra indicate which elements were last responsible for removing quanta from the wavelength bin (either by absorption or scattering/fluorescence).

Keeping in mind the results from our toy model, the models with lower WD masses could reproduce the spectral features of SNe Ia quite well if the shell material was not there. Alternatively a change in composition of the material in the initial helium shell to intermediate-mass elements, rather than iron-group material could help. The degree of burning in this shell material depends very sensitively on the initial abundance of carbon which in turn depends strongly on triple α-reactions during previous hydrostatic burning and dredge-up phases from the core (Shen & Bildsten 2009). Due to the large uncertainties in these values, it is possible that systems producing more intermediate-mass elements and less titanium and chromium exist. The exact effect of a non-zero carbon abundance in the initial helium shell, however, must be investigated by detailed follow-up studies.

7 Conclusions

The main objective of this work was to develop a multi-dimensional radiative transfer code that is capable of deriving synthetic observables for multi-dimensional hydrodynamic explosion models from first principles. For this purpose we followed the approach of Lucy (2002, 2003) and extended the grey time-dependent 3D Monte Carlo radiative transfer code of Sim (2007) to a non-grey opacity treatment. The new code, ARTIS (see Chapter 4), treats the γ-deposition and spectrum formation in detail and solves the ionization balance together with the thermal balance equation consistently with the radiation field. Line formation is treated in the Sobolev approximation using the macro-atom approach of Lucy (2002, 2003) to model atomic physics in detail. This allows parameter-free radiative transfer simulations for 3D hydro models with a maximum of predictive power to be made.

To test this code, we applied it to the well-studied one-dimensional deflagration model W7 (Nomoto et al. 1984) which is known to reproduce the spectroscopic features of observed SNe Ia quite well. From this we found good agreement with both earlier work using different codes [SEDONA (Kasen et al. 2006); STELLA (Blinnikov & Sorokina 2002, Blinnikov et al. 2006)] and observations [SN 1994D (Patat et al. 1996); SN 2001el (Krisciunas et al. 2003)]. Rather than adopting LTE, we assume photoionization equilibrium and solve the ionization balance equations using rates consistent with the radiation field. We showed that this leads to significant differences in the ionization structure after maximum light, which strongly affect spectra and light curves. The macro-atom formalism allows us to avoid introducing a parameterized treatment of line fluorescence, such that we account for the differing contributions of resonance scattering and fluorescence in different lines. This turns out to be a crucial point if the redistribution of flux due to the vast number of iron-group lines is to be modelled self-consistently (see Figure 5.8), which is of particular relevance for the NIR light curves and spectra. Another crucial point in modelling the redistribution is the atomic data set. For accurate results an atomic data set as complete as possible should be used. However, this poses enormous computational demands.

To demonstrate the multi-dimensional capabilities of the code we have presented calculations for an ellipsoidal toy model as an example. As expected [e.g. from the grey study by Sim (2007) for a similar model], light curves observed along the minor axes are brighter than those observed along the major axis. The sensitivity decreases with time, as the ejecta become less optically thick, and from blue to red wavelengths. If line-of-sight effects due to asymmetric explosions have a significant influence on the scatter around the Phillips relation of SNe Ia (Phillips 1993), this could explain why the NIR light curves seem to be more homogeneous and thus most promising for cosmological distance measurements. However more detailed studies are needed to investigate this fully for realistic models.

In Chapter 6 we started to apply our code to hydrodynamical explosion models of different explosion scenarios which have been recently studied by the MPA supernova group. Our results on this are mainly meant as a proof-of-concept and extended follow-up studies are needed to explore the full parameter space of the proposed explosion scenarios. However, we can already draw interesting conclusions from the limited set of models which we have investigated. Comparing a delayed detonation and a deflagration model which both synthesize about the amount of ^{56}Ni expected for faint SNe Ia, we found that the outcome of the delayed detonation scenario is in good agreement with the observational data. The deflagration model, in contrast, produces peculiar light curves and spectra. Interestingly the spectra of this model compare remarkably well to the highly peculiar 2002cx-like objects, for which a relation to the pure deflagration scenario was proposed (Branch et al. 2004, Jha et al. 2006, Phillips et al. 2007).

Moreover, we were able to show that the faint end of the recently-proposed scenario of nearly equal-mass WD mergers (Pakmor et al. 2009) reproduces the observational characteristics of subluminous 1991bg-like events remarkably well. For the first time this provides a theoretical model for these so far unexplained objects. Originating from a different progenitor scenario this strongly supports that these objects form a distinct sub-class of SNe Ia. Although indicated by their peculiar spectroscopic features, this was hotly debated since there are also objects of transitional character between the normal SNe Ia and 1991bg-like objects. Having studied only one particular realization of the proposed merger scenario there is clearly the need to extend this study in the future to explore the parameter space, i.e. the mass ratio of the merging WDs. Moreover, studying the outcome of the merger of more massive WDs will be interesting. Possibly these could provide a model for recently observed superluminous events such as SN 2003fg (Howell et al. 2006), SN 2006gz (Hicken et al. 2007) and SN 2009dc (Yamanaka et al. 2009).

Finally, we inspected one of the sub-Chandrasekhar-mass models of the simulations of Fink et al. (2009). Since such models have been proposed as an alternative explanation of 1991bg-like objects, we chose a model producing a similar amount of ^{56}Ni than the merger model of Pakmor et al. (2009) to compare the two scenarios. From this we find that the sub-Chandrasekhar-mass model cannot explain the 1991bg-like objects due to the comparably large amount of iron-group material which is synthesized by the initial detonation in the helium shell. This leads to a strong blocking of flux at UV and blue wavelengths which is redistributed to longer wavelengths. Thereby the characteristic absorption features of intermediate-mass elements are wiped out. This is expected to be a general problem of the sub-Chandrasekhar-mass models compared to observed SNe Ia. However, detailed follow-up studies for the full model sequence of Fink et al. (2009) are required to confirm this since different WD shell-mass ratios might lead to different results.

Currently a meaningful use of ARTIS is restricted to the early phase of the supernova evolution (i.e. maximum light and a few weeks thereafter). At later epochs our simplified treatment of the excitation state (Section 4.4.2) and the use of the van Regemorter and Seaton approximations (Section 3.4.3) for the collisional rates becomes questionable. This might be the reason for some of the discrepancies between our model spectra and the observational data at late epochs ($\sim$ 30 days after maximum light). To address this question a more sophisticated treatment of collisional interactions, based on tabulated cross-sections, should be added in the near future.

Another point which we lack at the moment is a detailed treatment of non-thermal excitation and ionization. This can already be relevant at early phases (see Baron et al. 1996 for a discussion). However, it is mainly important for the later epochs – particularly the modelling of the nebular phase. Since the outer ejecta are sufficiently optically thin at these times, nebular spectra provide a way to investigate the composition of the innermost regions of the supernova ejecta. Thus modelling nebular spectra makes it possible to probe those regions of an explosion model where thermonuclear burning is most effective (e.g. Mazzali et al. 1997). The most constraining results on explosion models will therefore come from self-consistent simulations of the whole spectral evolution from pre-maximum to the nebular phase. To our knowledge none of the codes simulating radiative transfer in supernovae is capable of doing this currently. Thus an appropriate extension of ARTIS which is straightforward in our Monte Carlo approach is of great interest and should be addressed in the near future. Moreover, a detailed treatment of polarization would provide a direct tool to investigate ejecta asymmetries and extend the range of data with which we can make meaningful comparisons.

Our development of a parameter-free multi-dimensional radiative transfer code is a major step towards closing the gap between hydrodynamical models of SN Ia explosions and observational data. It makes it feasible to directly compare the MPA in-house explosion models with observed spectra and light curves of SNe Ia. With the rapidly increasing quantity of observational data, this will help to identify the explosion mechanisms which drive these luminous objects and finally reveal the nature of the progenitor systems.

Acknowledgements

Here I would like to thank all the people who supported me during the past three years. First of all I thank my supervisor Wolfgang Hillebrandt for providing me the possibility to work on this interesting and challenging project and being there with help and advice when needed. By his scientific enthusiasm he created a very stimulating atmosphere in the supernova group.

Special thanks go to my advisor Stuart Sim for providing the grey Monte Carlo code on which the code developed during this thesis is based. The extensive discussions we had on radiative transfer, supernova physics, numerical problems in general and the secrets of Monte Carlo techniques in particular gave me a solid foundation to tackle this project. Finally I am indebted to him for proof-reading this thesis.

Moreover, I want to thank all the members of the thermonuclear supernova group at MPA for the good working atmosphere and inspiring discussions – not only at the institute but also during the time shared at the conferences at Ringberg Castle and in Cefalù. In particular I thank M. Fink, R. Pakmor and F. Röpke for providing the explosion models discussed in Chapter 6 and many discussions on hydrodynamics and nucleosynthesis modelling. S. Hachinger and S. Taubenberger shared their insight into the interpretation of observational supernova data with me, for which I am extremely grateful. A. Bauswein, R. Birkl, Á. Bogdán, L. Huedepohl and M. Obergaulinger have been excellent office mates.

D. Kasen (University of California, Santa Cruz), E. Sorokina (Sternberg Astronomical Institute, Moscow) and S. Blinnikov (Institute for Theoretical and Experimental Physics, Moscow) kindly provided light curves obtained with their radiative transfer codes which were used in Chapter 5 as comparison for our code.

Last but not least, I am deeply indebted to my parents, my brother and my grandmothers for their encouragement and unresting support throughout my life but particularly during the last few years. They have always been there to motivate me in difficult situations and provided the distraction needed once in a while.

Bibliography

Abbott D. C., Lucy L. B., 1985, Astrophysical Journal, 288, 679

Altavilla G., Fiorentino G., Marconi M., Musella I., Cappellaro E., Barbon R., Benetti S., Pastorello A., Riello M., Turatto M., Zampieri L., 2004, Monthly Notices of the Royal Astronomical Society, 349, 1344

Ambwani K., Sutherland P., 1988, Astrophysical Journal, 325, 820

Arnett W. D., 1969, Astrophysics and Space Science, 5, 180

Arnett W. D., 1982, Astrophysical Journal, 253, 785

Astier P., et al., 2006, Astronomy & Astrophysics, 447, 31

Auer L., 2003, in Ivan Hubeny D. M., Werner K., eds, Stellar Atmosphere Modeling Vol. 288 of ASP Conference Proceedings, Insight into Multi-Dimensional Transfer. Astronomical Society of the Pacific, p. 405

Auer L. H., 1968, Astrophysical Journal, 153, 783

Baade W., Zwicky F., 1934, Proceedings of the National Academy of Science, 20, 254

Barbon R., Buondí V., Cappellaro E., Turatto M., 1999, Astronomy and Astrophysics Supplement Series, 139, 531

Barbon R., Ciatti F., Rosino L., 1973, Astronomy & Astrophysics, 25, 241

Baron E., Bongard S., Branch D., Hauschildt P. H., 2006, Astrophysical Journal, 645, 480

Baron E., Hauschildt P. H., Mezzacappa A., 1996, Monthly Notices of the Royal Astronomical Society, 278, 763

Baron E., Hauschildt P. H., Nugent P., Branch D., 1996, Monthly Notices of the Royal Astronomical Society, 283, 297

Benetti S., Cappellaro E., Mazzali P. A., Turatto M., Altavilla G., Bufano F., Elias-Rosa N., Kotak R., Pignata G., Salvo M., Stanishev V., 2005, Astrophysical Journal, 623, 1011

Benetti S., et al., 2004, Monthly Notices of the Royal Astronomical Society, 348, 261

Benz W., Cameron A. G. W., Press W. H., Bowers R. L., 1990, Astrophysical Journal, 348, 647

Bessell M. S., 1990, Publications of the Astronomical Society of the Pacific, 102, 1181

Bessell M. S., Brett J. M., 1988, Publications of the Astronomical Society of the Pacific, 100, 1134

Bildsten L., Shen K. J., Weinberg N. N., Nelemans G., 2007, Astrophysical Journal Letters, 662, L95

Blinnikov S., Sorokina E., 2002, eprint arXiv:astro-ph/0212567

Blinnikov S. I., Röpke F. K., Sorokina E. I., Gieseler M., Reinecke M., Travaglio C., Hillebrandt W., Stritzinger M., 2006, Astronomy & Astrophysics, 453, 229

Branch D., Baron E., Hall N., Melakayil M., Parrent J., 2005, Publications of the Astronomical Society of the Pacific, 117, 545

Branch D., Baron E., Thomas R. C., Kasen D., Li W., Filippenko A. V., 2004, Publications of the Astronomical Society of the Pacific, 116, 903

Branch D., Buta R., Falk S. W., McCall M. L., Uomoto A., Wheeler J. C., Wills B. J., Sutherland P. G., 1982, Astrophysical Journal, 252, L61

Branch D., Fisher A., Nugent P., 1993, Astronomical Journal, 106, 2383

Branch D., Lacy C. H., McCall M. L., Sutherland P. G., Uomoto A., Wheeler J. C., Wills B. J., 1983, Astrophysical Journal, 270, 123

Branch D., Livio M., Yungelson L. R., Boffi F. R., Baron E., 1995, Publications of the Astronomical Society of the Pacific, 107, 1019

Caldwell R. R., Dave R., Steinhardt P. J., 1998, Physical Review Letters, 80, 1582

Cappellaro E., 2003, in Weiler K., ed., Supernovae and Gamma-Ray Bursters Vol. 598 of Lecture Notes in Physics, Berlin Springer Verlag, Supernova Rates. pp 37–46

Cappellaro E., Evans R., Turatto M., 1999, Astronomy & Astrophysics, 351, 459

Cappellaro E., Turatto M., 2001, in Vanbeveren D., ed., The Influence of Binaries on Stellar Population Studies Vol. 264 of Astrophysics and Space Science Library, Supernova Types and Rates. pp 199–+

Cardelli J. A., Clayton G. C., Mathis J. S., 1989, Astrophysical Journal, 345, 245

Carroll S. M., Press W. H., Turner E. L., 1992, Annual Review of Astronomy and Astrophysics, 30, 499

Castor J. I., 1970, Monthly Notices of the Royal Astronomical Society, 149, 111

Castor J. I., 2004, Radiation Hydrodynamics. Cambridge University Press, Cambridge, UK

Chandrasekhar S., 1931, Monthly Notices of the Royal Astronomical Society, 91, 456

Chiappini C., Matteucci F., Romano D., 2001, Astrophysical Journal, 554, 1044

Colgate S. A., McKee C., 1969, Astrophysical Journal, 157, 623

Conley A., et al., 2006, Astronomical Journal, 132, 1707

Crotts A. P. S., Yourdon D., 2008, Astrophysical Journal, 689, 1186

de Bernardis P., et al., 2000, Nature, 404, 955

de Vaucouleurs G., Corwin H. G. J., 1985, Astrophysical Journal, 295, 287

Dunkley J., Komatsu E., Nolta M. R., Spergel D. N., Larson D., Hinshaw G., Page L., Bennett C. L., Gold B., Jarosik N., Weiland J. L., Halpern M., Hill R. S., Kogut A., Limon M., Meyer S. S., Tucker G. S., Wollack E., Wright E. L., 2009, Astrophysical Journal Supplement Series, 180, 306

Eastman R. G., Pinto P. A., 1993, Astrophysical Journal, 412, 731

Efstathiou G., 2000, Monthly Notices of the Royal Astronomical Society, 317, 697

Efstathiou G., Sutherland W. J., Maddox S. J., 1990, Nature, 348, 705

Einstein A., 1917, Sitzungsberichte der Königlich Preußischen Akademie der Wissenschaften (Berlin), Seite 142-152., pp 142–152

Eisenstein D. J., et al., 2005, Astrophysical Journal, 633, 560

Elias J. H., Frogel J. A., Hackwell J. A., Persson S. E., 1981, Astrophysical Journal Letters, 251, L13

Elias J. H., Matthews K., Neugebauer G., Persson S. E., 1985, Astrophysical Journal, 296, 379

Ercolano B., Barlow M. J., Storey P. J., Liu X.-W., 2003, Monthly Notices of the Royal Astronomical Society, 340, 1136

Filippenko A. V., 1988, Astronomical Journal, 96, 1941

Filippenko A. V., 1997, Annual Review of Astronomy and Astrophysics, 35, 309

Filippenko A. V., Richmond M. W., Branch D., Gaskell M., Herbst W., Ford C. H., Treffers R. R., Matheson T., Ho L. C., Dey A., Sargent W. L. W., Small T. A., van Breugel W. J. M., 1992, Astronomical Journal, 104, 1543

Filippenko A. V., Richmond M. W., Matheson T., Shields J. C., Burbidge E. M., Cohen R. D., Dickinson M., Malkan M. A., Nelson B., Pietz J., Schlegel D., Schmeer P., Spinrad H., Steidel C. C., Tran H. D., Wren W., 1992, Astrophysical Journal Letters, 384, L15

Fink M., Hillebrandt W., Röpke F. K., 2007, Astronomy & Astrophysics, 476, 1133

Fink M., Röpke F. K., Hillebrandt W., 2009, Double-detonation sub-Chandrasekhar supernovae with minimum shell masses, in preparation

Friend D. B., Castor J. I., 1983, Astrophysical Journal, 272, 259

Gallagher J. S., Garnavich P. M., Berlind P., Challis P., Jha S., Kirshner R. P., 2005, Astrophysical Journal, 634, 210

Gamezo V. N., Khokhlov A. M., Oran E. S., Chtchelkanova A. Y., Rosenberg R. O., 2003, Science, 299, 77

Garavini G., Nobili S., Taubenberger S., Pastorello A., Elias-Rosa N., Stanishev V., Blanc G., Benetti S., Goobar A., Mazzali P. A., Sanchez S. F., Salvo M., Schmidt B. P., Hillebrandt W., 2007, Astronomy & Astrophysics, 471, 527

Garnavich P. M., Bonanos A. Z., Krisciunas K., Jha S., Kirshner R. P., Schlegel E. M., Challis P., Macri L. M., Hatano K., Branch D., Bothun G. D., Freedman W. L., 2004, Astrophysical Journal, 613, 1120

Guy J., Astier P., Nobili S., Regnault N., Pain R., 2005, Astronomy & Astrophysics, 443, 781

Hachinger S., Mazzali P. A., Tanaka M., Hillebrandt W., Benetti S., 2008, Monthly Notices of the Royal Astronomical Society, 389, 1087

Hachinger S., Mazzali P. A., Taubenberger S., Pakmor R., Hillebrandt W., 2009, Monthly Notices of the Royal Astronomical Society

Hamuy M., et al., 1993, Astronomical Journal, 106, 2392

Hamuy M., Phillips M. M., Suntzeff N. B., Schommer R. A., Maza J., Aviles R., 1996, Astronomical Journal, 112, 2391

Harkness R. P., Wheeler J. C., 1990, in Supernovae Classification of supernovae.. pp 1–29

Heger A., Fryer C. L., Woosley S. E., Langer N., Hartmann D. H., 2003, Astrophysical Journal, 591, 288

Hicken M., Garnavich P. M., Prieto J. L., Blondin S., DePoy D. L., Kirshner R. P., Parrent J., 2007, Astrophysical Journal Letters, 669, L17

Hicken M., Wood-Vasey W. M., Blondin S., Challis P., Jha S., Kelly P. L., Rest A., Kirshner R. P., 2009, Astrophysical Journal, 700, 1097

Hillebrandt W., Niemeyer J. C., 2000, Annual Review of Astronomy and Astrophysics, 38, 191

Höflich P., 1995, Astrophysical Journal, 443

Höflich P., Khokhlov A., 1996, Astrophysical Journal, 457, 500

Höflich P., Khokhlov A. M., Wheeler J. C., 1995, Astrophysical Journal, 444, 831

Höflich P., Stein J., 2002, Astrophysical Journal, 568, 779

Howell D. A., 2001, Astrophysical Journal Letters, 554, L193

Howell D. A., Höflich P., Wang L., Wheeler J. C., 2001, Astrophysical Journal, 556, 302

Howell D. A., Sullivan M., Nugent P. E., Ellis R. S., Conley A. J., Le Borgne D., Carlberg R. G., Guy J., Balam D., Basa S., Fouchez D., Hook I. M., Hsiao E. Y., Neill J. D., Pain R., Perrett K. M., Pritchet C. J., 2006, Nature, 443, 308

Hoyle F., Fowler W. A., 1960, Astrophysical Journal, 132, 565

Hubble E., 1929, Proceedings of the National Academy of Science, 15, 168

Hubble E. P., 1936, Realm of the Nebulae. Yale University Press, New Haven

Hubeny I., Mihalas D., Werner K., eds, 2003, Stellar Atmosphere Modeling Vol. 288 of ASP Conference Proceedings. Astronomical Society of the Pacific

Iben Jr. I., Tutukov A. V., 1984, Astrophysical Journal Supplement Series, 54, 335

Iben Jr. I., Tutukov A. V., 1985, Astrophysical Journal Supplement Series, 58, 661

Jeffery D. J., Leibundgut B., Kirshner R. P., Benetti S., Branch D., Sonneborn G., 1992, Astrophysical Journal, 397, 304

Jha S., Branch D., Chornock R., Foley R. J., Li W., Swift B. J., Casebeer D., Filippenko A. V., 2006, Astronomical Journal, 132, 189

Jha S., Riess A. G., Kirshner R. P., 2007, Astrophysical Journal, 659, 122

Jordan IV G. C., Fisher R. T., Townsley D. M., Calder A. C., Graziani C., Asida S., Lamb D. Q., Truran J. W., 2008, Astrophysical Journal, 681, 1448

Kahabka P., van den Heuvel E. P. J., 1997, Annual Review of Astronomy and Astrophysics, 35, 69

Karp A. H., Lasher G., Chan K. L., Salpeter E. E., 1977, Astrophysical Journal, 214, 161

Kasen D., 2006, Astrophysical Journal, 649, 939

Kasen D., Plewa T., 2005, Astrophysical Journal Letters, 622, L41

Kasen D., Plewa T., 2007, Astrophysical Journal, 662, 459

Kasen D., Röpke F. K., Woosley S. E., 2009, Nature, 460, 869

Kasen D., Thomas R. C., Nugent P., 2006, Astrophysical Journal, 651, 366

Khokhlov A., 1993, Astrophysical Journal Letters, 419, L77+

Khokhlov A. M., 1991, Astronomy & Astrophysics, 245, 114

Kippenhahn R., Weigert A., 1990, Stellar Structure and Evolution. Springer-Verlag, Berlin

Kowalski M., et al., 2008, Astrophysical Journal, 686, 749

Koyama K., Petre R., Gotthelf E. V., Hwang U., Matsuura M., Ozaki M., Holt S. S., 1995, Nature, 378, 255

Krause O., Tanaka M., Usuda T., Hattori T., Goto M., Birkmann S., Nomoto K., 2008, Nature, 456, 617

Krisciunas K., Phillips M. M., Suntzeff N. B., 2004, Astrophysical Journal Letters, 602, L81

Krisciunas K., Suntzeff N., Candia P., Arenas J., Espinoza J., Gonzalez D., Gonzalez S., Höflich P., Landolt A., Phillips M., Pizarro S., 2003, Astronomical Journal, 125, 166

Kromer M., Sim S. A., 2009, Monthly Notices of the Royal Astronomical Society, 398, 1809

Kuchner M. J., Kirshner R. P., Pinto P. A., Leibundgut B., 1994, Astrophysical Journal Letters, 426, L89+

Kuhlen M., Woosley S. E., Glatzmaier G. A., 2006, Astrophysical Journal, 640, 407

Kurucz R., Bell B., 1995, Atomic Line Data, Kurucz CD-ROM No. 23., Cambridge, Mass.: Smithsonian Astrophysical Observatory.

Kurucz R. L., 2006, in Stee P., ed., Radiative Transfer and Applications to Very Large Telescopes Vol. 18 of EAS Publications Series, Including all the Lines. EDP Sciences, pp 129–155

Lamers H. J. G. L. M., Cassinelli J. P., 1999, Introduction to Stellar Winds. Cambridge University Press, Cambridge

Landau L., Lifschitz E., 1987, Statistische Physik Teil 1. Vol. 5 of Lehrbuch der theoretischen Physik, Akademie-Verlag, Berlin

Landau L., Lifschitz E., 1991, Hydrodynamik. Vol. 6 of Lehrbuch der theoretischen Physik, Akademie-Verlag, Berlin

Leibundgut B., 1990, Astronomy & Astrophysics, 229, 1

Leibundgut B., 2000, Astronomy and Astrophysics Review, 10, 179

Leibundgut B., 2001, Annual Review of Astronomy and Astrophysics, 39, 67

Leibundgut B., 2008, General Relativity and Gravitation, 40, 221

Leibundgut B., et al., 1993, Astronomical Journal, 105, 301

Lentz E. J., Baron E., Branch D., Hauschildt P. H., 2001, Astrophysical Journal, 557, 266

Li W., Filippenko A. V., Chornock R., Berger E., Berlind P., Calkins M. L., Challis P., Fassnacht C., Jha S., Kirshner R. P., Matheson T., Sargent W. L. W., Simcoe R. A., Smith G. H., Squires G., 2003, Publications of the Astronomical Society of the Pacific, 115, 453

Li W., Filippenko A. V., Treffers R. R., Riess A. G., Hu J., Qiu Y., 2001, Astrophysical Journal, 546, 734

Lira P., et al., 1998, Astronomical Journal, 115, 234

Livio M., 2000, in Niemeyer J. C., Truran J. W., eds, Type Ia Supernovae, Theory and Cosmology The Progenitors of Type Ia Supernovae. Cambridge University Press, p. 30

Livio M., Truran J. W., 1992, Astrophysical Journal, 389, 695

Long K. S., Knigge C., 2002, Astrophysical Journal, 579, 725

Lucy L. B., 1999a, Astronomy & Astrophysics, 344, 282

Lucy L. B., 1999b, Astronomy & Astrophysics, 345, 211

Lucy L. B., 2002, Astronomy & Astrophysics, 384, 725

Lucy L. B., 2003, Astronomy & Astrophysics, 403, 261

Lucy L. B., 2005, Astronomy & Astrophysics, 429, 19

Lucy L. B., Abbott D. C., 1993, Astrophysical Journal, 405, 738

Lundmark K., 1925, Monthly Notices of the Royal Astronomical Society, 85, 865

Madau P., della Valle M., Panagia N., 1998, Monthly Notices of the Royal Astronomical Society, 297, L17+

Maeda K., Mazzali P. A., Nomoto K., 2006, Astrophysical Journal, 645, 1331

Mannucci F., Della Valle M., Panagia N., 2006, Monthly Notices of the Royal Astronomical Society, 370, 773

Mannucci F., Della Valle M., Panagia N., Cappellaro E., Cresci G., Maiolino R., Petrosian A., Turatto M., 2005, Astronomy & Astrophysics, 433, 807

Matheson T., Filippenko A. V., Ho L. C., Barth A. J., Leonard D. C., 2000, Astronomical Journal, 120, 1499

Maza J., van den Bergh S., 1976, Astrophysical Journal, 204, 519

Mazzali P. A., 2000, Astronomy & Astrophysics, 363, 705

Mazzali P. A., Chugai N., Turatto M., Lucy L. B., Danziger I. J., Cappellaro E., della Valle M., Benetti S., 1997, Monthly Notices of the Royal Astronomical Society, 284, 151

Mazzali P. A., Danziger I. J., Turatto M., 1995, Astronomy & Astrophysics, 297, 509

Mazzali P. A., Lucy L. B., 1993, Astronomy & Astrophysics, 279, 447

Mazzali P. A., Podsiadlowski P., 2006, Monthly Notices of the Royal Astronomical Society, 369, L19

Mazzali P. A., Röpke F. K., Benetti S., Hillebrandt W., 2007, Science, 315, 825

Mazzali P. A., Sauer D. N., Pastorello A., Benetti S., Hillebrandt W., 2008, Monthly Notices of the Royal Astronomical Society, 386, 1897

Meller H., 2003, Sterne und Weltraum, 42, 28

Metropolis N., 1987, Los Alamos Science, 15, 125

Mihalas D., 1978, Stellar Atmospheres, 2nd edn. W. H. Freeman and Company, San Francisco

Mihalas D., Weibel Mihalas B., 1984, Foundations of radiation hydrodynamics. Oxford University Press, New York

Minkowski R., 1941, Publications of the Astronomical Society of the Pacific, 53, 224

Misner C., Thorne K., Wheeler J., 1973, Gravitation. W.H. Freeman and Company, San Francisco

Motl P. M., Frank J., Tohline J. E., D'Souza M. C. R., 2007, Astrophysical Journal, 670, 1314

Napiwotzki R., Yungelson L., Nelemans G., Marsh T. R., Leibundgut B., Renzini R., Homeier D., Koester D., Moehler S., Christlieb N., Reimers D., Drechsel H., Heber U., Karl C., Pauli E.-M., 2004, in Hilditch R. W., Hensberge H., Pavlovski K., eds, Spectroscopically and Spatially Resolving the Components of the Close Binary Stars Vol. 318 of Astronomical Society of the Pacific Conference Series, Double degenerates and progenitors of supernovae type Ia. pp 402–410

Nelemans G., 2005, in Hameury J.-M., Lasota J.-P., eds, The Astrophysics of Cataclysmic Variables and Related Objects Vol. 330 of Astronomical Society of the Pacific Conference Series, AM CVn stars. pp 27–+

Niemeyer J. C., Hillebrandt W., 1995, Astrophysical Journal, 452, 769

Niemeyer J. C., Woosley S. E., 1997, Astrophysical Journal, 475, 740

Nomoto K., 1982, Astrophysical Journal, 253, 798

Nomoto K., Kondo Y., 1991, Astrophysical Journal Letters, 367, L19

Nomoto K., Sugimoto D., Neo S., 1976, Astrophysics and Space Science, 39, L37

Nomoto K., Thielemann F.-K., Yokoi K., 1984, Astrophysical Journal, 286, 644

Nugent P., Baron E., Branch D., Fisher A., Hauschildt P. H., 1997, Astrophysical Journal, 485, 812

Nugent P., Phillips M., Baron E., Branch D., Hauschildt P., 1995, Astrophysical Journal Letters, 455, L147+

Osterbrock D. E., 1974, Astrophysics of gaseous nebulae. W. H. Freeman and Co., San Francisco

Ostriker J. P., Steinhardt P. J., 1995, Nature, 377, 600

Pakmor R., Kromer M., Röpke F. K., Sim S. A., Ruiter A. J., Hillebrandt W., 2009, arXiv 0911.0926, accepted to Nature

Pastorello A., et al., 2007a, Monthly Notices of the Royal Astronomical Society, 377, 1531

Pastorello A., et al., 2007b, Monthly Notices of the Royal Astronomical Society, 376, 1301

Patat F., 2005, Monthly Notices of the Royal Astronomical Society, 357, 1161

Patat F., Benetti S., Cappellaro E., Danziger I. J., della Valle M., Mazzali P. A., Turatto M., 1996, Monthly Notices of the Royal Astronomical Society, 278, 111

Patat F., Benetti S., Cappellaro E., Turatto M., 2006, Monthly Notices of the Royal Astronomical Society, 369, 1949

Patat F., et al., 2007, Science, 317, 924

Perlmutter S., 2003, Physics Today, 56, 040000

Perlmutter S., et al., 1997, Astrophysical Journal, 483, 565

Perlmutter S., et al., 1999, Astrophysical Journal, 517, 565

Phillips M. M., 1993, Astrophysical Journal, 413, L105

Phillips M. M., et al., 2007, Publications of the Astronomical Society of the Pacific, 119, 360

Phillips M. M., Lira P., Suntzeff N. B., Schommer R. A., Hamuy M., Maza J., 1999, Astronomical Journal, 118, 1766

Phillips M. M., Wells L. A., Suntzeff N. B., Hamuy M., Leibundgut B., Kirshner R. P., Foltz C. B., 1992, Astronomical Journal, 103, 1632

Pinto P. A., Eastman R. G., 2000a, Astrophysical Journal, 530, 744

Pinto P. A., Eastman R. G., 2000b, Astrophysical Journal, 530, 757

Plewa T., 2007, Astrophysical Journal, 657, 942

Plewa T., Calder A. C., Lamb D. Q., 2004, Astrophysical Journal Letters, 612, L37

Pozdniakov L. A., Sobol I. M., Siuniaev R. A., 1983, Astrophysics and Space Physics Reviews, 2, 189

Press W. H., Teukolsky S. A., Vetterling W. T., Flannery B. P., 1992, Numerical recipes in C. The art of scientific computing. Cambridge University Press, Cambridge

Pskovskii I. P., 1977, Soviet Astronomy, 21, 675

Reinecke M., Hillebrandt W., Niemeyer J. C., 2002, Astronomy & Astrophysics, 391, 1167

Reinecke M., Hillebrandt W., Niemeyer J. C., Klein R., Gröbl A., 1999, Astronomy & Astrophysics, 347, 724

Renzini A., 1999, in Walsh J. R., Rosa M. R., eds, Chemical Evolution from Zero to High Redshift Chemical Evolution on the Scale of Clusters of Galaxies, and Beyond. pp 185–+

Rest A., Welch D. L., Suntzeff N. B., Oaster L., Lanning H., Olsen K., Smith R. C., Becker A. C., Bergmann M., Challis P., Clocchiatti A., Cook K. H., Damke G., Garg A., Huber M. E., Matheson T., Minniti D., Prieto J. L., Wood-Vasey W. M., 2008, Astrophysical Journal Letters, 681, L81

Riess A. G., et al., 1998, Astronomical Journal, 116, 1009

Riess A. G., et al., 2004, Astrophysical Journal, 607, 665

Riess A. G., et al., 2007, Astrophysical Journal, 659, 98

Riess A. G., Filippenko A. V., Li W., Treffers R. R., Schmidt B. P., Qiu Y., Hu J., Armstrong M., Faranda C., Thouvenot E., Buil C., 1999, Astronomical Journal, 118, 2675

Riess A. G., Press W. H., Kirshner R. P., 1996, Astrophysical Journal, 473, 88

Roelofs G., Bassa C., Voss R., Nelemans G., 2008, Monthly Notices of the Royal Astronomical Society, 391, 290

Röpke F. K., 2005, Astronomy & Astrophysics, 432, 969

Röpke F. K., Hillebrandt W., 2005, Astronomy & Astrophysics, 431, 635

Röpke F. K., Hillebrandt W., Niemeyer J. C., Woosley S. E., 2006, Astronomy & Astrophysics, 448, 1

Röpke F. K., Hillebrandt W., Schmidt W., Niemeyer J. C., Blinnikov S. I., Mazzali P. A., 2007, Astrophysical Journal, 668, 1132

Röpke F. K., Niemeyer J. C., 2007, Astronomy & Astrophysics, 464, 683

Röpke F. K., Woosley S. E., Hillebrandt W., 2007, Astrophysical Journal, 660, 1344

Rowan-Robinson M., 1985, The cosmological distance ladder: Distance and time in the universe. W. H. Freeman and Co., New York

Ruiter A. J., Belczynski K., Fryer C., 2009, Astrophysical Journal, 699, 2026

Rybicki G. B., Lightman A. P., 1979, Radiative Processes in Astrophysics. Wiley-Interscience

Saio H., Nomoto K., 1985, Astronomy & Astrophysics, 150, L21

Saio H., Nomoto K., 1998, Astrophysical Journal, 500, 388

Salvo M. E., Cappellaro E., Mazzali P. A., Benetti S., Danziger I. J., Patat F., Turatto M., 2001, Monthly Notices of the Royal Astronomical Society, 321, 254

Sauer D. N., Mazzali P. A., Blondin S., Stehle M., Benetti S., Challis P., Filippenko A. V., Kirshner R. P., Li W., Matheson T., 2008, Monthly Notices of the Royal Astronomical Society, 391, 1605

Scannapieco E., Bildsten L., 2005, Astrophysical Journal Letters, 629, L85

Schlosser W., 2003, Sterne und Weltraum, 42, 34

Schmidt W., Niemeyer J. C., Hillebrandt W., 2006, Astronomy & Astrophysics, 450, 265

Schmidt W., Niemeyer J. C., Hillebrandt W., Röpke F. K., 2006, Astronomy & Astrophysics, 450, 283

Seaton M. J., 1995, The opacity project. Institute of Physics Pub., Bristol, UK

Shen K. J., Bildsten L., 2009, Astrophysical Journal, 699, 1365

Shull J. M., van Steenberg M., 1982, ApJS, 48, 95

Sim S. A., 2007, Monthly Notices of the Royal Astronomical Society, 375, 154

Sim S. A., Sauer D. N., Röpke F. K., Hillebrandt W., 2007, Monthly Notices of the Royal Astronomical Society, 378, 2

Sobolev V. V., 1957, Soviet Astronomy, 1, 678

Stehle M., Mazzali P. A., Benetti S., Hillebrandt W., 2005, Monthly Notices of the Royal Astronomical Society, 360, 1231

Stritzinger M., Leibundgut B., 2005, Astronomy & Astrophysics, 431, 423

Stritzinger M., Mazzali P. A., Sollerman J., Benetti S., 2006, Astronomy & Astrophysics, 460, 793

Taubenberger S., et al., 2008, Monthly Notices of the Royal Astronomical Society, 385, 75

Thielemann F.-K., Nomoto K., Yokoi K., 1986, Astronomy & Astrophysics, 158, 17

Travaglio C., Hillebrandt W., Reinecke M., Thielemann F.-K., 2004, Astronomy & Astrophysics, 425, 1029

Truran J., Arnett D., Cameron A., 1967, Canad. J. Physics, 45, 2315

Turatto M., 2003, in Weiler K., ed., Supernovae and Gamma-Ray Bursters Vol. 598 of Lecture Notes in Physics, Berlin Springer Verlag, Classification of Supernovae. pp 21–36

Turatto M., Benetti S., Cappellaro E., Danziger I. J., Della Valle M., Gouiffes C., Mazzali P. A., Patat F., 1996, Monthly Notices of the Royal Astronomical Society, 283, 1

Turatto M., Cappellaro E., Benetti S., 1994, Astronomical Journal, 108, 202

Turner M. S., Tyson J. A., 1999, Reviews of Modern Physics Supplement, 71, 145

Unsöld A., Baschek B., 2002, Der neue Kosmos. Springer, Berlin

van den Bergh S., Tammann G. A., 1991, Annual Review of Astronomy and Astrophysics, 29, 363

Veigele W. J., 1973, Atomic Data, 5, 51

Verner D. A., Ferland G. J., Korista K. T., Yakovlev D. G., 1996, Astrophysical Journal, 465, 487

Verner D. A., Yakovlev D. G., 1995, Astronomy and Astrophysics Supplement Series, 109, 125

Voss R., Nelemans G., 2008, Nature, 451, 802

Wang L., Baade D., Höflich P., Khokhlov A., Wheeler J. C., Kasen D., Nugent P. E., Perlmutter S., Fransson C., Lundqvist P., 2003, Astrophysical Journal, 591, 1110

Wang L., Wheeler J. C., 2008, Annual Review of Astronomy and Astrophysics, 46, 433

Warner B., 1995, Cataclysmic Variable Stars. Vol. 28 of Cambridge Astrophysics Series, Cambridge University Press

Webbink R. F., 1984, Astrophysical Journal, 277, 355

Weiler K. W., Panagia N., Sramek R. A., van Dyk S. D., Williams C. L., Stockdale C. J., Kelley M. T., 2009, in G. Giobbi, A. Tornambe, G. Raimondo, M. Limongi, L. A. Antonelli, N. Menci, & E. Brocato ed., American Institute of Physics Conference Series Vol. 1111 of American Institute of Physics Conference Series, Radio Emission from Supernovae. pp 440–447

Weinberg S., 1989, Reviews of Modern Physics, 61, 1

Whelan J., Iben I. J., 1973, Astrophysical Journal, 186, 1007

Wilson O. C., 1939, Astrophysical Journal, 90, 634

Wood-Vasey W. M., et al., 2007, Astrophysical Journal, 666, 694

Wood-Vasey W. M., Friedman A. S., Bloom J. S., Hicken M., Modjaz M., Kirshner R. P., Starr D. L., Blake C. H., Falco E. E., Szentgyorgyi A. H., Challis P., Blondin S., Mandel K. S., Rest A., 2008, Astrophysical Journal, 689, 377

Woosley S. E., Taam R. E., Weaver T. A., 1986, Astrophysical Journal, 301, 601

Woosley S. E., Weaver T. A., 1986, Annual Review of Astronomy and Astrophysics, 24, 205

Woosley S. E., Weaver T. A., 1994, Astrophysical Journal, 423, 371

Woosley S. E., Wunsch S., Kuhlen M., 2004, Astrophysical Journal, 607, 921

Yamanaka M., et al., 2009, ArXiv e-prints

Yoon S.-C., Podsiadlowski P., Rosswog S., 2007, Monthly Notices of the Royal Astronomical Society, 380, 933

Zwicky F., 1939, Physical Review, 55, 726